Embankment breaching by overtopping: laboratory and field experiments monitored by photogrammetry

Thesis submitted to attain the degree of Doctor in Engineering Sciences and Technology by

Masoumeh Ebrahimi

Presented on 02 April 2026

Department of Civil and Environmental Engineering
Institute of Mechanics, Materials and Civil Engineering
Louvain School of Engineering
UCLouvain
Louvain-la-Neuve, Belgium

Thesis Comittee:

Prof. Sandra **Soares-Frazão** (supervisor)	UCLouvain, Belgium
Dr. Myron **van Damme**	Rijkswaterstaat WVL, the Netherlands
Dr. Kamal **El Kadi Abderrezzak**,	CNR, CESAME, France
Dr. Didier **Bousmar**,	SPW MI, Belgium
Dr. Sylvie **Van Emelen**,	ECAM, Belgium
Prof. Hadrien **Rattez**,	UCLouvain, Belgium
Prof. Grégoire **Winckelmans**	UCLouvain, Belgium

To the resilient women of my homeland, Iran,
for your tireless pursuit of freedom.
May this work inspire those
who dare to follow their path beyond borders.

Remerciements

Lorsque j'ai commencé mon doctorat, je voyais à peine l'horizon. Le chemin me semblait être un véritable parcours du combattant. C'était comme si j'entrais dans un monde dont je ne connaissais rien. Pourtant, le jour où j'ai decidé de suivre mes rêves, je me suis fait une promesse : quoi qu'il arrive, je n'abandonnerai pas. Si la vie m'offrait l'opportunité de suivre ce chemin comme je le souhaitais, c'est que j'étais probablement capable de le parcourir jusqu'au bout.

Cependant, tout ce travail, aujourd'hui présenté dans ce manuscrit, n'aurait jamais vu le jour sans le soutien, l'accompagnement, l'aide précieuse et la sagesse des personnes qui m'ont entourée au cours de ces six dernières années.

Je tiens tout particulièrement à remercier ma promotrice, Sandra Soares-Frazão, de m'avoir offerte cette extraordinaire opportunité d'apprentissage et d'immersion dans un environnement que tu ne cesses d'enrichir et de faire évoluer. Je sais que choisir une assistante qui ne parlait pas un mot de français au départ n'était pas une décision évidente, et j'imagine les incertitudes que cela a pu représenter. Pourtant, tu as cru en moi, et je t'en serai toujours reconnaissante.

Tu as aussi été, sans le savoir, ma meilleure professeure de français. J'ai énormément appris simplement en t'écoutant parler, enseigner et interagir avec les autres. Ce poste d'assistante m'a permis non seulement d'acquérir de nombreuses connaissances, mais aussi d'apprendre à communiquer dans un environnement pédagogique et humain particulièrement enrichissant. Il m'a également offert un équilibre essentiel, en me permettant parfois de prendre du recul par rapport à la recherche et de m'ouvrir à d'autres dimensions tout aussi importantes.

Travailler à tes côtés et t'observer au quotidien m'a apporté certaines des leçons les plus précieuses de ma vie. Dans le monde de la recherche et de l'académie, j'ai toujours admiré ta capacité d'analyse et d'interprétation, ton esprit critique, ainsi que ton incroyable mémoire. Tu as toujours fait le maximum pour mettre à ma disposition les moyens nécessaires à la réussite de mes recherches. Plus encore, tu m'as constamment encouragée à aller au bout de mes objectifs et à croire qu'avec de la volonté, tout devient possible.

I would like to express my sincere and profound gratitude to the members of my jury committee, Sylvie Van Emelen and Hadrien Rattez, as well as to the other members of my jury: Myron van Damme, Kamal El Kadi Abderrezzak, Didier Bousmar, and Grégoire Winckelmans. Thank you for the valuable time and effort you dedicated to reviewing this thesis, and for the thought-provoking questions that helped me improve this thesis over the past two months. Our discussions during the private defense were truly inspiring.

Je saisis ainsi l'occasion de ces quelques pages pour exprimer ma profonde gratitude envers toutes les personnes qui ont jalonné mon parcours. Si ma mémoire venait à me faire défaut et que certains noms manquaient dans ces lignes, sachez que votre soutien n'en a pas moins été précieux. J'espère que chacune et chacun se reconnaîtra dans ces mots, car vous méritez pleinement d'être associé·es à cette réussite.

L'ambiance au sein de l'équipe d'hydraulique et de GCE m'a profondément touchée à mon arrivée en Belgique. Vous m'avez tous donné ce sentiment extraordinaire de faire partie d'une équipe solidaire, qui n'hésite jamais à apporter son aide lorsque cela est nécessaire.

Je tiens à remercier tout particulièrement Yves Zech pour ses mots bienveillants dès mon arrivée, pour son encouragement constant et pour le regard plein de confiance et d'admiration qu'il a toujours porté sur mon parcours.

Parmi les personnes qui ont marqué ce parcours, je tiens à remercier tout particulièrement Robin Meurice, avec qui j'ai partagé mon quotidien de travail pendant plusieurs années. Merci, Robin, de m'avoir appris tant de choses avec simplicité et modestie, sans jamais me juger. Merci de m'avoir fait vivre cette expérience incroyable durant mes premières années à l'UCLouvain, grâce à ton aide, ta disponibilité et la générosité avec laquelle tu partageais tes connaissances. Merci aussi de m'avoir écoutée lorsque j'avais besoin de parler, toujours avec sincérité, sans interpréter mes propos ni jouer un rôle.

Je tiens également à remercier chaleureusement Catherine Doneux pour ses encouragements constants et son engagement dans le soutien de nos recherches en tant que directrice de la plateforme LEMSC. Tu ne peux pas imaginer à quel point ton soutien m'a été précieux lors des mesures de terrain réalisées dans le cadre du projet Polder2C. Sans l'aide de l'équipe d'Hydraulique et du LEMSC, tout cela n'aurait tout simplement pas été possible. Et bien sûr, Pierre Mertens de Wilmars, je n'oublierai jamais ton aide précieuse pendant cette campagne d'essais. Tu n'hésitais jamais à faire tous les efforts nécessaires pour que tout se déroule dans les meilleures conditions.

And while mentioning the Polder2C project, I would also like to express my sincere gratitude to Myron van Damme for offering me this unique opportunity, which gave profound meaning to my entire research journey. Thank you, Myron, for your trust and confidence, they were invaluable to me at that stage of my PhD. Our many discussions and meetings throughout the project taught me an enormous amount and helped me develop a strong confidence in myself. I would also like to warmly thank André Koelewijn for his insightful comments and for generously sharing his knowledge and experience throughout the project. Together, you both taught me many valuable lessons and helped me broaden my perspective in countless ways.

Mes profonds remerciements vont également à l'équipe du laboratoire hydraulique du SPW Mobilité et Infrastructures à Châtelet, et en particulier à Didier Bousmar et Catherine Swartenbroekx, pour votre soutien et votre confiance tout au long de nos campagnes d'essais durant ces trois dernières années.Vous m'avez accordé une grande liberté dans la gestion des essais, au point que j'avais parfois l'impression de faire pleinement partie du laboratoire de Châtelet. Cette expérience m'a permis de développer de nombreuses compétences, tant dans la gestion des campagnes expérimentales que dans la communication et le travail au sein d'une équipe aussi sympathique qu'engagée. Je suis également extrêmement reconnaissante envers toute l'équipe des techniciens du laboratoire pour les efforts fournis lors de la construction des dispositifs et de la réalisation des essais. Sans votre aide précieuse, une campagne expérimentale d'une telle ampleur n'aurait tout simplement pas été possible.

Et bien sûr, Nathan, ton rôle et ton aide dans le démarrage de ces essais resteront inoubliables et inestimables. Tu as toujours fait preuve de gentillesse et de patience à mon égard. Ta curiosité et ton ambition m'ont toujours impressionnée. Tous les efforts que tu as consacrés à l'amélioration des techniques de mesure méritent d'être soulignés, et ils ont largement contribué à la qualité du travail réalisé au terme de cette recherche. Tu m'as aussi énormément appris en français. Toi et Marie-Thérèse formez un couple formidable, et j'ai eu beaucoup de chance de faire votre connaissance.

J'ai également eu la chance de travailler avec plusieurs étudiants dans le cadre de leurs travaux de fin d'études, notamment Arthur Gilles, Corentin Zgajewski Delforge, Emy Jergeay, Wen-hui Zhang, Cyril Anspach, Arthur Eugène et Lucien Maron. Merci pour votre implication et votre aide précieuse durant les campagnes d'essais au SPW MI et au LEMSC.

Mes collègues au sein de l'équipe d'hydraulique ont grandement facilité mon quotidien, que ce soit à travers une simple conversation, un moment de soutien ou une aide précieuse dans le travail. Je tiens à remercier chaleureusement Gérardson, Pierre-Yves, Rotchild, Jiangtao, Charles, Nathan, Martin, Siyuan, Henriette et Benoît.

La diversité au sein de notre équipe m'a énormément apporté et m'a permis d'apprendre beaucoup sur d'autres cultures, d'autres façons de penser et d'autres horizons. Pierre-Yves, je te connais pour ta gentillesse, ta modestie et la compassion que tu portes aux autres. L'amour et l'attention que tu portes à ta femme et à tes enfants m'ont beaucoup inspirée. Vous m'avez tous aidée, que ce soit dans ma recherche ou dans les tâches didactiques du quotidien. Merci Charles pour ton aide précieuse dans les tâches d'encadrement, qui m'a permis de souffler lorsque j'en avais besoin, notamment pendant ma confirmation au doctorat et durant cette fin de thèse. Et toi Martin, tu sais que je savais toujours sur qui compter en cas de problème ou lorsque j'avais besoin d'une aide urgente : c'était toujours toi. Siyuan, I'm truly happy to have had the opportunity to work with you over the past year. Our discussions always brought new insights into our work, and I learned a great deal through the ideas we shared together. Et toi Henriette, je suis tellement contente que tu aies repris le défi du projet BONSAI et assuré la continuité des travaux initiés dans le cadre du projet Polder2C's. Je suis sincèrement impressionnée par ta capacité à absorber rapidement de nouvelles connaissances et par ta curiosité à découvrir d'autres aspects de la recherche. Avec Pauline, nous avons eu beaucoup de chance de créer et de partager une ambiance formidable dans notre bureau. Et toi Benoît, nos conversations autour des algorithmes derrière la photogrammétrie et des méthodes d'imagerie m'ont beaucoup inspirée au cours des derniers mois.

Au sein de l'équipe GCE, j'ai eu la chance de rencontrer des personnes particulièrement bienveillantes comme Pierre Latteur et João Almeida. Les portes toujours ouvertes de votre bureau m'ont souvent permis d'entrer simplement pour dire bonjour… avant de commencer des conversations philosophiques, géopolitiques ou économiques — comme nos discussions sur le prix de l'or avec Pierre haha — qui duraient parfois bien plus longtemps que prévu. Votre gentillesse et votre bienveillance m'ont toujours profondément touchée.

Mes jeunes collègues du GCE, notamment ceux qui sont partis depuis — Haythem, Mustafa, Jonas, Igor, José, Serena et Ryan — ont rendu mon arrivée et mes premières années particulièrement agréables.

Je remercie également mes collègues actuels Martin, Jens, Basile, Benjamin, Justin, Adèle, Nicolas, Hossein, Shijin et Guillaume, qui apportent aujourd'hui une dynamique différente et enrichissante à l'équipe GCE.

Sans l'aide régulière des membres de l'équipe du LEMSC, cette aventure n'aurait pas été la même. Je tiens à remercier chaleureusement Viviane pour nos conversations quotidiennes, Antoine pour tes nombreuses aides précieuses, et Nathalie pour ta bonne humeur et tout ce que tu fais pour le GCE. Alex, je t'appelle souvent « l'esprit de Vinci » tant ta mémoire vivante et tes belles anecdotes m'impressionnent. Laurent, merci pour nos longues discussions sur d'autres aspects de la vie que la recherche. Sophie, merci pour nos conversations pleines de joie et de rires. Je remercie également Christophe, Isabelle, Vincent, Stéphane, Quentin, Raphaël et Justin. Nos moments partagés et tous nos échanges continueront à m'apporter beaucoup de joie et de beaux souvenirs.

And you, Julia, you are undoubtedly one of those rare and genuine souls that only a few people are fortunate enough to meet in their lifetime. I became attached to you as if you were my own sister. You continuously inspired and encouraged me throughout my entire PhD journey. Be proud of the wonderful person you are. After your departure, our young colleague Pauline naturally took over your role of taking care of me with the same kindness and warmth.

J'ai également eu la chance d'être entourée de personnes merveilleuses, tant dans ma vie privée que professionnelle. Annik et Yves, vous m'avez énormément inspirée par votre parcours et votre manière de vivre. À mes yeux, vous êtes comme un jeune couple de vingt ans, rempli d'amour, de complicité, de compassion et de vivacité. J'ai eu énormément de chance de croiser votre chemin.

Je tiens aussi à remercier chaleureusement Cécile et Michel pour votre gentillesse et votre aide précieuse envers Sepehr. Je peux même dire que vous avez été comme des grands-parents pour lui. J'espère qu'un jour il réalisera la chance qu'il a eue d'apprendre autant de choses à tes côtés, Cécile, durant son enfance. Merci pour tout ce que vous faites pour nous. Et toi, Nanou, nos discussions ont souvent été pour moi comme de véritables séances de thérapie. Je sais auprès de qui me réfugier lorsque je suis triste.

Et toi, Hanane, merci pour tout ce que tu as fait pour moi. Avoir une amie comme toi m'a énormément aidée à traverser les moments difficiles, surtout durant ces dernières mois. Je t'admire profondément et je suis heureuse que Sepehr ait la chance de grandir entouré d'amis comme tes enfants.

My dearest Iranian friends, Roghayeh and Hamid, you made our first years of living in Belgium so much easier. The help and support you gave us were incredibly precious during the moments when we truly needed them. I am deeply grateful for our friendship and very proud of the bond we share.

Thank you as well to Nasim and Ali for always being there whenever we needed you. They say that family is sometimes the friends we choose in life, and you are a beautiful example of that. I also warmly thank my dear friends Elham, Mustafa, Somayeh and Mohammad for all the joyful moments we shared together.

Je tiens également à remercier mes parents, ma petite sœur, mon grand frère, ma belle-famille ainsi que mes amis en Iran pour tout ce que vous avez construit en nous avant notre départ. Vous faites profondément partie de mon identité, et penser à vous m'apporte toujours du sourire et de la joie. Vous êtes sans aucun doute ce que j'ai de plus précieux dans cette vie. Le fait de devoir vous quitter a été l'une des plus grandes douleurs de ma vie, mais aussi peut-être l'une des leçons les plus importantes : comprendre réellement la valeur de ce que l'on possède lorsqu'on en est éloigné.

Et enfin, ces derniers mots sont pour mon époux et mon fils, les êtres les plus précieux de mon univers. Je vous remercie tous les deux pour tous les sacrifices consentis au cours de ces dernières années. Je vous demande aussi pardon de vous avoir entraînés dans une vie qui n'a pas toujours été facile et qui nous a apporté beaucoup d'incertitudes. Ali, sans toi, une telle aventure de vie n'aurait même pas été imaginable. Merci pour tout ce que tu m'as apporté au cours de cette vie et d'avoir été mon miroir. C'est seulement dans le cœur d'une autre âme que l'on peut véritablement se retrouver soi-même et percevoir la présence du divin. Et toi, Sepehr, lorsque je regarde dans tes yeux, j'y vois déjà un grand homme — un homme qui marquera profondément la vie de nombreuses personnes.

Thesis Committee following private defence, 2nd April 2026. From left to right: Prof. Hadrien Rattez, Dr. Didier Bousmar, Dr. Myron van Damme, Masoumeh Ebrahimi, Prof. Sandra Soares-Frazão, Dr. Sylvie Van Emelen, Dr. Kamal El Kadi Abderrezzak, Prof. Grégoire Winckelmans.

Abstract

Earthen embankments—encompassing dams, dikes, and levees—have played a vital role in human history. The ultimate goal of these structures is to guarantee an integrated fluvial system within watersheds, providing essential services such as flood protection, water storage, and navigation.

Climate change impacts the stability and performance of levees, dikes, and earthen dams by simultaneously increasing the magnitude of hydraulic loads acting upon them and degrading their geotechnical resistance. With regards to hydraulic load magnitude, climate change introduces "non-stationarity," patterns where historical weather patterns are no longer reliable predictors of future loads. This results in intensified hydraulic stresses both in terms of frequency and intensity of extreme weather events on earthen structures.

Within this context, laboratory and field experimental studies play a crucial role in capturing and documenting the fundamental physical mechanisms of failure under different circumstances and providing high-quality datasets for validation of predictive tools.

This thesis developed a methodological experimental framework for monitoring these failure process, quantifying the erosion, and tracking the breach progression into earthen embankments under wave overtopping and overflowing loads. A major innovation of the study is the application of close-range Structure-from-Motion (SfM) photogrammetry to accurately to in-situ experiments conducted on a prototype levee at the Living Lab Hedwige Prosperpolder in frame of the Interreg Polder2C's and regional Lime in Clay projects. Furthermore, this research enhanced this photogrammetric technique for highly dynamic laboratory environments, specifically during small- and medium-scale sand embankment breaching.

To bridge the critical gap between small-scale laboratory tests and full-scale reality, the research features novel medium-scale (1-m-high, conducted at the Hydraulics Research Laboratory of SPW MI at Châtelet, Belgium) and small-scale (0.2-m-high, conducted at the UCLouvain LEMSC Laboratory) experimental modeling of sand embankments. Recognizing the fundamental challenge of satisfying simultaneous hydraulic and geotechnical similitude, this study adopts a 'scale-series' approach while implementing the Froude similarity to embankment dimensions and overtopping load.

The medium-scale models eliminate the scale effects induced in small models, especially inherent in models with sediment modeling, and enable the

replication of complex processes at a closer scale to the reality. A series of new medium-scale dike breaching tests have been conducted to examine the influence of (i) sediment granulometry and (ii) overtopping conditions (constant reservoir level versus constant reservoir inflow) on the temporal evolution of breach through sand embankments. The results of the present study were combined with well-documented experimental data from the literature for sand embankments ranging from 0.3 m to 1.6 m in height. This extended comparison highlights the profound influence of reservoir dimensions on breaching dynamics, across varying overtopping conditions.

To investigate the scale effects, two distinct analytical methodologies were applied: (i) hydraulic and morphologic comparative analysis, where direct comparison of upscaled variables (water levels, hydrographs, breach width) using Froude scaling were performed; and (ii) dimensionless analysis where a verification of the sediment transport regimes using the grain Reynolds number was used to quantify the divergence between model and prototype physics. The relevancy of Settling Velocity Adjustment application to sand embankment breaching was further investigated.

Table of contents

Chapter 1

Context and Motivation

1.1 Introduction to Earthen Embankments: Dams, Dikes, and Levees

Earthen embankments—encompassing dams, dikes, and levees—have played a vital role in human history. The ultimate goal of these structures is to guarantee an integrated fluvial system within watersheds, providing essential services such as flood protection, water storage, and navigation. Among the earliest engineering works, levees are the most common flood protection structures, safeguarding inhabited river valley areas against inundation.

Historically, the scale of these projects was immense. In ancient Egypt, a series of levees was built along the left bank of the Nile River for more than 966 km (600 miles), stretching from Aswan to the Mediterranean. The cooperative and coordinated enterprise involved in building such massive embankments likely served as a strong incentive for the development of organized societies and unified governments in ancient Egypt, Mesopotamia, and China (Britannica.com). Typically, these embankments are constructed from locally available earth materials, piled along riverbanks or foundation lines, and shaped into a trapezoidal form with a horizontal crest and inclined inner and outer slopes.

While sharing similar construction methods, embankments serve various purposes, including fluvial transportation, power generation, water supply, and flood mitigation (ASCE/EWRI Task Committee, 2011). In the United States, early earthen embankments were built primarily to deviate water streams for mechanical power in lumber and grain mills. Later, between the 1930s and 1970s, approximately 12,000 dams were constructed to mitigate watershed erosion and control floods. According to the National Inventory of Dams, there are currently about 85,000 dams distributed across the USA, of which approximately 74,000 (87%) are earthen dams.

It is important to distinguish between dams and levees or dikes, although they share similar geotechnical characteristics. Dams are typically designed to retain water permanently (or for long durations) to create a reservoir, subjecting them to constant frontal hydraulic loading and seepage (see Figure 1.1a). In contrast, levees (or dikes) are designed to protect land from seasonal inundation or temporary flood events (see Figure 1.1b,c).

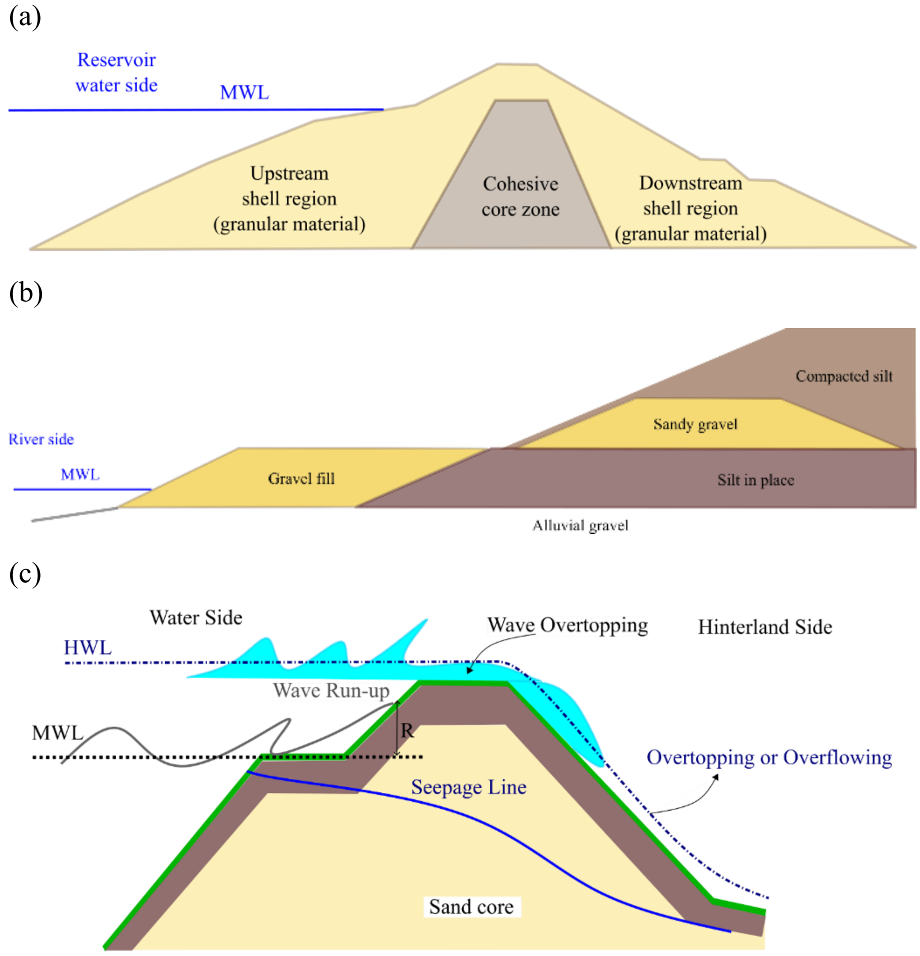

Figure 1.1 Schematic representation of typical earthen embankment profiles and their dominant hydraulic loading conditions: (a) Composite dam with central cohesive core and granular shells subjected to frontal reservoir loading and seepage; (b) Zoned river dike featuring cohesive and granular zones (adapted from Bonelli, 2021); and (c) Typical Dutch levee comprising a sand core protected by a cohesive clay layer and grass cover, exposed to wave overtopping (MWL: Mean water level, and HWL: High water level).

A river levee may undergo both frontal and lateral flow simultaneously, as well as small wave overtopping events. Sea dikes, on the other hand, are highly exposed to dynamic coastal forcing, including storm surge overflowing, wave run-up resulting in wave overtopping, and combined surge-wave overtopping loads (Figure 1.1c).

A fundamental distinction therefore lies in the hydraulic boundary conditions (ASCE/EWRI, 2011). Dams impound finite storage, where significant outflow causes upstream head dissipation. Conversely, levees withstand effectively infinite upstream volumes, maintaining sustained hydraulic loads. Consequently, while failure mechanisms are similar, the hydraulic drive differs: reservoir depletion governs dams, whereas downstream tailwater evolution often controls levees.

Design criteria and structural composition further differentiate these embankments. While dams are typically designed to strictly preclude overtopping throughout their service life, river and sea dikes are often engineered to withstand occasional wave overtopping during extreme storm events.

Structurally, man-made earthen dams often feature a composite cross-section with a central impervious core (e.g., clay, concrete, or steel sheet piles) supported by granular shells (shoulders) to resist constant hydraulic pressure. Conversely, levees — particularly in deltaic regions — often consist of a granular sand core protected by a cohesive clay layer and a grass cover to resist transient erosion forces. Furthermore, unlike dams which typically maintain a fixed geometry, levees are frequently raised over decades to adapt to subsidence or rising flood levels. This historical evolution often results in a heterogeneous internal structure, creating stratified layers with varying erodibility that complicate the failure process.

On the other hand, natural dams typically form when a drainage path is blocked by landslides, debris flows, glaciers, or moraines, or when water fills closed depressions like tectonic basins and calderas. Landslide dams, specifically, are created by mass movements of earth and rock into a valley bottom (Walder and O’Connor, 1997). They are highly diverse in their geometry and internal composition — often containing large, heterogeneous materials like rocks and tend to be very broad. Because they form suddenly and lack engineered spillways, they pose a significant flood hazard if they are overtopped and breach. These factors result in different failure processes and timings.

1.2 Socio-Economic Impact and Climate Context

The global reliance on these structures is significant. About 60% of the Netherlands is protected from storm surges and river overflowing by a complex system of dikes, dams, and natural sand dunes (Visser, 1998). A secondary flood control system, consisting of drainage canal levees, further manages rainfall and seepage water at the local scale (Rikkert, 2022). Similarly, in England and Wales, more than 35,000 km of embankments serve as flood defense structures, protecting deltas and lowlands from river and estuarine flooding. On the Chinese mainland, 91.4% of reservoir dams were classified as embankment dams by the end of 2018, playing a critical role in socio-economic development. The US levee system is vast, with estimates suggesting over 100,000 miles of levees nationwide, though the National Levee Database (NLD) currently tracks approximately 30,000 miles. 97% of these systems are primarily earthen embankments (Janga et al., 2024). The average age of levees within the US Army Corps of Engineers (USACE) authority is roughly 50 years, with many predating modern engineering standards.

In Europe, levees and flood defenses protect an estimated economic value of over 2 trillion Euro. In the absence of these defenses, annual flood damage would run into the billions

1.2.1 Historical significance and recent failure statistics

The consequences of an inundation due to a levee failure can be catastrophic loss of life, extensive property damage, and long-term adverse environmental impacts. The socio-economic exposure protected by these systems is immense; for instance, the National Levee Database in the United States estimates that levees safeguard approximately $2.3 trillion in property value (Janga et al., 2024), while in Europe, flood defenses protect an economic value estimated at over €2 trillion reported by EUCOLD Working group on levees and flood defences (2018). To underscore the consequences of structural inadequacy, several historical cases and recent statistics are examined below.

The North Sea storm surge of 1953 (Figure 1.2) remains a benchmark for flood disaster management in Europe. This event caused widespread levee failures and resulted in over 2,500 casualties across Belgium, England, and the Netherlands. In the Netherlands alone, the disaster prompted a paradigm shift in flood defense planning, ultimately leading to the construction of the Delta Works. Even in the absence of a full breach, the threat of failure can necessitate massive emergency interventions. For example, during the 1995 river floods in the Netherlands, the imminent threat of piping failure and dike instability forced the preventive evacuation of approximately 200,000 people.

Figure 1.2 A levee breach (Ouderkerk aan de IJssel) during North Sea storm surge of 1953 (source: Van Veen 1962)

In the United States, Hurricane Katrina (2005) serves as the most devastating modern example of levee failure. The breaching of the levee system protecting New Orleans, primarily due to overtopping and structural weaknesses, resulted in the flooding of approximately 80% of the city. The event caused 1,836 fatalities and economic damages estimated between $125 billion and $200 billion.

More recently, the Mississippi River floods of 2011 demonstrated the operational stress placed on flood defense systems during extreme hydrological events (see Figure 1.3a). Exceptional snowmelt and rainfall stressed the levee system to the point where the U.S. Army Corps of Engineers activated floodways—effectively a deliberate, controlled breaching of levees—to relieve pressure on the mainline system see (Figure 1.3b). While this emergency action prevented uncontrolled failures in populated centers, it resulted in the inundation of vast agricultural lands downstream.

(a) (b)

Figure 1.3 Controlled breaching of levees at: (a) The confluence of the Ohio and Mississippi Rivers; (b) Aerial view of the controlled breach at the Birds Point-New Madrid Floodway. This strategic measure diverted record Mississippi River floodwaters into 130,000 acres of Missouri farmland to reduce critical pressure on the levee system protecting Cairo, Illinois. (Source: TW)

Central Europe has also experienced significant failures in recent decades. The floods of June 2013, characterized as the most severe in at least 60 years for Germany, caused levee breaches along the Elbe, Danube, and Saale rivers. These failures led to the flooding of several towns and resulted in over €4 billion in damage. Furthermore, recent climatic trends indicate increasing vulnerability; for instance, the summer floods of 2021 severely impacted Western Europe, exposing the susceptibility of riverine flood defenses in regions such as southern Belgium and Germany to extreme precipitation events.

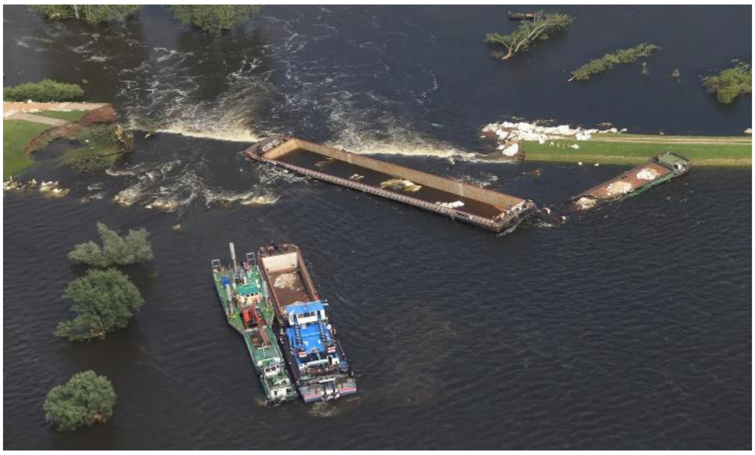

Figure 1.4 Deliberate sinking of three barges to close a breach in the Elbe River levee during the 2013 floods. This reactive measure was used to obstruct the torrent and allow for permanent repairs to the failed dike system near Fischbeck (source: www.spiegel.de).

1.2.2 Climate change and the impact on hydraulic loads and structural integrity

Climate change impacts the stability and performance of levees, dikes, and earthen dams by simultaneously increasing the magnitude of hydraulic loads acting upon them and degrading their geotechnical resistance.

With regards to hydraulic load magnitude, climate change introduces "non-stationarity," patterns where historical weather patterns are no longer reliable predictors of future loads. This results in intensified hydraulic stresses both in terms of frequency and intensity of extreme weather events on earthen structures. This leads to higher peak river discharges and prolonged flood durations. Longer flood durations maintain high water levels against the embankment for extended periods, leading to deeper saturation and higher pore water pressures within the soil, which are critical drivers of instability

For coastal levees, rising sea levels and more frequent storm surges increase the hydraulic head and wave action load. This necessitates raising flood defense elevations (potentially by 1–2 meters by 2100) to prevent overtopping (Figure 1.5). For river levees, the variability of river flows (coefficient of variation) is expected to increase, making the reliability of run-of-river and small storage facilities more sensitive to climate shocks.

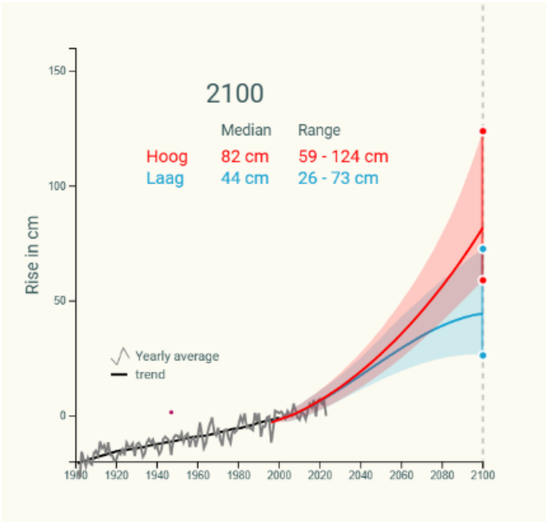

Figure 1.5 Annual averages and predicted sea level rise in the Netherlands by 2100 under highest (red) and lowest (blue) scenarios (www.klimaateffectatlas.nl)

Hotter, drier summers cause clay soils to shrink and crack. These desiccation cracks create networks of fissures that extend deep into the embankment reducing the resistance of protection covers. In the Netherlands, drought-induced drying of peat levees has caused them to lose mass and structural integrity, leading to failures where the levee essentially floats away or shears. Warmer climates are altering the migration patterns of burrowing animals (e.g., porcupines, badgers, muskrats). In Italy, animal burrows were identified as a specific failure mechanism in recent floods (e.g., the Secchia River failure, 2014), as burrows create voids that facilitate piping and collapse (UCOLD Working group on levees and flood defences).

While grass provides erosion protection, trees on embankments can be problematic. Their roots abstract large amounts of water during droughts, exacerbating shrinkage and desiccation cracking. Conversely, decaying roots from removed trees can leave void networks that promote seepage.

The deterioration of embankments materials during design life (Dyer 2004) in addition to raising the height of older levees to keep their functional state over time, can endanger their stability and expose them to a higher failure risk.

To address these risks, engineering practices are shifting from deterministic safety factors to probabilistic, risk-based assessments that account for climate uncertainty.

To systematically address the inherent uncertainties in structural performance during extreme events, civil engineering risk assessments frequently utilize fragility curves. These curves offer a probabilistic framework, quantifying the likelihood that a structure will exceed a specific damage threshold when subjected to varying hazard intensities (Shinozuka et al., 2000, Kurter et al. 2025). For example, fragility curves can be used to quantify the probability of failure under varying hydraulic loads, helping levee managers prioritize interventions. Effective management now requires continuous monitoring of internal and external conditions in the field and under real meteorological conditions. This probabilistic approach is briefly addressed in section 1.5.4 Probabilistic Risk Assessment.

Therefore, a higher flood risk probability accompanying less favorable structural conditions exacerbates the failure of these defense structures. Regular maintenance of structure as well as periodic inspection and resolving the weaknesses may decrease the increasing threats by climate change impacts yet not fully eliminate them.

1.3 Failure Mechanisms in Earthen Embankments

The nature of failure in earthen embankments is mainly related to the geotechnical and hydraulic aspects. Worldwide, the main causes of failure in earthen embankments failure can be divided into (see Figure 1.6): (i) Overflowing and wave overtopping (34%), (ii) Foundation and structural defects (30%) such as: sliding of inner slope or outer slope, and erosion of outer slope, and (iii) piping and seepage (28%) reported by (Costa, 1985).

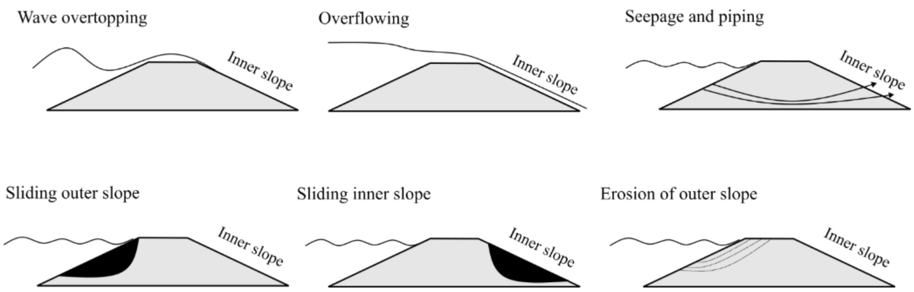

Figure 1.6 Dominant failure causes in earthen embankments.

Overflowing and wave overtopping. Hydraulic loads on embankments manifest primarily as either overflowing or wave overtopping (Figure 1.7a-c). Overflowing (or steady overtopping) occurs when the static reservoir or river water level rises above the embankment crest elevation illustrated in Figure 1.7a. This may result from extreme inflow due to prolonged precipitation, design deficiencies, or physical settlement of the crest structure. In contrast, wave overtopping occurs when the mean water level remains below the crest, but wind-induced wave run-up periodically surmounts the structure (see Figure 1.7b). Together, these mechanisms constitute the leading causes of embankment failure globally. The critical consequence of these phenomena is the initiation of high-velocity flow on the landward slope; if not mitigated, this flow triggers surface erosion that progressively incises the embankment.

(a)

(b)

(c)

Figure 1.7 Hydraulic loads including: (a) river overflowing (river-side view) (b) wave runup (sea-side view) and (c) wave overtopping (land-side view)

during a storm event along North Sea near Wilhelmshafen, Germany in 1954 (A. Koelewijn, personal communication, 2026).

Wave overtopping affects embankments in two primary ways: it either independently generates intermittent flow over the crest or, when coinciding with steady overflow, exacerbates the hydraulic impact on the downstream slope. Both mechanisms trigger surface erosion that progressively excavates a channel across the crest (initial breach) and the downstream face. Within this initial breach, flow velocities typically reach critical or supercritical regimes, generating high tractive shear stresses that drive the initiation and subsequent development of the breaching process

In particular, Hurricane Katrina (2005) demonstrated the catastrophic consequences of wave overtopping during storm surge overflowing (ASCE Hurricane Katrina External Review Panel, 2007).

Foundation and structural defects. According to ASCE/EWRI Task Committee on Dam/Levee Breaching (2011), various geotechnical factors predispose embankments to foundation-driven failure. Key mechanisms include differential settlement, slope instability (sliding), excessive uplift pressure, and uncontrolled foundation seepage. Differential settlement is particularly critical as it generates transverse cracks and discontinuities within the embankment body, which can accelerate the breaching process. Similarly, uncontrolled seepage through permeable foundation strata can compromise structural integrity and lead to failure if not effectively restricted.

Piping and seepage. This failure mode is driven by internal erosion rather than external overflow. When high hydraulic gradients develop through or beneath the embankment, seepage forces can initiate the transport of fine sediments, typically exiting near the downstream toe. In sandy foundations, this process often manifests as 'sand boils' discharging water and sediment. These eroding flow paths progressively enlarge into continuous tunnels or 'pipes' moving upstream toward the reservoir. As the pipe widens, it undermines the embankment's structural integrity, eventually causing the crest to collapse (slumping) and forming an open breach. Notably, piping can trigger failure even when water levels are below the crest, often exacerbated by defects such as animal burrows, tree roots, or desiccation cracks (Fell et al., 2004; Foster et al., 2000; Richards & Reddy, 2007).

Figure 1.8 Embankment (dam) breaching induced by piping: (a) breach initiation; (b) t=5 min; (c) t=8 min; (d) t=13 min; (e) t=13 min, immediately following the collapse of the pipe roof; and (f) t=60 min, illustrating continued lateral widening. Reprinted from Hanson et al. (2010).

1.4 Breach Characteristics and Outflow Hydrograph

In the context of embankment failure, a breach is defined as the opening formed in the dam body that leads to the uncontrolled release of the impounded water. To characterize this process for risk assessment and hydraulic modeling, the breach is defined by both physical geometric parameters (depth, width, side slopes) and temporal parameters (initiation and formation times).

Figure 1.9 Breach formation in a cohesive embankment (IMPACT Project, form Morris & Hassan (2009))

While the cross-sectional geometry of a breach is frequently simplified into trapezoidal, rectangular, triangular, or parabolic forms for modeling purposes , evidence from historical dam failures and experimental studies suggests that real-world breach channels often exhibit vertical, near-vertical, or undercut side slopes across various soil types (ASCE/EWRI Task Committee on Dam/Levee Breaching, 2011; Morris & Hassan, 2009)

Physical Parameters

The idealized breach cross-section is illustrated in Figure 1.10, and its geometric parameters are defined as follows (T. L. Wahl, 1998):

Breach depth (h_b): Also referred to as breach height, this is the vertical distance measured from the original dam crest elevation down to the invert of the breach channel

Breach width (B): This is the lateral dimension of the opening. Because the width may vary from the crest to the invert, it is typically reported as the average breach width (B_{avg}) or specified at the top and bottom (B_{top} , B_{bottom}). The ultimate breach width is the most critical parameter influencing the magnitude of the peak discharge.

Breach Side Slope (Z :1): This parameter defines the angle of the breach sides, usually expressed as Z horizontal to 1 vertical (Z:1). While often estimated using the angle of repose for non-cohesive soils or simplified slopes (e.g., 1:1 or 1:2) for cohesive soils in predictive models. However, physical evidence suggests that slopes are frequently vertical ($Z = 0$) due to the hydrogeotechnical mechanics (high flow velocities and apparent cohesion) of block failure.

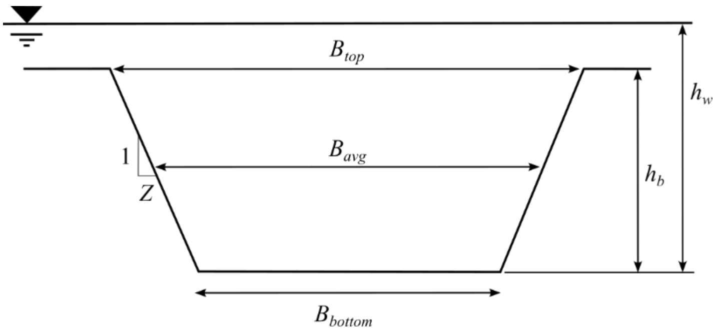

Figure 1.10 Parameters of an ideal breach cross section (adapted from Wahl (1998)).

Temporal Parameters

In the context of flood risk assessment and emergency planning, it is critical to distinguish between two distinct temporal phases of the failure process: Breach Initiation Time and Breach Formation Time (Morris & Hassan, 2009; T. L. Wahl, 1998).

Breach initiation time: The duration from the first flow over or through the embankment (e.g., initial overtopping or piping) until the onset of rapid, self-sustaining erosion. During this period, the breach discharge remains relatively small and increases gradually. Crucially, this phase represents the window of opportunity where emergency intervention, such as sandbagging or flow diversion, may still successfully stop the erosion and prevent complete failure.

Predicting the exact moment when breaching will start in the field remains highly challenging due to the significant influence of the grass cover quality and the underlying soil resistance. The field experiments from the Polder2C's project clearly demonstrated this: a well-maintained grass cover can withstand high flow velocities and overflowing for hours. In fact, because of this high resistance, the 20-cm grass cover had to be artificially removed prior to testing just to study the initiation of erosion in the underlying bare clay. However, once damage is present and the soil is exposed, erosion initiates locally and can develop into a breach within a few hours.

Regarding thresholds, critical values of the velocity and shear stress for erosion initiation were defined for the soil using the Erosion Function Apparatus (EFA). For the natural bare clay at the test site, the critical flow velocities ranged from 0.4 to 0.6 m/s, and critical shear stresses were between

0.6 and 1 Pa. While these empirical thresholds provide a valuable baseline, applying these directly to predict field initiation involves high uncertainty. Real-world initiation is indeed often triggered by local anomalies — such as existing damage, animal burrows, or tree roots — rather than the average flow parameters exceeding a uniform theoretical threshold. This aligns with findings in the broader literature, such as Morris (2005), which explicitly describes the time needed for breach initiation as highly unreliable to predict.

Breach formation time: This phase begins when the erosion process accelerates significantly, transitioning from a gradual removal of material to a rapid expansion of the breach channel. Characterized by a dramatic surge in outflow and violent vertical and lateral erosion, this phase marks the point where structural failure becomes unavoidable and intervention is no longer feasible.

While theoretically distinct, accurately defining the transition point between initiation and formation remains a challenge, even for experts analyzing forensic case studies. However, recognizing this distinction is vital, as the initiation phase dictates the available advance warning time for downstream population evacuation, while the formation phase governs the shape and magnitude of the flood hydrograph. This transition time is indicated by $t_{i,f}$ in Figure 1.11.

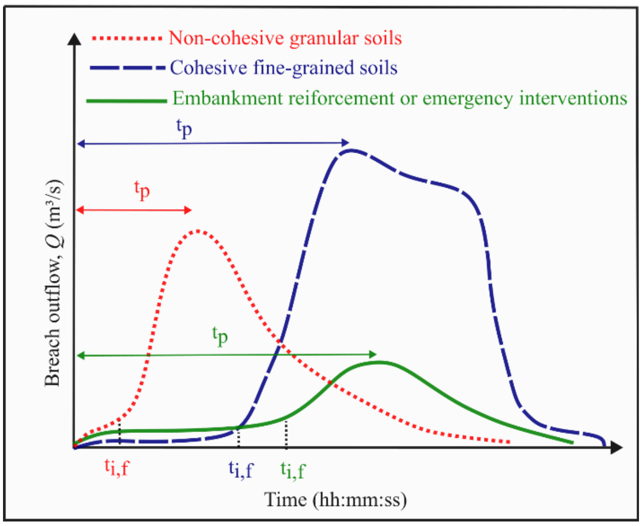

Figure 1.11 Idealized breach outflow shape in different materials the transition time between initiation and formation is indicated by $t_{i,f}$.

Constituted soil and cross-section configuration influence the most these parameters and the overall generated breach outflow shown in Figure 1.11.

For instance, the soil's erosion resistance directly governs the rate of breach widening and the time-to-peak (t_p); cohesive soils often result in a delayed but sudden surge in discharge following headcut breakthrough, whereas non-cohesive soils tend to produce a more progressive rise in outflow. Furthermore, the peak discharge is controlled by the relation between the reservoir volume and the erosion rate: in small reservoirs, the peak is often 'erosion-limited' and occurs before the breach reaches its maximum dimensions due to rapid drawdown, whereas in large reservoirs, the peak is determined by the hydraulic capacity of the fully formed breach.

Once overtopping initiates, emergency interventions aimed at arresting breach formation typically only hinder or postpone the process; in most cases, complete structural failure becomes inevitable. Consequently, the development of effective emergency response plans and flood warning systems relies heavily on the accurate prediction of the breach outflow hydrograph and the duration of the failure process. Beyond immediate safety, the outflow hydrograph is the fundamental input for defining flood risk maps and delineating downstream impact zones.

Furthermore, this predictive capability is critical for 'deliberate breaching' as an emergency measure executed for instance in the 2011 Mississippi River operation. The success of such high-stakes operations depends entirely on the accuracy of the modeled peak discharge and failure timing.

1.5 State-of-The-Art of Earthen Embankment Breaching

In this context, a synergistic approach is required to address the uncertainties in flood risk management. The continued advancement of laboratory and field experimental studies is crucial for capturing the fundamental physical mechanisms of failure and providing high-quality datasets for validation of predictive tools. Simultaneously, the development of robust numerical tools capable of modeling the complex spatiotemporal evolution of embankment breaching is indispensable. Only by integrating these experimental insights with advanced modeling techniques can engineers accurately predict breach outflow hydrographs and effectively manage the catastrophic risks associated with embankment failure.

1.5.1 From field experimentation to laboratory modeling

Many research projects have been dedicated to studying breach formation and development in large scale embankment dams or levees, e.g., IMPACT (Hassan et al., 2004; Morris et al., 2007) USDARS (Hanson et al. 2005), Sigmaplan (Peeters et al. 2015). Partially destructive experiments aimed at studying the resistance of prototype levees and dikes are widely conducted in the Netherlands and more recently in France along the Rhône River. Some examples of these projects are briefly addressed in the following sections.

IMPACT and FLOOD*site*

The IMPACT (Investigation of Extreme Flood Processes & Uncertainty, 2001–2004) project focused on evaluating the performance of dams and flood defense structures under extreme loading conditions. A major component of the project was the investigation of breach formation processes to reduce the uncertainty inherent in predictive numerical modeling. To achieve this, the project executed a unique program of physical modeling:

Field Tests: Five large-scale failure tests were conducted at a dedicated site in Norway. These tests involved embankments 4.5 to 6 m high, constructed of cohesive (clay) (Froehlich, 2004), non-cohesive (gravel), and composite (moraine core) materials, tested to failure by overtopping and piping.

Figure 1.12 Aerial view of the Røssvass dam breach test site of IMPACT project (Source: Løvoll et al (2004))

Laboratory Tests: Twenty-two controlled laboratory experiments were performed at HR Wallingford (UK) at a 1:10 scale to replicate the field tests and isolate governing parameters.

Numerical Modeling: An extensive blind benchmark testing program was conducted to assess the performance and uncertainty of various breach models (e.g., HR BREACH, NWS BREACH) against the collected physical data

As the largest EC research project on floods, FLOOD*site* (Integrated Flood Risk Analysis and Management Methodologies, 2004–2009) expanded the scope to integrated flood risk analysis, covering the physics of failure, risk management practices, and long-term decision support (Hassan and Morris, 2009). Crucially, FLOOD*site* provided the resources to perform the detailed data treatment that was not completed during IMPACT. Besides, detailed analysis of video footage (over 36 DVDs) allowed for the precise identification of failure mechanisms, such as headcut erosion in cohesive soils and the composite behavior of layered embankments.

The FLOODsite project achieved significant research advances in three primary domains: (i) flood risk analysis, encompassing extreme value statistics, defense structure reliability, and post-flood consequence assessment; (ii) flood risk management practices; and (iii) the development of supportive decision-making processes for long-term flood management (Morris et al. 2007, Morris et al. 2009). Beyond these specific technical outputs, the project fulfilled a fundamental and ambitious objective by establishing comprehensive conceptual and methodological guidance for the integrated analysis, assessment, and management of flood risks and events (Klijn 2009).

OVERCOME Project

Co-funded by Électricité de France (EDF) and Compagnie Nationale du Rhône (CNR), the OVERCOME project was established to investigate erosion processes specially within coarser and mixed-grained embankment material (Monteiro-Alves et al., 2023; Morris et al., 2021). The primary objective was to determine how breach erosion mechanisms are governed by soil grading and associated geotechnical parameters, such as fines content and permeability. To achieve this, a multi-scale experimental program was implemented: small- and medium-scale tests (0.55 m and 1.0 m high embankments) were conducted at the Universidad Politécnica de Madrid

(UPM), while larger-scale replications (2.5 m high) were performed at CNR (see Figure 1.13a,b).

(a) (b)

Figure 1.13 Laboratory experiments on coarser grain granulometries at: (a) UPM (1-m-high embankment, Morris et al., 2021) and (b) CNR (2-m-high embankment) (source: CNR).

Additionally, in collaboration with INRAE, field overflow tests were executed on a section of the Rhône river levee to quantify the in-situ erosion resistance of the cover layer (Figure 1.14). Ultimately, the project aimed to evaluate and improve the performance of numerical breach models by validating them against this integrated dataset of laboratory and field-scale experiments.

(a) (b)

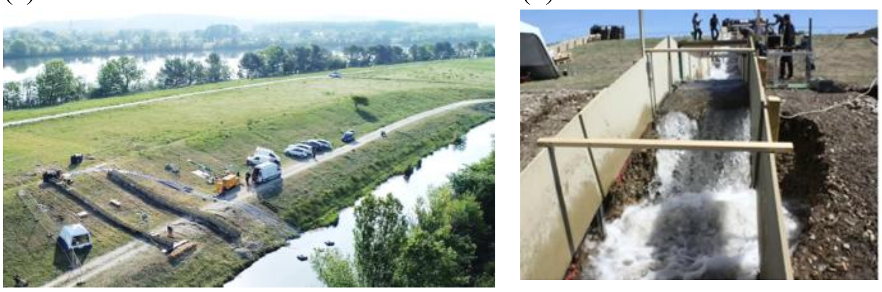

Figure 1.14 Overflow erosion tests on the site of Montfaucon (Gard): (a) test site global view and (b) levee cover erosion due to overflowing (Source: INRAE).

INTERREG Polder2C's Project

A more recent and unique initiative is the Polder2C's project (https://polder2cs.eu/), centered at the Living Lab Hedwige-Prosperpolder (LLHPP) on the border between Belgium and the Netherlands (Figure 1.15).

Driven by the managed realignment of the polder into a tidal nature area, the project leveraged the decommissioning of the existing levees to create a 'living laboratory' for full-scale destructive testing.

Figure 1.15 Hedwige and Prosper Polder area turning into a Living Lab by the end of Polder2C's Project (Photo: Vilda-Yves Adams).

This site provided a rare opportunity to subject real embankments to extreme hydraulic loads until failure (Figure 1.16a). Experiments focused on assessing the actual erosion resistance of levee covers (grass and clay) under wave overtopping and overflow conditions, specifically investigating the influence of real-world anomalies such as animal burrows, tree roots, and infrastructure transitions. These in-situ tests were complemented by laboratory analyses to validate numerical models and reduce uncertainties in safety assessments.

Beyond physical parameters, the project served as a training ground for crisis management. Large-scale emergency response exercises were conducted, including deliberate breach initiation tests (e.g., using explosives) and the testing of innovative repair measures like the 'Breachdefender' (Figure 1.16b). These exercises aimed to bridge the gap between theoretical flood resilience and practical operational response, ensuring that the knowledge gained is transferred to flood managers and incorporated into educational curricula via a dedicated Field Station.

Figure 1.16 Example of field experimentation and emergency response activities: (a) levee overflowing and (b) 'Breachdefender' (source: https://polder2cs.eu/).

INTERREG BONSAI Project

Building on the momentum of Polder2C's, the BONSAI project (Boosting flood resilience in estuarine systems anticipating shifting climate zones, https://bonsai.nweurope.eu/) addresses the accelerating threats of climate change—specifically increased rainfall, storms, and sea-level rise—in the North-West Europe (NWE) region. With extensive estuarine systems being particularly vulnerable, the project aims to enhance both short- and long-term flood defense resilience by facilitating transnational cooperation and capacity building. A defining feature of the project is its strategy to simulate "shifting climate zones." By applying insights from southern European regions to northern areas, the project fosters a "north learning from south" exchange to anticipate future climate scenarios.

The project is structured around a series of pilot actions implemented across various international test sites. A primary location is the Vlassenbroek Polder (Figure 1.17a) in Dendermonde, Belgium, a flood control area developed within the framework of the Sigma Plan to mitigate the risks of future storm surges (see Figure 1.17b). This site offers a unique opportunity to execute a wide range of field tests in the context of climate change and where some adaptation measures are already taken. Experimental plans for this site focus on quantifying the erosion resistance of innovative levee revetments, specifically: (i) lime-treated soil covers reinforced with grass subjected to wave impact loads, and (ii) Open Stone Asphalt revetments subjected to overflow conditions. The ultimate objective is to evaluate the in-situ performance of these reinforcement techniques and to establish critical correlations between these prototype-scale results and small-scale laboratory tests performed on identical soil samples.

Figure 1.17 Vlassenbroek flood control area: (a) aerial view (Google maps, 2026) and (b) schematic representation of flood control area in function (source: Van Nederkassel et al.,(2015)

In this context, acquisition of high-quality data during full-scale experimental campaigns through cost-effective and user-friendly measurement techniques is of the utmost importance for the development and calibration of mathematical models describing underlying physical processes (ASCE/EWRI Task Committee on Dam/Levee Breaching 2011). However, most available data on damage initiation and progression are limited to either pixel-based image analysis or pointwise ground survey measurements (van der Meer et al. 2009). Despite recent advancement in field experimentation, monitoring temporal evolution of progressive levee breaching in case of steady and wave overtopping remains a challenge.

1.5.2 Experimental modeling

Hydraulic physical modeling serves as a critical tool for investigating design and operational challenges in hydraulic engineering as a complementary of numerical models. It offers essential insights into the physical processes governing failure phenomena, forming the basis for the development and verification of mathematical models A comprehensive state-of-the-art review on embankment breaching is detailed in Appendix A: Earthen embankment experimental review; a summary of these experimental modeling tendencies is presented here.

The earliest laboratory experiments, dating back to the 1950s, focused primarily on fuse-plug embankments—sacrificial structures designed to wash out and increase spillway capacity during extreme floods. Pioneering works by Tinney and Hsu (1961) and later Pugh (1985) investigated washout mechanics to predict discharge through these controlled breaches.

Concurrently, extensive testing by Chen and Anderson (1986) and Clopper (1989) focused on embankment protection systems and stability under overtopping conditions.

Significant research was subsequently dedicated to simulating the failure of non-cohesive, homogeneous embankments. Notable studies by Visser (1998), Coleman et al. (2002), and Chinnarasri et al. (2004) characterized the evolution of breach geometry and peak outflow. These experiments identified surface erosion and the transition to rapid lateral widening as the dominant mechanisms in granular soils.

Conversely, research on cohesive embankments, led prominently by Hanson and Temple (2002, 2005), distinguished headcut migration as the primary failure mode, differing fundamentally from the surface erosion observed in non-cohesive sands. These findings were supported by large-scale tests conducted by the USDA-ARS (Hunt et al., 2005) and within the IMPACT project, which demonstrated that soil properties, ranging from silty sands to lean clays, are the decisive factors in characterizing the rate and nature of breach development.

More recent laboratory studies have focused on capturing the complete breaching process, specifically the transition from vertical deepening to lateral widening. To isolate these mechanisms, researchers have employed distinct geometric configurations. Planar embankments (2D) overtopping, i.e. experiments in which the overtopping flow occurs over the full width of the embankment such as those by Schmocker and Hager (2009) and Van Emelen et al. (2015) (see Figure 1.18), utilize full-width overtopping to investigate vertical erosion, sediment transport, and seepage protection effects under simplified frontal flow conditions. Conversely, three-dimensional (3D) breach evolution has been investigated using symmetrical half-dike setups against transparent channel walls (Coleman et al., 2002; Pickert et al., 2011; Schmocker and Hager, 2011) or full-dike configurations (Spinewine et al., 2004). These setups allow for the detailed observation of complex hydro-morphological features, such as the curved breach channel, scour hole formation, and mass block failures driven by apparent cohesion.

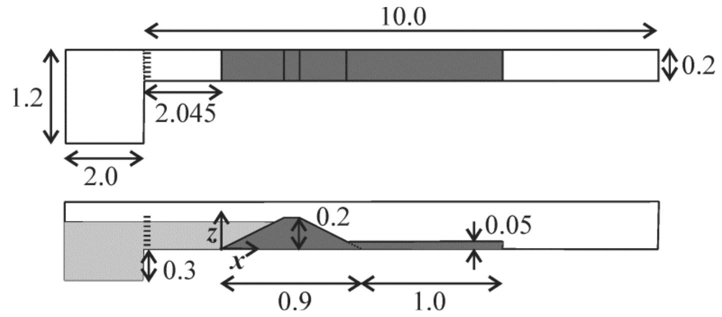

Figure 1.18 Planar dike tests to study the impact of sediment transport formulation on breaching modelling (source: Van Emelen et al. (2015))

Parallel to geometric investigations, many research has focused on 'scale series' tests to quantify scale effects and verify Froude similarity laws. Researchers including Visser (1998), Chinnarasri et al. (2003), Pickert et al. (2011), and Al-Riffai (2011) have systematically varied governing parameters—such as dike geometry, scale reduction factors, and soil properties (compaction, moisture content, and granulometry) in order to characterize their influence on erosion rates, failure timing, and peak discharge. However, a large limitation in these studies is the dimensions of models often limited to the small-scale tests with embankment height limited to 60 cm.

In this research, the embankment height (H_{Em}) serves as the primary metric to define the physical scale of the experimental models. Small-scale models, defined as embankments with $H_{Em} < 0.6$ m, are prevalent in literature due to their ease of construction in standard hydraulic laboratories. Subsequent scales are classified as medium ($0.6 < H_{Em} \leq 1.5$ m), large ($1.5 < H_{Em} \leq 2.5$ m), and full scale ($H_{Em} > 2.5$ m). The term 'prototype scale' is reserved specifically for experiments conducted on actual, existing embankment structures. Applying this classification framework, a comprehensive review of the literature identified a total of 1,364 experimental tests. These are compiled and summarized in Appendix A: Earthen embankment experimental review, which builds upon and updates previous compilations by Wahl (2007), ASCE/EWRI Task Committee on Dam/Levee Breaching (2011), Al-Riffai (2014). Overall, 60% of these tests were conducted at a small scale, compared to only 13% at the medium scale (see Figure 1.19). Furthermore, homogeneous sand embankment experiments account for approximately 40% of all studies, with up to 75% of these specific sand tests restricted to the small scale.

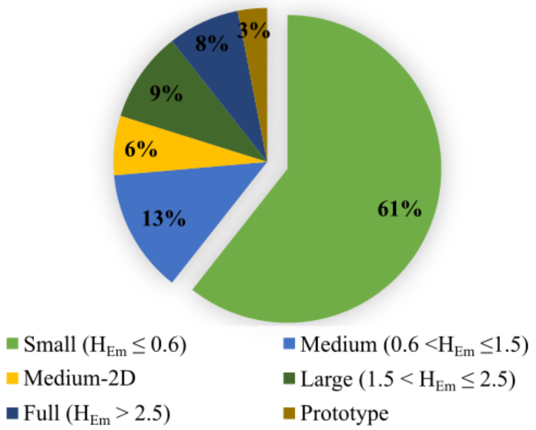

Figure 1.19 Model scale statistics in earthen embankment experimental studies.

1.5.3 Numerical modeling

While hydraulic experimental modeling is crucial for collecting reliable data and studying complex processes under controlled conditions, it cannot replace numerical modeling. Numerical models are essential for designing new earthen embankments and simulating breach-induced floods, which is critical for developing hazard maps and defining inundation zones.

Embankment breach modeling generally follows two main approaches: parametric models and physically-based models. Parametric models use statistical analyses of historical dam failure data to estimate final breach characteristics, such as width, depth, side slope angles, formation time, and peak outflow. While they are computationally inexpensive and easy to use, their accuracy is limited by the scarcity and high uncertainty of well-documented historical events. Furthermore, they only predict ultimate breach parameters and do not provide a temporal breach outflow hydrograph.

Alternatively, physically-based models simulate the actual mechanics of the breaching process. Simplified physically-based models (e.g., DAMBRK) rely on analytical flow solutions such as broad-crested weir or orifice flow equations and assume simple, pre-determined breach cross-sections without distinguishing specific erosion processes. In contrast, detailed physically-based models (e.g., BRES, HR-BREACH, WinDAM, DLBreach, WATLAB) incorporate complex flow conditions, soil mechanics, and morphological evolution to predict the temporal development of the breach accurately. These detailed models often utilize depth-averaged two-dimensional (2D) or three-dimensional (3D) shallow-water and sediment transport equations.

Nevertheless, a significant challenge in these numerical models remains the accurate simulation of lateral bank failure, specifically mass block detachment, which heavily dictates the breach outflow hydrograph. While solutions utilizing coupled slope-stability criteria, such as the 2D bank-failure operator proposed by Swartenbroekx et al. (2010), have proven robust for purely granular, non-cohesive soils like medium and coarse sands (Delpierre et al., 2024), they face distinct limitations. Specifically, these models struggle to reproduce the behavior of fine sediments, where transient matric suction induces apparent cohesion, allowing the formation of near-vertical breach walls that violate standard angle-of-repose assumptions and reproducing large mass block failure (Ebrahimi et al., 2022, Wang et al 2025).

(a) (b)

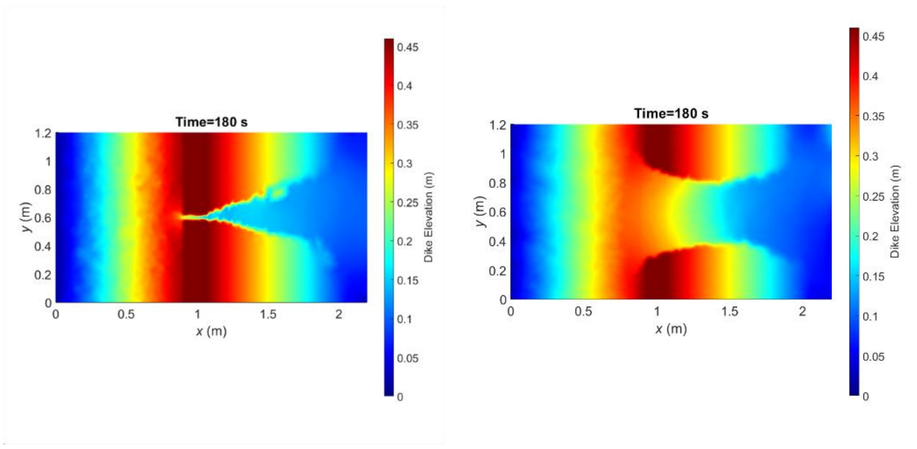

Figure 1.20 Dam breach modeling using Shallow water equations coupled with Exner equations: model sensitivity analysis to bank failure operator accounting for lateral widening (a) without operator and (b) with operator (blind benchmark modeling organized by Dam&DikeCare project, Ebrahimi et al.(2022))

A promising advancement is proposed by Elalfy et al. (2025), who treat bank collapse as a discrete source term in the sediment mass conservation equation, rather than purely as hydraulic erosion. This aligns well with the "episodic" nature of widening in embankments constituted of fine material.

Looking forward, next-generation approaches such as Particle Finite Element Method (PFEM) based models offer the potential to account for large displacements induced by the coupling of infiltration and overtopping flow (Delpierre et al., 2025). While these models successfully detect geotechnical instabilities, further development is required to fully resolve the lateral widening driven by the complex stress field of the breach outflow.

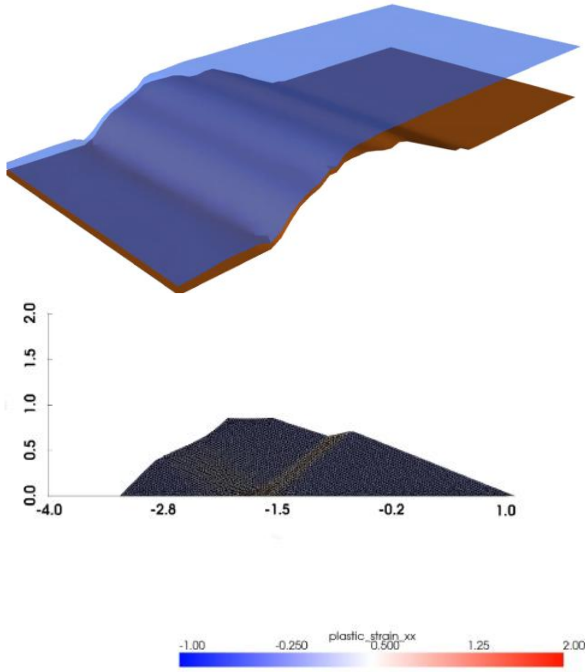

Figure 1.21 Accounting for large displacement using the PFEM method in earthen embankment overtopping by solving the 2D Richards equation coupled by the 1D shallow-water equations (source: Delpierre et al. (2025)).

The development and verification of these advanced numerical models rely heavily on the high-resolution topographic and hydrodynamic data acquired from physical breaching experiments.

1.5.4 Probabilistic Risk Assessment

Methods exist to predict the possibility of erosion failure by using probabilistic approaches, which account for uncertainties in rainfall intensity, water flow, and the strength of dam materials (Kurter et al. 2025). Unlike conventional deterministic models that yield a singule failure prediction, this stochastic framework generates a probabilistic spectrum of potential outcomes. By quantifying the inherent uncertainties, it provides a far more robust decision-making tool for engineers, policymakers, and emergency planners tasked with mitigating embankment failures and minimizing downstream flood damage A stochastic approach employs random variables, such as varying flood hydrographs and fluctuating initial reservoir levels, to account for natural uncertainties in environmental modeling. While embankment breaching prediction models simulate physical failure processes — including breach widening, failure time, and peak outflow hydrographs — they inherently suffer from modeling inaccuracies, physical shortcomings, and significant uncertainties related to soil properties, compaction, and hydraulic loads. Fragility curves serve to bridge this gap by quantifying the probability of structural failure under varying hydraulic loads.

The Monte Carlo simulation procedure involves generating random samples from the probability density functions of rainfall depth and critical shear stress. Next, regression functions are utilized to estimate the applied shear stresses for the generated rainfall depths. By pairing the applied and critical shear stresses, the corresponding performance (Z) values are calculated and subsequently classified into distinct erosion severity levels for the scenarios where erosion occurs.

By running a breach prediction model across thousands of stochastically generated flood scenarios for instance via Monte Carlo simulations, the variability of these parameters can be systematically evaluated. Ultimately, the stochastic framework generates the varied boundary conditions, the breaching model simulates the physical failure mechanisms, and the resulting fragility curve summarizes the overall probabilistic risk.

Well-documented systematic data collection is of utmost importance across all approaches. Initiatives such as the International Levee Performance Database[1] (ILPD, Özer et al. 2020) have been established to aggregate embankment breaching failures, and accidents may lack reporting all necessary parameters affecting the breach. Comprehensive database, such as Levee Loading and Incident Dataset- Overtopping (LLID-OT, Flynn et al. 2025) reports historical riverine levee overtopping events supported by data on hydraulic loading, soil and foundation classifications,

[1] *leveefailures.tudelft.nl*

construction/maintenance characteristics, geometry, and breach dimensions. Comprising a subset of 487 overtopping events from the U.S. National Levee Database (NLD), the dataset enables systemic risk assessment and data-driven breach modeling. Furthermore, OpenDELvE2 (Nienhuis et al. 2022) strengthens levee data by integrating high-resolution spatio-geometrical, overcoming previous documentation limits by mapping the often poorly documented locations and characteristics of flood-protection levees on river delta. While such databases are crucial for flood hazard modelling and mapping, they do not report the dominant physical processes at the very high spatial and temporal resolutions of individual failure events. Datasets capturing these processes, however, are of paramount importance for the development and validation of numerical models simulating a single failure event.

1.6 Research Needs and Knowledge Gap

In practice, earthen embankments are constructed from a wide range of materials, including sand, clay, silt, gravel, rockfill, and dredged materials, resulting in complex, wide granulometries. These soils often contain organic materials, and the presence of grass covers, tree roots, and animal burrows can significantly impact the structure's overall behavior, potentially leading to sudden failures. Furthermore, the morphological behavior of in-situ soils varies due to compaction and consolidation over time. These physical realities, combined with overtopping boundary conditions that fluctuate unpredictably during prolonged storm events, remain highly difficult to reproduce in small-scale laboratory models or represent accurately in mathematical models.

Consequently, achieving a sound understanding of erosion and failure processes necessitates more field and full-scale experiments. To meet new climate-adapted safety standards, there is a growing demand for real-scale, partially destructive experiments. Because they induce limited damage, these tests are easier to execute and monitor, offering an advantageous method for evaluating the instantaneous strength of protective cover layers under extreme events. Additionally, the effectiveness of innovative, sustainable soil-based reinforcement techniques, such as lime treatment, must be verified through such full-scale in-situ experiments prior to widespread application. In this context, acquiring high-quality spatial data during field campaigns using cost-effective, user-friendly measurement techniques is of the utmost importance for developing and calibrating predictive mathematical models.

However, due to the significant costs and logistical complexities associated with field campaigns, recent research prioritizes a combined approach utilizing both field data and reduced-scale laboratory experiments. Extrapolating knowledge from small laboratory tests requires near-prototype data for validation due to severe scale effects. For instance, modeling cohesive soils reinforced by grass roots is highly complex; these materials can strongly resist steady overflowing but remain vulnerable to the dynamic loads of wave overtopping.

Conversely, for non-cohesive sand and gravel embankments, scaling down prototype sediments geometrically yields very fine laboratory sediments. These fine sediments exhibit apparent cohesion and altered permeability, fundamentally misrepresenting the erosion mechanics of the real structure and inducing significant scale effects. As shown in the experimental modeling review, the vast majority of research on sand embankments is restricted to small-scale laboratory tests, with very few conducted at an intermediate scale. Therefore, scale-series studies that include medium-scale models which are large enough to accurately reproduce prototype failure processes without severe sediment distortion, are critically needed to quantify scale effects and bridge the knowledge gap between small-scale models and full-scale prototype behavior.

Chapter 2

Objectives and Structure

2.1 Objectives and scope of the research

The central objective of this research is to establish a comprehensive, high-resolution experimental framework for quantifying the erosion and breaching processes of earthen embankments under diverse hydraulic loads. By integrating full-scale prototype testing with medium- and small-scale laboratory experiments, and using non-intrusive measurement techniques based on image processing, this thesis seeks to bridge the gap between surface protection resilience and the fundamental physics of sand core failure.

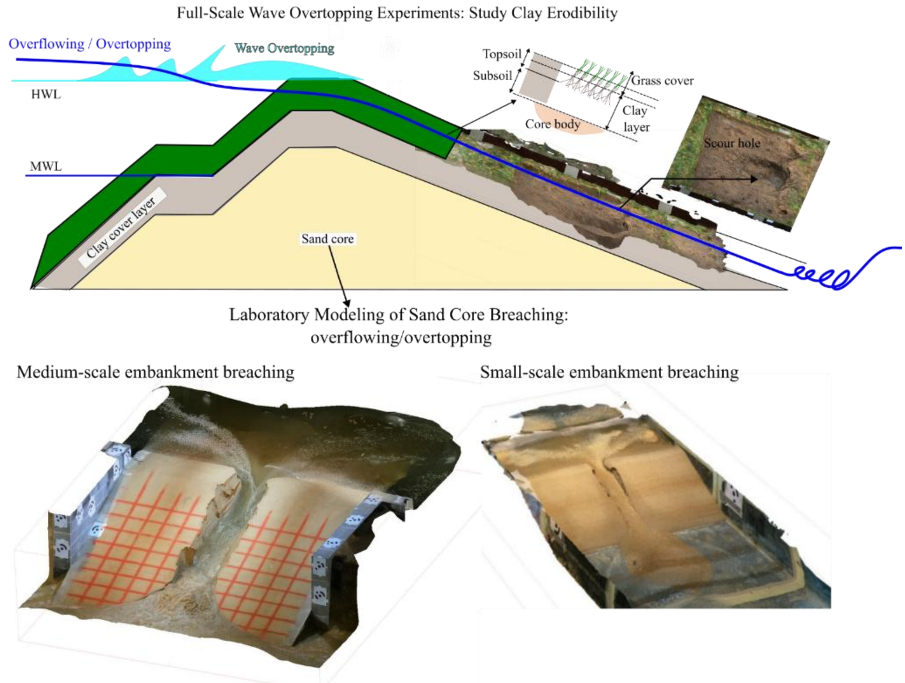

Figure 2.1 Global overview of the primary axes and objectives of this research study.

The specific objectives of this thesis are organized into the following pillars:

I. A Novel Enhanced SfM-Photogrammetry Application, Methodological Development, and Validation

A primary goal is the application of Structure-from-Motion (SfM) photogrammetry to accurately monitor rapid morphological changes in two series of field experiments with distinct camera setups. This methodology was first developed for a 1:1 scale application at the Living Lab Hedwige Prosperpolder (facilitated by the Interreg Polder2C's (https://polder2cs.eu/) and regional Lime in Clay projects). These tests investigate the erosion of a 1-m-thick clay protection layer on the landward slope subjected to wave overtopping. Within this context, two distinct image acquisition strategies were employed for the 3D scene reconstruction: a multi-stationary synchronized camera system (Figure 2.2a), and a single mobile camera (Figure 2.2b). This work specifically focuses on validating the temporal resolution of SfM to capture discrete erosion events, ensuring the methodology can operate at speeds relevant to real-world flood scenarios. This methodology and measurement development was a milestone and the first inventory of this research.

Furthermore, this research refines these photogrammetric techniques for highly dynamic laboratory environments, specifically during small- and medium-scale sand embankment breaching (Figure 2.2c,d). Key challenges at these scales include capturing the submerged bed and tracking the dynamic water surface. To mitigate limitations caused by poor surface texture, light reflections, and turbulent water motion, synchronized imaging is combined with the use of floating surface tracers. Additionally, strategically embedding colored marker balls within the dike allows for the precise tracking of vertical breach deepening, significantly improving the accuracy and completeness of the 3D SfM reconstructions. Finally, through collaborative efforts, an optical fiber system is integrated into the small-scale models to complement the photogrammetric measurements and track internal erosion progression.

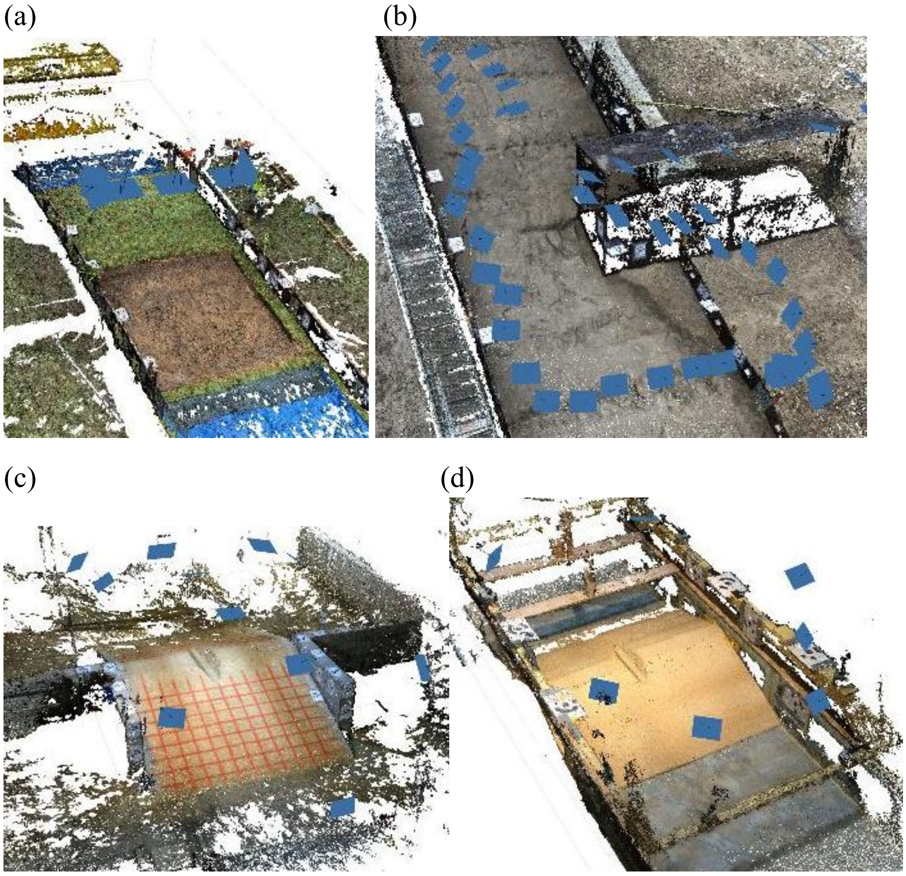

Figure 2.2 Close-range SfM-photogrammetry application to prototype levee erosion monitoring: (a) bare-clay erosion tests, (b) lime-treated clay erosion tests; and laboratory embankment breaching tests at (c) medium scale at SPW MI hydraulic research laboratory and (d) small-scale at UCLouvain.

The outcomes of this phase are compiled in a data descriptor paper, *Spatiotemporal levee erosion and wavefront velocity dataset from in-situ wave overtopping experiments*[2], developed through collaborative work within the BONSAI Interreg project. This published dataset encompasses measurements from four full-scale experimental campaigns designed to evaluate the erosion resistance of both existing and newly constructed clay covers under controlled overtopping loads.

[2] Submitted to the Scientific Data of Nature Journal (under review).

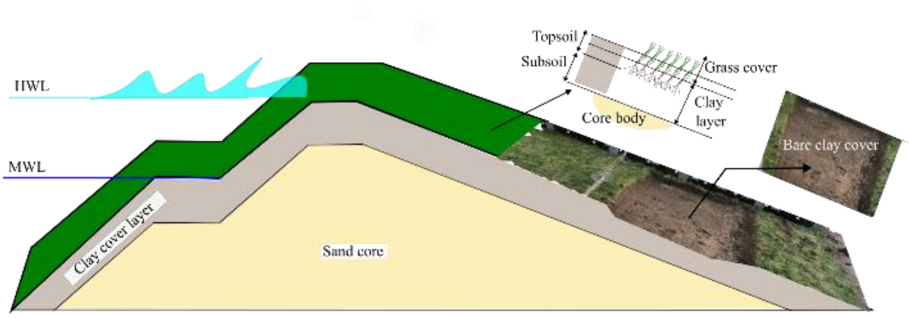

Figure 2.3 Monitoring levee clay cover erosion using SfM-photogrammetry within Polder2C's project.

II. Analysis of breach physics and material influence at intermediate scale

Once the protective cover fails, the erosion mechanisms shift from local erosion scours towards a uncontrolled and fast erosion progression into the embankment core sand. This creates a breach channel through the embankment body, conveying huge water flood toward the hinterland. The breach outflow hydrograph form, timing and peak discharge is a vital input for risk and hazard assessment models and determining the inundation maps and the flood extension area.

To investigate this, a highly controlled series of medium-scale (1-m-high) experiments was conducted at the Hydraulics Research Laboratory of SPW MI (Châtelet, Belgium) through a collaborative program with UCLouvain. The primary objective is to quantify the effects of grain size and hydraulic boundary conditions (constant reservoir inflow versus constant reservoir level) on breach evolution. This includes characterizing the transition from progressive surface erosion to discrete mass block failures (e.g., sliding and tilting) governed by apparent cohesion in finer sediments.

III. Scale-series laboratory modeling and scale-effect investigation

To address the inherent difficulties of satisfying simultaneous hydraulic and geotechnical similitude in physical modeling, the medium-scale tests were systematically replicated at a small scale at the LEMSC (Laboratoire Essais Mécanique, Structures et génie Civil or Mechanical testing, structures, and civil engineering laboratory in English) laboratory of UCLouvain. This research adopts a 'scale-series' approach—a strategy designed to isolate and quantify the scale effects that inevitably arise from incomplete similitude.

While the hydraulic loads were downscaled strictly according to Froude similarity, the sand grain sizes were maintained identical across both scales. By evaluating this sequence of models, this objective focuses on assessing theoretical sediment scaling approaches and systematically tracking how hydraulic and morphological behaviors deviate as physical dimensions decrease.

2.2 Structure of this thesis

The following five chapters are organized as follows:

Chapter 3 Close-Range Photogrammetry Application to Monitor Levee Erosion in Case of Wave Overtopping This chapter details the application of close-range photogrammetry to monitor the continuous and intermittent morphological evolution of a prototype levee subjected to wave overtopping. By observing full-scale levees in-situ, this research investigates morphological profile evolution and volumetric soil loss—quantified via high-resolution Digital Elevation Models (DEMs). This approach expands the scope of investigated hydraulic loads beyond steady overflowing to include the episodic, highly dynamic impacts of wave-driven failure modes. To capture these processes and quantify erosion rates, two distinct image acquisition strategies were utilized: a system of ten multi-stationary synchronized cameras and a single mobile camera. Finally, the accuracy of the resulting photogrammetric models is evaluated against manual measurements conducted with an RTK GNSS GPS system.

Chapter 4 Application of Enhanced SfM-Photogrammetry to Medium-Scale Earthen Embankment Breaching Experiments This chapter presents the application of Structure-from-Motion (SfM) photogrammetry to monitor breach evolution in medium-scale experiments on non-cohesive sand embankments (median grain size 0.61 mm) conducted at the Hydraulic Research Laboratory of SPW MI, Châtelet, Belgium. Breach development under overtopping was captured using a close-range, static multi-camera SfM system, providing high-resolution reconstructions of dike topography. The accuracy of the 3D reconstructions was assessed through root-mean-square reprojection errors of ground control and check points, and by comparison with dense point clouds obtained from a FARO terrestrial LiDAR scanner and an iPhone LiDAR sensor, both confirming centimetre-scale precision. Key challenges included capturing the submerged bed and dynamic water surface. Limitations from poor texture, reflections, and water motion were mitigated using floating tracers and synchronised imaging. Embedding coloured balls within the dike enabled tracking of breach deepening, improving the accuracy and completeness of SfM-photogrammetry reconstructions.

Chapter 5 Effects of Grain Size and Overtopping Conditions on Breach Evolution at Medium Scale The medium-scale embankment breaching tests have been expanded to examine the influence of sediment granulometry (using two sands with median grain sizes of 0.61 mm and 0.31 mm) and overtopping conditions on the temporal evolution of breaches through sand embankments. The primary objective of this chapter is to quantify how variations in sand grain size and overtopping regimes, specifically constant reservoir level versus constant reservoir inflows, dictate the morphological development and hydraulic capacity of the breach. Unlike the majority of previously reported laboratory experiments, which are constrained by small-scale limitations, this study presents a novel medium-scale approach. By conducting these tests at a significantly larger scale and employing highly advanced spatial measurement techniques, this research provides high-resolution data on the breaching process. Moreover, the high-resolution dataset generated from these experiments bridges the gap between small-scale laboratory observations and full-scale failure scenarios. This comprehensive data serves as a robust foundation for the validation of numerical models and the training of machine learning tools. Finally, the results of the present study were combined with well-documented experimental data from the literature for sand embankments ranging from 0.3 m to 1.6 m in height. This extended comparison highlights the profound influence of reservoir dimensions on breaching dynamics, across varying overtopping conditions.

Chapter 6 Experimental Investigation of Scale Effects in Sand Embankments Breaching To address the inherent difficulties of physical modeling, this chapter investigates the scale effects present in sand embankment breaching experiments. Recognizing the fundamental challenge of achieving simultaneous hydraulic and geotechnical similitude, this study adopts a 'scale-series' approach. The experimental campaign systematically replicates breach tests at two distinct geometric scales: a medium-scale baseline embankment (1 m high) and a small-scale model (0.2 m high), applying a geometric scale factor of 5. The new small-scale test series was conducted at the LEMSC laboratory of UCLouvain. While the hydraulic boundary conditions were strictly downscaled according to Froude similarity, the embankment material (utilizing the identical fine and medium sands) remained constant across both scales. Ultimately, this controlled distortion enables a comprehensive comparative analysis of breach evolution and discharge, successfully isolating the specific scale effects arising from complex hydro-morphodynamic interactions.

Chapter 7 Conclusion and Perspectives providing a summary of the research, main conclusions and recommendations for the future work.

Chapter 3

Close-Range Photogrammetry Application to Monitor Levee Erosion in Case of Wave Overtopping[3]

3.1 Summary

Coastal and riverine levees are prone to wave and steady flow overtopping which can result in breaching and consequential flooding of the hinterland. Full-scale field experiments on a levee appear as a sound approach for understanding the underlying physical processes without suffering from scale effects, provided that accurate and valuable data can be collected. This paper outlines how close-range photogrammetry was applied to monitor a levee's morphological evolution continuously and intermittently during wave overtopping. High-resolution spatial topographical models were obtained from which erosion rates can be quantified. Two different camera set-ups including a system of multi-stationary synchronized cameras, and a single mobile camera were used for photo acquisition. The first configuration enables reconstruction of the target zone as a dynamic scene and reduces the photogrammetric analysis time through simultaneous processing of several frames (4D processing). The second configuration consists in applying the Structure-from-Motion (SfM) technique using multiple, overlapping photographs to obtain three-dimensional elevation models at specific moments. Both approaches result in high resolution Digital Elevation Models (DEMs) with low Mean Absolute Errors (MAE) in the order of magnitude of a few centimeters. Furthermore, the technique proved to be highly flexible and

[3] The contents of this chapter are based on the following publication: Ebrahimi et al. (2025a).

can be applied to different types of levees with various cover layers, hydraulic loads, and meteorological conditions.

3.2 Background

Levee breaching induced by steady overtopping (overflowing) and wave overtopping is one of the dominant causes of failure (ASCE/EWRI Task Committee on Dam/Levee Breaching 2011). During overtopping, the breach initiates due to continuous surface erosion of the crest and landward levee slope. Many research projects have been dedicated to studying breach formation and development in large scale embankment dams or levees, e.g., IMPACT (Morris et al. 2007), USDARS (Hanson et al. 2005), Sigmaplan (Peeters et al. 2015). A series of large-scale riverine levee breaching experiments were conducted at the Chiyoda experimental field flume (Shimada et al. 2009, Shimada et al. 2010, Tobita et al. 2014, and Kakinuma and Shimizu 2014). All these projects concerned fully destructive breaching experiments to investigate the general breach expansion due to frontal or longitudinal riverine overtopping.

Furthermore, reinforcement of existing flood protection levee systems, without necessarily increasing the height of levees, requires in-depth research on the erosion resistance and strength of the levee's landward side slope and quantifying the erosion progression into the soil. Furthermore, to meet the new standards and regulations, there is a growing demand for the safety and strength assessment of levees through real-scale, partially destructive experiments (van Damme et al. 2016, Rikkert et al. 2022, Picault et al. 2022). ASCE/EWRI Task Committee on Dam/Levee Breaching (2011) emphasizes the importance and necessity of conducting large-scale and prototype experiments to accurately replicate complex physical processes and avoid scale effects (e.g., levee material reproduction and vegetation impact) inherent in small-scale modeling. Partially destructive experiments are widely conducted in the Netherlands (van Damme et al. 2016, Koelewijn et al. 2022) and more recently in France along the Rhône River (Picault et al. 2022). The limited damage in these experiments is easier to execute and monitor. These tests also enable a closer observation of the soil-flow interaction over a limited area and therefore offer an advantageous way to evaluate the instantaneous strength of a protective cover layer under extreme events. Particularly during the last two decades, a large number of partially destructive full-scale experiments were conducted on real levees, investigating the behavior of landward slope under overflowing and wave overtopping conditions, or WOCs, (van der Meer et al. 2009, Steendam et al. 2012, van Damme et al. 2016, Koelewijn et al. 2022; Ponsioen et al. 2019). In addition, there is scarce information on the erosion progression into the soil underneath the grass cover. According to Dutch regulations (van der Meer et al. 2015) the protective grass layer is considered to have failed when the damage penetrates the turf layer. However, the erosion processes in clay after failure of the grass cover need to be investigated further (D'Eliso, 2007).

These field tests have been used to investigate the strength of grass-cover on the landside slope under wave overtopping conditions (van der Meer et al. 2009, Steendam et al. 2012, Steendam et al. 2013) or they have been implemented to gain more insight into the correlation between flow characteristics and the overtopping volumes (van der Meer et al. 2010, Hughes et al. 2012).

Furthermore, treating clay with lime is increasingly recognized as an effective cover reinforcement method. As highlighted in recent reviews of lime-treated clay (LTC) applications for earth-fill dikes (Puiatti et al., 2018), the addition of lime significantly enhances the soil's erosion resistance (Bennabi et al., 2016). Alternatively, eco-friendly additives such as biopolymers can decrease soil erodibility, thereby improving levee resilience against steady overflow and wave overtopping (Ko and Kang, 2018). Ideally, the effectiveness of these soil-based reinforcement techniques should be verified through full-scale, in-situ experiments prior to their widespread application.

Despite a large quantity of research conducted in this field, most available data on damage initiation and progression are limited to either pixel-based image analysis or pointwise ground survey measurements. Recent advancements in Light Detection and Ranging (LiDAR) scanners and Structure-from-Motion (SfM) photogrammetry have made them robust, non-intrusive tools for capturing high-resolution topography changes. Terrestrial LiDAR, although becoming more affordable, requires relatively long scanning durations (e.g., minimum of 2 minutes) that force interruptions during experiments. Furthermore, the infrared light used by LiDAR is strongly absorbed by water, limiting its effective measurement range underwater. In contrast, close-range SfM-photogrammetry — particularly when utilizing a synchronized multi-camera setup — offers a cost-effective solution for rapid, continuous monitoring without interrupting the flow. Nevertheless, a major limitation of both techniques is their inability to accurately capture the submerged portions of the levee topography due to light refraction, water turbidity, and high aeration.

3.3 Objectives

Monitoring erosion processes due to wave overtopping of levees is achieved here using the close-range photogrammetry in two series of field experiments with distinct camera set-ups. The tests were conducted at 1:1 scale at the Living Lab Hedwige Prosperpolder to study the erosion processes of the levee's clay's protection layer (1-m thick clay) on the landward-side slope subjected to loads by overtopping waves. The experiments were conducted on a levee cover in (i) the natural state, and (ii) after treating clay with lime for reinforcement.

In the first series of experiments, a system of ten synchronized stationary cameras was used to capture photos. To focus on the erodibility of the natural clay cover, the 0.2-m thick grass cover was removed over an area of 14 m^2 at three different locations on the slope prior to the testing. In the second series, a single camera was moved around the scene at specific time intervals. An object featuring a building was also embedded in each new slope revetment, to evaluate the effects of the flow around obstacles on the erosion process. Both methods allowed generating accurate erosion maps, with slightly higher accuracy and ease of post-treatment for the multiple-camera set-up.

This chapter shows the capacity of close-range photogrammetry to monitor the morphological evolutions of the landward side slope of a prototype levee subjected to simulated overtopping waves. The levee slope evolution was photographed using two different camera installation set-ups during the experiments. The photogrammetric reconstruction (3D model) of the scene was carried out using Agisoft Metashape (Agisoft Metashape User Manual 2022). The main processing parameters of the software for both camera set-ups (fixed multiple-camera, single mobile camera) had been verified and optimized to obtain high-resolution accurate elevation models. The experiments were conducted in the Living Lab Hedwige-Prosperpolder (LLHPP) located near the border of Belgium and the Netherlands next to Western Scheldt River (Figure 3.1).

Figure 3.1 Aerial view of Polder2C's project site, LLHPP, and locations for bare-clay (BC) and lime-treated clay (LTC) experiments.

3.3.1 Polder2C's project at LLHPP area

The INTERREG Polder2C's project aimed at investigating current and innovative techniques, processes, methods and products in support of adapting the Interreg 2Seas Region to climate change. The old levee surrounding the LLHPP area had to be demolished and was used to perform a wide range of experiments and practicing emergency responses.

A series of experiments conducted to assess the residual strength of the bare clay underneath the grass cover exposed to the wave overtopping conditions. To study both the influence of the test location along the slope, and the magnitude and releasing order of waves, 2 test flumes and in total 5 test sections were prepared and tested. The main goal of these experiments was investigating the erosion behavior of clay cover under various wave overtopping conditions and wave patterns.

3.3.2 Lime in Clay project at LLHPP area

A second series of experiments was performed within the Dutch Lime in Clay project on the same levee as the previous Polder2C's campaign, though at different specific test sections within the LLHPP area. The objective of these series of tests was to investigate the erosion resistance of lime-treated clay at the soil-structure transition when exposed to wave overtopping loads. In this context, the soil-structure transition is defined as the interface and the immediate area surrounding a solid physical obstacle placed within the clay layer, where local flow dynamics and soil erodibility are heavily influenced by the presence of the structure. For that reason, the original clay levee cover was replaced with three newly constructed test sections, each featuring a distinct clay type stabilized with lime.This chapter is organized as follows: first the in-situ setup and testing procedures are described. Then, the close-range photogrammetry application using the two different camera set-ups are presented. The performance of the technique for field-scale measurements are discussed and assessed, and finally, conclusions and perspectives of this research are provided.

3.4 In-situ Setup and Testing Procedures

The Living Lab Hedwige Prosperpolder (LLHPP) was a 6-km^2 agricultural area (Figure 3.1) that was converted into a natural tidal zone. With the creation of a new levee, the old levees protecting the polder became redundant, offering a vast laboratory to conduct a wide range of destructive experiments on actual levees (Rikkert et al. 2021, Koelewijn et al. 2022, van Damme 2023) at different scales and to practice innovative levee emergency response strategies within the Polder2C's project. The levees in the LLHPP area consisted of a sand core protected by an approximately 1-m thick well-grassed clay layer cover (Figure 3.2), and have an average steepness of 1V:2.6H. Soil investigation pits excavated next to the testing zones indicated that the clay cover layer had an average thickness of 0.8 m, with values ranging from 0.75 m near the toe and crest to 1 m in the middle of the slope. Heterogeneities within the soil profiles were observed both in-depth and along the levee slope, exhibiting variations from clay soil to silty sand containing grass roots. The median grain diameter (d50) ranged from 88 to 150 µm in different soil samples taken from different depths in the cover layer (van Damme et al., 2023). The upper part of the protective clay layer included grass and roots with crumbled soil (0.1 meter thick).

The first series of tests investigated the performance of natural clay, hereafter called bare-clay (BC) erosion tests, while the second series aimed at evaluating the resistance of three different lime-treated clay (LTC) mixtures developed to enhance the erosion resistive properties of clay. Critical flow velocities and shear stresses for erosion initiation were determined by performing tests with the Erosion Function Apparatus (EFA) for both BC and LTC soils. While critical flow velocities and shear stresses ranged from 0.4 to 0.6 m/s, and 0.6 to 1 Pa, respectively, for samples taken from BC test sections, almost no erosion was observed in case of LTC soil samples for flow velocities under 2.6 m/s. The levee stretches where BC and LTC experiments were conducted are indicated in Figure 3.1. The Wave Overtopping Simulator (WOS) (van der Meer et al. 2007) was placed on the levee crest to release either Weibull distributed wave volumes or constant wave volumes. This will be further discussed in Section 3.4.3.

The exact locations of all test sections were recorded using an RTK GNSS GPS tool with a precision of 1-2 cm, in RD 2008 (Netherlands/RD) - EPSG:28992 coordinate reference system (CRS). In this system, the position of each point is defined as Easting, Northing, and Elevation. The Elevation is the absolute upward elevation of each point in meters with regard to the Normaal Amsterdams Peil (NAP) which is the Amsterdam ordnance datum. As illustrated in Figure 3.2, the Easting and Northing were then transferred into a conventional coordinate systems called Global (X,Y,Z), while distances along the dike slope were measured in a local system (x,y,z) located at the top left corner of the testing flumes. The xz plane is obtained by rotating the XZ plane clockwise around the Y-axis by an angle equal to the levee gradient. Thus, x-axis is aligned with the slope and is perpendicular to z-axis.

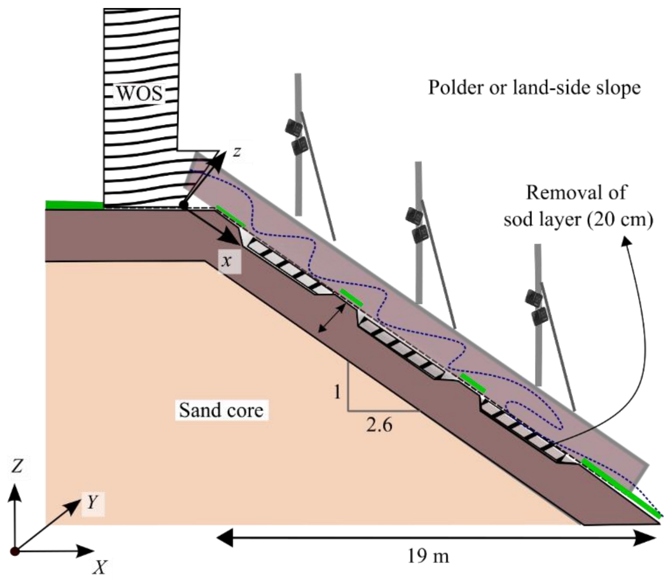

Figure 3.2 (a) schematic view of levee cross-section at LLHPP site as well as BC test layout, and (b) example of prepared testing section for BC experiments.

3.4.1 Bare-clay (BC) erosion tests

These tests focus on the damage initiation and progression into the top-clay layer below the grass cover. The erosion tests were repeated several times locally in this area (Koelewijn et al. 2022). Two separate 4-m wide test flumes were constructed on the landward-side slope of the levee by installing wooden lateral walls. As illustrated in Figure 3.2 (a) and Figure 3.3 (a), each flume was divided into a series of test sections over which a 20-cm grass cover layer was removed using a crane bucket. An example of the prepared test section is shown in Figure 3.2 (b). This preparation appeared necessary after the preliminary tests showed that the grass cover itself was able to withstand the wave overtopping loads for a long time duration. The test sections were prepared and tested respectively from the toe towards the crest, to allow for three tests on the same portion of the levee, i.e., test section BC1-1 was tested before test section BC1-2 for example. Due to the supercritical wave velocities, the loads would not be affected by the erosion of the lower lying test sections, whereas the grass cover present on test section BC1-2 would prevent erosion of this while testing section BC1-1. Only shortly prior to testing the sections, the grass cover was removed. The test sections were approximately 3.5 m long, ensuring that waves would not overshoot the test sections, and that the test section would indeed constitute the weakest parts of the levee. As a result, during each test, a section of roughly 14 m2 of clay was exposed to the waves. Sections BC2-1 and BC2-2 were prepared in a similar way. The resulting initial dike profiles for test BC1 are illustrated in Figure 3.3 (b).

The clay layer was considered to have failed as soon as the erosion reached the sand core (D'Eliso 2007). This criterion is highly conservative, as erosion may occur locally, and form deep, narrow holes, without leading to an immediate failure of the levee. However, such holes constitute weak points in the levee that significantly affect its strength and ultimately lead to a full failure.

(a)

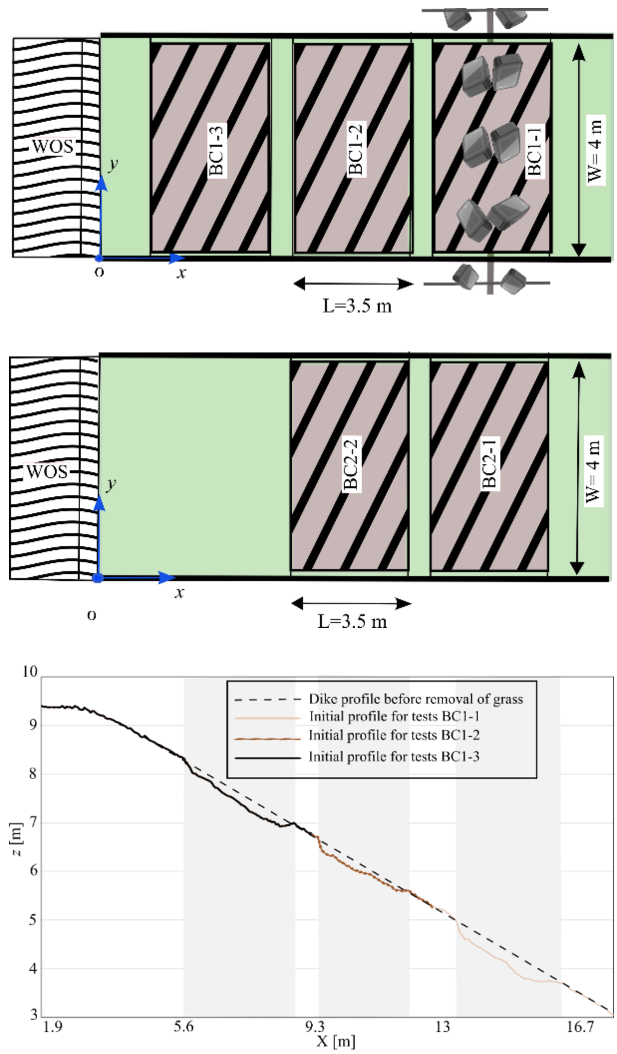

(b)

Figure 3.3 (a) BC test flumes and section layouts including camera layout; and (b) initial and excavated levee slope profiles for all BC1 sections (obtained from photogrammetry).

3.4.2 Lime-treated clay (LTC) erosion tests

To investigate the improvement in erosion resistance brought by the lime treatment, especially in the vicinity of transitions and obstacles on the levee slope (Steedman et al. 2014), the original clay cover of the levee was replaced by a lime-treated clay cover over the entire levee stretch as shown in Figure 3.4a. This stretch was divided into three main sections (LTCB1, LTCB2, and

LTCB3), each test section being constructed with a specific clay and equipped with a wooden block, representing a structure partially embedded in the levee.

(a)

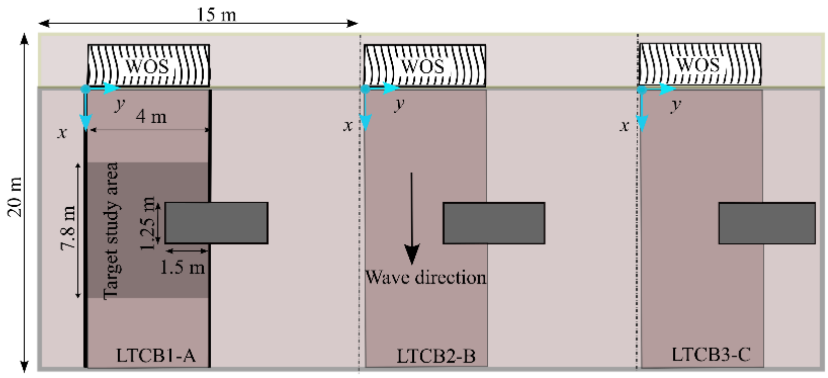

(b)

Figure 3.4 . (a) LTCB test location including layout of all sections and target study area; and (b) constructed section.

Three types of clay were tested and used in accordance with the Dutch Dike Construction Manual (Halter et al. 2018). To properly estimate the erosion resistance of clay, the Dutch Dike regulations use Atterberg limits, including the A-line from the plasticity graph of Casagrande (Halter et al. 2018) and classify the original soils into three categories. Figure 3.5 displays that the three clay soils (A, B, C) are within the limits of erosion-resistant clay for levee revetment utilization. Meanwhile, clay types A and B are located close to the moderately erosion-resistant clay category limits and less favorable for dike revetment. Hence, soils type A and B are referred to as lesser quality clays, and clay type C as good quality clay in this paper. Clay type C was transported to and stored in the LLHPP while clays A and B originated from the LLHPP. These clays can turn into very resistant material once treated with lime. The lime content of treated soil is 5 % of the dry soil weight for clay type C, and 4 % for both clay soils type A and B according to Stoutjesdijk (2022). The amount of required lime depends on a soil property known as Lime Fixation Point (LFP) slightly above which (1 to 2%) the pozzolanic reaction occurs and leads to the soil strengthening. The LFP can be determined from the Atterberg limits tests on clay soils mixed with varying amounts of lime (Hilt and Davidson 1960). The plastic limit remains almost constant slightly above the LFP in all clay soils. The agglomeration and the binding of the particles to each other, under the action of lime, increase the shear stress required to tear off the soil particles (Bennabi et. al. 2016). The EFA tests on the treated soils (types A, B, C) indicated a significantly increase in erosion resistance (Stoutjesdijk 2022).

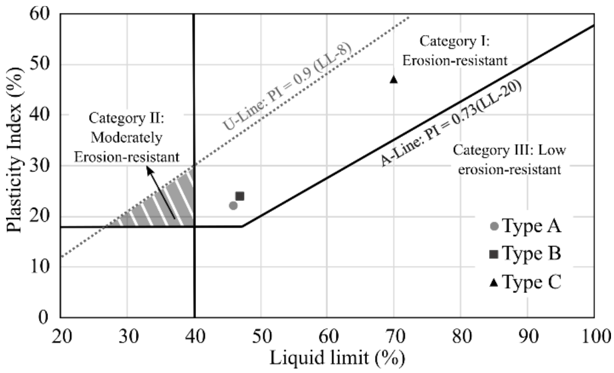

Figure 3.5 Clay soil classification for Polder2C's levee revetment according to Dutch dike regulations.

The clay soil types A, B, and C are used respectively to reconstruct the levee cover including three 4 m wide flumes in which a scaled-down building (wooden box) was constructed in the middle of each flume named respectively as LTCB1-A, LTCB2-B and LTCB3-C (Figure 3.4a). Apart from the variability in soil properties between test sections, a stronger compacter was used to compact the soil around the obstacle in test flumes LTCB2-B and LTCB3-C than in flume LTCB1-A. This construction modification was made to improve the soil-structure transitory strength through improved soil compaction and resistance to erosion.

Preparation of the levee revetment started with removal of the existing protective layer. To prevent geotechnical instability of the new cover, the grass cover and the upper clay soil layer were removed in a staircase shape (width 1 m × height 0.4 m) as depicted in Figure 3.4a. The new levee cover, therefore, was constructed on this staircase profile following the same form.

The final cover layer had a variable thickness changing between 0.4 to 0.75 m along the slope after cutting the final slope as shown in Figure 3.6 (Stoutjesdijk 2022). Each layer was compacted horizontally and in stretches parallel to the crest line with a Padfoot or Sheepsfoot drum compactor machine. The Proctor Compaction Test parameters after lime-treatment (4%) were determined to be ω_{optimum} = 27 % and $\gamma_d^{max} = 15$ kN/m^3; however, this was not strictly controlled during construction. The final slope of 1:2.6 was created by cutting and removing excess material. Despite that, remnants of the compactor and soil layers are still visible on the prepared test flumes, as can be recognized in Figure 3.6a.

(a) (b)

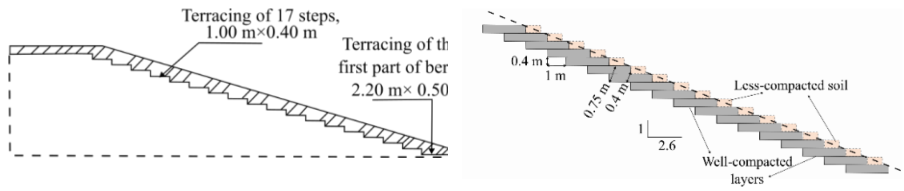

Figure 3.6 Removal of levee’s old cover layer and (b) construction of new lime-treated clays cover layer.

3.4.3 Wave overtopping load conditions

Waves were generated in a controlled way using the WOS located on the levee crest as shown in Figure 3.7. The simulator allowed for predetermined volumes of water to be released (see Figure 3.7b) as a series of pulses, imitating natural wave overtopping events. The volume of water in the simulator was measured with a pressure transducer that caused valves to open automatically when the prescribed volume was reached. The operational details of the simulator are explained by van der Meer et al. (2007).

(a) (b)

Figure 3.7 Wave overtopping simulator (WOS) located on levee crest, (a) the gate or opening valve and (b) an example of releasing wave.

The WOS can generate periodic waves with regular or irregular (i.e., more realistic) patterns, as illustrated in Figure 3.8. Irregular waves (Figure 3.8 a) were released over a fixed period with random volumes according to a Weibull distribution, corresponding to a prescribed average discharge. These waves are defined by the significant wave height and peak period of incident waves that can overtop the levee. Here, the tests are generally named with an acronym that includes the mean discharge q in L/s/m or m^3/s/m and the significant wave height H_s (van der Meer et al. 2007) e.g., a test called 0.5m60lsm corresponds to an average discharge of 60 L/s/m and a significant wave height of 0.5m. Regular waves (Figure 3.8b) consisted of a combination of 10 or 20 waves with constant volumes over a time interval, to produce a prescribed average discharge. During the experiments small wave volumes were omitted to reduce the experimental duration. For the regular waves, a descending or increasing total volume trend was imposed during the tests, with a stepped-form pattern as illustrated in Figure 3.9 (a), (b), and (c).

(a) (b)

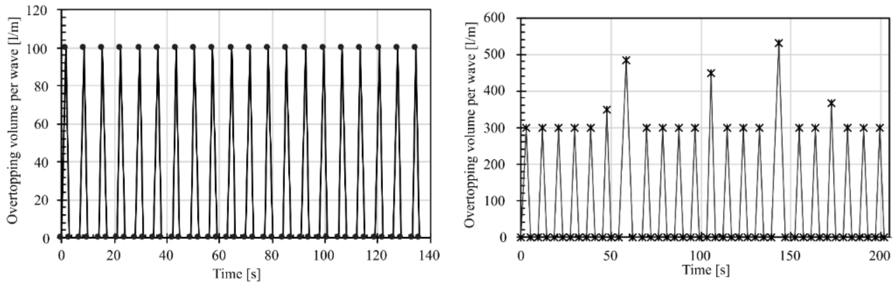

Figure 3.8 Examples of distributions for (a) regular waves, and (b) irregular waves patterns (clusters of 20 waves with different volumes).

Figure 3.9 (a), (b), (c), and (d) illustrate the regular and irregular waves used to simulate wave overtopping storms of approximately 2 hours at BC test sections. The BC1-1, BC1-2 and BC1-3 sections were tested under a series of regular wave groups of similar wave volumes per group. An increasing trend was applied for BC1-1 that was then adjusted for the other tests BC1-2 and BC1-3, located higher on the levee, i.e., closer to the crest. At these higher sections, the experiments began with high overtopping volumes, followed by an intermittent stepwise decrease in overtopping volumes and an instantaneous increase at the end. This modification of the wave pattern was done to examine the soil reaction under different scenarios and to identify the dependence of the erosion progression on the release order of the wave volumes and soil strength. The second series of tests, performed on flume BC2, concerned more realistic wave overtopping conditions with irregular waves corresponding to river (BC2-1) and coastal wave conditions (BC2-2), as shown in Figure 3.8(d) and summarized in Table 3.1. Both the height and peak period of coastal waves are larger than those of river waves for the same mean discharges. As a result, the number of waves with higher volumes is significantly larger for coastal dikes (van der Meer et al. 2010), whereas the total number of waves is smaller. The average discharge of storm events simulated at test sections BC2-1 and BC2-2 are 0.06 m^3/s and 0.05 m^3/s, and wave significant heights of 0.5 and 1 m, respectively (Table 3.1).

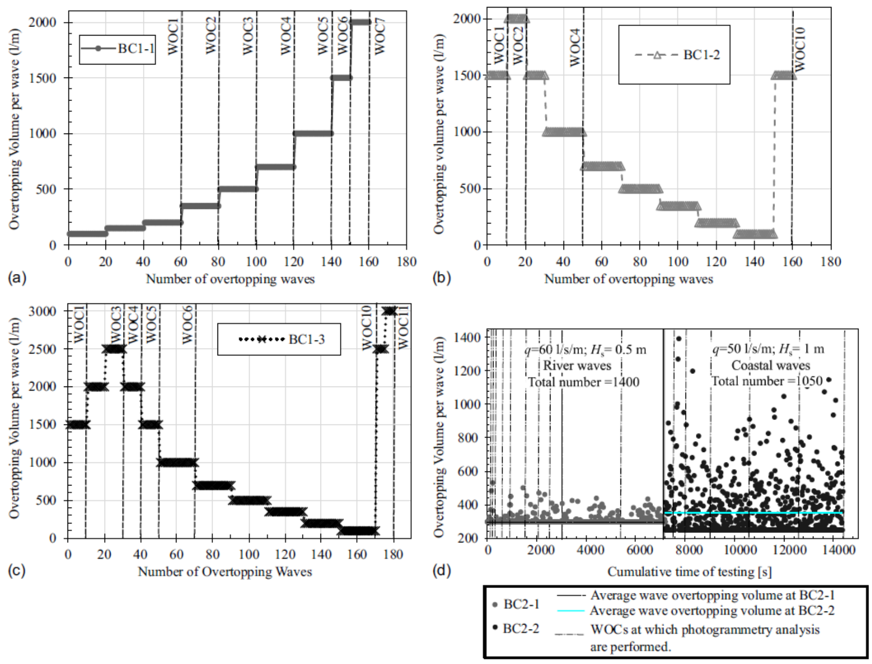

Figure 3.9 Regular waves with arbitrary patterns released during BC1 experiments at (a) BC1-1, (b) BC1-2 and (c) BC1-3 sections; (d) Irregular waves released during BC2 experiments.

The LTCB experiments, summarized in Table 3.1, comprised a series of overtopping events, with irregular waves. The overtopping storm lasted nearly 9 hours of continuous testing at LTCB1-A (halted at the beginning of 2m50lsm due to obstacle failure), and 11 hours at both LTCB2-B and LTCB3-C. This duration is typically sufficient to simulate an entire wave overtopping event during a design storm and consequently produce the maximum erosive load (EurOtop 2018). For the simulated storm events executed at LTCB sections the mean wave overtopping discharge was incrementally increased in a step wise manner (see Figure 3.10).

Table 3.1 Irregular wave overtopping programs.

Test name	Wave pattern acronym	Height H_s (m)	Discharge q ($m^3/s/m$)	probability of overtopping per wave	Total Wave numbers
BC2-1	0.5m60lsm	0.5	0.060	0.992	1419
BC2-2	1m50lsm	1	0.050	0.725	1045
LTCB1-A, LTCB2-B and	1m10lsm	1	0.010	0.340	585
LTCB1-A, LTCB2-B and LTCB3-C	1m30lsm*	1	0.030	0.590	222
LTCB1-A, LTCB2-B and LTCB3-C	1m50lsm	1	0.05	0.725	1045
LTCB1-A, LTCB2-B and LTCB3-C	1m190lsm*	1	0.190	1.000	1991
LTCB2-B and LTCB3-C	2m50lsm	2	0.050	0.435	510

*Except 1m30lsm and 1m190lsm which lasted respectively 30 minutes and 4 hours all other wave programs simulate 2-hour storm events.

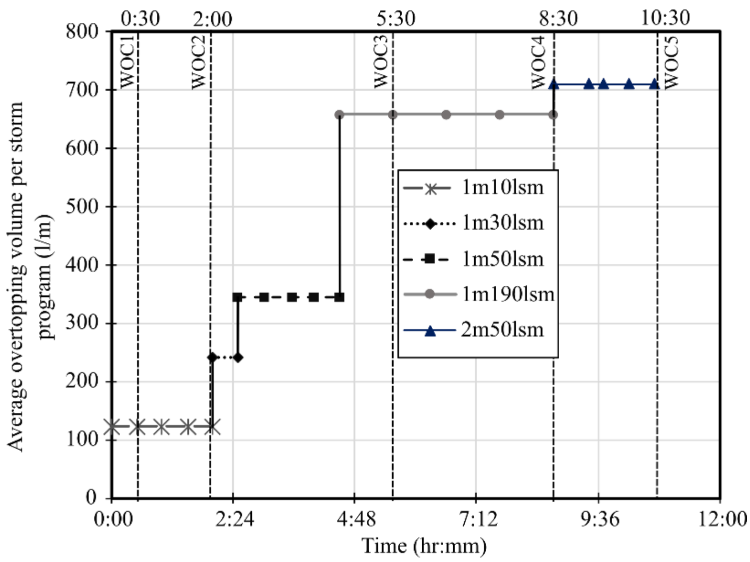

Figure 3.10 Wave overtopping storm programs tested at LTCB sections.

3.5 Photogrammetry Measurement Technique: Application and Verification

Close-range photogrammetry may also be an attractive method for monitoring field-scale experiments. This is becoming increasingly popular and efficient as a nonintrusive laboratory measurement technique (Lane et al. 2001, Carlier d'Odeigne et al. 2018, Bento et al. 2022). The Structure-from-motion (SfM) technique (Snavely 2008, Westoby et al. 2012) generate high-resolution 3D models of objects or terrain for remote sensing purposes. The method has already been applied to a wide range of studies such as monitoring changes in water surfaces, river bed topography, morphology, soil and river bank erosion (e.g. Barker et al. 1997, Lane et al. 2001, Heng and Chandler 2010, Barkker and Lane 2017, Carlier d'Odeigne et al. 2018, Zhang et al. 2022). Dezert and Sigtryggsdóttir (2024) employed SfM technique to monitor the displacement of levee riprap protection layer exposed to levee constant overtopping in a small-scale setup. Rieke-Zapp and Nearing (2005) showed that high-resolution Digital Elevation Models (DEMs) with 1-mm vertical precision for an erodible surface of 16 m2 are achievable to measure micro topographical changes. Bento et al. (2022) implemented this technique to accurately characterize the final shape of a scour hole formed in the vicinity of a bridge pier in the laboratory environment. All these studies demonstrated the capability of close-range photogrammetry in reconstructing highly accurate 3D models across a wide range of hydraulic engineering problems. However, field applications of close-range photogrammetry to continuous monitoring of erosion under less favorable weather and lighting conditions are required to further investigate the applicability of this technique.

Photographs of the different tests were recorded to apply the photogrammetry technique, i.e., 3D geometry reconstruction from multiple overlapping images based on scene triangulation principle, using the commercial software Agisoft Metashape. The principles of close-range photogrammetry and recent advancements in this field i.e., 'Structure-from-Motion' (SfM) are discussed by Lane (2001), Snavely (2008) and Westoby et al. (2012). In contrary to traditional photogrammetry, the SfM method does not require the exact position of cameras or the 3D location of some known points to resolve the 3D structure. However, to represent the results in a global coordinate system, Ground Control Points (GCP) with known coordinates were positioned around the scene and visible on the images (see Figure 3.11). To achieve the highest accuracy in detecting elevation changes, each photograph should ideally include at least three well-distributed GCPs positioned at opposite corners of the scene. The photogrammetric processing (Agisoft Metashape User Manual 2022) is summarized in Table 3.3 as an example taken from the BC tests: after loading raw images (Figure 3.11 (a)), these were orthorectified and aligned using the identification of the GCPs (Figure 3.11 (b)); a dense point cloud was produced (Figure 3.11 (c)). Finally, the georeferenced Digital Elevation Model (DEM) was constructed on a regular grid (Figure 3.11 (d)) and corresponding orthophotos were created (Figure 3.11 (e)).

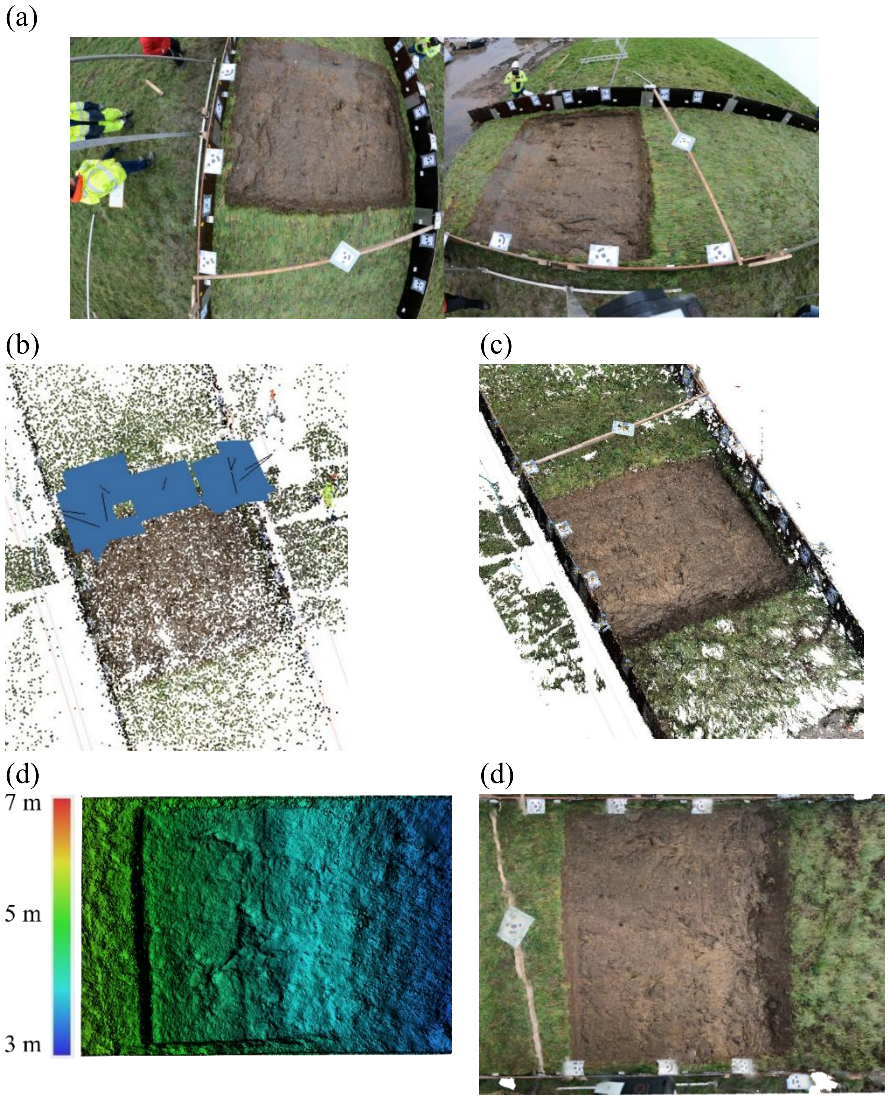

Figure 3.11 Photogrammetry processing: (a) Importing raw photos, (b) Aligning Photos, Generating (c) Dense Point Cloud, (d) Digital Elevation Model (DEM), and (e) Orthophoto.

The process was robust in reproducing constant and repeatable DEMs with low standard deviations (also shown by Zhang et al. 2022, Kingsland 2020, Bento et al. 2022, Dezert and Sigtryggsdóttir 2024). During the experiments, GoPro HERO9 cameras (GoPro, Inc, San Mateo, California, USA) were used in wide-angle lens mode to increases the field of view on each picture. This enabled a good overlap of images, which was a key condition for an accurate analysis, but it also resulted in highly distorted images (Figure 3.11 (a)), which required correction to obtain an orthorectified image. This correction is automatically applied during photo alignment, provided that the proper camera distortion type (Frame, Fisheye, and Spherical) is selected in the Camera Calibration step. The software uses the corresponding camera model (here, Fisheye) and applies the appropriate distortion model to orthorectify the photos. The resulting DEMs have a spatial resolution of 0.002 m in the *x*- and *y*-directions.

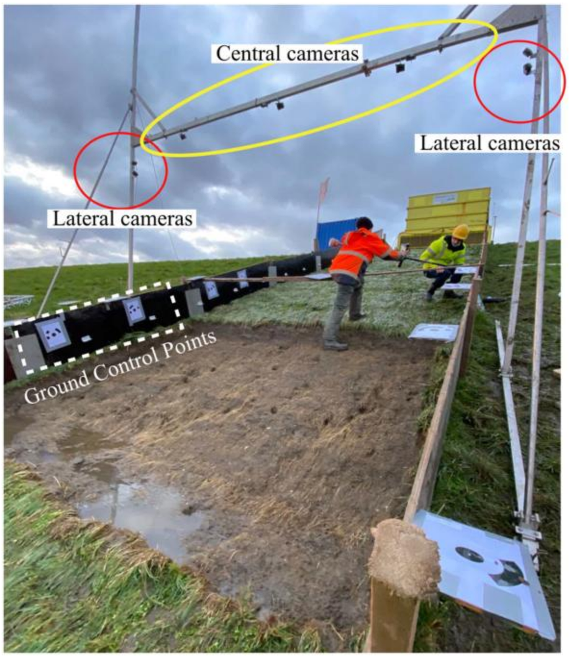

Figure 3.12 Multiple fixed camera set-up.

In this study, the method was applied in two different ways: (i) using a set of 10 cameras located at fixed positions for the BC tests, and (ii) using one single camera moved around the scene for the LTCB tests, as in the original Structure from Motion (SfM) technique developed by Westoby et al. (2012). A major advantage of the SfM technique is that prior knowledge of the camera positions is unnecessary. Instead, the software automatically estimates these locations during photo alignment by calculating the camera's interior and exterior orientation parameters alongside the specific lens model. To apply the photogrammetry technique from a set of images, it is necessary to have a sufficient overlap between images including at least one GCP. However, identifying at least three common well-distributed GCPs, which include two opposite corners of the scene on each image, allows to achieve the highest accuracy. To determine the optimal number of cameras or photos in each set-up, the following procedure was applied: using one single camera, photos were taken from various angles and locations around the scene, followed by the reconstruction of an initial 3D model in the software. The optimal number of cameras was determined based on the quality of the resulting 3D models. In the present case, it was found that 10 cameras, located as illustrated in Figure 3.12, provide an optimal 3D reconstruction of the scene. The camera set-ups corresponding to each type of application are presented in the next sections, followed by a discussion of the resulting accuracies. Table 3.2 summarizes all erosion test types and the corresponding image acquisition method at each test section.

Table 3.2 Summary of all erosion tests and photo acquisition method.

Test name	Test monitoring type	Location on slope	Overtopping wave type	Duration (hr:mm)
Bare-clay 1				
BC1-1	Multicamera on fixed frame	Lower	Regular waves	0:35
BC1-2	Multicamera on fixed frame	Middle	Regular waves	0:45
BC1-3	Multicamera on fixed frame	Upper	Regular waves	1:00
Bare-clay 2				
BC2-1	Multicamera on fixed frame	Lower	Irregular waves	2:00
BC2-2	Multicamera on fixed frame	Middle	Irregular waves	2:00
Lime-treated clay				
LTCB1-A	One mobile camera	Entire	Irregular waves – with building	8:45
LTCB2-B	One mobile camera	Entire	Irregular waves – with building	10:45
LTCB3-C	One mobile camera	Entire	Irregular waves – with building	10:45

3.5.1 Multiple fixed cameras supported by a rigid frame

In order to monitor the BC experiments in a continuous way, a system of multi-stationary synchronized cameras was employed. Photogrammetry could be then employed at any moment between wave groups to quantify morphological changes. In case of irregular waves with arbitrary volumes, the recognition of interesting moments was difficult prior to the experiments and a complete set of photos covering the entire experimentation facilitated the choice of interesting moments to be analyzed. Furthermore, the autonomy in photo acquisition led to minimum interruption of the tests and field work. The bare-clay test sections (BC1 and BC2) were monitored by means of 10 GoPro HERO9 cameras that were mounted on a mobile rigid frame illustrated in Figure 3.12. Six of the ten cameras were installed on a frame spanning across the flume, while the remaining four were positioned on lateral columns (Ebrahimi et al. 2022). The position and angle of view of the cameras ensured maximum overlap and complete coverage of the monitored area. The precise location of each camera was not important for the photogrammetric analysis provided that GCPs were installed and that their three-dimensional coordinates were known precisely. As can be seen in Figure 3.12, the GCPs were installed around the test section perimeters vertically and horizontally. The coordinates of the GCPs were measured via an RTK GNSS GPS system.

The cameras were configured to take photos in time-lapse mode with a 1-second interval, capturing the test section continuously during the experiments. Sets of five cameras were synchronized with a remote control, allowing for simultaneous cameras manipulation. The cameras have a resolution of 5184×3888 in time-lapse mode and a focal length of 3 mm, achieving a high ground spatial resolution of 1.25 mm/pixel.

After each series of waves corresponding to a prescribed volume of water, an interruption of a few minutes was imposed. This allowed the test section to partially dry out to minimize the adverse effects of measuring the water-level instead of the bed elevation. During these interruptions, pictures of the scene were taken by the 10 cameras and manual measurements of a series of arbitrary points were performed. Coordinates of these random points were recorded over the testing section providing accurate checkpoint data for assessing the accuracy of the photogrammetry technique.

The software processed several batches of photos per camera i.e., several frames in parallel, in a multi-camera setup, to reconstruct a dynamic scene of the target zone at different time moments. This feature, called 4D processing in the software, highly accelerated the photogrammetry processing but was limited to statically mounted synchronized cameras. The processing parameters introduced in Metashape and the resultant model features are outlined in Table 3.3. The photogrammetric workflow initiates with photo alignment to generate a Tie Point model, or sparse point cloud, which defines the overall scene geometry. Tie points consist of key features that are consistently identified and matched across multiple overlapping images. The density and accuracy of this alignment are governed by two primary parameters: the Key point limit, which defines the maximum number of feature points extracted per image, and the Tie point limit, which sets the upper boundary for the number of matched points retained between images.

In case of multicamera system, these parameters were determined by trial and error to achieve a high number of sparse points in the study region. These parameters were maintained at their default values in the software for the mobile camera set-up (SfM).

The accuracy of the photogrammetric measurements was evaluated by comparing them to the manual measurements conducted using the RTK system.

Table 3.3 Agisoft Metashape processing parameters and output model characteristics.

Operation	Parameters	Multicamera	Mobile camera
Photo selection	No. of photos	10	80
Image	resolution	5184×3888 (1.25mm/pix)	5184×3888 (1.25mm/pix)
Camera calibration	Camera type	Fisheye	Fisheye
Detect markers	GCP detection	Automatic	Automatic and manual
Align photos	Key point limit	10×10^4	4×10^4
	Tie point limit	5×10^4	4×10^3
	Accuracy	Highest	Highest
	Sparse points	7.5×10^4	7×10^4
Build Dense Cloud	Quality	High	High
	Dense points	10×10^6	30×10^6
	Total Error* (m)	1.7×10^{-2}	2.7×10^{-2}
Build DEM	Resolution (m)	2.62×10^{-3}	2.9×10^{-3}

* Total error is calculated as root mean square errors (distance between input and estimated coordinates) of all GCPs.

(a)

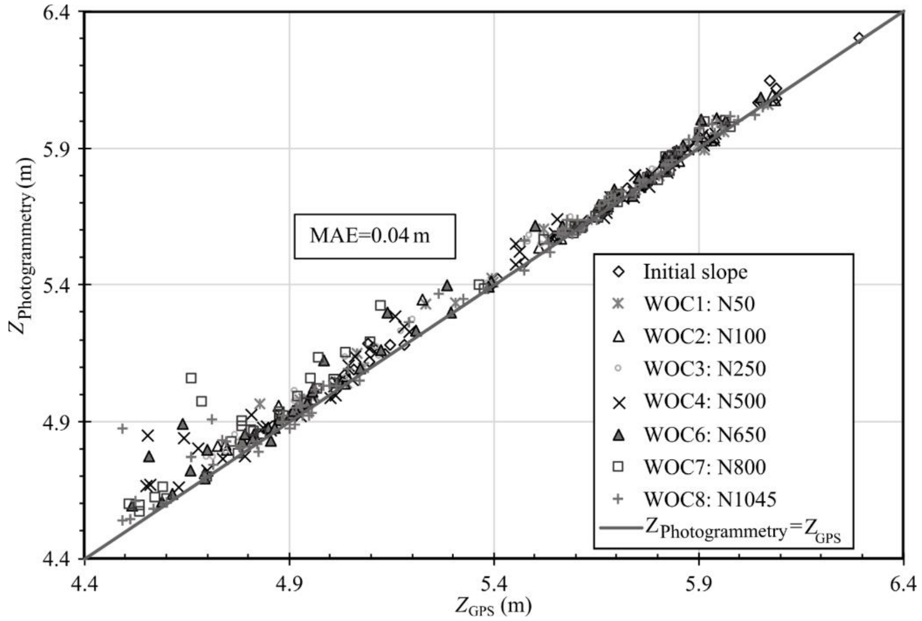

(b)

Figure 3.13 (a) Photogrammetric verification versus RTK measurements for multicamera set-up at section BC2-2; (b) water-shadow negative effects.

Figure 3.13a presents the comparison between the two methods throughout the wave overtopping experiments at BC2-2 test section. The results indicate a good correspondence between two methods, with a Mean Absolute Error (MAE) of 0.04 m at this section. While this margin of error might be significant in small-scale laboratory settings, it is highly acceptable for 1:1 prototype field experiments measuring macroscopic morphological changes within a 0.8 to 1.0 m thick clay cover. This 0.04 m MAE represents an aggregate error in a dynamic outdoor environment, primarily influenced by residual water trapped in erosion pits causing light refraction and dark shadows cast during sunny conditions. Furthermore, this accuracy aligns well with comparable large-scale breach studies; for instance, Walder et al. (2015) reported acceptable errors of 20 to 28 mm using photogrammetry on a 1-meter-high dam breach. Additionally, in highly controlled medium-scale laboratory tests discussed later in Chapter 4, the precision of the SfM technique significantly improved, yielding a mean distance error of just 0.0114 m when compared to FARO LiDAR. This demonstrates that the 4 cm field error is largely attributable to environmental noise rather than methodological flaws.

Overall, the photogrammetry tends to underestimate the levee erosion by overestimating the elevations. This discrepancy can be also attributed to the estimation of lens and exterior orientation parameters using SfM methods, which introduces an inherent systematic error in the resulting point clouds (Bakker and Lane 2017). Also, some scattered points were observed towards the downstream end of the test section (around z = 4.6 m). This inaccuracy, on one hand, was caused by water trapped into the erosion pits: in this case, the water surface is identified by the photogrammetry technique instead of actual bed elevation. On the other hand, the inaccuracy was caused by dark shadows cast on a sunny day. However, because Structure-from-Motion (SfM) photogrammetry relies entirely on high-contrast feature points to successfully align photos, dark spot lacking sufficient pixel variation cannot be accurately reconstructed and are consequently omitted from the topographic model.

Figure 3.13b shows such zones where water was stuck in the erosion pits, primarily located at the lowest extremity of the test section. One solution would have been to leave enough time between the wave pulses to allow most of the water to naturally drain away, but the time scheduling of the experiments limited the drainage effectiveness. Therefore, it was attempted to select the photos with a minimum of residual water present in the eroded area. For the measurement of the final state, little water remaining in the erosion pits was pumped out.

The technique was applied under various meteorological conditions, including cloudy, rainy, and sunny weather in the field. Cloudy weather proved to be the most favorable condition for obtaining high-resolution sharp photos. While light reflection, contrast, or shadows may influence the quality of photos during sunny days, they do not diminish the applicability of this technique.

3.5.2 One mobile camera

For the lime-treated clay experiments, continuous filming of the test section was not a priority, as the soil was less erodible. Consequently, the number of monitoring intervals during the experiments was reduced. Moreover, the tests could be interrupted over a longer duration between wave pulses, allowing sufficient time for photography. Acquisition of photos were performed every 30 minutes using just one GoPro camera attached to a monopod. The camera was moved around the entire test flume, capturing a higher number of photos close to the obstacle taking approximately 1 to 2 minutes. The region of interest for these tests was the area around the obstacle as indicated on Figure 3.14a. The GCPs were densely placed over a certain radius around the obstacle (Figure 3.14a), where flow concentration was expected to result in significant erosion. On average, 100 photos were captured to encompass the entire flume, of which 80 to 90 photos were successfully aligned. The software finds and matches common points in overlapping regions of the images, while the GCPs are essential to locate them geospatially, and to scale the 3D model. The resulting orthophoto image is shown in Figure 3.14b.

(a)

(b)

(c)

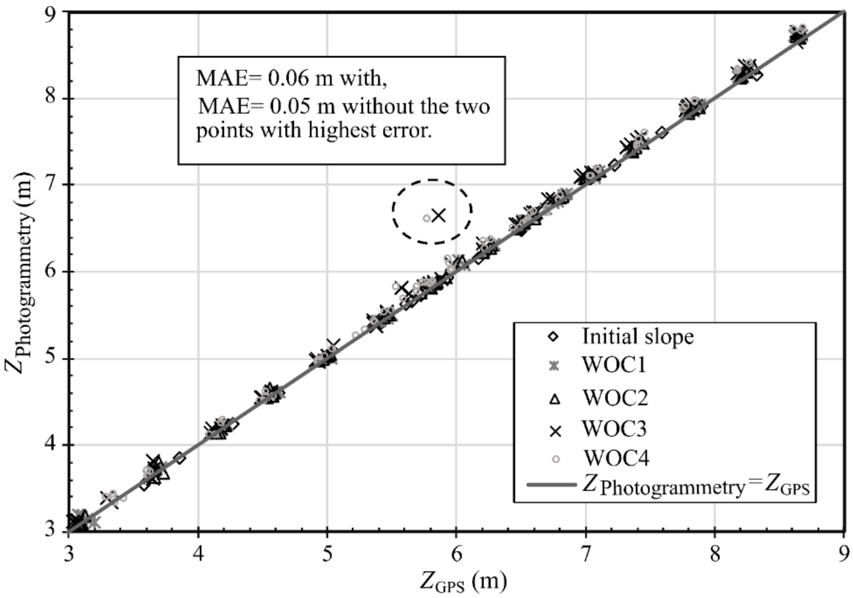

Figure 3.14 . (a) LTCB1-A final state highlighting the adverse effect of water, (b) corresponding orthophoto (b), and (c) Photogrammetric verification versus RTK measurements for one mobile camera at this section.

Manual measurements were taken to evaluate the accuracy of the method, as illustrated in Figure 3.14c for the tests at LTCB1-A. In this section, the accuracy was found to be of the order of 0.05 m (MAE) which is similar to the one obtained using the fixed multi-camera method, even for the furthest points situated near the crest and toe of the levee. Except for two encircled points in Figure 3.14c, all other points closely align with the inclined line representing equality of measurement and calculations. The points with maximum errors are located next to the obstacle in a deep narrow trench, which was difficult to reach with the camera. As in the previous case, the elevations are generally overestimated by the photogrammetry technique.

The comparison between Figure 3.13 (a), derived for a multicamera system, and Figure 3.14 (c), resulting from a single mobile camera setup, suggests that increasing the number of images does not automatically result in more accurate DEMs. The key factors influencing the accuracy are the overlap and configuration of the images. These influential factors are further studied and discussed through some examples in Chapter 4

3.6 Results from the photogrammetry measurements

Table 3.4 summarizes the photogrammetry analysis performed throughout BC experiments, after different number of waves indicated in Figure 3.9a,b, and c for BC1 experiments. For LTCB tests, the moments at which the analysis was conducted for each storm condition is indicated in Figure 3.10.

3.6.1 BC experiments

The observations indicate that the clay cover failure was mostly a local phenomenon whereby a deep scour hole formed, which either developed into a headcut moving upwards or remained locally restricted. In fact, as soon as a relatively weak point in the prepared soil became affected, the erosion concentrated around this point. This is illustrated in Figure 3.15 showing the final state of bare-clay tests and the bed changes (ΔZ) at the end of experiment. In the BC1-1, BC2-1 and BC2-2 sections, the erosion concentrated at some spots that developed more rapidly and got dominant afterward. In BC2-1 test, the erosion grew upward while it remained more restricted in the BC1-1 and BC2-2 sections. This evolution is depicted in Figure 3.16 for BC2-2, which showed that the erosion was not evenly distributed along the width, and that a localized erosion pit formed. This observation is in accordance with the large-scale experiments conducted by Hanson et al. (2005) emphasizing the development of an initial scour hole into a steep headcut migrating upstream from the test section.

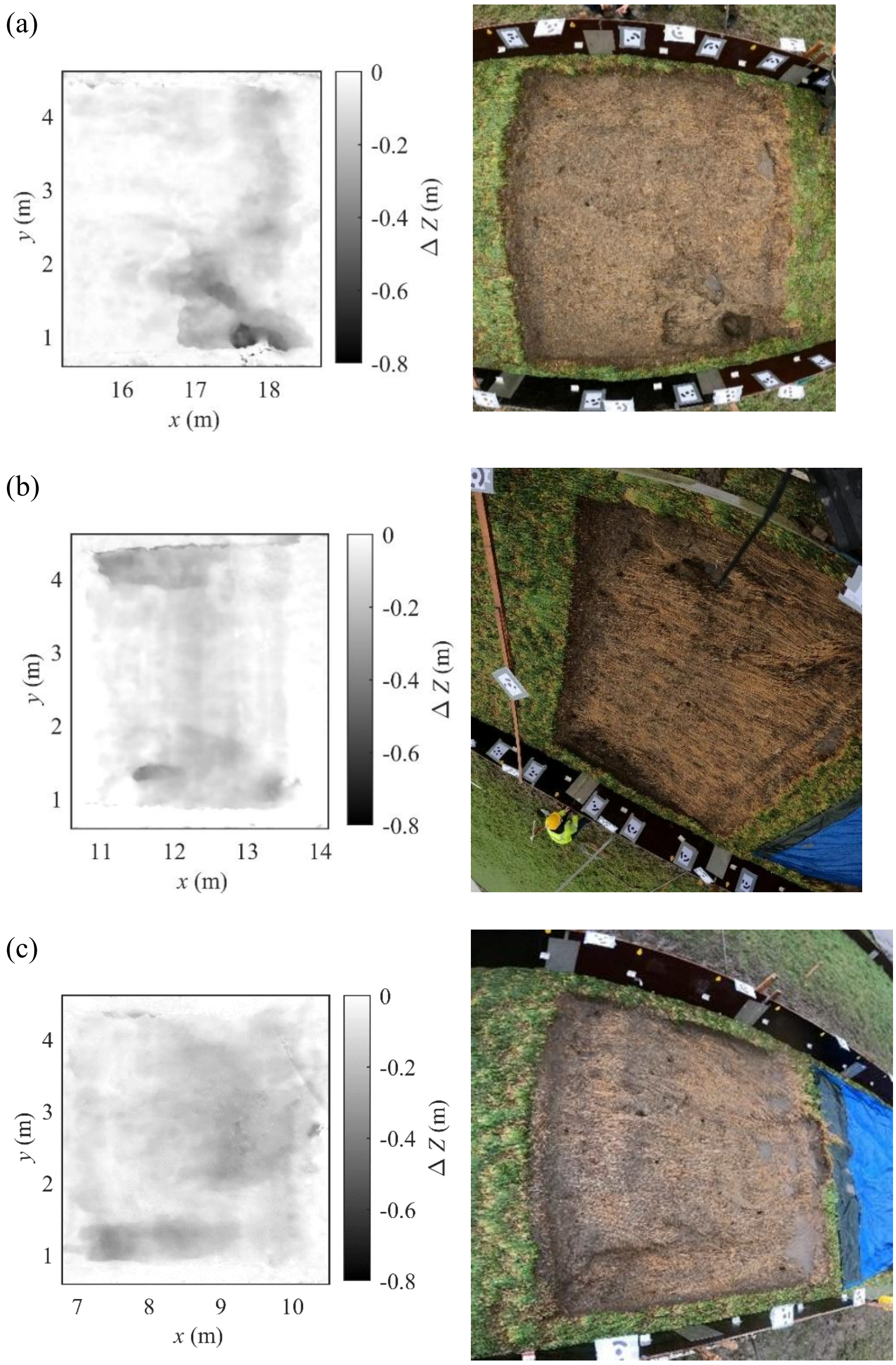
(a)
y (m)
x (m)
Δ Z (m)
0
-0.2
-0.4
-0.6
-0.8
16
17
18
(b)
y (m)
x (m)
Δ Z (m)
11
12
13
14
(c)
y (m)
x (m)
Δ Z (m)
7
8
9
10

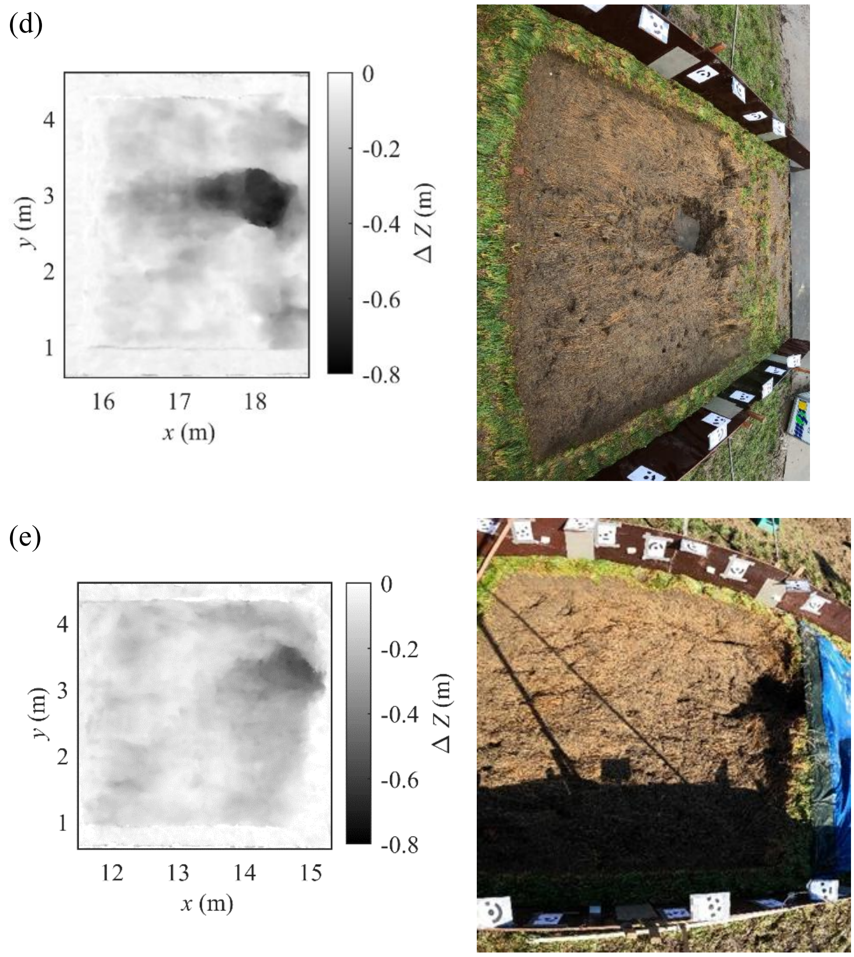

Figure 3.15 Total erosion depth at test sections (a) BC1-1, (b) BC1-2, (c) BC1-3, (d) BC2-1 and (e) BC2-2 and corresponding GoPro photos. Flow direction is from left to right.

Another interesting point is the slope steepening of the levee side at the end of tests. Regarding test BC1-3, located close to the levee crest and thus close to the WOS, the erosion depth was observed to be more uniformly distributed, and on average larger than for the other test sections located further downstream. This is due to the strong increase in wave volumes at the beginning and end of the test (Figure 3.9c). Interestingly, even after generating waves at maximum capacity of the simulator i.e., 3000 l/m, the erosion did not penetrate as deep as at the lowest sections BC1-2 and BC1-1. This is explained by the way how waves attack the slope i.e., normal, or tangential. The dominant load direction close to the crest is normal to the levee slope and it progressively turns into tangential with high shear stresses as the wave travels towards the levee toe due to flow acceleration. At that location where the wave front changes direction due to a local change in levee slope, the normal stresses increase significantly again (see Figure 3.17, app. X = 13 m).

(a)

(b)

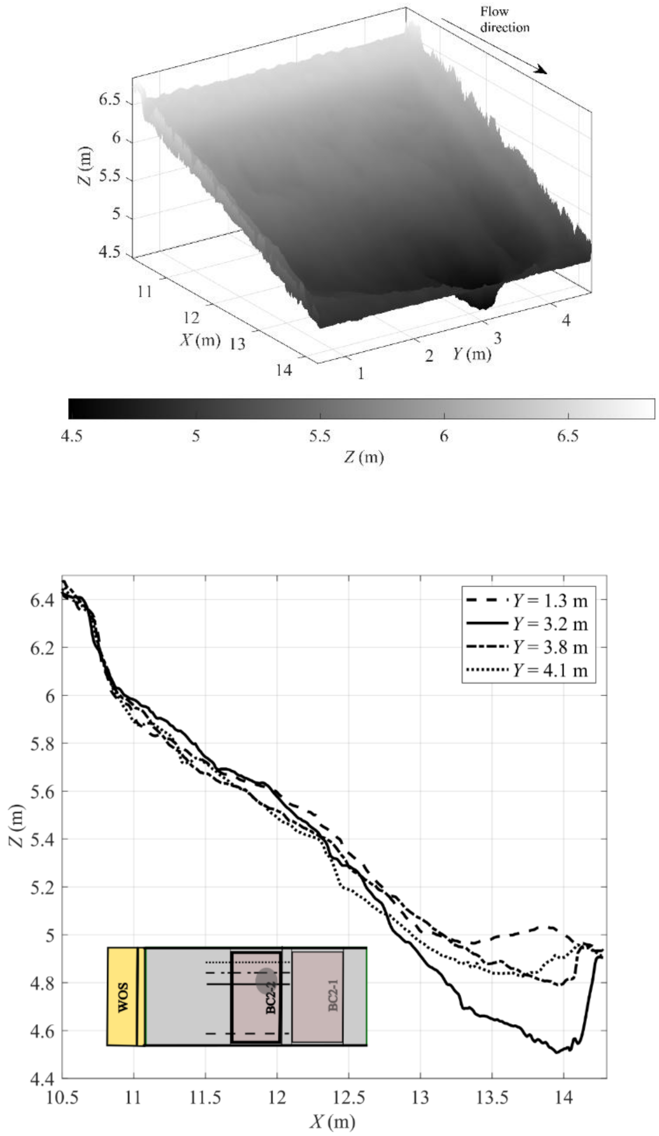

Figure 3.16 (a) 3D view of BC2-2, and (b) longitudinal bed level profiles at different transversal distances.

A detailed examination of the influence of test location on soil damage magnitude revealed that higher flow velocities near the toe, combined with the shape of the test section, led to stronger wave jumps at the lowest test sections, as illustrated in Figure 3.17a, b. This is confirmed when comparing the magnitude of soil loss at the lower (BC1-1 and BC2-1) and middle (BC1-2 and BC2-2) sections. Although stronger overtopping storm events are simulated at the BC1-2 and BC2-2 sections, which are located at the middle of the levee slope, a lower maximum and average erosion depths were observed at these sections compared to BC1-1 and BC2-1 (located at the lowest part of the levee). This implies that the loads exerted by the waves on the clay were significantly reduced at the transitory area i.e., halfway down the slope from the crest inner line.

(a) (b)

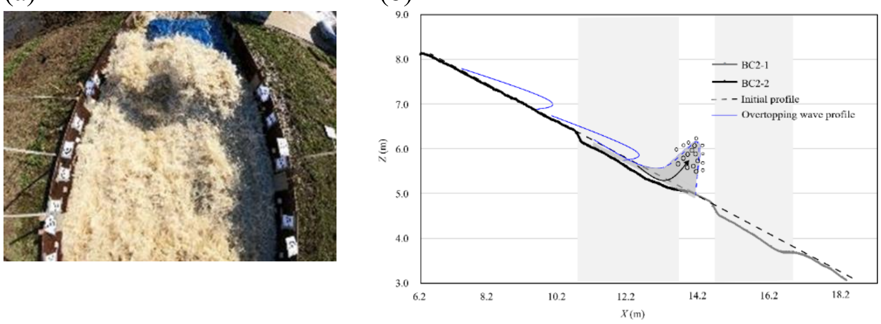

Figure 3.17 Large wave break and jump at section (a) BC2-2, and (b) schematic illustration of the trajectory of an overtopping wave.

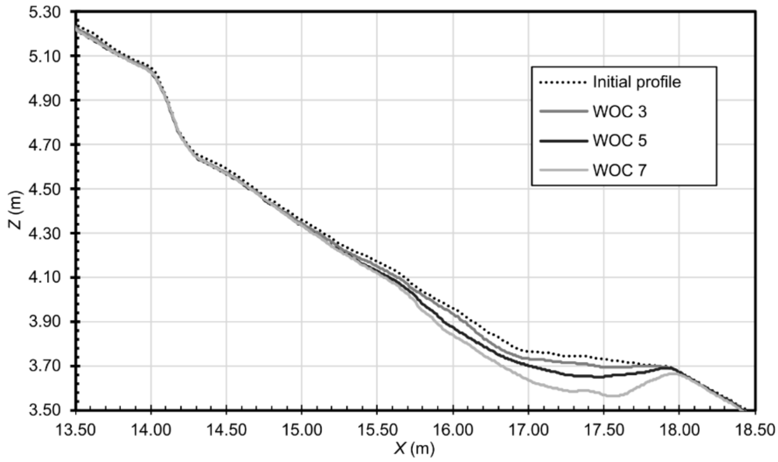

Figure 3.18 Average longitudinal bed profiles at BC1-1.

The evolution of longitudinal profiles representing average levee elevation across the flume (averaged over the transversal direction, i.e., *y*-axis), and the maximum bed level changes along the *x*-axis where a scour hole was formed at BC1-1 test section are shown in Figure 3.18 and Figure 3.19a. While the temporal evolution of the average profiles shows a smooth evolution of the bed level along the slope, the profiles of levee where maximum erosion occurred present significantly higher and variable erosion depths (Figure 3.19b).

(a)

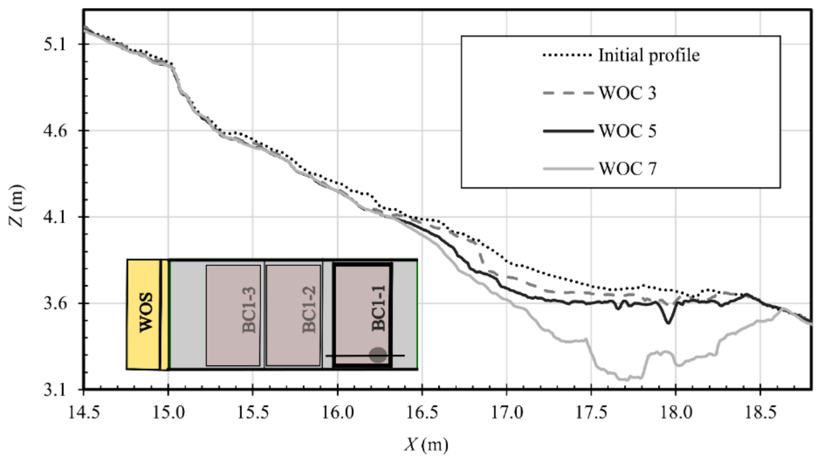

(b)

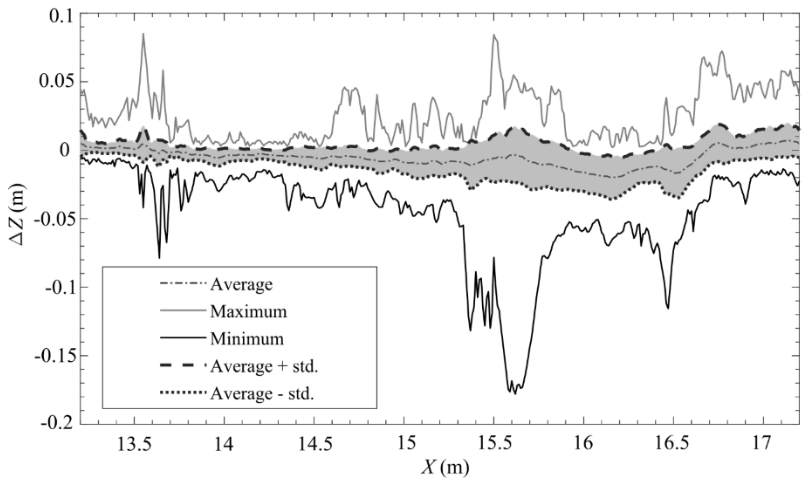

Figure 3.19 (a) Maximum bed level changes at BC1-1, and (b) bed level irregularity across BC1-1 at WOC3.

Table 3.5 outlines the total mass loss as well as the maximum and average erosion depth per test section. The results indicate that the maximum erosion depth is greater for the irregular wave tests (BC2) compared to the regular wave tests (BC1), despite the average overtopping discharge being lower for BC2. This implies that the total overtopping volume and the number of waves—both of which were significantly higher in the BC2 tests—dictate the progression of erosion more critically than the average overtopping discharge. This finding is vital for emergency response and evacuation planning, as the clay cover effectively is considered to completely fail the moment erosion penetrates to the underlying sand core.

Figure 3.20 illustrates the cumulative soil volume removed from the test sections as a function of the cumulative overtopping volume. While erosion initiates at a relatively constant rate across all bare clay (BC) tests, this rate subsequently decelerates, with the BC2 series exhibiting a more pronounced decrease than the BC1 series. The BC1-3 curve displays a sharp increase in slope toward the end of the test, driven by an abrupt escalation in wave overtopping volume (from 100 l/m to over 2500 l/m), which induced significant erosion. Within the BC2 series, simulated river wave (BC2-1) and coastal wave (BC2-2) conditions initially produced similar impacts on the bare clay. Their cumulative erosion curves remain closely aligned until a total overtopping volume of 700 m^3, after which they diverge. Ultimately, BC2-1 surpasses BC2-2 in total soil mass loss. This divergence is primarily attributed to a sudden surge in erosion between wave numbers 500 and 650, likely caused by the exposure of a weaker soil pocket that eroded rapidly.

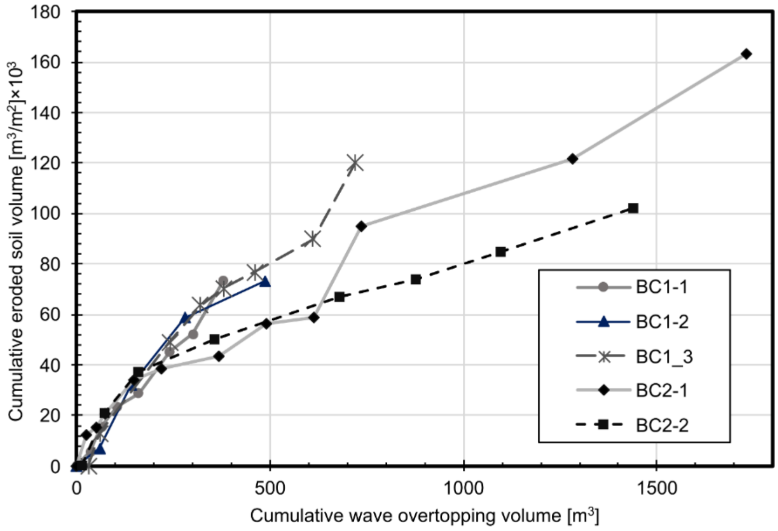

Figure 3.20 Cumulative soil mass loss per unit area during bare-clay experiments.

Table 3.4 Moments for which photogrammetry processing were performed at BC1 and BC2 sections.

Section	Waves condition	WOC1	WOC2	WOC3	WOC4	WOC5	WOC6	WOC7	WOC8	WOC9	WOC10	WOC11
BC1-1	*V*ol [l/m] N	200 60	350 80	500 100	700 120	1000 140	1500 150	2000 160	-	-	-	-
BC1-2	*V*ol [l/m] N	1500 10	2000 20	-	1000 50	-	-	-	-	-	1500 160	-
BC1-3	*V*ol [l/m] N	1500 10	-	2500 30	2000 40	1500 50	1000 70	-	-	-	100 174	3000 184
BC2-1	N	20	40	60	120	180	300	400	500	600	1050	1419
BC2-2	N	50	100	250	500	650	800	1045	-	-	-	-

Table 3.5 Overall performance of BC and LTCB under wave overtopping tests.

Test name	Test duration (hr:mm)	Average wave overtopping volume per storm event (l/m)	Total wave overtopping volume (m^3)	Total area (m^2)	Total erosion volume (m^3)	Average erosion depth (cm)	Maximum erosion depth (cm)
BC1-1	0:35	590	380	13.0	0.95	7.36	64
BC1-2	0:45	760	488	10.8	0.79	7.34	36
BC1-3	1:00	980	721	12.6	1.52	12.04	34
BC2-1	2:00	305	1730	9.9	1.62	16.34	75
BC2-2	2:00	345	1440	12.92	1.32	10.2	55
LTCB1-A	8:45	123-242-345-658	7416	26	0.85	3.26	54
LTCB2-B	8:45	123-242-345-658	7416	26	2.56	10.09	45
LTCB3-C	8:45	123-242-345-658	7416	26	1.59	6.16	26

3.6.2 LTCB experiments

In all three test flumes, the remaining loose and less compacted soil were washed away after 30 minutes (WOC1), corresponding to Figure 3.21.b at LTCB1-A. The morphological evolution of the levee slope at this section is illustrated Figure 3.21. After this transitory stage, the levee slope changes remained limited. Besides, morphological changes over the target study zone after 1m190lsm (WOC4 in Figure 3.21c) were negligible in all LTCB experiments, and this 1m190lsm was selected as the final state of soil.

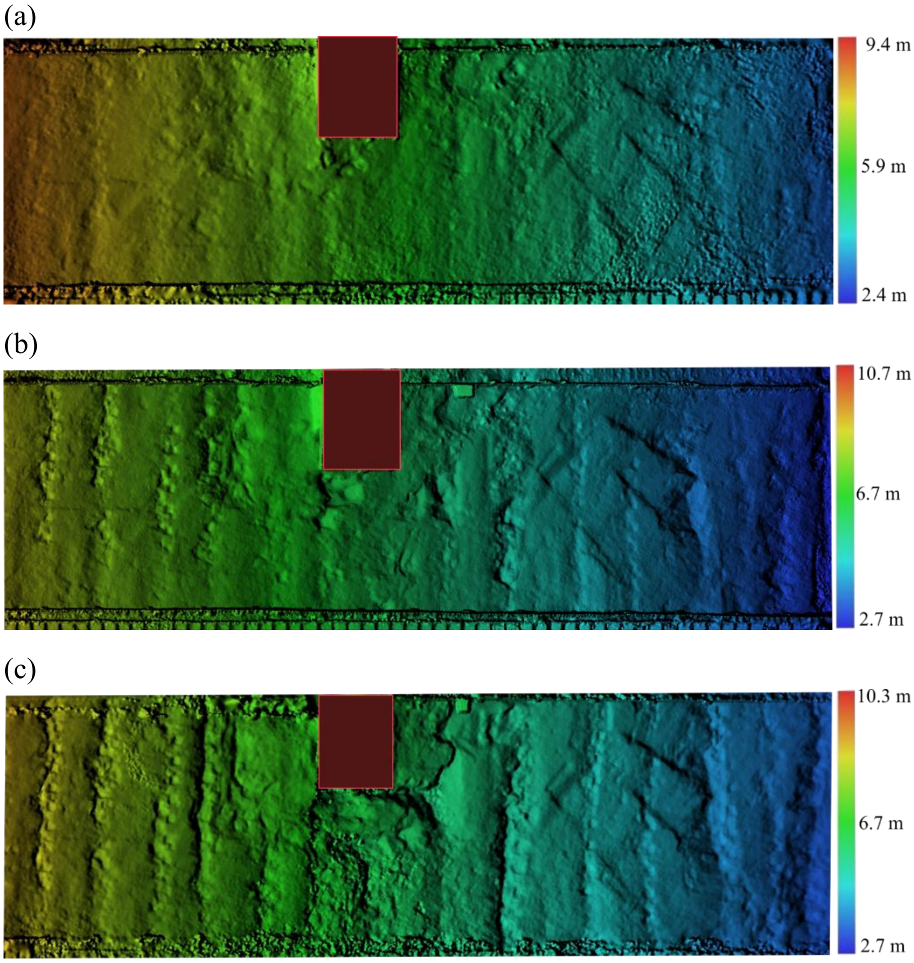

Figure 3.21 Levee slope evolution during wave overtopping experiments at LTCB1-A: for (a) Initial state; (b) WOC1, and (c) WOC4 (flow direction left to right).

The erosion initiated along a series of lines that were the footprints of the compactor. Then, the erosion concentrated where the flume width was limited by the installation of the wooden box, particularly against the obstacle parallel to the flow. As previously mentioned, the protection layer of the levee at LTCB1-A was reconstructed from lesser quality clay type A treated with lime, and using a smaller compactor around the obstacle than that of LTCB2-B (of a similar property to clay A) and LTCB3-C. The dominant form of erosion of clay at LTCB1-A was the formation of a narrow deep trench in the vicinity of the obstacle and next to the downstream corner (Figure 3.22 (a)) At the beginning of the 2m50lsm test, the obstacle was even torn from the soil terminating the experiments earlier than programmed.

(a)

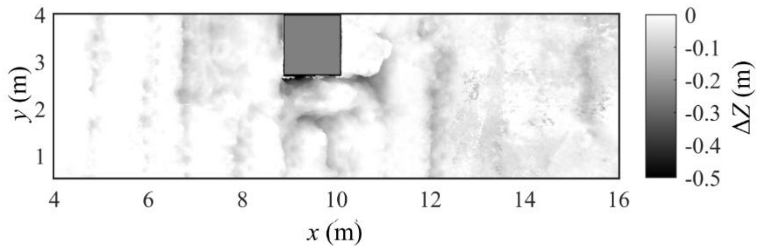

(b)

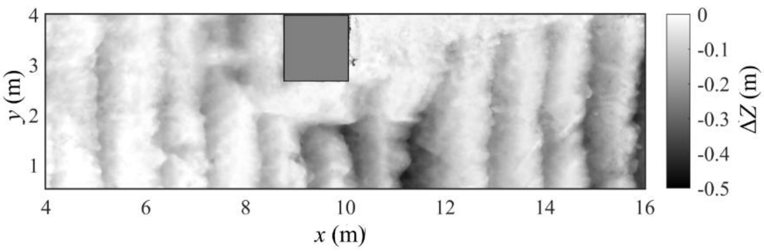

(c)

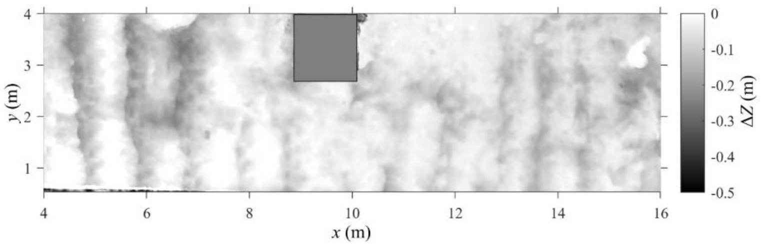

Figure 3.22 Final soil erosion in *xy* plane: (a) LTCB1-A; (b) LTCB2-B; and (c) LTCB3-C.

Figure 3.22 (b) and (c) demonstrate that the use of a powerful compactor around the obstacle at LTCB2-B and LTCB3-C hardly allowed for any erosion around it. All tests generally exibited erosion in a stairstep form. However, the erosion patterns differs across the target study area for all LTCB flumes as shown in Figure 3.22 (a), (b), and (c). While less erosion occurred over the target study zone at LTCB3-C, steep steps or sharp cliffs were formed at this area and on the opposite side of the obstacle in case of LTCB2-B. Both clay types B and C highly eroded in stair-step patterns as shown in Figure 3.23 at higher and lower extremities of the levee slope dictated by the construction procedure. It appears that the vertical discontinuities between adjacent layers (see Figure 3.6), dictated by the construction protocol, accelerated the erosion and triggered more erosion at the layer situated at the lower side. where the soil was less compacted during construction. This is also where the soil was compacted less during construction and hence was eroded faster leading to formation of a series of stair step cascades in clay layer.

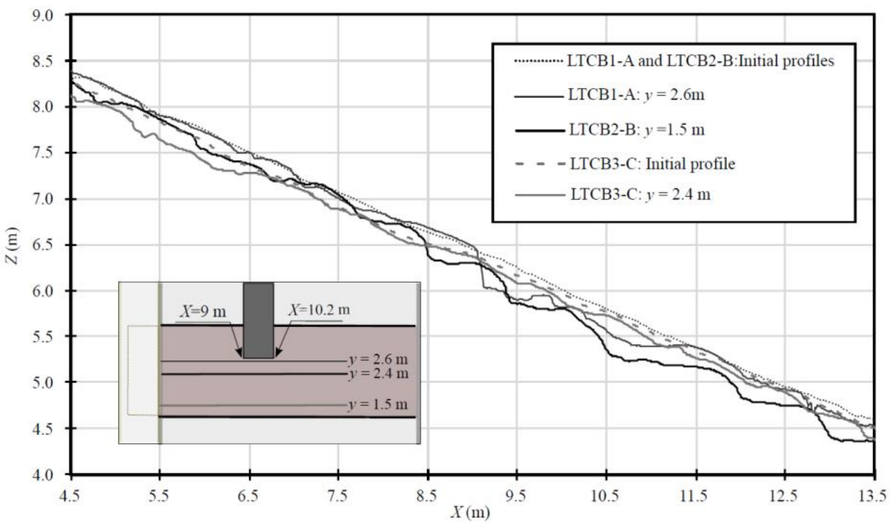

Figure 3.23 Initial, and final bed level profiles of maximum erosion depth for WOC4.

The average and maximum erosion depths of all LTCB sections are given in Table 3.5. Despite a larger maximum erosion depth next to the obstacle at LTCB1-A, under similar overtopping conditions, it has a better performance than the LTCB2-B and LTCB3-C in terms of total mass loss over the target zone. It was observed that the maximum erosion depth was less for LTCB3-C than for the other test sections. One possible explanation is that the heavier compaction close to the obstacle at LTCB2-B and LTCB3-C had an adverse influence on the overall morphological evolution, transferring erosion to other regions of the slope. LTCB2-B experienced a substantially higher soil loss, and with a maximum erosion depth close to that of the LTCB1-A, had the worst performance between all test flumes. Therefore, the construction procedure had an important impact on the erodibility of the materials. Less compacted materials were removed more easily from the levee at the beginning by the low overtopping waves and therefore lead to significant erosion at the beginning.

The cumulative mass loss diagram for the LTCB flumes (Figure 3.24) illustrates significant erosion within the target study zones of the LTCB2-B and LTCB3-C sections during the early stages of the wave overtopping experiments. Table 4 details the average and maximum erosion depths for all LTCB tests. Despite exhibiting a greater maximum erosion depth adjacent to the obstacle, LTCB1-A demonstrated better overall performance than both LTCB2-B and LTCB3-C regarding total mass loss. The maximum erosion depth for LTCB3-C was the lowest among the test flumes; this suggests that the heavier compaction applied near the obstacle in LTCB2-B and LTCB3-C may have adversely influenced the overall morphological evolution by transferring the erosive energy to other regions of the slope. Consequently, LTCB2-B suffered the highest total soil loss and, with a maximum erosion depth approaching that of LTCB1-A, yielded the poorest overall performance.

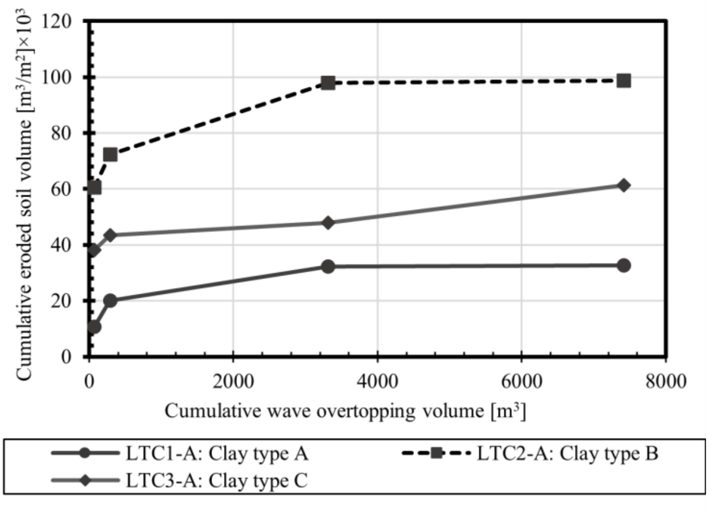

Figure 3.24 Cumulative soil mass loss from the target study zones of LTCB sections.

These results highlight the critical impact of the construction procedure on material erodibility. Less-compacted soils were easily washed away by smaller overtopping waves at the onset, leading to substantial initial mass loss. Nevertheless, the lime-treated clay (LTC) mixtures remain highly promising for levee revetments, eroding minimally under enormous wave overtopping volumes compared to the bare clay (BC) sections. When the initial wash-out of loose soil is excluded from the cumulative eroded volume curves, these new clay mixtures demonstrated outstanding performance and stabilization compared to the original levee clay.

3.7 Conclusion

This chapter has outlined the applicability of the close-range photogrammetry for in-situ levee erosion measurements through high-resolution spatial data (DEM) production. Two series of wave overtopping experiments were conducted in the LLHPP next to Scheldt River to assess the in-situ resistance of the clay covers of the levee exposed to different wave overtopping storm events. The morphological changes and soil loss were monitored and quantified using photogrammetry technique. The accuracy of the technique was assessed by comparing the resulted DEM models to manual measurements of random points over the test sections using the RTK GNSS GPS tool. It was found that the photogrammetry technique slightly overestimated the bed elevation, with a mean average error (MAE) of a few centimeters, including the adverse effects due to water presence in the section. No significant differences in accuracy were observed between the multiple-camera or single-camera setups since both provided enough photographs for accurate 3D reconstruction of test sections. The main source of error was found to be due to the presence of water remaining in the erosion pits, preventing the detection of the actual bed elevation.

The photogrammetry technique is, however, considered to be a valuable method to obtain relatively accurate results over an entire field in quite short times. The technique can be applied to similar levee problems such as levee overflowing if intermediate flow interruptions are feasible, allowing cameras to capture the soil level instead of the water surface. It can also be used to measure erosion differences due to variations in levee material, top protection (grass or artificial cover) or spatial scale. The flexibility of the method, minimal field work requirement, and its independence from meteorological conditions make it highly favorable. Still, one limitation is the required degree of precision to meet the expectations, as a general overestimation of the elevation was observed. Therefore, a preliminary analysis of the accuracy of the generated model in test conditions using alternative methods is recommended to assess the case-specific accuracy.

The wave overtopping impact on the levee bare clay (BC) cover was mainly the formation of scour holes regardless of the waves overtopping storm events patterns. The LTCB tests were conducted to examine the increase in erosion resistance levee cover layer constructed from three different clay soils treated by lime, serving as a levee reinforcement alternative. These soils had shown an excellent performance in the vicinity of the obstacle embedded halfway down the slope. However, a good soil compaction is essential to provide soil-structure integrity. Lime treatment of clay proved to be an excellent reinforcement method for turning clay into very high-resistant soil. Nevertheless, utmost attention should be given to the construction and curing of treated clay since they can highly influence the whole erosion procedure. Furthermore, a long-term monitoring of these clay mixtures is essential to evaluate how the erosion resistance of the LTCB evolve over time.

The influence of the degree of compaction on soil erodibility and the influence of the wave overtopping regime on the erosion rates should be investigated further. For the BC experiments, erosion may be primarily driven by the total wave overtopping volume, regardless of the type of wave. The correlation between the soil loss and wave overtopping volumes should be further investigated for the presented test sites and other test cases. Further analysis may enable the translation of the present research outcomes to other levees in terms of erosion rate and failure time. Additionally, the comparison between soil erodibilities at different scales (i.e., EFA and prototype results) may lead to a better understanding of the potential links between different scale tests and eventually more accurate predictions of erosion rate based on the laboratory experiments. Finally, the spatial and temporal variations in soil erodibility can be studied further by analyzing the variability in hydraulic loads, like the bed shear stress, along the slope as a function of an overtopping wave. However, this investigation requires numerical simulations, which will be conducted in the future.

While the full-scale field experiments successfully demonstrated the capability of SfM photogrammetry to quantify surface erosion on levee covers, they were limited to the initial stages of damage prior to full embankment breaching. Once a protective cover fails, the erosion mechanism shifts to a rapid, uncontrolled progression through the underlying core. To investigate this highly dynamic phase under controlled conditions, the research transitions to intermediate-scale laboratory modeling. Consequently, the next chapter presents the application of an enhanced multi-camera photogrammetric system designed to monitor the complete spatiotemporal evolution of breach formation in medium-scale sand embankments.

Chapter 4

Application of Enhanced SfM-Photogrammetry to Medium-Scale Earthen Embankment Breaching Experiments[4]

4.1 Summary

This chapter presents the application of Structure-from-Motion (SfM) photogrammetry to monitor breach evolution in medium-scale experiments on non-cohesive sand embankments (median grain size 0.61 mm) conducted at the Hydraulic Research Laboratory of SPW MI, Châtelet, Belgium. Breach development under overtopping was captured using a close-range, static multi-camera SfM system, providing high-resolution reconstructions of dike topography. The accuracy of the 3D reconstructions was assessed through root-mean-square reprojection errors of ground control and check points, and by comparison with dense point clouds obtained from a FARO terrestrial LiDAR scanner and an iPhone LiDAR sensor, both confirming centimetre-scale precision. Key challenges included capturing the submerged bed and dynamic water surface. Limitations from poor texture, reflections, and water motion were mitigated using floating tracers and synchronised imaging. Embedding coloured balls within the dike enabled tracking of breach deepening, improving the accuracy and completeness of SfM-photogrammetry reconstructions.

4.2 Background and objectives

The consequences of climate change, including rising mean sea levels, increasing storm frequency and intensity, and prolonged drought periods, are

[4] The contents of this chapter are based on a manuscript currently under review for publication in the Journal of Hydraulic Research.

expected to intensify the hydrological loading conditions on earthen flood defence structures. This climate-induced stress, often exceeding original design criteria, means that the failure probability of earthen embankments, particularly due to overtopping, is projected to rise (Ward et al., 2020). Overtopping by flow and waves is a historically dominant failure mechanism, accounting for nearly 34% of earth dam and embankment failures (Foster et al., 2000). Such overtopping processes initiates continuous erosion, rapidly leading to the formation of a breach through the embankment body and complete structural failure. A reassessment of the functionality and overtopping risk of earthen embankments (e.g., sea dikes and riverine levees) is therefore essential in light of climate change consequences and the escalating threat of extreme weather events. Such an evaluation relies on a thorough understanding of the physical processes governing failure, which can be gained through physical modelling. Both full-scale and reduced-scale experiments have played vital roles in improving our knowledge of embankment breaching dynamics.

While full-scale and prototype embankment experiments provide the most accurate replication of real-world processes (e.g. Hahn et al., 2000; Hanson et al., 2005; Kakinuma & Shimizu, 2014; M. W. Morris et al., 2007; Pan & Loukola, 1993; Tobita et al., 2014; Visser, 1998), they are often constrained by high costs and logistical complexity, limiting the availability of study sites. Furthermore, they are difficult to instrument and monitor in high resolution due to their scale and environment.

In contrast, scaled models conducted in laboratory flumes allow for more detailed measurements. Early laboratory studies on embankment breaching focused on fuse-plug embankments consisting of impermeable cores covered by erodible materials (Tinney & Hsu, (1961), Chee (1978), Pugh (1985), & Halso et al., 2025a). These experiments aimed to investigate erosion mechanisms and estimate washout times in order to predict the passage of extreme floods through reservoirs equipped with such secondary safety structures under controlled conditions.

Subsequent laboratory studies by Coleman et al., (2002), Pickert et al., (2011), and Schmocker & Hager, (2012) extended these investigations to assess the effects of grain size on the overall breaching process, geometry and outflow hydrographs, using small-scale dikes with heights up to 0.2 m. Schmocker & Hager, (2012) and Al-Riffai, (2014) further investigated scale effects through scale-series experiments in small laboratory experiments.

Additional insight into breach formation under lateral overtopping was provided by fluvial dike breaching experiments conducted by Wahl et al. (2011), Rifai et al. (2017), and Schmitz et al. (2021). These studies demonstrated the advantages of laboratory flume experiments in terms of flexibility, repeatability, and the ability to capture detailed hydraulic and morphodynamic data.

A key distinction must be made between three-dimensional breaching processes where flow overtopping initiates over a limited embankment length and creates a breach channel through the structure, and two-dimensional (2D) flow overtopping or planar breaching, where overtopping occurs uniformly across the entire embankment crest (Schmocker & Hager, 2012; Tingsanchali & Chinnarasri, 2001; Van Emelen et al., 2015; Zhu et al., 2011).

In these 2D breaching experiments, the flow can be accurately monitored through the lateral channel walls, if transparent, as done by Van Emelen et al. (2015) for example. However, this only offers a limited insight into the complex breaching process. Three-dimensional experiments better represent real breaching processes, but at the cost of an increased difficulty to properly detect the breach evolution. This difficulty is further enhanced when increasing the spatial scales of the experiments and with the presence of fine sediment resulting in turbid water, that make the breach topography detection under water almost impossible. Accurate measurement of breach topography is however critical for determining both cross-sectional and longitudinal breach profiles, quantifying erosion rate, estimating breach outflow, and characterizing the underlying physical processes.

Several researchers have sought to simplify the detection of submerged breach geometry by constructing a half-dike model against transparent sidewalls (Coleman et al., 2002; Frank & Hager, 2014; Pickert et al., 2011; Yang et al., 2024). This experimental configuration assumes negligible wall effects and a symmetric breaching process. This method enables direct visualization of the underwater breach channel geometry as well as the water level evolution through the breach and along the transparent wall. However, unlike planar breaching experiments mentioned earlier, the flow features are not constant over the channel width, and accurate measurements can only be obtained along the symmetry wall.

Other approaches involve temporarily interrupting the experiment and rapidly lowering the reservoir water level to fully expose the breached dike for topographic measurements (Coleman et al., 2002; Amaral et al., 2020; Jónatas et al., 2025). However, such methods either require multiple test repetitions or are limited to cases where draining the flume does not alter the breach morphology, thereby allowing the experiment to resume after intermittent measurements.

The following sections review imaging-based measurement techniques developed to monitor breach topography continuously, without interrupting or intruding upon the experiments. Imaging techniques such as laser profilometry and sweeping laser light sheet methods, as applied by Spinewine et al. (2004), Rifai et al. (2020), and Delpierre et al. (2024), have proven effective in small-scale laboratory experiments under clear-water conditions. However, their applicability is limited in turbid flows, where sediment surfaces cannot be reliably detected. Moreover, synchronising individual profiles remains a major challenge for reconstructing high-resolution, three-dimensional breach topography.

Stereophotogrammetry combined with grid projections is another technique used to capture and track the breach evolutions. For instance, Pickert et al. (2011) used a side fringe projection system with a side camera to perform continuous and non-intrusive measurements of breached dike topography across a glass wall. Using the same principle, Frank and Hager (2014) used an improved AICON 3D System to capture 3D models of dike evolution during breaching. The system consists of three synchronized CCD cameras enabling stereophotogrammetric measurements and relying on a high-power grid projector installed above the dike to highlight the sediment level. This technique is highly suitable and accurate in coarse granular dikes where a smooth water surface will form through the breach.

Stereophotogrammetry using pairs of still-camera images without grid projector was also used by Walder et al. (2015) and Morris et al. (2021) to track the morphological evolution of 1-m-high earthen dams and dikes during breaching.

Early infrared (IR)-based sensing technologies on the basis of the commercially available Microsoft® Kinect® sensor, was used by Wallner (2014) to measure dike breach surfaces with an optical system resulting in interesting dike surface images, yet their quality was relatively poor due to lack of refraction correction. Recent advancements in Kinect sensor utilizing the Time-of-Flight (ToF) method (Jónatas et al., 2025) offer efficient depth sensing capabilities. In contrary to terrestrial LiDAR scanners, Kinect sensors are capable of generating 3D dike models at higher frequencies e.g. of up to five point cloud model per second including submerged portions of breached dike in the experiments conducted by Jónatas et al., (2025). However, IR light is strongly absorbed by water, typically within a few centimetres, significantly limiting the effective measurement range of such device as a stand-alone technique at larger dimensions.

Terrestrial LiDAR scanner technology, although becoming more and more affordable, does not appear as completely appropriate. Indeed, it requires relatively long scanning durations and only provides measurements of the unsubmerged dike portions, hence is not adapted to rapidly evolving breach morphology in embankments made of non-cohesive, fine granular material susceptible to apparent cohesion (Amaral et al., 2020; Bento et al., 2022; Herrero-Huerta et al., 2016).

Modern photogrammetry i.e. Structure-from-Motions (SfM) photogrammetry (Snavely 2008; Westoby et al. 2012) has emerged as a leading technique for 3D model reconstruction. It has been proven to be a robust and cost-efficient tool for generating high-resolution digital elevation models (DEMs) across a variety of domains and in particular for hydraulic applications as shown by Ebrahimi et al., (2025a) who used close-range SfM photogrammetry to monitor erosion progression in the protective layers of a prototype levee. Two types of photographic acquisition setups were used: multiple fixed cameras supported by a rigid frame, and a single mobile camera. As demonstrated by Ebrahimi et al. (2025b), the dynamic nature of dike geometry during breach evolution necessitates a multi-camera setup that enables simultaneous imaging from different orientations. Such an arrangement allows for accurate and temporally consistent reconstructions of dike geometry, even in rapidly evolving conditions. In contrast, the single mobile camera setup taking sequential photographs from multiple viewpoints takes significantly more time, missing rapid morphological changes (Ebrahimi et al. 2025a, Bento et al. 2022 and Jónatas J. et al 2025).

Furthermore, photogrammetric techniques enable the reconstruction of 3D models of the water surface over a large area provided enough texture is available on the surface through the presence of tracers, to eliminate the light refraction. This technique was applied by Carlier d'Odeigne et al. (2018) to capture the water surface elevation in a scaled river model. Frank & Hager, (2014) were also able to capture water surface elevation using white water, coloured with TiO2 and using the AICON 3D photogrammetric system. Jónatas et al (2025) stated the difficulties in mapping water surface in the vicinity and inside the breach channel due to the light refraction when using SfM-photogrammetry.

However, SfM-photogrammetry, like other imagery techniques, is limited to reconstructing the emerged parts of the dike and portions of the water surface that exhibit sufficient texture. Consequently, the water depth and the submerged geometry within the breach channel remain unresolved. Underwater photogrammetry (Walder et al. 2015, Woodget et al. 2015) may offer insights into the breach evolution on the reservoir side, but it is generally impossible on the landside slope due to the shallow water depths and the rapid changes in bed elevation. Therefore, underwater accuracy is limited due to (i) water turbidity, which obscures visibility, and (ii) light refraction on the free surface, which causes the bed level to be inaccurately detected.

To fully resolve the breach geometry, especially the channel bed elevation, additional measurement techniques beyond traditional laser scanning are required. Electronic sensors embedded in the dike present a promising approach for a more comprehensive breach evolution monitoring, as they detect the precise time the erosion process reaches them (Morris et al. 2007, Tobita et al. 2014). Similarly, physical tracers, such as brightly painted pebble gravel (Walder et al. 2015) and coloured balls (Ebrahimi et al. 2025b), tracked through video recordings, have proven effective for identifying hydraulic cross-section and bed elevation during breaching.

This study presents a new series of medium-scale (1-m high) 3D sand dike breaching experiments conducted at the Hydraulic Research Laboratory of the Public Service of Wallonia (SPW MI -Direction des Recherches Hydrauliques) in Châtelet, Belgium. While our previous work (Ebrahimi et al., 2025b) introduced the experimental facility and provided preliminary results on the application of close-range SfM-photogrammetry, the present paper delivers three key advancements. First, a comprehensive and reproducible photogrammetric workflow based on a system of multiple fixed cameras is presented, including a practical strategy for optimising camera number and layout in dynamic breaching applications. Second, water-surface reconstruction is enhanced by seeding the free surface with wood chips to improve image texture, while coloured balls embedded within the dike are used to track breach deepening with improved temporal resolution. Third, the accuracy and performance of the SfM-photogrammetry system, implemented using Agisoft Metashape, are assesed through comparison with alternative techniques, namely a FARO terrestrial LiDAR scanner and an iPhone LiDAR sensor. Dense point cloud models generated from these different techniques were aligned and compared using the open-source software CloudCompare (GPL software, 2025).

The resulting high-resolution datasets are subsequently used to analyse the spatiotemporal evolution of breach geometry and to compare the observed breaching mechanisms with those reported in previous experimental studies. The study further highlights the advantages, current limitations, and practical challenges of deploying SfM-photogrammetry in highly dynamic breach scenarios.

4.3 Experimental setup and measurement devices

This section describes the experimental setup: embankment geometry, overtopping conditions and hydraulic instrumentation such as flowmeters and water level sensors. The entire experimental procedure from the dike construction protocol established to guarantee repeatability of the runs, to test procedure is explained.

4.3.1 Experimental setup

The platform of the Hydraulic Research Laboratory of SPW-MI located at Châtelet in Belgium was designed to perform dike breaching experiments of dikes up to 1 m high. The platform illustrated in Figure 4.1a,b,c is 23.5 m long, 13 m wide, the upstream reservoir has a useful surface of 190 m², and is surrounded by concrete walls of 1.2 m height. Water is pumped from the adjacent river, the Sambre, towards the platform (d). The pipe intakes are protected by filter screens to avoid the entrance of debris into the system. The pumping system consists of 5 pumps including one small, one medium and three large pumps allowing for accurate control of the inflow discharge. The small-capacity pump (0.006–0.042 m³ s-1) and medium-capacity pump (0.030–0.090 m³ s-1) serve to initiate the pumping system and subsequently enable the activation of larger pumps (0.122–0.341 m³ s-1). The pumping system thus operates within a flow range from a minimum of 0.006 m³ s-1 to maximum of 1 m³ s-1 when all three large pumps are operating. Each pump is controlled by a variable frequency drive allowing a progressive passage between smaller pumps to larger pumps, which means that one decreases the flow rate while the other one is turned on. The water kinetic energy is reduced right before entering the main reservoir by means of a perforated (at the bottom) concrete wall separating the water arrival zone and the main reservoir (Figure 4.1c). The outflow is redirected to the Sambre channel after slowing down in the downstream reservoir where sediments are trapped. The downstream reservoir has a surface of 85 m² and is located 1.5 m below the principal platform in order to eliminate tailwater effects on the experiments. The basin can replicate different spatio-temporal flow conditions of overtopped dike, simulating either an infinite waterbody (e.g. lake, wetland or sea) by maintaining a constant level in the upstream reservoir or supplying a steady inflow.

(a)

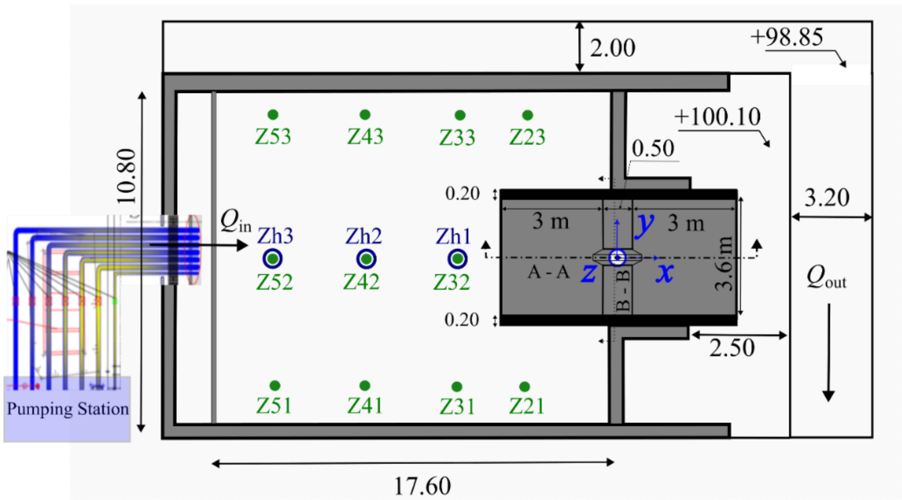

(b)

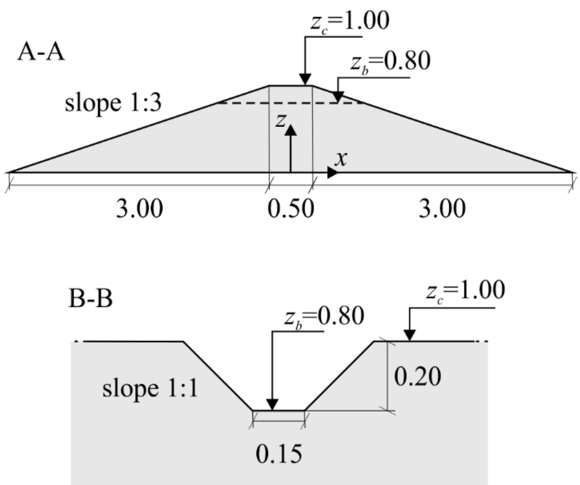

(c)

(d)

Figure 4.1 Dike breaching experimental setup at the Hydraulics Laboratory of SPW-MI (Châtelet, Belgium) : (a) platform plan view, dimensions in (m), (b) longitudinal and cross-sectional dike profiles, dimensions in (m) (c) experimental platform including the upstream and downstream reservoirs (view from downstream) (d) water intake from the adjacent Sambre River and outfall locations.

The dike was constructed 14.5 m downstream from the water entrance point in the reservoir. It is 1 m high, 0.5 m and 6.5 m wide respectively at the crest and dike toe (parallel to overtopping flow), and 3.6 m long (perpendicular to overtopping flow), constructed between the two guide walls (in black in Figure 4.1a). The upstream and downstream slopes are equal to 1V:3H. To ensure repeatability across tests, a trapezoidal pilot channel was excavated at the centre of the crest, extending from the upstream to the downstream slope after the dike construction was completed. The pilot channel had a fixed depth of 0.2 m, a bottom width of 0.15 m, and side slopes of 1:1 (V:H).

Three experiments with the same geometrical configuration, hereafter referred to as *mS_Q_1*, *mS_Q_2*, and *mS_Q_3* were performed. The detailed characteristics and test-specific parameters are described in the subsequent sections.

4.3.2 Embankment material

The dikes were built with homogeneous uniform sand with a median diameter (d_{50}) of 0.61 mm. This soil is classified as poorly graded sand (SP) according to the ASTM D2487 with uniformity coefficient C_u = 1.32 and a coefficient of curvature C_c = 0.99. The grain-size distribution of the sand is illustrated in Figure 4.2. Such a material composition could be considered as representative of dikes in the Netherlands for example, where many dikes consist of a sand core beneath an external protection layer (van Damme et al., 2023).

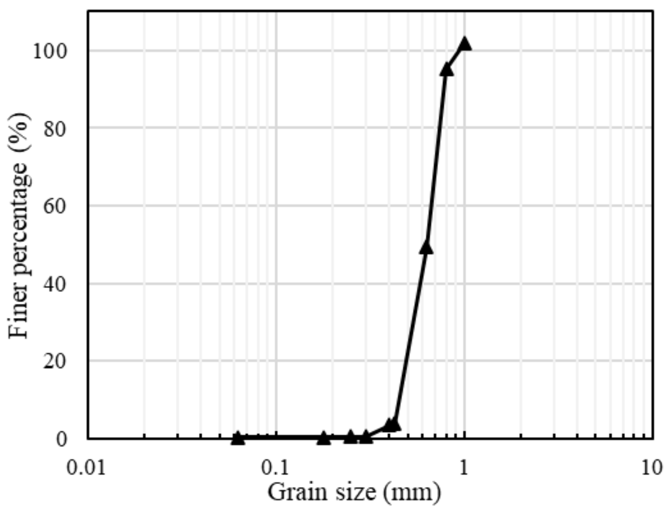

Figure 4.2 Grain size distribution (USCS) of the soil used for embankment construction.

4.3.3 Soil compaction and construction procedure

Prior to construction, the soil compaction properties were determined using the Standard Proctor Test (ASTM D698), yielding an optimum moisture content (w_{opt}) of 8 % and maximum dry density (γ_d) of 1550 kg m^{-3}. However, as described Arcement & Wright (2001) who conducted extensive laboratory compaction tests, poorly graded sands (SP) do not exhibit a well-defined compaction peak with the typical contrary bell-shape compaction curve observed in silty sands. This is confirmed in Figure 3 showing the results obtained for the current tests.

The embankments were constructed following a standardized protocol to ensure repeatability and consistency. The process commenced with the installation of a drainage pipe connected to a drainage exit point. The embankment was built in horizontal layers of 0.1 m thickness that were compacted with the aim of reaching the Optimum Proctor compaction. The moisture content of the soil was regularly checked, and additional water was added to the soil as necessary to reach the optimum water content of 8 % (see Figure 4.3), using the following procedure. A small loader was used to transport the soil from the storage area to the construction location. The bucket volume was taken as the reference volume to verify the soil water content. The required volume of water calculated to achieve the target moisture content was added directly to the loader's bucket, which had a known capacity. The soil was mixed while being placed to ensure its homogeneity. A vibration plate compactor (Ammann APF-10/33) was used to compact the soil with 4 to 7 passes over the entire surface of the 0.1 m thick layer. After the placement of each layer, non-disturbed soil samples were taken to verify both the moisture content and compaction degree to ensure compliance with protocol specifications.

In order to study the influence of compaction on the breaching process in such sand, more efforts were made to obtain a higher in-situ compaction in the third test, e.g. *mS_Q_3*. The in-situ compaction is compared to Optimum Proctor compaction for all tests in Figure 4.3.

Due to the vibration effects, the water infiltrated rapidly in the dike and drained from the bottom of the embankment reducing the water content by 3-4% compared to the optimal value after compaction of approximately 8% as shown in Figure 4.3. Therefore, to reach the target moisture content of the soil, a higher initial water content (10 to12%) was implemented in *mS_Q_3* comparing to the other tests (7 to 9%). On average, the in-situ compaction achieved only 88% of the Maximum Dry Density in *mS_Q_1* and *mS_Q_2* compared to 93% in *mS_Q_3*. Despite these adjustments, the maximum laboratory Optimum Proctor density could not be fully attained, as the overall compaction was ultimately limited by the weight and energy capacity of the compactor.

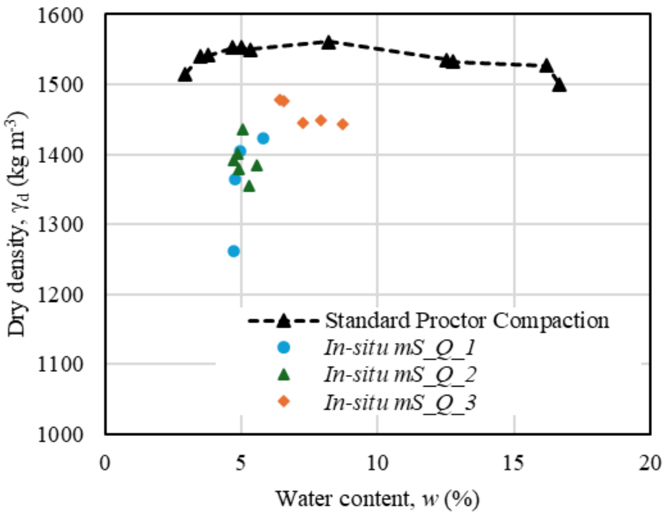

Figure 4.3 Optimum Proctor and in-situ compaction curve for the sand soil used for the embankment construction.

(a) (b)

Figure 4.4 Embankment compaction procedure: (a) compacting soil in layers of 0.1 m and (b) vibration plate compactor (Ammann APF-10/33).

4.3.4 Water level, inflow and outflow discharge measurements

To achieve high spatial resolution in water level measurements, the basin is equipped with eighteen water level gauges, including fifteen ultrasonic sensors and three hydrostatic sensors. Both the hydrostatic and ultrasonic sensors are installed within vertical tubes made of transparent PVC. These tubes are positioned outside the basin and serve as the dedicated water level measuring spots. These measuring tubes are connected to the main reservoir via piezometers distributed across the reservoir floor. This setup ensures that the water level in the PVC tubes accurately reflects the reservoir level at its corresponding location. Figure 1a shows the location of the intake points of these gauges spreading over the entire reservoir area. The measurement range of the ultrasonic sensors is from 0.030 to 0.350 m, while the hydrostatic probes can measure from 0 to 1.3 m. The ultrasonic sensors were positioned to measure water levels between 0.850 m to 1.005 m. Beyond this range, only the hydrostatic gauges provide water level measurements, covering the whole water level range in the reservoir. As regards the inflow discharge, each pump and associated pipe is equipped with an electromagnetic flowmeter providing the discharge with an accuracy of approximately 1%. The breach outflow was then measured indirectly by applying mass conservation given in Eq. (4-1) to the reservoir volume.

$$Q_{breach} = Q_{in} - A(z)\frac{dz}{dt} - Q_{drainage} \qquad \text{4-1}$$

where Q_{in}, $Q_{drainage}$, Q_{Breach} are the inflow discharge, infiltrated discharge measured through the drainage system, and breach outflow discharge. $A(z)$ is the plane area of the reservoir surface at level z, and dz / dt is the variation of the water level in the reservoir, averaged over the reservoir surface using the data from the different water level gauges. The water level and discharge measurements were recorded continuously at a sampling frequency of 5 Hz.

4.3.5 Embankment drainage

The embankment was constructed on the fixed bed of platform. To minimise the seepage risk and prevent internal erosion during the experiments, a 50-mm perforated PVC drainage pipe wrapped in geotextile was installed beneath the dike crest at floor level. The infiltration water collected inside the drain was then transferred via an underfloor conduit towards a V-notch weir installed in the downstream reservoir (Figure 4.5). The V-notch weir has a standard shape and allows for accurate measurement of the dike throughflow. Measurements confirmed that the infiltration and throughflow discharge ($Q_{drainage}$) remained negligible (less than 0.001 m^3/s) relative to the breach outflow over the entire breaching process

(a) (b)

Figure 4.5 Embankment drainage system: (a) drainage pipe placed on the channel bed and (b) triangular weir for throughflow measurement (the container is equipped with two water-level ultrasonic sensors).

4.4 Description of the experiments

New earthen embankment breaching experiments were designed and conducted at an intermediate dimension using a uniform sand with a median diameter of 0.61 mm. Three tests (*mS_Q_1*, *mS_Q_2* and *mS_Q_3*). All three tests were conducted with a constant discharge of 0.224 m³ s^{-1}. Overtopping was initiated when the reservoir's water level exceeded the invert elevation of the pilot channel. This condition allowed water to flow freely into the pilot channel and down the downstream slope. The characteristic dimensions and parameters of each test are reported in Table 4.1.

Table 4.1 Summary of experimental conditions and measurements.

Test No.	Test acronym	Overtopping condition	Inflow (m³ s^{-1})	d_{50} (mm)	z_c (m)	z_b (m)	Measurement techniques
1	*mS_Q_1*	Constant Inflow	0.224	0.61	1	0.8	Photogrammetry
2	*mS_Q_2*	Constant Inflow	0.224	0.61	1	0.8	Photogrammetry
3	*mS_Q_3*	Constant Inflow	0.224	0.61	1	0.8	Photogrammetry, FARO LiDAR and iPhone LiDAR

The first two tests (*mS_Q_1* and *mS_Q_2*) validated experimental repeatability and demonstrated the SfM capabilities for 3D breach reconstruction. To improve water surface detection, wood chips were utilized as tracers with two different supply strategies compared accross these tests.

Test *mS_Q_1* also assessed the impact of camera configuration on model quality, while the use of embedded tracers proved essential for completely reconstructing the submerged breach cross-sections. Finally, the accuracy of SfM-Photogrammetry was evaluated under static conditions (initial topography) by comparing it to a reference model captured by a FARO LiDAR terrestrial scanner. Both techniques were subsequently compared with model constructed from a low-cost iPhone LiDAR sensor to assess its viability as an accessible alternative. A comprehensive overview of the specific features and methodological objectives for each test is detailed in Table 4.2.

Table 4.2 Experimental program highlighting test-specific features, objectives and assessment methodology.

Test	Specific feature	Primary purpose	Secondary role
mS_Q_1	Wood chips supplied immediately upstream of the dike	Test repeatability; demonstration of SfM capability for reconstructing breach evolution and cross-sections	Influence of the number and position of the cameras; analysis of temporal morphological changes, evaluation of camera layout
mS_Q_2	Wood chips supplied at the reservoir inlet	Test repeatability; Assessment of tracer supply strategy for improving water-surface reconstruction	Validation of combined photogrammetry-tracer cross-sections
mS_Q_3	Higher in-site compaction (app.93% vs. 88%) and additional monitoring techniques	Accuracy assessment of SfM against FARO LiDAR and iPhone LiDAR	Influence of compaction

4.4.1 Breaching process

The reservoir inflow discharge was kept constant throughout the experiments. Water entered the initial pilot channel, directing the flow toward the downstream slope. The establishment of overtopping took a few seconds, partly due to minor infiltration within the dike during the initial stage. However, this infiltration remained limited and had a negligible effect on the overall breaching process. The reference time (t = 0 s) was defined as the moment when water first reached the downstream end of the pilot channel before spilling over the slope. The overtopping flow was considered as fully established once the reservoir water level rose approximately 5 cm above the initial pilot channel crest, i.e., at 85 cm. Figure 4.6 illustrates key phases of the breach morphological evolution during test *mS_Q_1*.

The breach initiated and formed by continuous surface erosion driven by a shallow water flow (Figure 4.6a). At this stage, eroded sediments were deposited at the dike toe. The breach formation phase encompasses the period from the onset of overtopping (t = 0 s) to approximately t = 80 s. By this instant, the initial breach channel is considered fully formed. As erosion progressed, the breach invert retreated toward the upstream reservoir. As the process advanced, the breach channel deepened and progressively started widening across the entire landward slope (Figure 4.6b, c,), while the flow completely washed away the deposited sediments at the toe of embankment (Figure 4.6d).

During the breach formation phase (Figure 4.6a, b), the invert slope of the breach channel remained relatively gentle, with a gradient slightly larger than the initial slope. After this stage, the upstream point of this invert slope continuously migrated towards the upstream reservoir (Figure 4.6c, d) and became steeper. Simultaneously, the breached channel widening accelerated leading to faster lateral expansion of the breach. During breach formation stage, only small block failures occurred along the breach sides. The vertical erosion dominated breach formation stage until flow reached the non-erodible flume base under the dike crest, which simulates a fixed, non-erodible foundation in prototype scenarios. Beyond this point (Figure 4.6d), the breach evolution is primarily governed by lateral widening through mass slumping and block detachment (ranging from a few mm to a few cm in width) induced by flow undermining (Figure 4.6e, f).

At high flow velocities that are characteristic of breaching, erosion in densely compacted sand shifts from grain-by-grain entrainment to the bulk shearing of sediment layers (Van Rhee 2010, Bisschop et al. 2011; 2016). To shear these dense layers, the interlocked sand grains must undergo volume expansion, or dilatancy. This dilatancy creates a negative pore pressure (suction) that draws water into the soil matrix, drastically increasing the effective stress and providing the shear strength necessary to maintain steep, overhanging banks according to Bisschop et al. (2016) and van Damme (2021).

Also, the formation and propagation of tension cracks were observed prior to block detached (Figure 4.6e, f). Sliding was the dominant mechanism of block displacement, ultimately leading to their collapse into the flow. The time interval between crack formation and block failure varied, ranging from rapid to prolonged processes, reflecting the influence of apparent cohesion produced by capillary forces during the breaching in fine sediments (Pickert et al. 2011). This apparent cohesion also contributed to maintaining steep breach channel banks, which often approached vertical throughout the breaching process.

The ability to capture these complex, highly dynamic mechanisms ranging from progressive surface wear to abrupt, localized mass collapses, presents a significant monitoring challenge. The enhanced SfM-photogrammetry approaches detailed in Section 4 provides more insight into the capabilities of the technique for monitoring breaching experiments, but also the limitations, as a detailed observation of the onset of mass collapse at the very local scale is not possible.

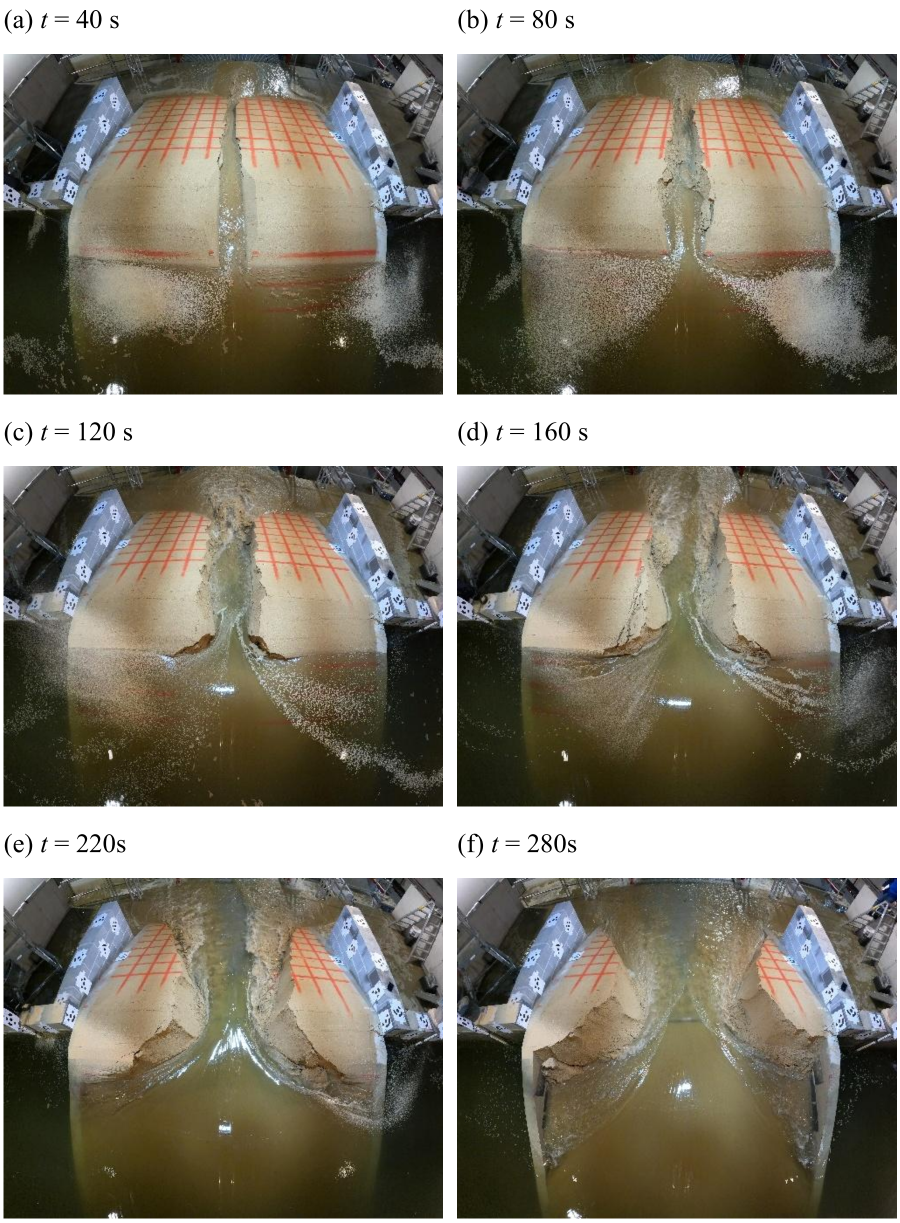

Figure 4.6 key phases of the breach morphological evolution during *mS_Q_1* experiment.

In all experiments reported in this study, the breach developed in an almost symmetrical manner. Breach hourglass form (Coleman et al., 2002) can be observed over the entire experiment.

4.4.2 Repeatability of the tests

Reservoir inflow, the average upstream water level, and the resulting breach outflow are illustrated in Figure 4.7 for all tests. The reservoir inflow was maintained constant and identical across the three tests. However, a slight decrease in inflow was observed in test *mS_Q_1*, most likely caused by a minor mechanical fluctuation in the pumping system, probably a temporary partial blockage of the intake filter screens by river debris or water level fluctuations in the Sambre channel from where the water is pumped. This variation slightly affected the upstream reservoir level after t = 200 s in *mS_Q_1*, as evidenced by the marginally lower water-level curve of *mS_Q_1* compared with the other tests. In contrast, the water level in *mS_Q_3* remained slightly higher than the other two tests towards the end. Overall, all average water level curves exhibited a similar trend, with a mean standard deviation (STD) of 0.007 m including a progressive rise to a maximum value followed by a progressive decline. The upstream reservoir level increased progressively during overtopping until the breach expanded sufficiently to convey the entire inflow of 0.224 m^3 s^{-1} (t = 160 s).

After this stage (Figure 4.6d) the water level began to decrease, while the breach outflow continued to increase, reaching maximum values of 0.714, 0.721, and 0.740 m^3 s^{-1} for *mS_Q_1*, *mS_Q_2*, and *mS_Q_3*, respectively. The peak outflow persisted toward the end of the experiments, during which the drainage of the reservoir storage primarily governed breach evolution. The peak breach outflow in *mS_Q_3* occurred later than in the other tests, likely due to the dike being compacted to a slightly higher degree.

The standard deviation of the breach outflow was 0.015 m^3 s^{-1} until t= 390 s, when the pumps were stopped in test *ms_Q_1*. The maximum outflow was reached when erosion extended to the upstream slope, creating an enlarged flow section (after Figure 4.6e). The breaching process was considered complete when the dike was almost entirely eroded, leaving only small remnants adjacent to the guiding walls (after Figure 4.6f). The drainage discharge ($Q_{drainage}$) was negligible (less than 0.001 m^3 s^{-1}) over the entire process in all tests.

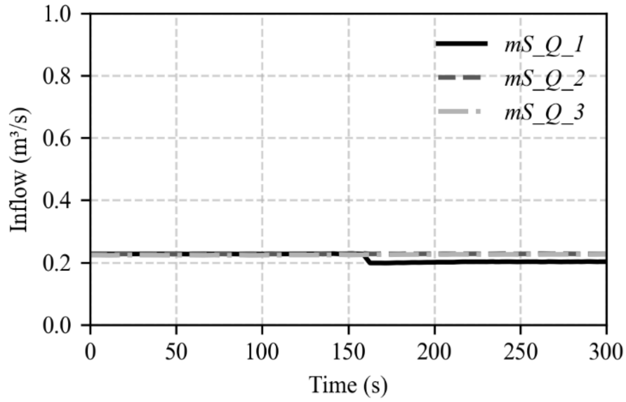

(a)

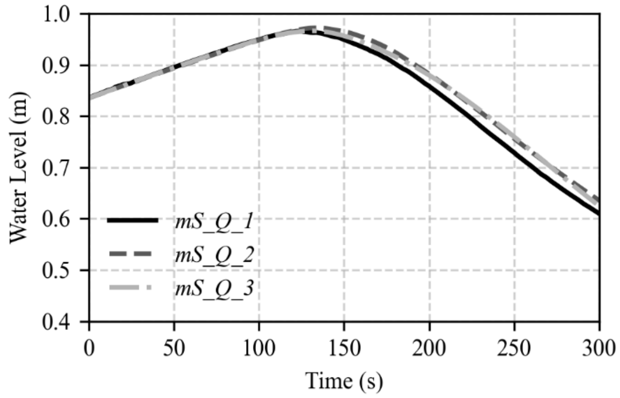

(b)

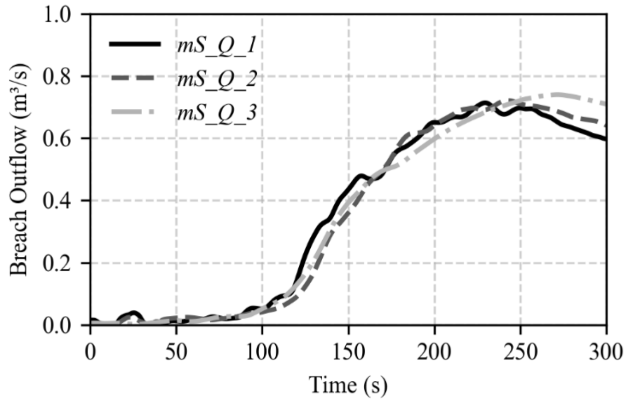

(c)

Figure 4.7 Flow characteristics during the breaching including (a) reservoir inflow, (b) water level evolution (mean STD is 0.007 m), and (c) breach outflow (mean STD is 0.015 $m^3 s^{-1}$) in experiments *mS_Q_1, mS_Q_2, mS_Q_3*.

4.5 Monitoring and 3D reconstruction of the dike breaching process

4.5.1 Application of Close-range SfM-Photogrammetry

A multi-stationary camera system, previously implemented by Ebrahimi et al. (2025a) at prototype scale, was employed to capture images of the dike throughout the breaching process. In the present study, a maximum number of 11 GoPro Hero9 cameras were used to capture photographs with a total coverage area of approximately 35 m². The cameras have a resolution of 5184×3888 and a focal length of 3 mm, achieving a high ground spatial resolution of 1.25 mm/pixel.

Different positions of the fixed cameras were tested to obtain the most accurate 3D reconstruction of the dike. Therefore, eight to ten cameras were attached to the frame structure assembled around the dike, as shown in Figure 4.8a, and one to three cameras were placed on tripods in front on the lateral sides of the dike in the downstream area.

A wide-angle lens configuration with a fisheye effect was used during photo acquisition to ensure maximum overlap between photos. Figure 4.8b shows one example of the original photographs taken by the GoPro cameras. The cameras were operated in time-lapse mode, capturing images a rate of 2 images/second to effectively track rapid morphological changes during the breaching process. A triggering system was used to ensure that the images are all captured at the same time, which is important to enable an accurate 3D reconstruction of the scene that is changing fast in time. A total of 31 Ground Control Points (GCPs), designed as easily recognisable targets for the software, were installed across the scene around the dike (see Figure 4.8a). The GCPs were installed both vertically and horizontally at a high density, guaranteeing the presence of several targets per image and capturing the full elevation variation across the scene (at least 3 GCPs visible on each photo). The coordinates of all GCPs were measured manually within a common local reference system. Of these points, 27 points were used during the photogrammetric processing for image alignment and georeferencing to maximize the robustness of the 3D reconstruction. The remaining four points were explicitly excluded from the alignment procedure and used as independent check points (CPs) to assess the accuracy of the reconstructed DEM. These CPs were strategically selected across the scene to provide an unbiased, independent assessment of the reconstructed DEM's spatial accuracy.

The images were post-processed using Agisoft Metashape (Agisoft LLC., 2022) to generate 3D models representing the temporal evolution of the dike. The software operates on Structure-from-Motion (SfM) photogrammetry principles (Snavely, 2008; Westoby et al., 2012). The key steps are illustrated in Figure 4.9 for the initial configuration of the dike:

(a) Identification of common features (called “keypoints”) across overlapping images and reconstructing their 3D spatial positions to generate a sparse point cloud or Tie Point model (Figure 4.9a) which enables the estimation of cameras positions and orientations.
(b) Generation of a dense cloud model (Figure 4.9b) by densifying the sparse point cloud, using techniques like depth map creation and stereo matching.
(c) Mesh generation (Figure 4.9c), in which the dense cloud is projected onto a structured mesh with a user-defined refinement; in the present case, a mesh of 0.014 m was used.
(d) Construction of DEM represented as a regular grid (Figure 4.9d), generated from the dense point cloud by interpolating the reconstructed elevations at each grid node.

The parameters associated to each of these steps in the current setup as well as the quality and resolution of the obtained models are reported in Table 4.3.

(a) (b)

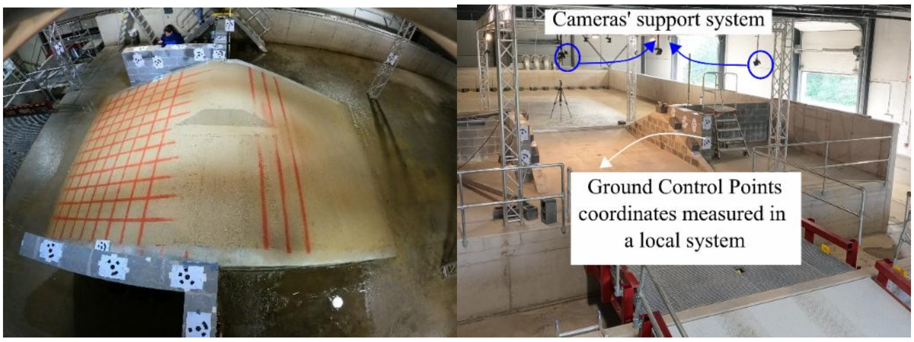

Figure 4.8 Multiple fixed camera support system composing of 10 cameras (a) camera set-up, and (b) example of images captured by GoPro Hero 9 cameras (Resolution . 5184 x 3888 corresponding to 1.25 mm/pix at ground).

(a) (b)

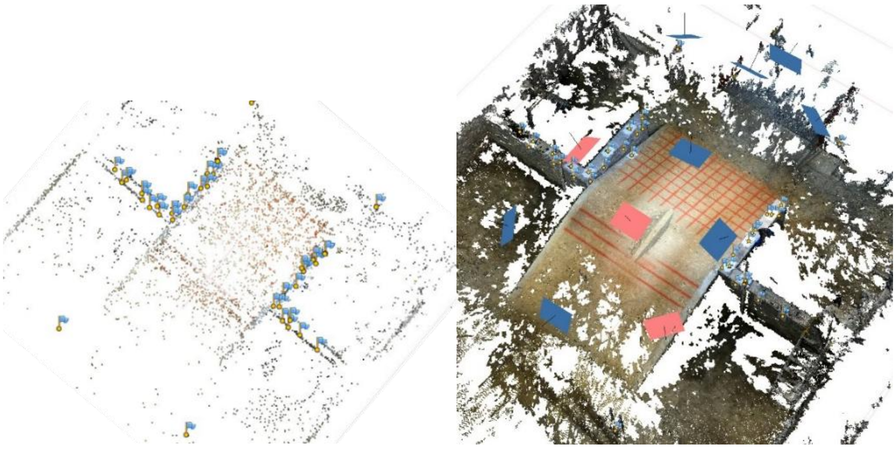

(c) (d)

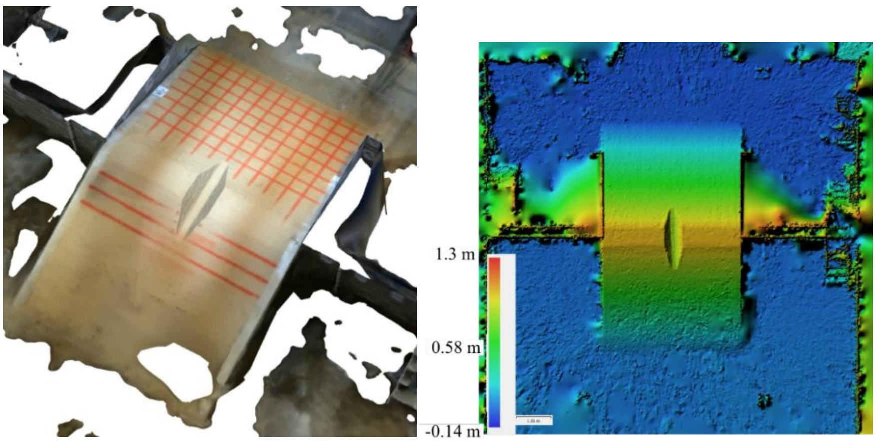

Figure 4.9 Photogrammetry workflow in Agisoft Metashape to reconstruct the dike geometry illustrated for the initial dike topography of test *mS_Q_1* recorded by 11 cameras*:* (a) Tie (sparse) point Cloud with 8000 points, (b) Dense cloud with 3000000 points, (c) Mesh with a resolution of 0.014 m, (d) Digital Elevation Model (DEM) with a resolution of 0.005 m.

Table 4.3 Photogrammetric processing parameters and average computational time per step for initial dike topography reconstruction using Agisoft Metashape software.

Photogrammetric workflow	**Parameters: Configurations**	**Resolution**	**Manipulation and computational time (s)**
Add photos			
Camera calibration	*Camera type*: Fisheye		1 s/photo
GCPs detection	Automatic and manual		60 s/photo
Image	NA	5184 x 3888 (Ground resolution 1.25 mm/pix)	
Image alignment (Tie points)	*Accuracy*: high *Key point limit*: 100,000 *key point limit per Mpx*: 10,000 *Tie point limit*: 7,000	2000 to 15000 points	40 s
Depth maps and dense point cloud generation	*Quality*: Medium *Filtering mode*: Mild	1,000,000 to 3,000,000 points	900 s/model
Mesh generation	*Quality*: Medium or High	90,000 faces 0.014 m	30 to 60 min
DEM generation	*Quality*: determined by Dense cloud	5 mm/pix	10 s/model
Orthophoto	*Quality*: determined by photos' resolution	1.53 mm/pix	20 s/model

The accuracy of the photogrammetric models was evaluated at the 4 CP but also for the 27 GCPs used for the model alignment. The Root Mean Square Error (RMSE) of the GCPs and CPs were calculated in all spatial directions (x,y,z) within Agisoft Metashape, and for the final 3D model, based on its internal calculation of reprojection and positional errors. This approach provides an independent estimate of model accuracy by comparing manually measured coordinates at selected points (source) and estimated coordinates after analysis. Manual measurements were conducted using a conventional measuring tape and level. The error associated with this standard technique is typically estimated to range from a few millimeters to a few centimeters in both the horizontal and vertical directions, accounting for various sources of field error. The overall RMSE values are reported in Table 4.4. In both cases, the RMSE is below 0.03 m, confirming the consistency and systematic reproducibility of the photogrammetric models.

Table 4.4 Ground Control Points and Check Points RMSE estimates within Metashape Agisoft in case of *mS_Q_1* initial dike topography.

Count	RMSE per category (m)	*x*	*y*	*z*
27	**GCPs**	0.0145	0.0280	0.0097
4	**CPs**	0.0178	0.0240	0.0128

4.5.2 Influence of the number and position of the cameras

The practical success of SfM-photogrammetry for breach monitoring hinges on maximizing image overlap from multiple viewing angles. To systematically achieve this criterion, a practical methodology for optimizing camera setups was adopted as follows. The optimal camera setup in terms of both number of cameras and orientation was determined through a preliminary analysis using a single mobile camera. By capturing images of a static scene, for example the initial condition, at rest, from various viewpoints (position and angle), different configurations can be simulated. These images can be processed by selectively activating or deactivating specific images or camera positions within the photogrammetry software to identify the combination that results in the most detailed and accurate 3D reconstruction, with the minimum number of cameras. This approach helps establishing the cameras positions and orientations that best capture key features during the dike breaching.

Based on this preliminary analysis, an optimal 11-camera setup was adopted to provide comprehensive, high-redundancy coverage of the entire dike (see Figure 4.8b, and Figure 4.10a). Three cameras were mounted on the reservoir-side support frame to monitor the water surface in the reservoir in the presence of tracers, and the breach control section at the crest. Lateral cameras captured the breach channel evolution, while centrally aligned cameras along the breach axis ensured sufficient image overlap and detailed monitoring of the morphological changes.

To explicitly demonstrate the necessity of this redundancy, two reduced configurations with only 4 cameras are tested a posterior and compared to the full setup with 11 cameras as illustrated in Figure 4.10: (i) one employing only the frontal cameras providing a view from downstream and (ii) another using cameras placed above the central part of the dike providing a top view. In both cases, the cameras are placed high enough to ensure that the entire breach is visible, but the overlap between images is reduced because of the reduced number of cameras compared to the full setup with 11 cameras. For each setup, the dense point cloud is illustrated as well as a confidence map indicating the number of images used to reconstruct the position of each point of the cloud. In the case of the full setup, the dense point cloud (Figure 4.10a) provides a detailed view and the confidence can be considered as high because the points pertaining to the dike are usually reconstructed based on at least 5 images (Figure 4.10d). The setup involving the 4 cameras placed at the downstream side of the dike providing a downstream view (Figure 4.10b and Figure 4.10e) is able to provide an accurate reconstruction of the breach channel and lateral banks, with a good confidence considering the reduced number of cameras. The last setup, with the 4 cameras placed in the top view configuration (Figure 4.10c and Figure 4.10f), appears to be much less accurate, as it failed to capture the breach banks. This can be related to a lack of enough overlap between images specially due to insufficient frontal perspectives, in the bank zones, as the top view configuration does not allow to properly identify the steep sides of the banks in the dense cloud model of Figure 4.10c.

For a dense point cloud of good quality, at least three overlapping images (or their corresponding depth maps) should be available for each point of the 3D scene to be reconstructed. This redundancy is crucial for accurate stereo matching and noise reduction. The models created by reduced number of cameras demonstrate this principle, as the flow free surface cannot be properly reconstructed with fewer views. In contrast, the full model with 11 cameras allows identifying parts of the free surface, both in the breached area and in the upstream reservoir.

Overall, it can be concluded that the four-camera configuration consisting of the frontal cameras (Figure 4.10b and Figure 4.10e) offers the best compromise between minimising the number of cameras, and thus computational cost (reducing it to one-third of the full camera configuration), while maintaining a sufficiently high level of accuracy for the reconstructed models.

4.5.3 Embedded Coloured balls as bed level indicators

A key methodological advancement of the proposed monitoring framework is the integration of embedded colored plastic balls to estimate the submerged breach geometry, with the aim of overcoming a major limitation of standard photogrammetry. Coloured plastic balls of 0.04 m diameter were embedded at specific locations approximately at 0.10 m vertical intervals along the dike's central axis, spanning its full height, as illustrated in Figure 4.11. Their small size relative to the dike ensured they did not affect hydraulic processes or disrupt the experimental procedure. Video footage from a camera positioned above the dike crest, covering the entire landward slope, was used to continuously monitor and identify the precise moments when each ball was released. By correlating these release times with the known initial elevations of the embedded balls, the eroding submerged portion of the breach cross-section was successfully reconstructed. This spatial extrapolation relies on the standard assumption that earthen breach cross-sections can be reasonably approximated as trapezoidal (see Figure 1.10).

4.6 Results and discussion

The following sections present the accuracy assessment of SfM-photogrammetry models constructed from photographs acquired using a multi-stationary camera system, in comparison with alternative LiDAR sensors. The performance of the technique in capturing the water surface in the upstream reservoir and through the breach flow is examined, along with potential improvements for such applications. The resulting 3D models were further integrated with information from embedded coloured balls to reconstruct complete cross-sections of the breached channel. The temporal evolution of the breach, derived from the photogrammetric models, is illustrated and compared with findings reported in the literature. Finally, the main challenges encountered and the corresponding recommendations for improvement are discussed.

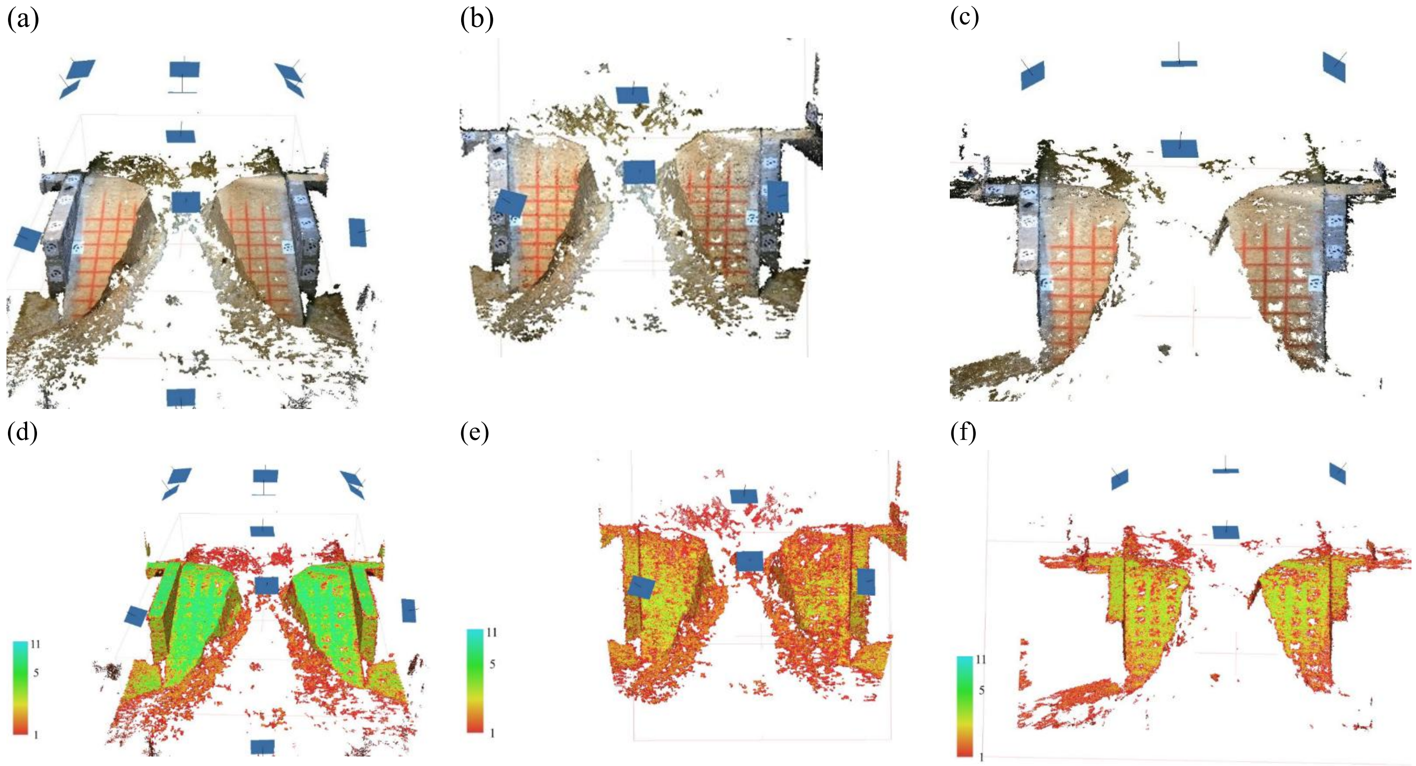

Figure 4.10 Dense point cloud (top), and confidence map indicating the depth maps used to generate a point (bottom) for test *mS_Q_1* at t = 200 s : (a, d) 11 cameras, (b, e) 4 cameras, frontal configuration, (c, f) 4 cameras, top view configuration.

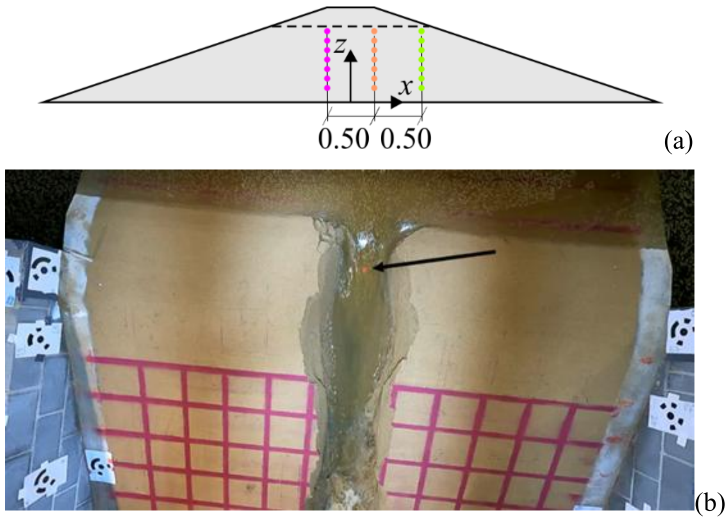

Figure 4.11 Coloured balls position embedded within the dike: (a) sktech of the positions of the balls, placed 0.10 m intervals over the vertical started from z = 0.15 m, along the dike centreline (y = 0), (b) identification of a ball released from the photographs of the flow.

4.6.1 Comparison of SfM-Photogrammetry with alternative techniques

To assess the accuracy of SfM-photogrammetry results, the dense point cloud model of the initial dike topography obtained in experiment *mS_Q_3* was compared against models acquired using a FARO LiDAR scanner. The FARO LiDAR is a professional-grade terrestrial laser scanner offering millimeter-level precision, making it a highly reliable absolute reference baseline for this comparative analysis (Chrbolková et al., 2025). Additionally, an iPhone LiDAR sensor utilizing the free Scaniverse application (Askar & Sternberg, 2023) was included in this comparison to demonstrate its viability as a publicly available, low-cost alternative to the FARO scanner for such static state validations. The FARO dataset was treated as the reference surface against which the SfM and iPhone LiDAR reconstructions were evaluated. Figure 4.12 illustrates the point clouds obtained from these three techniques, processed using CloudCompare software (GPL software, 2025).

(a) (b) (c)

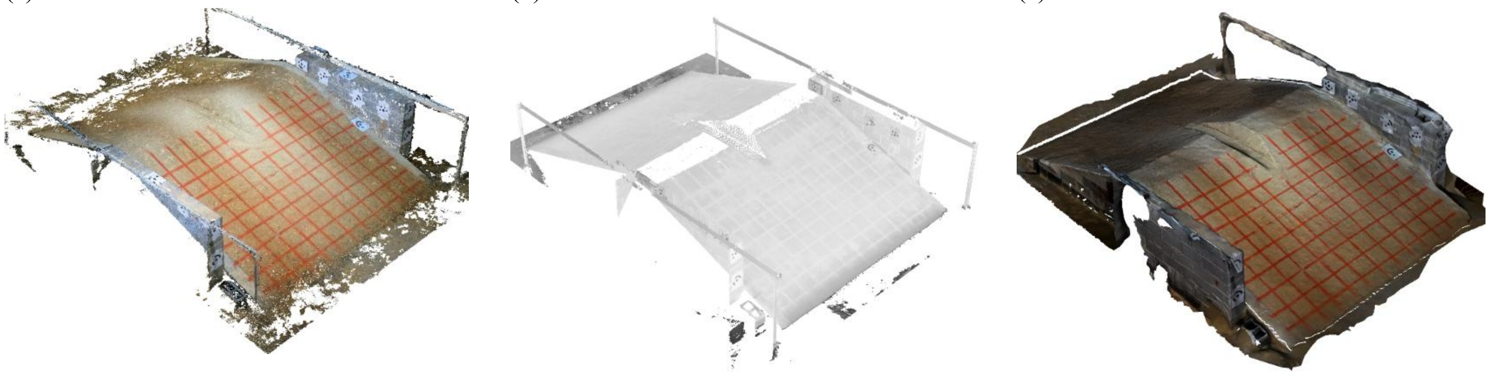

Figure 4.12 Dike topography model obtained from (a) SfM-photogrammetry, (b) LiDAR FARO, (c) iPhone LiDAR.

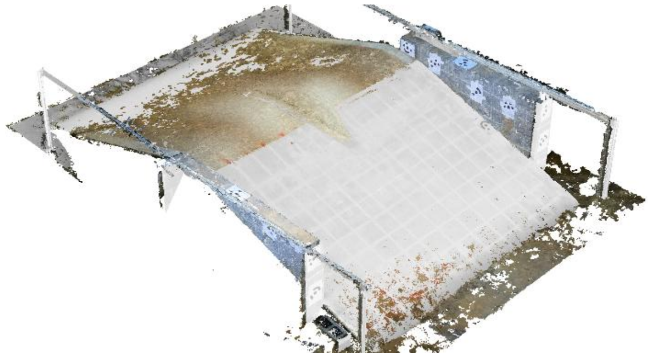

Figure 4.13 Registered SfM-photogrammetry and LiDAR FARO models.

To quantitatively compare the resulting Dense cloud model, it is first necessary to ensure a perfect spatial alignment of the data in x and y directions. This alignment procedure is called registration in CloudCompare and consists of two main steps: (i) the models are first aligned manually by selecting a set of point pairs on the two datasets to bring them into good spatial agreement, (ii) this alignment is then enhanced by using the Iterative Closest Point (ICP) algorithm, which iteratively minimizes the Euclidean distances between corresponding points in overlapping regions. This registration process ensures optimal spatial correspondence between the models, enabling quantitative comparison of surface deviations and accuracy assessment. An example of this registration process is shown in Figure 4.13, illustrating the alignment between the SfM-photogrammetry and FARO LiDAR models.

Following registration, the two dense cloud models issued from SfM-photogrammetry and iPhone LiDAR were quantitatively compared to the reference measurements by LiDAR FARO using the Cloud-to-Cloud (C2C) comparison tool. This comparison calculates the shortest distance between the compared cloud (SfM or iPhone) and the reference cloud (LiDAR) using a Least Squares Plane local fitting method with 6 nearest neighbours to ensure a robust surface deviation measurement. The result is a color-coded point cloud where colours indicate the distance deviation between the aligned clouds as shown in Figure 4.14 for the SfM photogrammetry, where it can be observed that most of the points present a deviation below 0.02 m.

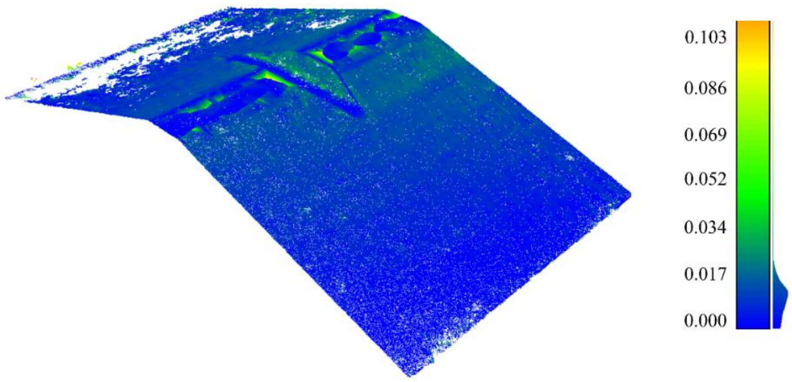

Figure 4.14 Absolute Surface Deviation in meter (Cloud-to-Cloud) between SfM Photogrammetry and FARO LiDAR Models (initial dike topography in *mS_Q_3*) using the Least Squares Plane Method (k = 6).

The results, summarized in Table 4.5, indicate a high degree of precision for the SfM data. The comparison against the high-resolution FARO LiDAR yielded a mean distance (μ) of 0.0114 m and a standard deviation (σ) of 0.0078 m. Similarly, the iPhone LiDAR data demonstrated close agreement with the FARO reference data resulting in a mean distance of 0.0127 m and a similar standard deviation of 0.0077 m. These small μ values confirm successful registration and minimal systematic bias, while the consistently low σ values demonstrate that the SfM technique provided consistently high precision for static bed topography, comparable to the reference data. It should be noted that the larger deviations observed along the embankment crest are an artifact of the scanning setup rather than physical deformation. Because the LiDAR FARO scanner was positioned only marginally higher than the crest elevation, it could not fully capture the horizontal crest surface, resulting in a scarcity of reference data points in this specific region.

Although the FARO LiDAR scanner generates highly precise and detailed models, its minimum acquisition time of two minutes makes it impractical for capturing the rapid morphological shifts characteristic of active breaching. Furthermore, the strong attenuation of infrared light by water severely restricts the utility of LiDAR in these settings, particularly at depths exceeding a few centimeters.

Table 4.5 Summary of Quantitative Accuracy Assessment of SfM-Photogrammetry Point Cloud against LiDAR Reference Models.

Comparison	Registration Method	Mean distance (μ) (m)	Standard deviation (σ) (m)
SfM to LiDAR-FARO	Cloud to Cloud	0.0114	0.0078
iPhone to LiDAR-FARO	Cloud to Cloud	0.0116	0.0073

4.6.2 Enhanced water surface and bed level detection methods

The application of SfM photogrammetry to high-speed dike breaching necessitates overcoming the inherently "texture-less" nature of moving water. Because photogrammetric accuracy is contingent upon the identification of stable tie-points, the transition from stagnant water to fast flow introduces two primary failure modes: specular reflection on clean water and the obscuration of submerged features by turbidity. Photogrammetry relies on stable, textured surfaces for the identification of common key (tie) points across images, which are essential for accurate reconstruction. Moving water presents two main problems: (1) clean, reflective conditions lack the necessary surface texture, and (2) highly turbulent or turbid flows obscure submerged features. Although strong water-surface fluctuations can create texture through aeration, this requires simultaneous and high-resolution image acquisition.

In this study, free-surface detection was addressed through three key measures:(i) throwing wood chips onto the flow surface to act as tracers and enhance surface texture, (ii) synchronizing all cameras to ensure simultaneous image capture, and (iii) optimizing lighting conditions and image quality (sharpness). These steps were critical for producing high-quality 3D reconstructions of both the approaching flow and the through-breach flow.

To illustrate these effects, selected model results are presented in Figure 4.15 and Figure 4.16, comparing two different methods of wood chips supplement to the flow. In Figure 4.15 (test *mS_Q_1*), wood chips were supplied immediately upstream of the dike from the moment when the water level reached the initial pilot channel elevation. In contrast, in Figure 4.16 (test *mS_Q_2*) the chips were supplied at the upstream end of the reservoir during the reservoir filling and overtopping phases. The latter approach (Figure 4.16a, b) produced a well-covered water surface, enabling a full photogrammetric reconstruction of the reservoir water surface. Conversely, injection wood chips right at the dike upstream (Figure 4.15a, b) resulted in only limited coverage and allowed only partial water-surface reconstruction.

Agisoft Metashape's interpolation option can fill gaps in the digital elevation model (DEM) caused by texture shortages, visible as white areas in the dense point clouds, with interpolated areas appearing as blurry regions. This emphasizes the importance of the presence of tracers for accurate flow surface reconstruction, as erroneous interpolation can introduce non-physical local depressions in the DEMs that do not correspond to the reality.

As the flow intensified and velocity increased (Figure 4.15b and Figure 4.16b at t = 120 s), wood introduced from the reservoir inlet became more dispersed, having minimal impact on 3D model accuracy at the breach control section, resulting in empty zones at the breach inlet (Figure 4.16b). In contrast, large quantities of wood supplied near the dike produced a continuous tracer layer at the breach control section upstream of the dike crest (Figure 4.15b).

Following full breach expansion (Figure 4.15c and Figure 4.16c), the presence of water aeration and aerated water from hydraulic jumps can aid model construction, even without tracers, provided that high-resolution images are captured simultaneously. For example, the 3D dense cloud model of the breached dike in Figure 4.15c contained more points inside the breach channel than the test illustrated in Figure 4.16c conducted under the same conditions, but in which images were recorded with a lower image resolution, lower sharpness, and slight timing delays between images. These differences highlight how the presence and distribution of tracers, image resolution, sharpness, and synchronization affect the quality of 3D photogrammetric reconstructions of moving water surfaces.

(a) $t = 0$ s

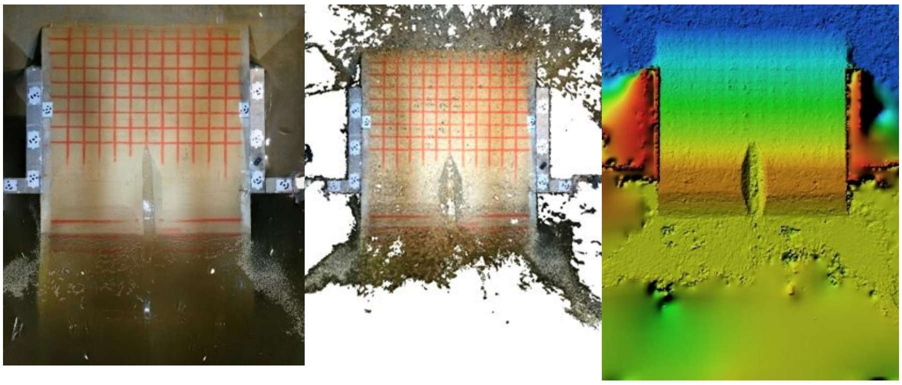

(b) $t = 120$ s

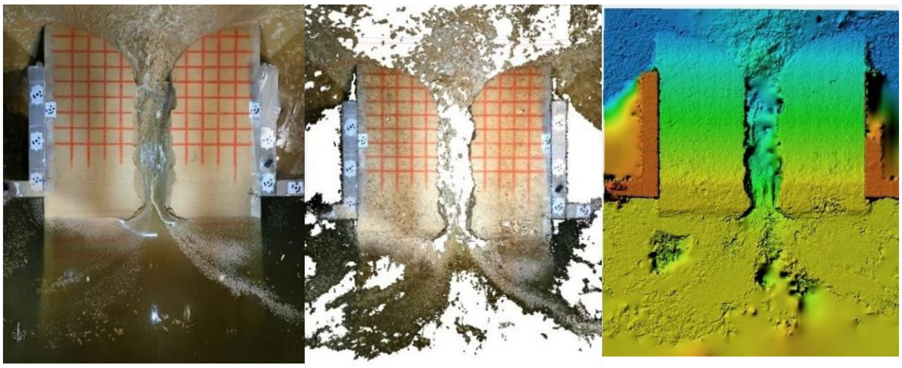

(c) $t = 220$ s

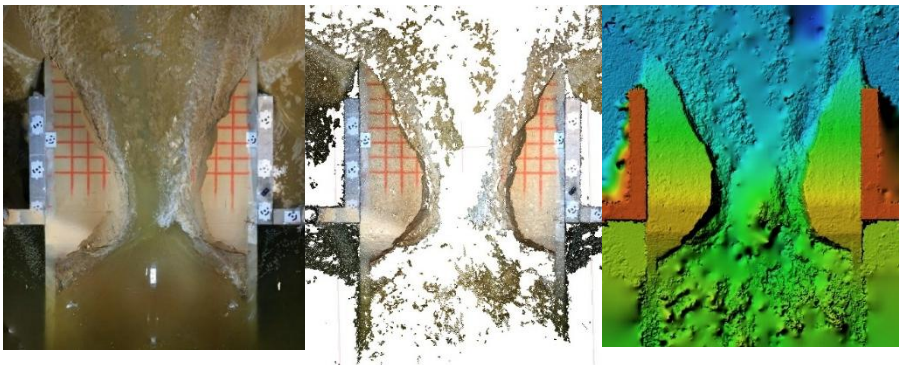

Figure 4.15 Orthophotos, dense point cloud and DEM models at selected moments for test *mS_Q_1*, with wood chips supplied immediately upstream from the dike.

(a) $t = 0$ s

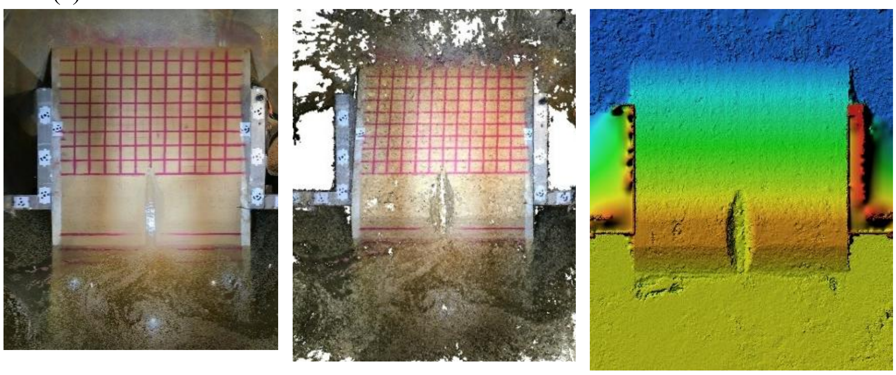

(b) $t = 120$ s

(c) $t = 220$ s

Figure 4.16 Orthophotos, dense point cloud and DEM models at selected moments for test *mS_Q_2*, with wood chips supplied at the upstream end of the reservoir.

It is also interesting to add that while specular reflections on the water surface vary depending on the camera orientation, they are inherently filtered out by the photogrammetric process. Structure-from-Motion (SfM) algorithms require physical feature points to remain spatially stable across multiple overlapping images to be successfully matched. Because reflections shift or disappear when viewed from different angles, the software cannot match them across frames and automatically rejects them as invalid tie points. To overcome the lack of valid texture on the reflective water surface and enable accurate 3D reconstruction, wood chip tracers were introduced to provide stable, view-independent features, supported by the redundant overlap of the multi-camera setup.

Optimal photogrammetry relies on consistent and reliable surface texture, making the control of lighting conditions essential. For reconstructing surfaces prone to glare and shifting reflections, such as moving water or uniform materials like sand, smooth and homogeneous lighting is generally preferred over sharp, contrasted light. By optimizing for smooth light, the captured images maintain consistent feature contrast across the dataset, thereby maximizing the accuracy and point density of the reconstructed 3D models.

These improvements however do not allow the detection of the breach bed elevation, that is limited due to the water turbidity, which obscures visibility, and light refraction, which causes erroneous estimates of the bed level. Therefore, the dike cross-sections derived from the DEMs (indicated as XS-

SfM in Figure 4.17) were complemented with the information obtained from the tracer balls, knowing their release timing. This allowed the reconstruction of the complete cross-sections as illustrated in Figure 4.17: extrapolating the bank slopes of the emerged banks until the level of the detected ball (indicated as XS-EXT) allows to estimate the actual wetted area.

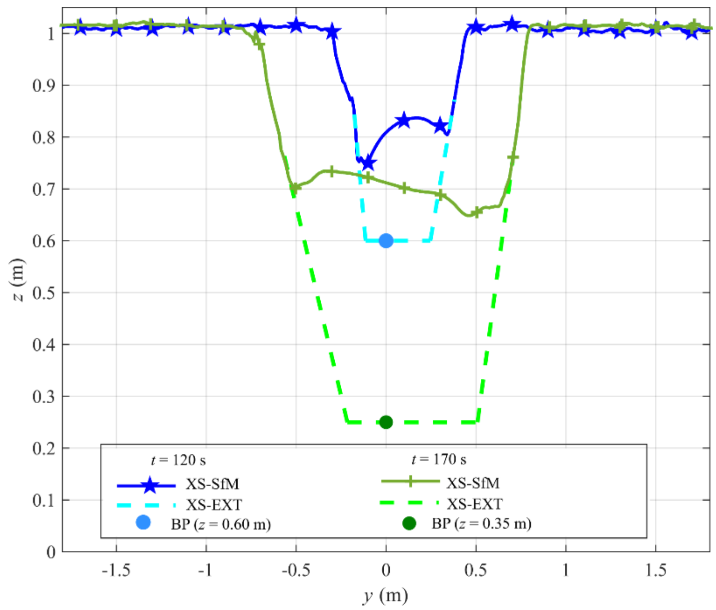

Figure 4.17 Complete dike cross-sections combing photogrammetric and tracer ball information capturing both exposed and submerged portions of the dike at $x = -0.25$m for *mS_Q_2*.

The novel methodology presented in this section — integrating artificial tracers, precise camera synchronization, and a hybrid extrapolation approach (utilizing embedded indicators) — successfully extends SfM capabilities to capture both dynamic water surfaces and hidden bed levels during high-speed breaching processes. Operationally, conducting sufficient experimental repetitions is highly recommended to ensure comprehensive data collection. Furthermore, future studies would benefit from higher image resolutions, the use of larger wood chip tracers, and automated, continuous seeding mechanisms. Despite these advancements, direct optical detection of the submerged bed remains inherently restricted by turbidity and light refraction. Future studies may overcome this limitation by employing alternative technologies, such as green-wavelength bathymetric LiDAR and Time-of-Flight (ToF) Kinect sensors, to enable continuous and direct underwater bed detection.

4.6.3 Spatiotemporal evolution of the breached dike and comparison with previous studies

To capture the highly dynamic breaching process, photogrammetric processing was performed at 20-second intervals to reconstruct temporal evolution of the breached dike. The resulting three-dimensional (3D) models, corresponding to the time instants described in Section 3.1, are presented in Figure 4.18. These reconstructions provide a detailed visualization of the breach morphology and enable quantitative analysis of both the crest cross-sectional evolution and the longitudinal profile development without disrupting the flow. Consequently, the novel insight provided by this enhanced methodology is the ability to continuously and simultaneously correlate the rapid spatiotemporal degradation of the hidden breach invert with the lateral expansion of the crest, overcoming the limitations of traditional single-point or post-event measurements.

The breaching mechanisms observed in this study are consistent with those reported in previous experimental investigations on sand dikes (Visser, 1998, Coleman et al., 2002, and Walder et al., 2015), showing similar sequences of surface erosion, headcut migration, and lateral widening.

In particular, the five stages of breaching defined by Visser (1998) in the full-scale Zwin'94 sand dike (see Figure 4.19) can also be clearly distinguished in the present tests.

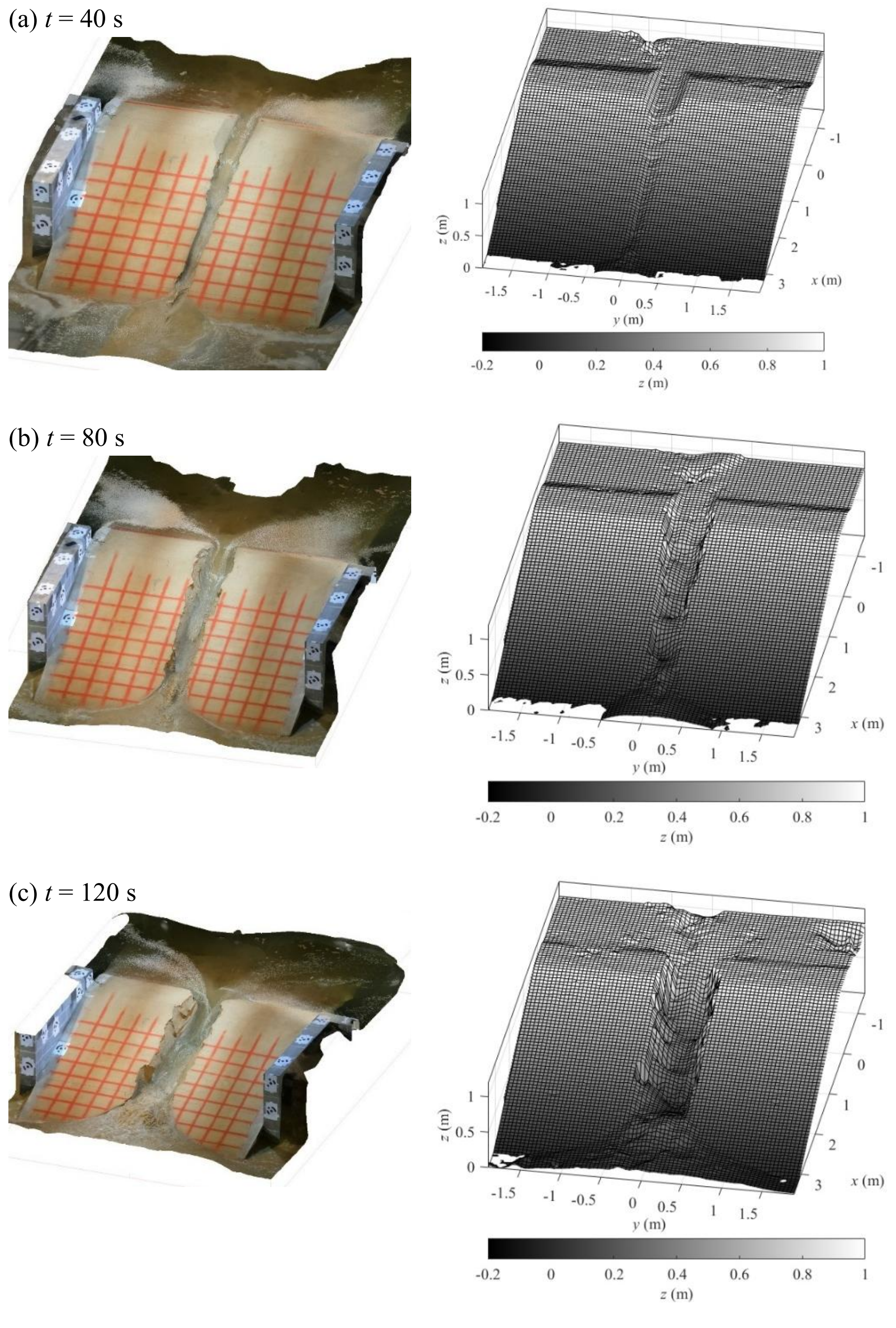
(a) t = 40 s
z (m)
y (m)
x (m)
(b) t = 80 s
z (m)
y (m)
x (m)
(c) t = 120 s
z (m)
y (m)
x (m)

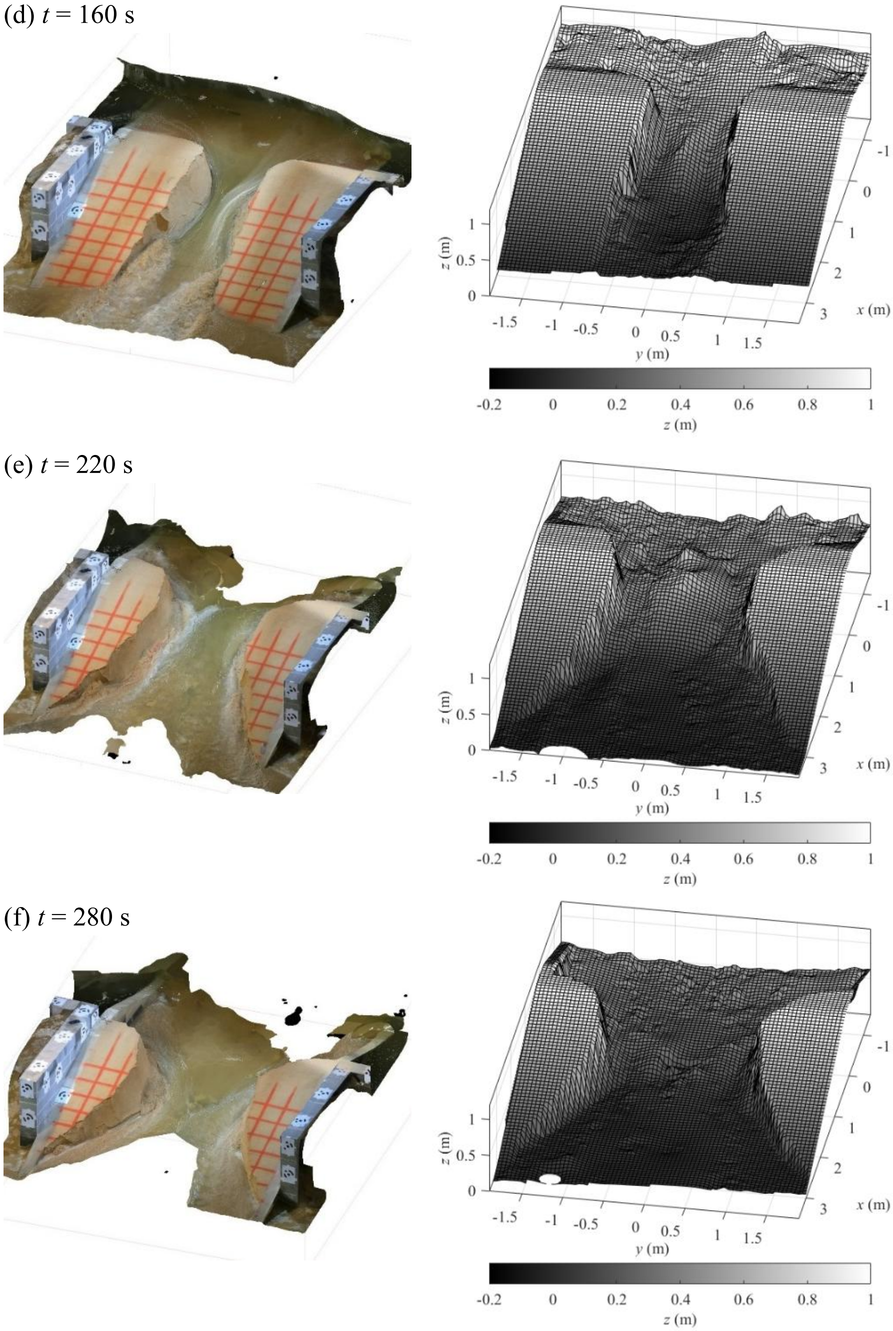

Figure 4.18 Breach evolution through the sand dike at selected instants, reconstructed from SfM-photogrammetry. Shown on the left

are the tiled models, and on the right the digital elevation models (DEMs), for test *mS_Q_1*.

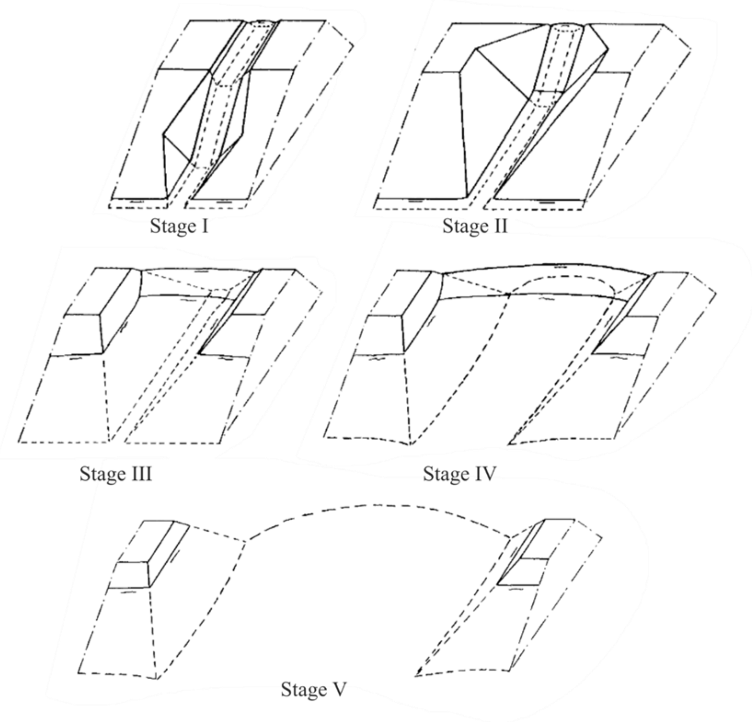

Figure 4.19 Schematic illustration of the temporal evolution of breach formation in a sand dike (Visser, 1998).

In Stage I, overtopping begins as water flows over the crest, forming an initial channel across the crest width and downstream slope. The downstream slope steepens progressively until it reaches a critical angle (t = 40 s; Figure 4.18a). During Stage II, the erosion migrates upstream from the outer slope toward the crest, widening the breach channel almost uniformly (t = 80 s; Figure 4.18b). This leads to a shorter crest width at t = 120 s in Figure 4.18c marking the end of stage II. At this point, the breach channel becomes directly connected to the upstream reservoir, and crest lowering accelerates breach widening. In Stage III, the flow becomes fully supercritical, the vertical erosion develops until reaching the non-erodible flume base at the downstream slope. The bank slope remains almost constant and close to the vertical (t = 160 s in Figure 4.18d). Throughout stage IV, the breach is mainly governed by lateral widening (t = 220 s in Figure 4.18e). The upstream slope erodes progressively, leading to further reservoir drawdown as the breach outflow reaches its maximum. Finally in Stage V, the water level declines, and as the breach widens further, the flow gradually decelerates until the erosion ceases (t = 280 s; Figure 4.18f).

The resulting breach channel exhibits a curved, hourglass-shaped planform similar to that reported by Coleman et al. (2002). The rotation of the breach invert slope about a fixed pivot point under constant reservoir level conditions, as described by Coleman et al. (2002), is also evident after t = 120 s as shown in Figure 4.21. The sediments deposition at the toe of the dike in form of an alluvial fan was also observed by Walder et al. (2015). This alluvial fan grew over time and visible until t = 120 s was finally washed away due to the strong stream after t = 160 s.

The through-breach flow can be divided into three conceptual flow stages, defined by the changing hydraulic head, flow contraction, and erosion mechanism (Damme & Visser, 2015). For a sand dike, these three stages are summarized as follows:

Stage 1 (Initiation) begins when the embankment overflows. The flow accelerates rapidly down the landside slope and mainly contracts vertically. The vertical velocity component is significant. In this stage, the erosion mechanism is dominated by surface erosion.

In Stage 2 (Development and Retreat), the flow has established a steep, receding front (breach head). The hydraulic head increases rapidly, and the flow contracts both horizontally and vertically, resulting in a complex, fully 3D flow as the channel rapidly deepens. Erosion shifts to rapid longitudinal recession via granular slumping and mass sediment transport driven by the concentrated flow. The non-linear vertical evolution of the breach invert elevation at the two locations indicated in Figure 23 confirms this physical process, aligning with the dilatancy-reduced erosion frameworks discussed by Bisschop et al. (2011, 2016) and van Damme (2021).

Throughout Stage 3 (Full Breach and Widening), a full breach has developed. The flow primarily contracts horizontally as the primary source of sediment is now the banks, and the flow stabilizes through the breach channel. The breach reaches its final depth (often limited by a non-erodible layer). Widening dominates through lateral bank slumping triggered by high horizontal shear and the gravity-driven collapse of over steepened, non-cohesive banks.

The temporal evolution of the exposed dike cross-sections, together with the interpolated water surface within the breach, is presented in Figure 4.20a, b. The reliability of these interpolated profiles depends on the quality of the dense point cloud within the breached zone. In particular, hydraulic jumps and local flow aeration generate elevated, hill-shaped free-surface features near the centre of the cross-section, especially at $x = -\,0.25$ m corresponding to the upstream edge of the crest. Similar hydraulic effects are observable in the longitudinal profiles extracted along the breach centreline at several time instants, as shown in Figure 4.21. The onset of the pivot-point effect can likewise be identified after approximately $t = 120$ s.

Nevertheless, limitations related to insufficient surface texture and gap-filling by interpolation introduce local artefacts e.g. depression areas in the digital elevation models (DEMs) discussed in Section 4.6.2, are subsequently reflected in the extracted profiles presented in Figure 4.21. These effects can be observed in Figure 20. For example, as a local depression at the upstream end of the longitudinal profile ($x = -\,1.7$ m) at $t = 120$ s, and near the crest region at $x = -\,0.6$ m at $t = 200$ s.

(a) (b)

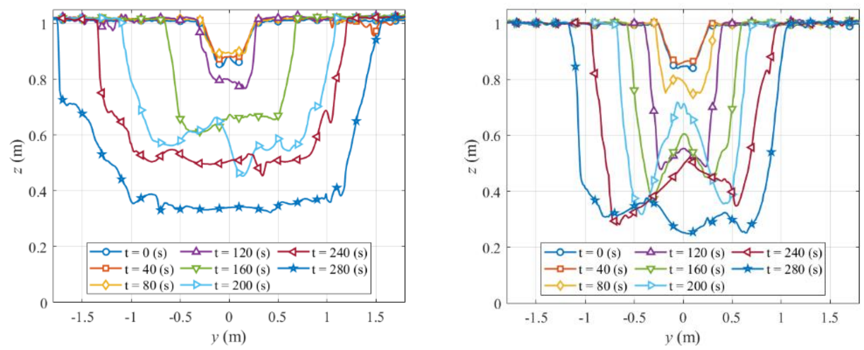

Figure 4.20 Breached dike (above water) cross-section evolution over time at (a) $x = -\ 0.25$ m and (b) $x = +\ 0.25$ m for test *mS_Q_1* (corresponding to respectively the upstream and downstream edge of the crest).

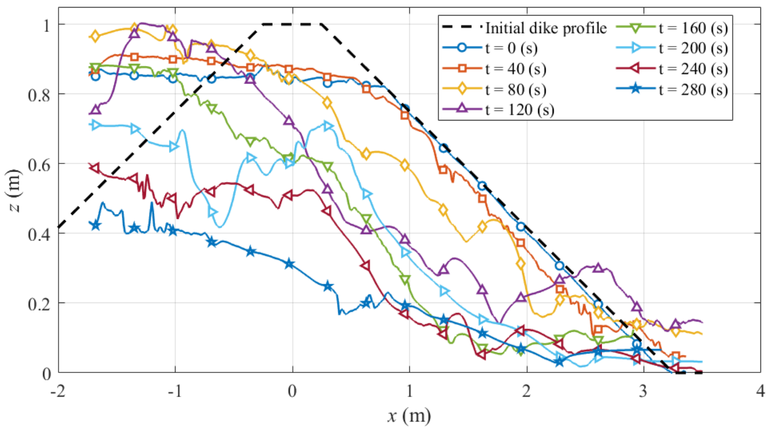

Figure 4.21 Longitudinal evolution of the flow profile through the breached dike at y = 0 m (breach axis) in case of *mS_Q_1*.

Consequently, quantitative geometric analyses derived from these specific interpolated zones must be interpreted with caution, as they may locally deviate from the true surface elevation.

To accurately analyse breach evolution, the DEMs were combined with data from the embedded balls, which indicate the true breach bottom level. This approach provided a more reliable basis for assessing breach development over time. The combination of the photogrammetric data with the balls releasing instants results is a full breach cross-section including the exposed portion of the dike and the submerged portion of the breached channel through the dike. This is shown for experiment *mS_Q_1* at the same instant when the balls located at (x, y) = (−0.25 m, 0 m) are released. This vertical string of balls acted as a set of discrete reference markers that indicate bed elevation at known embedment depths (BP: Ball Position in Figure 4.22).

To reconstruct the submerged portion of the breach geometry at those same instants, the instantaneous breach-bank slopes derived from the photogrammetric models were linearly extrapolated downward to the elevation of each ball (XS-EXT in Figure 4.22). This provided underwater cross-sectional profiles consistent with the morphology captured above the waterline (XS-SfM in Figure 4.22).

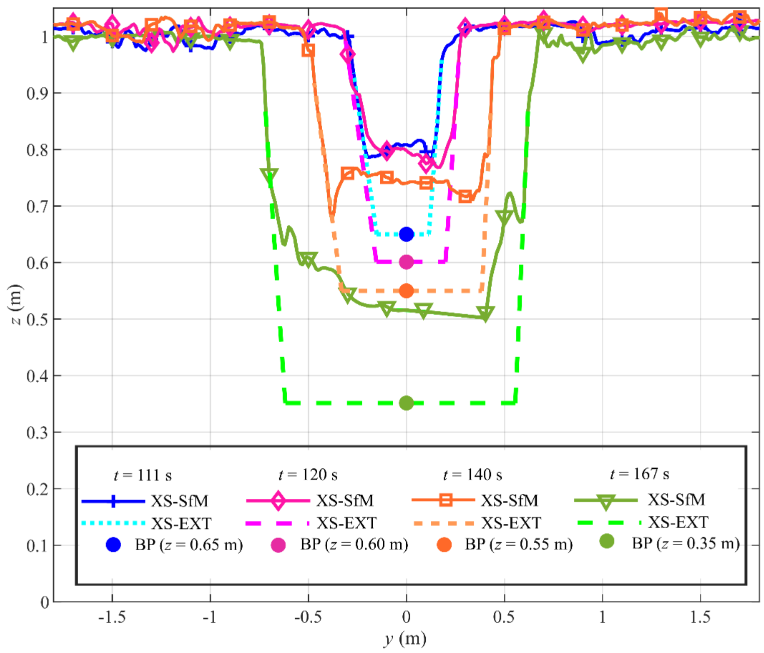

Figure 4.22 Complete dike cross-sections combing photogrammetric and tracer ball information capturing both exposed and submerged portions of the dike at $x = -0.25$m for *mS_Q_1* at balls appearing instants (XS-SfM: SfM-photogrammetry cross-section ball elevation points; XS-EXT: extrapolated cross-section; BP: Ball Position)

The lateral enlargement of the breach at the locations of ball strings e.g. $x = -0.25$m and $x = +0.25$m along the dike is shown in Figure 4.23a. At both locations, two distinct phases can be identified: an initial stage with a relatively gentle widening rate, followed by a much steeper expansion rate occurring after approximately $t = 120$ s. A similar two-phase behaviour is observed in the breach-invert deepening at the same locations, as indicated by the tracer-ball measurements in Figure 4.23b. The flow acceleration after this turning point results in a relatively rapid process governing the full breach development and complete failure of the structure.

The static water level measured at the central reservoir gauge (Zh2) is compared to water surface elevation detected by photogrammetry immediately upstream of the dike. In this near-field region, the flow is highly contracted as it enters the breach, and the discrepancy between these two measurements represents the localized drop in water surface elevation due to the flow acceleration rather than a measurement error. As the area captured by photogrammetry does not include the location of gauge Zh2, a direct comparison is not possible.

(a)

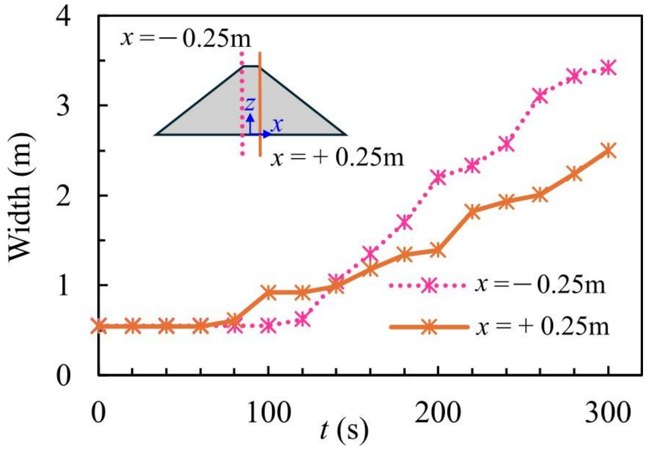

(b)

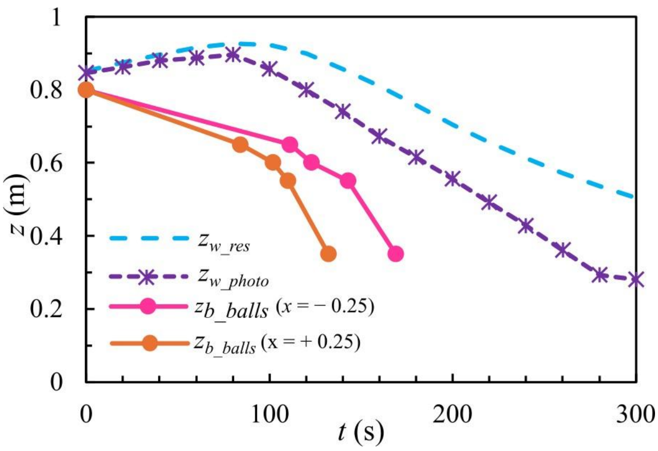

Figure 4.23 Temporal evolution of the breached channel: (a) breach width at the dike crest level (z = 1 m), and (b) combined direct (Zh2) and photogrammetric measurements of water level and bed level at the reference location ($x = -$ 0.25 m), using tracer balls as visual markers for *mS_Q_1*.

4.7 Conclusions

This study successfully reproduced and quantified the highly dynamic breaching process of non-cohesive earthen embankments at a medium scale. By demonstrating a high level of experimental reproducibility, the results firmly corroborate the principal physical mechanisms of breach evolution established in prior literature.

While the FARO LiDAR scanner provided precise and detailed models, its relatively long acquisition time (minimum ~2 minutes) limits its applicability during active breaching, when rapid morphological changes occur. In addition, the strong absorption of infrared (IR) light by water, particularly beyond a few cm, further reduces the effective range of LiDAR devices in such environments.

Notably, this research demonstrates the significant added value of deploying a synchronized, multi-camera Structure-from-Motion (SfM) photogrammetry framework. Traditional measurement approaches, such as terrestrial LiDAR, are severely constrained during active breaching by long acquisition times and the absorption of infrared light by water. In contrast, the enhanced SfM approach and validated to a high spatial accuracy (RMSE < 0.03 m) overcomes these temporal limitations. It uniquely enables the continuous, high-frequency, and non-intrusive tracking of rapid morphological changes across the entire embankment without disrupting the flow.

Despite these distinct advantages, the SfM methodology has inherent limitations that must be acknowledged. Most notably, highly turbulent and aerated flows obscure underwater geometry and render optical refraction corrections ineffective, preventing the direct photogrammetric reconstruction of the submerged breach invert. Furthermore, capturing the rapidly changing, dynamic water surface relies heavily on strict camera synchronization to successfully identify stable feature points across successive images. Finally, verifying the accuracy of these dynamic surface reconstructions necessitates supplementary measurement techniques, such as Time-of-Flight (ToF) sensors, highlighting a need for further investigation into their robustness at the medium-scale dimensions examined in this research.

To overcome these operational constraints and maximize the efficacy of SfM-photogrammetry, this study highlights several critical methodological advancements. First, it was demonstrated that dual-zone tracer seeding i.e., combining homogeneous reservoir distribution with targeted near-dike supplementation, is essential for capturing the highly accelerated, converging water surface at the breach inlet. Second, integrating embedded internal tracers successfully mitigates the inability of optical methods to penetrate turbid flows, providing a robust, cost-effective solution for continuously tracking the hidden breach invert. Finally, the results establish clear application boundaries based on soil mechanics: while single-camera mobile setups may suffice for slow-eroding cohesive embankments, synchronized multi-camera frameworks are strictly required to capture the rapid morphological evolution of non-cohesive granular dikes.

To further advance SfM-based monitoring in highly dynamic breaching conditions, future research must prioritize the development of integrated, multi-sensor frameworks. Specifically, investigations should focus on coupling continuous SfM photogrammetry with Unmanned Aerial Systems (UAS)-mounted bathymetric LiDAR (green laser technology) and Time-of-Flight (ToF) sensors. While theoretically promising for resolving submerged geometries, rigorous experimental assessment is required to determine if green laser systems can reliably penetrate the highly aerated, turbid waters characteristic of active breach flows. Validating this integrated approach represents the critical next step in fully closing the data gap for medium- and large-scale physical modelling.

Chapter 5

Effects of Grain Size and Overtopping Conditions on Breach Evolution at Medium Scale[5]

Having successfully established and validated the enhanced SfM-photogrammetry and tracer-ball methodology in the previous chapter, a robust framework is now available to accurately quantify the complete 3D morphological evolution of breached embankments. Building upon this measurement capability, the research now shifts from methodological development to physical analysis. Consequently, the next chapter utilizes this high-resolution experimental dataset to systematically investigate the underlying mechanics of the breaching process, specifically focusing on how variations in sediment granulometry and hydraulic overtopping conditions dictate the macroscopic erosion mechanisms, breach geometry, and resulting outflow hydrographs.

5.1 Background and Objectives

Numerous studies have investigated the influence of sediment characteristics, composition, and grading on breach formation and evolution in earthen embankments e.g. dams, dikes, and levees. Sediment properties are dominant factors controlling erosion resistance, failure duration, and the resulting breach outflow hydrograph. Early experimental work focused mainly on washout mechanisms in non-cohesive fuse-plug spillways (Chee, 1978; Pugh, 1985; Tinney & Hsu, 1961). Subsequent studies shifted focus toward homogeneous sand embankments, notably the large-scale Zwin’94 sand-dike experiments (Visser et al., 1995) and laboratory flume studies (Visser, 1998). Later research extended these investigations to assess the effects of grain size

[5] The research presented in this chapter is intended for publication in the Journal of Hydraulic Research.

on breach geometry and outflow hydrographs in sand embankments (Al-Riffai, 2014; Coleman et al., 2002; Pickert et al., 2011; Schmocker & Hager, 2012). Most recently, van den Berg et al. (2025) investigated the effect of foreshores—such as mudflats or beaches located at the waterside of the embankment—on breach development in sand dikes through medium-scale experiments.

In parallel, extensive research on cohesive embankments (Hahn et al., 2000; Hanson et al., 2005; Powledge et al., 1989; Ralston, 1987; T. L. Wahl, 1998) identified headcut formation and cascading profiles as major failure processes controlling the breach formation and development. Furthermore, apparent cohesion arising from negative pore pressures in unsaturated fine non-cohesive sediments can produce similar failure mechanisms addressed and measured by Pickert et al. (2011) and Al-Riffai (2014).

In addition to sediment characteristics and grading, Walder and O'Connor (1997) established that the upstream hydraulic loading is a governing factor for peak discharge, determining whether the outflow is limited by the breach geometry or the available reservoir volume. While Coleman et al. (2002) investigated the breach evolution under constant reservoir levels, simulating in this way infinite upstream water bodies, Chinnarasri et al. (2004) investigated the breach geometry evolution in homogeneous embankments under falling reservoir level, concluding that the peak outflow is governed by storage volume and water depth. Similarly, Schmocker and Hager (2012) demonstrated the influence of inflow magnitude on the erosion rate in planar overtopping experiments (i.e. erosion occurs over the entire width of the dike). Results of numerical modeling by Elalfy et al. (2025), further identify that breaching is highly sensitive to the inlet discharge and reservoir volume, parameters that must be explicitly captured to predict peak discharge accurately.

Frank (2016) conducted extensive experimental modeling to investigate how parameters such as inflow discharge, grain size, pilot channel width, dike cross-section, bed mobility, water surface topography, and reservoir geometry affect the breaching process in coarser non-cohesive sediments (sand to gravel). Halso et al. (2024) extended this work by examining the effects of sediment gradation, compaction, reservoir head, and physical scale on homogeneous embankments. Furthermore, Halso et al. (2025) investigated the breaching of zoned dams with central mineral cores to evaluate how geometric, material, and hydraulic conditions influence the failure of composite structures.

To bridge the knowledge gap in the limited data available in the literature, at the medium scale, a series of medium-scale dike breaching tests have been conducted to examine the influence of sediment granulometry and overtopping conditions on the temporal evolution of breaches through sand embankments. The primary objective is to quantify how variations in sand grain size and overtopping regimes, specifically constant reservoir levels (H) versus constant reservoir inflows (Q), dictate the morphological development and hydraulic capacity of the breach. Unlike the majority of previously reported laboratory experiments, which are constrained by small-scale limitations, this study presents a novel medium-scale approach. By conducting these tests at a significantly larger scale and employing highly advanced spatial measurement techniques, this research provides high-resolution data on the breaching process.

The results of the present study were combined with well-documented experimental data from the literature for sand embankments ranging from 0.3 m to 1.6 m in height. This extended comparison highlights the profound influence of reservoir dimensions on breaching dynamics, across varying overtopping conditions.

Therefore, this chapter details the experimental procedure, the observed morphological processes and the measured data. Before the results are presented, the principal physical mechanisms governing the morphological evolution of the breach are discussed to establish a theoretical framework for the macro-scale erosion processes observed.

By analyzing these mechanisms on a medium scale, this research aims to refine the understanding of physical processes such as periodic bank slumping, which significantly impacts the breach outflow hydrograph. Moreover, the high-resolution dataset generated from these experiments bridges the gap between small-scale laboratory observations and full-scale failure scenarios. This comprehensive data serves as a robust foundation for the validation of numerical models and the training of machine learning tools.

This chapter is organized as follows: first, a brief review of the macro-scale erosion processes across different materials is performed to provide context for the observed morphological evolutions. This is followed by a description of the detailed experimental conditions, including the overtopping regimes, embankment material properties, construction characteristics, and the complete test program.

The repeatability of experiments conducted on fine sand embankments is then addressed, followed by a systematic presentation of the influence of sand size and overtopping conditions (*H* vs. *Q*) in two distinct sections. Finally, the chapter concludes with additional discussions of the experimental results, their implications for numerical modeling, and identified future research needs.

5.2 Macro-Scale Erosion Mechanisms in Earthen Embankments

The experimental modelling of earthen embankment breaching—the failure of dams, dikes, or levees—requires the accurate replication of distinct macro-scale erosion mechanisms driven by the flow dynamics: surface erosion, headcut migration, and mass block failure. Driven by the interplay between hydraulic loading and soil resistance, these mechanisms dictate the morphological evolution of the breach cross-section. This geometric progression governs the flow capacity, ultimately determining the erosion rate and the resulting breach outflow hydrograph in terms of shape and peak discharge.

5.2.1 Surface erosion and the dilatancy effect

Surface erosion is primarily driven by tractive shear stresses exerted by the flow that remains attached to the embankment surface. At relatively low flow velocities (typically under 1 to 1.5 m/s), this manifests as a continuous process involving the gradual, grain-by-grain removal of individual soil particles once the hydraulic shear stress exceeds the critical threshold for incipient motion.

However, under the high flow velocities characteristic of active breaching, the erosion mechanics fundamentally shift. Rather than individual particle detachment, the intense tractive forces shear off multiple layers of the well-compacted soil simultaneously. In dense sands, this shearing induces a dilative behavior where the porosity of the top soil layer increases, creating an underpressure that draws water into the bed. Consequently, under these extreme conditions, the bulk properties of the sand mass — specifically its in-situ porosity and permeability — dictate the surface erosion rate rather than the characteristics of single grains.

.

5.2.2 Mass block failure and headcut erosion

In cohesive soils (e.g., clay), erosion is characterized by headcut migration. The process typically initiates with the formation of a scour hole at the toe or slope discontinuities where tractive shear stresses exceed the soil's critical threshold. This evolves into a vertical drop (headcut), where the flow separates from the surface and forms an impinging jet (Figure 5.1). Erosion is then driven by high turbulence and impact pressures at the base of the headcut, which causes undercutting (Figure 5.2). This destabilization leads to mass block failures (often defined by tension cracks), where the soil collapses in discrete, coherent chunks rather than particle-by-particle disintegration. This cycle often produces a 'stair-step' profile as headcuts retreat upstream toward the crest. Figure 5.2 illustrates the major processes at a headcut during breach formation.

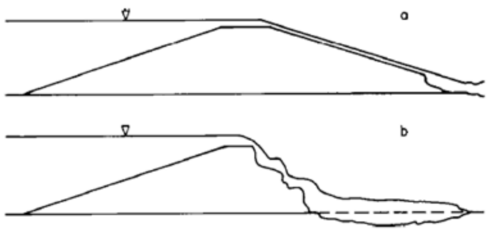

Figure 5.1 Progressive headcutting breach of a cohesive soil embankment (Powledge et al., 1989)

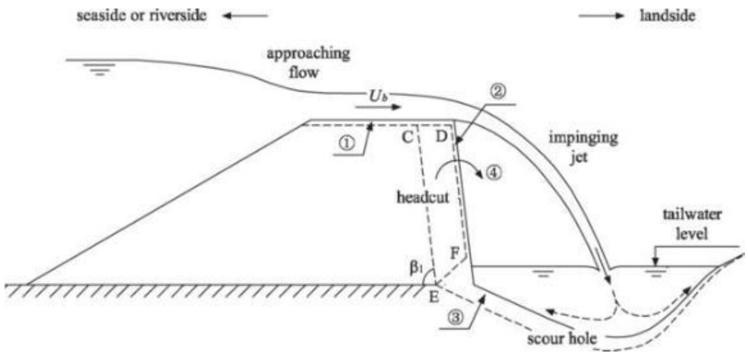

Figure 5.2 The four erosion mechanisms at a headcut during embankment breaching: ① shear erosion along headcut topsurface; ② shear erosion along headcut slope; ③ headcut undercutting and foundation jet scour (if any) and ④ slope masswasting adapted from (Zhu et al., 2005).

However, in non-cohesive granular soils (e.g., sand), the breaching process is initiated by surface erosion. In fine sand, this develops into a steep, rapidly receding front or cascade profiles (similar to Figure 5.1). In medium and coarser sand, the surface erosion results in regular progressive erosion profiles. In general, in sand embankments, the erosion is dominated by combined surface erosion which results in undermining of the banks, discrete mass slumping, and mass sediment transport. The discrete mass slumping is driven by gravity when the internal friction (loss of the angle of repose, Figure 5.3) and additional resistance due to negative pore pressure (apparent cohesion) is overcome. Lateral widening of the breach is mainly dominated by such mass slumping detachment on the breach channel banks (Figure 5.3c). The dimensions of these blocks are governed by the degree of apparent cohesion, which allows non-cohesive material to sustain steep, near-vertical slopes temporarily.

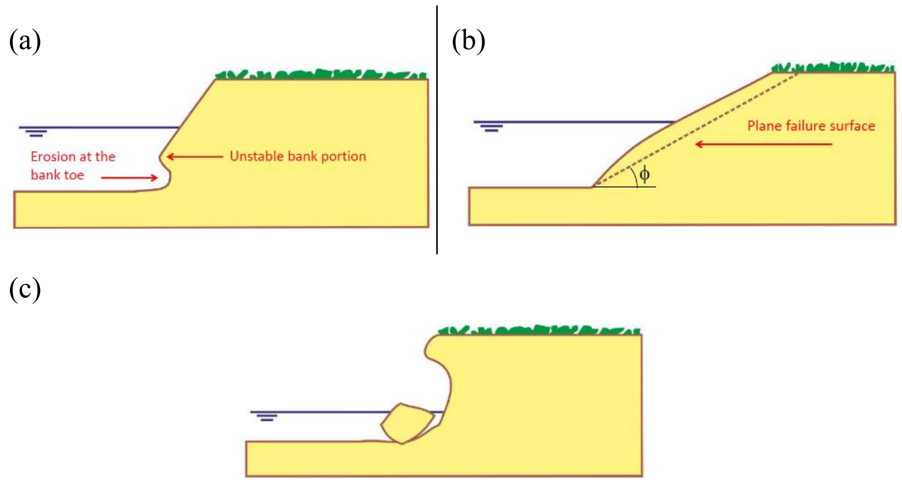

Figure 5.3 Bank erosion mechanisms: (a) Bank under cutting, (b) Planar failure in non-cohesive material, and (c) Mass block failure in cohesive material (Fluvial Hydraulics Course, Sandra Soares Frazão).

While addressing these instability mechanisms have long been a challenge in river engineering and alluvial channels where streambanks composed of loose unsaturated materials are highly susceptible to bank instabilities (Osman & Thorne, 1988; Rinaldi & Casagli, 1999; Rinaldi & Nardi, 2013) they are equally fundamental to defining the morphological evolution and non-linear erosion rates of embankment breaches. Table 5.1 provides a comprehensive summary of the primary failure mechanisms discussed throughout this section.

Table 5.1. Erosion and morphological process in cohesive and non-cohesive soils.

Mechanism	Dominant Force	Material State	Failure Trigger
Surface Erosion			
Cohesive Soils	Tangential shear stress (τ_0) exerted by the flow on the soil surface.	Particles bound by strong electrochemical forces, forming a coherent surface layer.	τ_0 must exceed the high critical shear stress (τ_c) required to overcome electrochemical bonds.
Non-Cohesive soils	Tangential shear stress (τ_0) exerted by the flow on the soil surface.	Particles bound only by inter-particle friction and gravity/submerged weight	τ_0 must exceed the low critical shear stress (τ_c) required to overcome inter-particle friction and gravity.
Headcut and Mass loss Erosion			
Headcut formation.in Cohesive Soils	High normal impact stress causing undercutting and tensile failure.	Block remains intact (coherent) as it falls known	Loss of shear strength due to water saturation or impact energy.
Mass Slumping in non-cohesive soil	Gravity acting on an oversteepened bank face resulting from toe erosion.	Block disintegrates immediately upon hitting the water, becoming loose sediment available for transport.	Exceeding the material's angle of repose due to toe removal.

5.2.3 Breach hydrograph

The macro-scale erosion mechanisms described above govern the resulting breach outflow hydrograph. Morris (2009) defined a generic hydrograph that links these physical processes to specific time markers (T_0 to T_5), emphasizing the dependence on hydraulic loading duration and intensity (Figure 5.4).

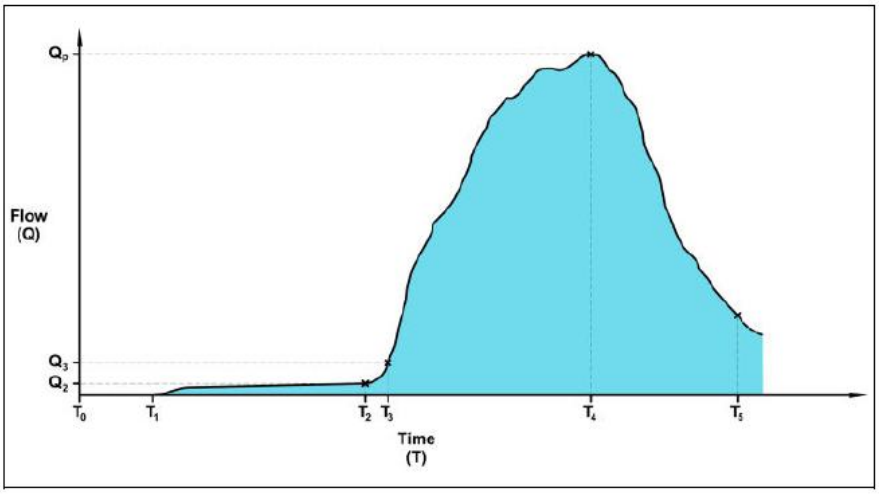

Figure 5.4 Generic breach flood hydrograph (Morris 2009):

These stages are summarized as follows:

Stable Phase (T_0): At time T_0, the hydraulic load is insufficient to trigger failure; the water level remains below the crest or critical seepage thresholds, preventing breach initiation.

Breach Initiation (T_1 to T_2): T_1 marks the onset of 'breach Initiation', where water begins to pass over (overtopping) or through (piping) the embankment. This moment is critical for early warning systems, as potential failure becomes foreseeable. From T_1 to T_2, the breach flow increases gradually, driven by either increased hydraulic loading (e.g., storm surge, rising flood) or the progressive, slow removal of surface material. During this phase, the geometry changes slowly, often characterized by apparent steady seepage or shallow overtopping.

Transition to Breach Formation (T_2 to T_3): Critical stage where steady (and relatively slow) erosion cuts through to the upstream face of the embankment initiating relatively rapid and often unstoppable breach growth. Transition may occur within hours.

Breach Formation (T_3 to T_5): The **Breach Formation** phase is characterized by rapid vertical erosion followed by continuous lateral widening. This stage exhibits rapid breach growth, high turbulence, and strong sediment entrainment, resulting in a sediment-laden flow.

Peak Discharge (T_4): The **Peak Discharge** occurs at marker within the formation phase. The magnitude of this peak is governed by the available flood water volume and the embankment's geotechnical resistance. Notably, the peak discharge at the breach (T_4) does not necessarily coincide with the worst flooding conditions downstream, due to flood wave attenuation and travel time.

5.3 Overtopping Conditions

The new experimental program was designed to evaluate breach morphology under two distinct hydraulic loading scenarios. These regimes are categorized based on whether the boundary condition is defined by a fixed water elevation, hereafter referred to as constant reservoir level conditions (*H*), or a fixed inflow discharge, hereafter referred to as constant reservoir inflow conditions (*Q*).

5.3.1 Constant reservoir level conditions (*H*)

In the constant reservoir level tests, the regulation system targeted a fixed upstream water elevation. This was achieved by dynamically adjusting the inflow rate to match the increasing discharge through the growing breach.

This condition simulates breaching scenarios in large reservoirs or lakes where the total volume is vast enough in such a way that the breach outflow does not immediately cause a significant drawdown of the water level. Under these conditions, the hydraulic head driving the erosion remains relatively stable, subjecting the embankment to a sustained maximum erosive potential. This typically leads to a more rapid and aggressive lateral widening of the breach compared to drawdown level scenarios. These tests are essential for determining the "potential" maximum breach dimensions and erosion rates under a (quasi) steady hydraulic load, serving as an upper-bound baseline for risk assessment.

The regulation system in constant reservoir level mode functions as follows:

- **Filling Phase:** The system supplied a constant inflow rate based on the filling rate (mm/s) indicated by user to reach the experimental starting point.
- **Experimental Phase:** As the water level approached the prescribed value, the system automatically decelerated the filling rate to ensure a smooth transition and reach zero.

- **Water-level Regulation:** Once the target elevation was reached, the regulation system switched to "water level mode," maintaining a constant head (*H*) throughout the duration of the breaching process.

The regulation system was designed to operate within a specific reservoir water level range of 0.87 m to 1.05 m, which served as the primary constraint for the setup's conceptual design (i.e. testing 1-m-high dams/dikes). Accordingly, the ultrasonic sensors used for real-time water level monitoring (indicated in Figure 4.1) were limited to a water level detection between 0.86 m and 1.11 m across the reservoir.

In this study, the prescribed water level was set to 0.05 m above the invert of the initial pilot channel. This channel is required for triggering erosion at a fixed location on the crest, as well as for facilitating a gradual and controlled breach initiation. As overtopping begins and the downstream slope erodes, the increasing discharge through the breach causes a localized drop in the reservoir level. The regulation system immediately reactivates and adjusts the pump speeds to compensate for this decline (Analyse Fonctionnelle Automatisms Report, 2022).

5.3.2 Constant reservoir inflow conditions (*Q*)

In the second overtopping regime, the experiments were conducted under constant reservoir inflow conditions, representing scenarios where a steady discharge enters a basin of limited storage capacity. A fixed discharge (Q_{in}) was maintained throughout both the reservoir filling phase and the subsequent overtopping phase. To enable the investigation of scale effects, this inflow was determined by applying Froude similarity scaling to prior small-scale experiments conducted at the LEMSC laboratory(conducted by Descantons & Dujardin, 2014 and Van Emelen et al., 2015, and later reported by Delpierre et al., 2024) A comprehensive analysis of these scaling criteria and the scale-series laboratory modeling is presented in Chapter 6. As the breach deepened and widened, the breach outflow eventually exceeded the constant inflow, resulting in a drawdown of the reservoir water level. This depletion of the reservoir volume led to a progressive reduction in the hydraulic head and the discharge capacity through the breach. This hydraulic sequence continued until the flow was no longer capable of further eroding the breach boundaries, leading to the eventual stabilization of the breach geometry.

5.4 Embankment Material

5.4.1 Sediment selection and characterization

To investigate the influence of sediment granulometry on breach formation and development, two distinct sand types were selected. This choice builds upon past experimental frameworks established within the Hydraulic Research Group of UCLouvain (Spinewine et al. 2004, Descantons et Dujardin, 2014, Van Emelen et al 2015, and Delpierre et al., 2024). Furthermore, these specific grain sizes align with those widely employed in foundational small-scale literature (e.g., Visser, 1998; Coleman et al., 2002; Pickert et al., 2011), ensuring that the present medium-scale experiment results are directly comparable for the assessment of scale effects and enabling comparative analysis with small-scale and full-scale experimental data. Inspired by prior small-scale experiments at the LEMSC laboratory (conducted by Descantons & Dujardin, 2014 and Van Emelen et al., 2015, and later reported by Delpierre et al., 2024), a novel medium-scale testing framework (at a geometrical scale factor of 5) was implemented at the Hydraulics Research Laboratory of SPW MI (Châtelet, Belgium). This is further discussed in Chapter 6.

The choice of the sand grain sizes was constrained by both logistical factors—limiting selection to regional production available within a feasible distance—and current limitations of the setup. Coarser sands were excluded to preclude excessive infiltration, which can lead to premature internal erosion or "seepage-induced" instability rather than the intended overtopping-driven breaching. However, future investigations into coarser and wider granulometries could be enabled through enhanced seepage mitigation strategies, such as optimized internal drainage systems or upstream surface sealing.

The materials selected for the experimental program consist of two uniform silica sands with distinct granulometric profiles:

- **Fine Sand (*fS*):** A river sand commercially designated as Rhin Sand 0/2 (Kaliwaal 41), characterized by a median diameter (d_{50}) of 0.31 mm.
- **Medium Sand (*mS*):** A processed silica sand designated as Silica 0.4-0.8 DS (Wessem), with a median diameter (d_{50}) of 0.61 mm.

The grading curves for both soils were determined in our laboratory facility the LEMSC, using sieve analysis in accordance with the ISO 3310 standard. The results of these analyses are presented in Figure 6.2 and Table 5.2.

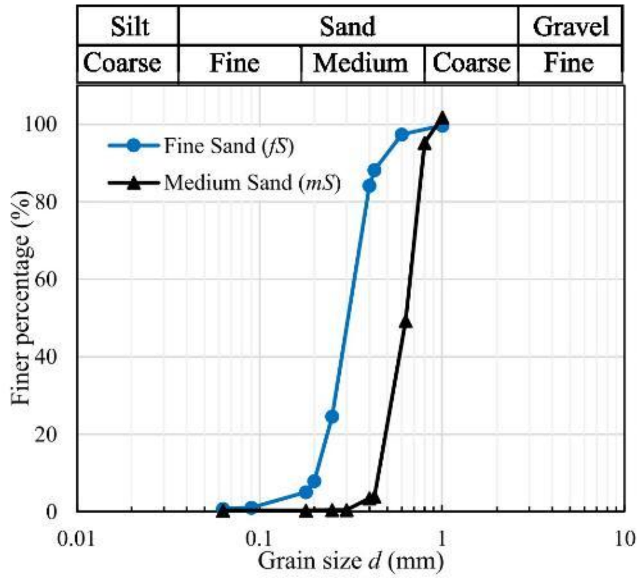

Figure 5.5 Particle size distribution of fine and medium sand soils used in medium-scale experiments (ISO 3310 standard).

Table 5.2 Geotechnical characteristics of the sand used in the experiments.

Parameters	Fine sand (*fS*)	Medium sand (*mS*)
Median diameter d_{50} (mm)	0.31	0.61
Optimum dry density ρ_d (kg m^{-3})	1800	1550
Optimum water content w_{opt} (%)	14	8
Coefficient of uniformity C_u	1.61	1.32
Coefficient of curvature C_c	1.00	0.99
Classification	Uniform Sand	Uniform Sand
Saturated hydraulic conductivity* (m/s)	3.17×10^{-4}	NA

*Permeameter with constant pressure;

5.5 Experimental Program

It should be noted that while the constant reservoir inflow (*Q*) regime was applied to both the fine and medium sand dikes (*fS* & *mS*), the constant reservoir level (*H*) condition was exclusively investigated using the fine sand (*fS*). Besides, the initial dimensions of the pilot channel were specifically adapted for the *H*-conditions to remain compatible with the technical specifications and safety protocols of the experimental setup.

The comprehensive experimental program conducted for this research is summarized in Table 5.3, which details the specific material and hydraulic parameters for each individual test run. This campaign was supported by three master's theses (Gilles & Zgajewski Delforge, 2023; Jergeay & Zhang, 2024; Maron, 2026) conducted under the supervision of Prof. Soares Frazão and the author. While these studies contributed to experimental preparation, monitoring, and preliminary post-processing, all data and analyses presented in this chapter are the original contribution of the author.

The depth of the initial pilot channel was tailored to the specific constraints of the two overtopping regimes. For the constant reservoir level (*H*) tests, the depth was dictated by the operational limits of the automated water regulation system, which required an initial water surface elevation between approximately 0.90 m and 1.00 m. Conversely, for the constant inflow (*Q*) tests, the pilot channel depth was governed by geometric scaling criteria. To ensure proper execution, the initial throughflow was estimated using hydraulic profiles that assumed critical flow depth at the downstream edge of the crest, supported by empirical formulas (Gilles & Zgajewski Delforge, 2023; Jergeay & Zhang, 2024). Furthermore, preliminary numerical simulations using the WATLAB[6] model (assuming a non-erodible embankment) were conducted to verify that this chosen depth provided adequate time for localized breach development before the rising water could overtop the entire embankment crest.

[6] https://sites.uclouvain.be/hydraulics-group/watlab/

Table 5.3 Summary of the experimental test program and parameters.

Overtop.	Test Acronym	Hydraulic Load (Q_{in} or H_{res})	d_{50} (mm)	z_c (m)	z_b (m)	Peak Inflow ($m^3 s^{-1}$)	Peak Outflow ($m^3 s^{-1}$)	Test objective	Experiment Remarks
Constant Inflow (Q)	*mS_Q_1*	0.224 $m^3 s^{-1}$	0.61	1	0.8	0.224	0.690	Influence of grain size; influence of overtopping conditions (finite reservoir volume recharged by a constant discharge); Scale effects	
	mS_Q_2	0.224 $m^3 s^{-1}$	0.61	1	0.8	0.224	0.725		
	mS_Q_3	0.224 $m^3 s^{-1}$	0.61	1	0.8	0.224	0.734		
	fS_Q_4	0.224 $m^3 s^{-1}$	0.31	1	0.8	0.224	0.911		
	fS_Q_5	0.224 $m^3 s^{-1}$	0.31	1	0.8	0.224	0.921		
Constant Level (H)	*fS_H_6*[a]	0.95 m	0.31	1	0.90	0.290[a]	0.678	Influence of finite (or fixed) reservoir volume	Pumping systems was stopped before the test ended.
	fS_H_7	0.98 m	0.31	1	0.93	0.870	1.430	Influence of infinite reservoir volume; soil compaction	
	fS_H_8	0.95 m	0.31	1	0.90	0.680	1.220	Influence of infinite reservoir volume; soil compaction	

Note: z_c *denotes the dike crest elevation;* z_b *denotes the pilot channel invert elevation.* [a] The peak inflow before the pumping system was stopped (t= 200s).

[1] *Unsuccessful runs have been omitted from this list; detailed records of these tests are provided in Appendix*

5.5.1 Soil compaction

The Standard Proctor test results for the fine sand series establish a well-defined reference, with a peak dry density (ρ_d) of approximately 1800 kg m^{-3} attained at an optimum moisture content (w_{opt}) of 14 % and maximum dry density. This curve serves as the baseline for evaluating the in-situ compaction state across the experimental series, as illustrated in Figure 5.6. The construction protocol was described in detail in the previous chapter through the medium sand (*mS*) test series. The same standardized procedure was followed during the construction of all tests to ensure cross-series comparability and minimize experimental variability.

Measurements from *fS_Q* series indicate that dry densities remained consistently below the Standard Optimum Proctor, a trend aligning with the preparation characteristics observed in the earlier medium sand (*mS*) experiments. Between the two fine sand constant-inflow tests, *fS_Q_4* achieved marginally higher degree of compaction than *fS_Q_5*. In contrast, the *fS_H* series (*fS_H*_6, 7 and 8) exhibits greater variability (up to 28% deviation from the optimum Proctor value). Notably, test *fS_H*_6 achieved a dry density of 1830 kg m^{-3}. This value, which slightly exceeds the laboratory Proctor maximum, is attributed to the substantial mechanical effort delivered by the vibratory machine (see 4.3.3 Soil compaction and construction procedure) and a high number of compactions passes during the layer-by-layer construction.

These results emphasize that achieving high compaction in fine sand is highly dependent on both elevated initial moisture and significant mechanical energy. This variation in initial density is a critical determinant in the subsequent breach development; higher compaction levels enhance the material's resistance to initial surface erosion, thereby delaying the onset of the breach formation phase and altering the overall temporal evolution of the failure.

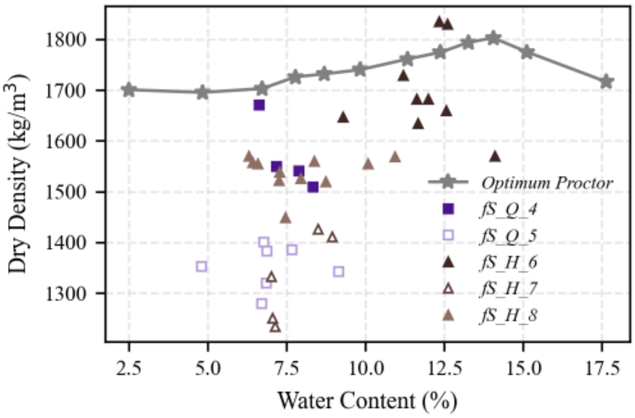

Figure 5.6 Optimum Proctor and in-situ compaction curve for the dike breaching tests conducted with fine sand (*fS*)

5.6 Test Repeatability in Fine Sand

To evaluate the reliability of the experimental protocol and the consistency of the dike construction method, a repeatability analysis was performed using the fine sand tests conducted under constant reservoir inflow conditions (i.e. *fS_Q_4* & *fS_Q_5*). It should be noted that the repeatability of the experimental results under constant inflow conditions in case of medium sand (*mS*), was established and discussed in Chapter 4 , where near-identical hydraulic and morphological behaviors were observed across duplicate test runs.

Tests *fS_Q_4* and *fS_Q_5* were performed using identical target parameters: a constant inflow of 0.224 $m^3 s^{-1}$ as shown in Figure 5.7a, and a pilot channel invert (z_b) of 0.80 m as for *mS_Q tests*. The temporal evolution of the average reservoir water level and the resulting breach discharge for these two runs show a high degree of agreement (see Figure 5.7 b and c).

(a)

(b)

(c)

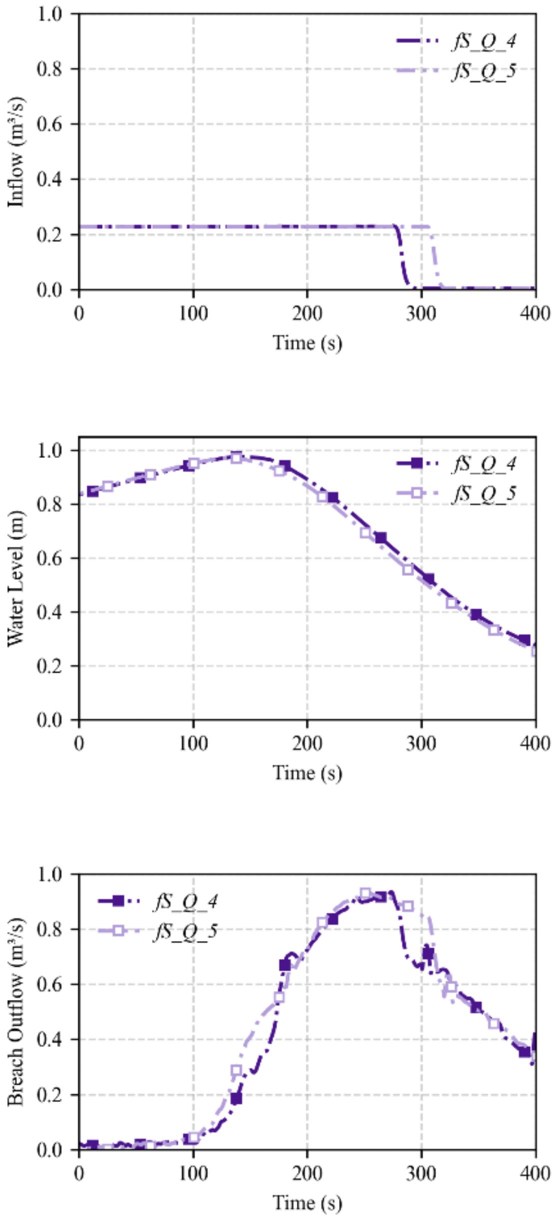

Figure 5.7 Flow characteristics including (a) reservoir inflow, (b) water level evolution (mean STD is 0.012 m), and (c) breach outflow (mean STD is 0.018 m^3 s^{-1}) in experiments *fS_Q_4* and *fS_Q_5*.

While the time to overtopping and the peak discharge values exhibit minimal variance, slight differences in the reservoir water level (mean standard deviation of 0.012 m) and the plateau duration or constant head duration (150 s $< t <$200 s) are observed. The reservoir water level in *fS_Q_4*exhibited higher peak and a relatively slower drawdown, particularly during the widening phase ($t > 150$ s). This confirms the higher compaction effects in test *fS_Q_4*. The sharper outflow increase in test *fS_Q_5* after this instant (Figure 5.7c) is, therefore, the consequence of a faster water level decline in the reservoir.

Under constant inflow discharge (Q), the reservoir water level initially rises until the expanding breach cross-section is capable of conveying the total system inflow (0.224 $m^3 s^{-1}$). Following this hydraulic equilibrium, the water level exhibits a brief plateau—referred to as the constant head duration—before the drawdown phase begins. Notably, the peak breach discharge consistently lags behind the peak water level. This time delay occurs because the maximum outflow is not driven solely by hydraulic head, but by the rapid lateral expansion of the breach which mobilizes the reservoir storage. Beyond this point, the hydrograph is governed primarily by the reservoir depletion dynamics rather than the inflow boundary condition.

In addition, as a morphological indicator, the widening rates at three longitudinal cross-sections are compared and illustrate in Figure 5.8. Figure 5.8a shows the breach width evolution for test *fS_Q_4*, illustrating the spatial non-uniformity of the breaching process. At the upstream section, beginning of the crest i.e. $x = -0.25$ m, the widening is driven by the acceleration of the flow entering the breach, remaining limited over first stage i.e. breach formation. As the flow progresses downstream to $x = +0.75$ m, the widening rate is influenced by the established hydraulic gradient within the breach channel. The overall agreement between tests *fS_Q_4* and *fS_Q_5* across all three locations, as shown in Figure 5.8 (a–c), demonstrates the high level of reproducibility achieved in the medium-scale applying a consistent construction protocol despite slight compaction differences. Figure 5.9a-b depicts this effect in form of small-time lag in erosion rate during the breach formation phase.

(a)

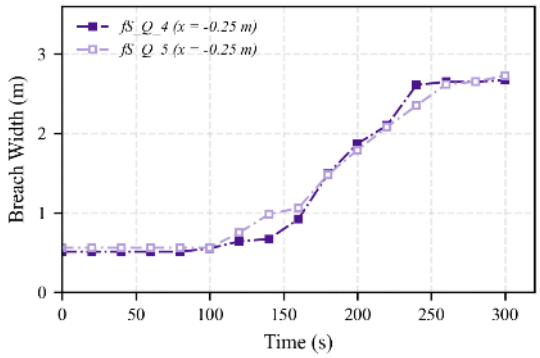

(c)

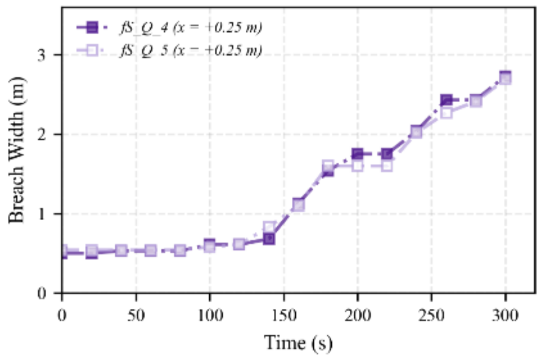

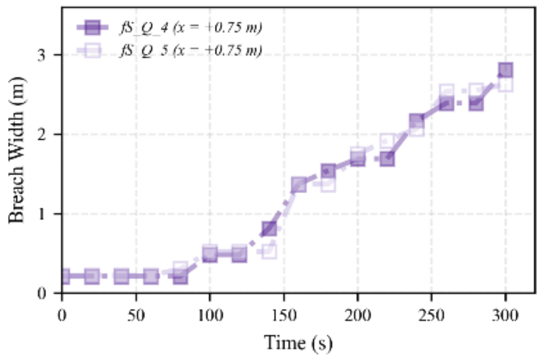

Figure 5.8 Comparison of breach widening dynamics for fine sand embankments under constant inflow (*Q*): (a–c) synchronized width evolution for tests *fS_Q_4* and *fS_Q_5* at longitudinal cross-sections $x = -0.25$, $+0.25$, and $+0.75$ m, respectively.

(a) (b)

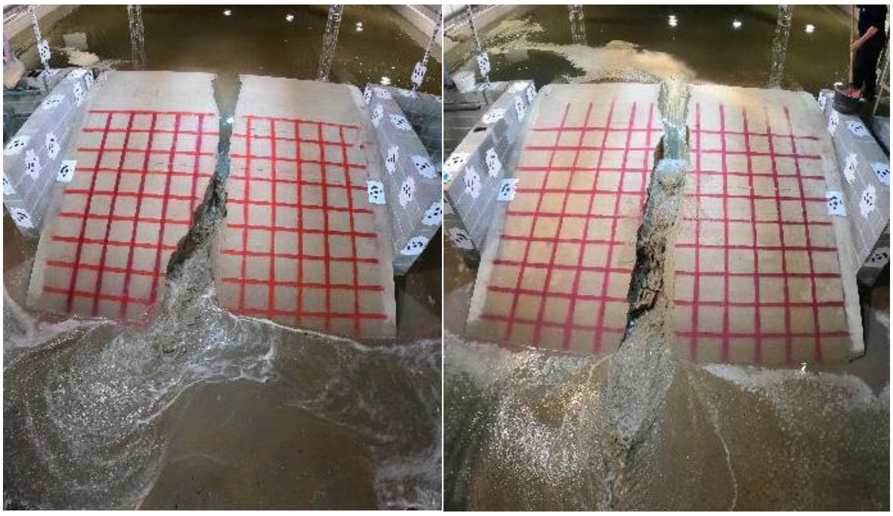

Figure 5.9 Effect of compaction in form of small erosion time lag in tests (a) *fS_Q_4* and (b) *fS_Q_5* at t = 80 s.

With the reliability of the construction and measurement systems established, the subsequent sections analyze the hydraulic performance of the dikes under varying overtopping regimes. While the constant reservoir level (*fS_H*) tests involved specific setup adaptations, such as variations in the initial pilot channel invert (z_b) and regulation system parameters (H), their results are analyzed as individual cases of hydraulic forcing rather than as direct replicates.

5.7 Influence of Overtopping Conditions: Constant Water Level vs. Constant Discharge

This section investigates the influence of overtopping conditions, specifically constant reservoir level (H) versus constant reservoir inflow (Q), on the breach formation and development in fine sand embankments. This section presents and discusses the results of tests *fS_Q_5, fS_H_6,7,* and *8.* As indicated in

Table 5.3 it is important to note that the initial pilot channel dimensions were adapted for the *H*-series to remain within the operational constraints of the water regulation system. Given the inherent differences in how erosion is triggered under these two regimes, the definitions of overtopping initiation and the experimental reference time ($t = 0$) are first clarified to ensure a consistent comparative framework.

5.7.1 Overtopping initiation and time zero (t = 0)

As detailed in Section 5.3.1, the regulation system automatically decelerates the pumping rate as the reservoir approaches the prescribed water level. This control logic dampens the initial hydraulic impact, resulting in a more gradual overtopping initiation and a slower initial erosion rate compared to the constant inflow (Q) tests. In this research, overtopping was considered to be initiated as soon as the flow reached the end of the pilot channel before descending over the downstream slope corresponding to $t = 0$.

The transit time required for the flow to reach the embankment toe varies depending on the available hydraulic head. As an example, Figure 5.10(a-d) illustrates this timing for *fS_H_6.* After the water reached the end of the pilot channel, it took 20 s to reach the midpoint of the slope and 28 s to reach the toe of the dike. The overtopping flow remained weak at this instant (breach outflow equal to zero); it was only after 40 s that the flow was established.

(a)

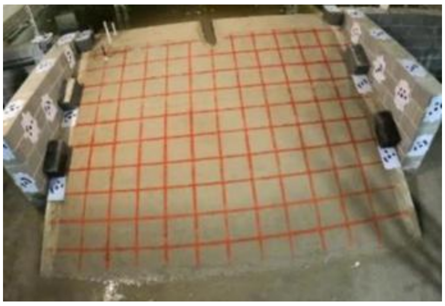

(b)

(c) (d)

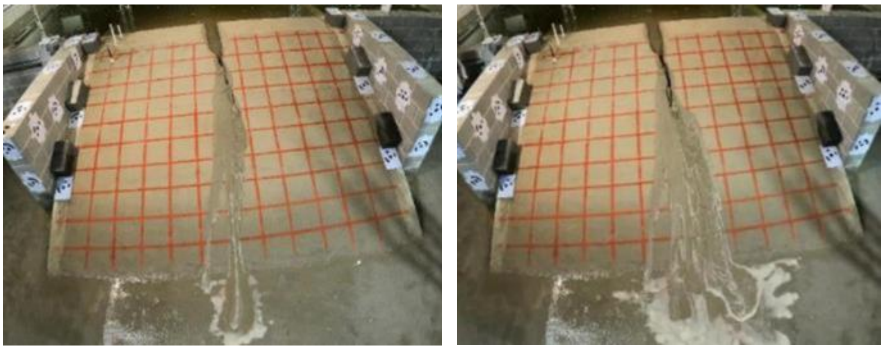

Figure 5.10 Overtopping development sequence under constant reservoir level (*H)*: (a) water reaching the end of the initial pilot channel; (b) flow progression after 20 s; (c) flow arrival at the dike toe after 28 s; and (d) fully established overtopping after 40 s.

In contrast, the establishment of overtopping was almost twice as fast under the constant reservoir inflow condition with the flow reaching the dike toe after about only 10 s. This process is depicted by a series of equivalent images from test *fS_Q_5* in Figure 5.11 (a-d).

(a) (b)

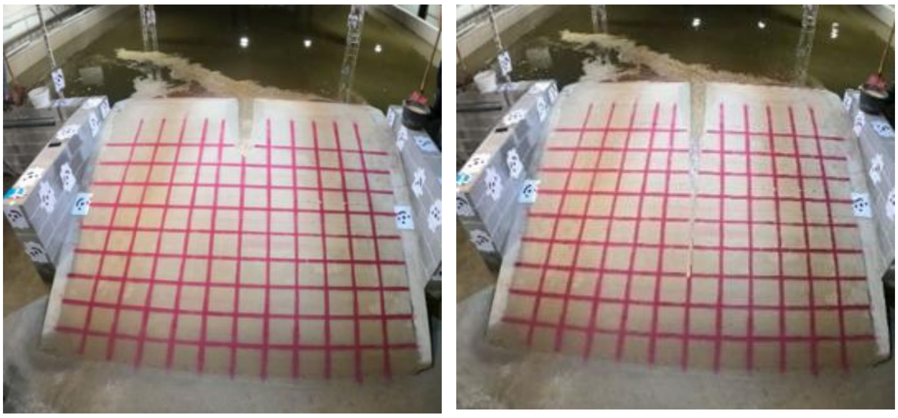

(c) (d)

Figure 5.11 Overtopping development sequence under constant reservoir inflow (*Q)*: (a) water reaching the end of the initial pilot channel; (b) flow progression after 3 s; (c) flow arrival at the dike toe after 10 s; and (d) fully established overtopping after 20 s.

Furthermore, in the *fS_H* series, the inflow discharge decreased to zero and remained at zero for a short period before the pumps restarted in response to the water level decline in the reservoir. This intermittency extended the duration for seepage and infiltration within the dike body. In contrast, the inflow was continuous in the constant discharge (*Q*) tests; consequently, the breach grew at a sustained and higher pace as soon as overtopping commenced, driven by the uninterrupted supply of hydraulic energy. This is further discussed in the next section.

5.7.2 Reservoir dynamics and discharge hydrographs

The temporal evolution of the upstream water level, the inflow rate, and the calculated breach discharge provide a direct measure of the system's response to these distinct overtopping conditions.

In the *H*-series tests, it is important to note that overtopping initiated before the inflow had completely reached zero, occurring during the pumping deceleration phase (the transition between the Experimental Phase and Water-level Regulation). Subsequently, the inflow remained at zero for approximately 60 s, a period that covered the entire breach formation phase. This implies that initial breach formation was governed by the reservoir’s falling head rather than the hydraulic energy supplied by active inflow (Figure 5.12a-c).

For test *fS_H_7*, an intermediate adjustment to the prescribed water level was essential to trigger the overtopping due to the higher pilot channel elevation (0.98 compared to the standard 0.95). This necessitated a higher initial inflow at t = 0 s which temporarily increased the breach outflow compared to tests *fS_H_6* and *fS_H_8*. In these latter two tests, the pumping deceleration patterns differed slightly as they approached the target water level. Furthermore, the pumping system was stopped earlier in *fS_H_6* due to some instrumental constraints. However, by that point, the breach had already entered the widening phase. Nevertheless, these conditions represented perfectly the influence of a finite (or fixed) reservoir volume on breach development.

As the breach channel enlarged sufficiently to cause the reservoir level to decrease, the pumping system reinitiated to compensate for the water level depletion. In erodible materials such as fine sand, this increase in reservoir inflow triggered a feedback loop of accelerated erosion, causing the pumping discharge to ramp up rapidly until it reached its maximum capacity. After this instant, the inflow remained constant. For this highly erodible material, the speed of this discharge increase was notably fast. Therefore, once the breach reached a critical size, the reservoir inflow could no longer compensate for the outflow and maintain the desired reservoir level as shown in Figure 5.12a.

The regulation system was capable of maintaining a nearly constant level in the *H*-series experiments for a significant portion of the experimental duration (approximately 180 s). This constant level phase was then followed by a visible, gradual decrease. In experiment *fS_H_7*, higher reservoir head resulted in faster vertical erosion rate and breach formation. Subsequently, the regulation system reactivated earlier to compensate for the water drawn down in the reservoir and therefore a breach outflow increased at a higher pace compared to *fS_H_6,* and *fS_H_8* tests and a shorter time-to-peak outflow. Despite this difference in reaction time, the inflow and outflow curves follow the same patterns. Moreover, due to an interruption in the pumping system, test *fS_H_6* essentially simulated a fixed-volume reservoir scenario. Consequently, the breach development and resulting peak outflow in this test were governed entirely by the depletion of the available reservoir storage.Conversely, in the *Q*-series, as the constant discharge exceeds the initial capacity of the pilot channel (app. 60 l/s), the water level increased in the reservoir until it reached a peak approximately 0.02 m below the crest level. After this moment, the breach becomes wide enough allowing the entire inflow flow through the breach channel. Reservoir drawdown was only observed once the breach discharge capacity exceeded the fixed inflow rate.

While breach outflow hydrographs in tests *fS_H_6,* and *fS_H_8* follow each other closely, *fS_H_7* conducted with a higher reservoir head closely follows *fS_Q_4* (in the beginning of the process i.e. Figure 5.12c). Interestingly, this shows that the hydraulic loading conditions govern the process rate and failure time in sand embankments. In fact, a faster and higher inflow and reservoir head results in a shorter breach formation duration and earlier widening phase.

It is only when approaching the peak discharge that the hydrographs detach from each other. The breach peak discharge is indeed governed by the maximum inflow rate, thus the higher inflow in *fS_H_7* test towards the end of the test results in higher breach outflow discharge. Whenever the pumps stop working, it is the reservoir emptying that governs the breaching process and therefore the breach outflow. These differences in hydraulic head maintenance significantly influence the "power" available for erosion throughout the test duration.

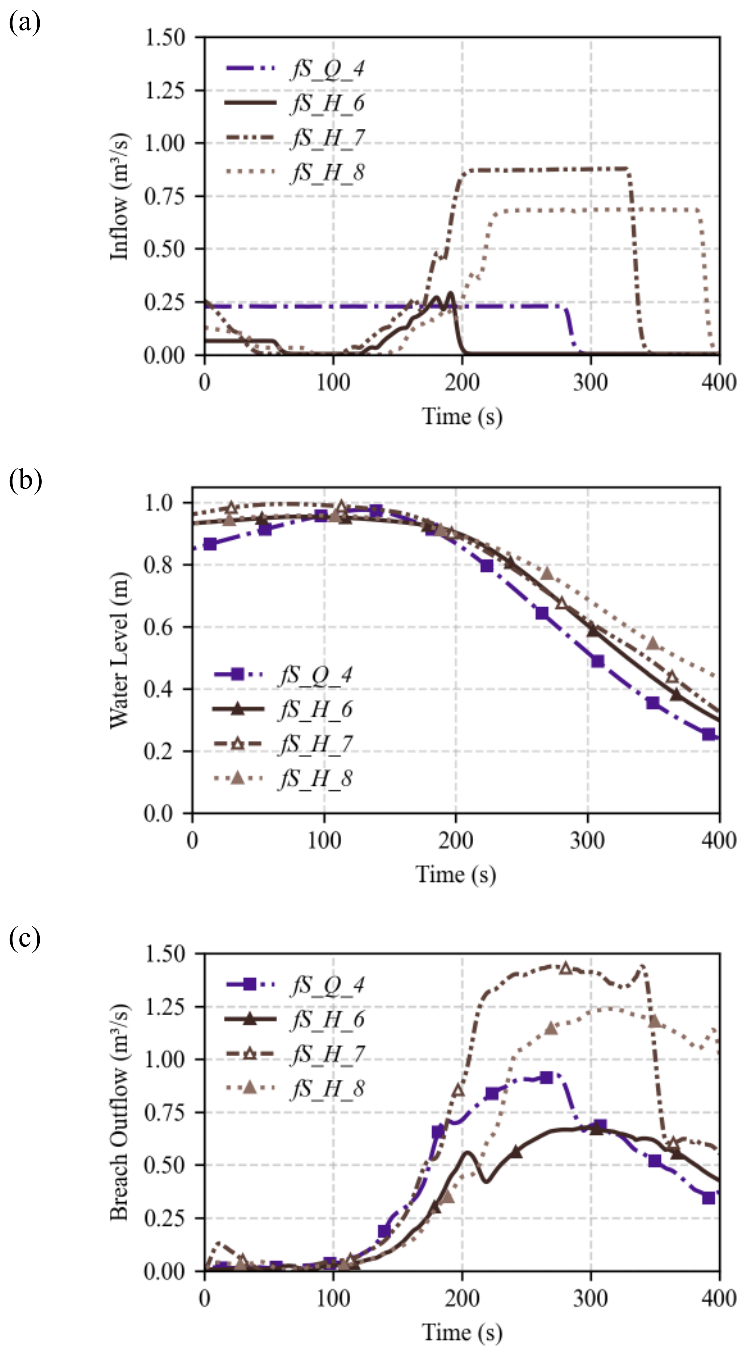

Figure 5.12 Flow characteristics including (a) reservoir inflow hydrographs, (b) water level evolution, and (c) breach outflow hydrographs in experiments *fS_Q_4* and *fS_H_6*, *7* and *8*.

It is observed that the calculated breach hydrograph exhibits a sharp decline coinciding with the cessation of the pump inflow. While this appears as a sudden drop in the mass balance result, it represents a combination of the physical reduction in hydraulic forcing and a mathematical sensitivity to the instantaneous change in the Q_{in} term in Eq. (4-1) the mass conservation equation. In reality, the breach outflow follows a smoother depletion curve as the remaining reservoir volume continues to exit through the evolving breach geometry.

5.7.3 Macro-scale erosion and morphological processes

The breaching of non-cohesive sand dikes is driven by a succession of macro-scale erosion processes that dictate the morphological evolution from initial overtopping to final breach stabilization. While typically characterized by continuous granular detachment, the process exhibits a rapid transition from surface erosion leading to hydrodynamic gully incision to gravity-driven mass failures. These major morphological processes, observed in the new medium scale experiments, are illustrated in Figure 5.13 and can be described as follows:

Surface Erosion and Gully Incision (Figure 5.13a): The process initiates with surface erosion on the downstream slope, driven by tangential shear stress (τ_0) exerted by the overtopping flow. Once τ_0 exceeds critical shear stress (τ_c) of the sand, particles are removed layer-by-layer. This erosion progresses in a vertical direction, "digging" a gully channel through the downstream face of the embankment.

Formation of a Receding Front (Figure 5.13b): As the channel deepens, the vertical erosion develops into a steep, rapidly receding front or cascade. This represents a form of longitudinal recession where the high energy of the water falling over the crest accelerates the headward migration of the erosion zone toward the upstream reservoir. During this stage, sediment deposition at the toe of the dike occurs in the form of an alluvial fan. This fan continues to grow as the gully incision deepens, temporarily stabilizing the toe until the increasing stream power during the subsequent development stages (Figure 5.13c and Figure 5.13d) eventually washes the deposit away.

Mass Loss via Granular Slumping (Figure 5.13c): Once the flow becomes sufficiently strong due to a deeper wetted breach cross-section, mass loss mechanisms become dominant. These failures primarily occur as granular slumping along the downstream slopes. These losses are driven by gravity following the erosion of the "toe" of the slope. As the bank height exceeds the material's stable angle of repose, the sand mass loses structural integrity and collapses into the breach channel.

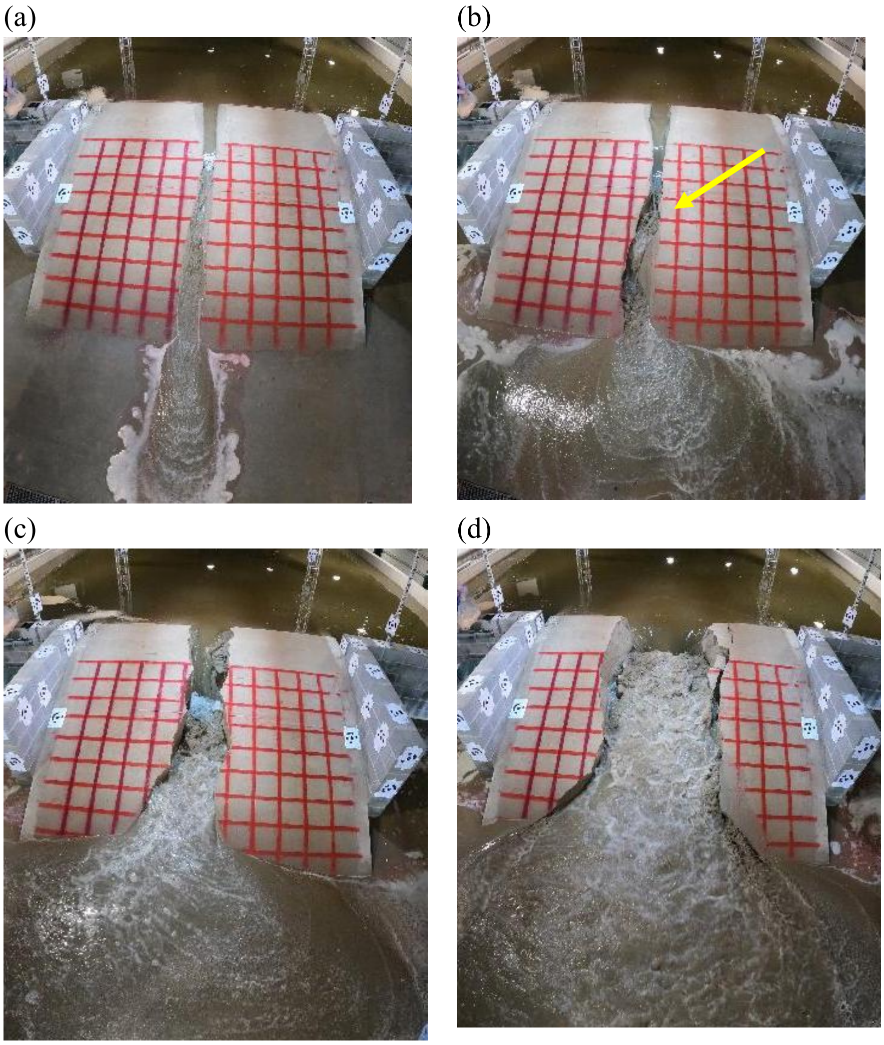

Figure 5.13 Principal macro-scale erosion and morphological processes during the breaching of fine sand embankments based on the new medium-scale tests (*Q*-type tests): (a) Initial surface erosion and gully incision on the downstream slope; (b) formation of a receding headcut/cascade and vertical deepening; (c) initiation of granular slumping and mass loss due to oversteepened slopes; and (d) rapid lateral widening driven by flow contraction and bank instability.

Lateral Widening and Mass block failure (Figure 5.13d): The final stage is characterized by rapid lateral expansion. Strong flow contractions at the breach entrance result in significant shear stresses along the breach flanks. This causes continuous bank instability, often manifested as shear planes or tension cracks in the moist sand, followed immediately by slumping. The collapsed material is then transported downstream as loose sediment, further facilitating the widening of the breach until the reservoir is empty.

Synthesizing the observed macro-scale erosion mechanisms with the resulting outflow hydrographs, the breaching process is divided into two distinct stages: (i) **breach formation,** dominated by vertical incision and low discharge and (ii) **the breach widening** (or '**expansion**') characterized by rapid lateral expansion and the exponential rise of the outflow hydrograph.

Breach formation stage: In the constant reservoir level (*H*) experiments, the maintenance of a steady hydraulic head resulted in a prolonged breach formation phase. During this interval, hydraulic energy was primarily dissipated through vertical incision of the pilot channel rather than lateral expansion. This behavior, governed by apparent cohesion which sustained near-vertical breach banks, delayed the upstream migration of the headcut compared to the constant inflow (*Q*) tests. These are depicted in detail in Figure 5.14(a-p) for experiments *fS_Q_5*, *fS_H_6*–8.

Breach widening stage: The temporal evolution of embankment during the breach widening stage is illustrated in Figure 5.15(a-p) for *fS_Q_5*, *fS_H_6*– 8 experiments Once the vertical incision reached the non-erodible foundation, the erosion mechanism transitioned to rapid lateral expansion driven by increasing outflow velocities. This process shaped the breach into a characteristic hourglass planform, a morphological feature that was notably more pronounced under the sustained hydraulic head of the constant reservoir level tests (*fS_H_6* and *fS_H_7*).

fS_Q_5 (a) t = 0 (s) | *fS_H_6* (b) | *fS_H_7** (c) | *fS_H_8* (d)

(e) t = 20 s | (f) | (g) | (h)

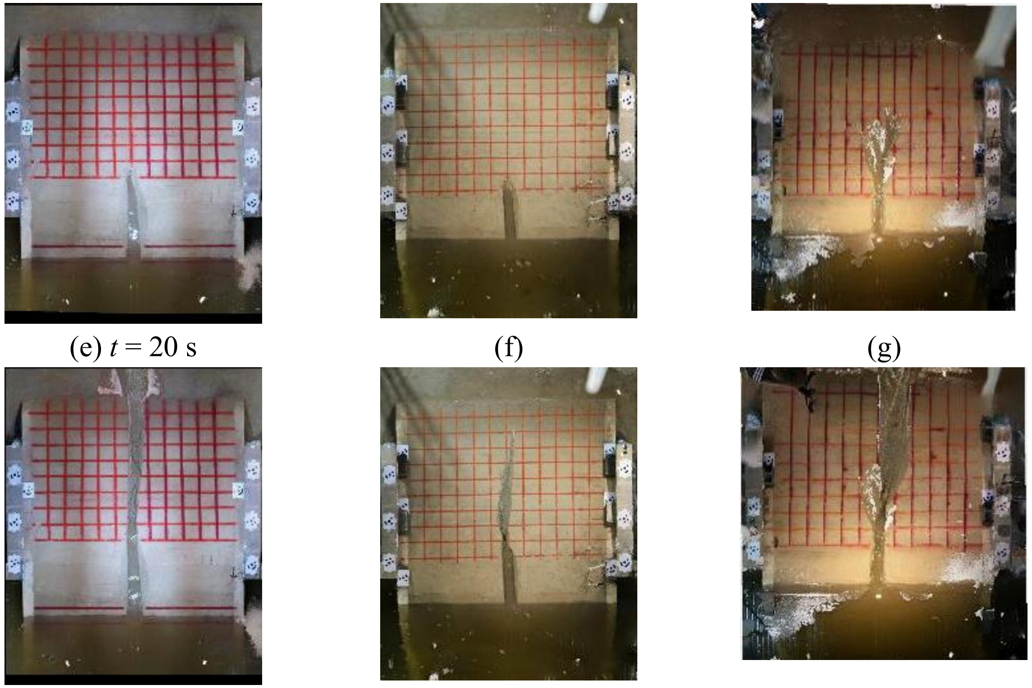

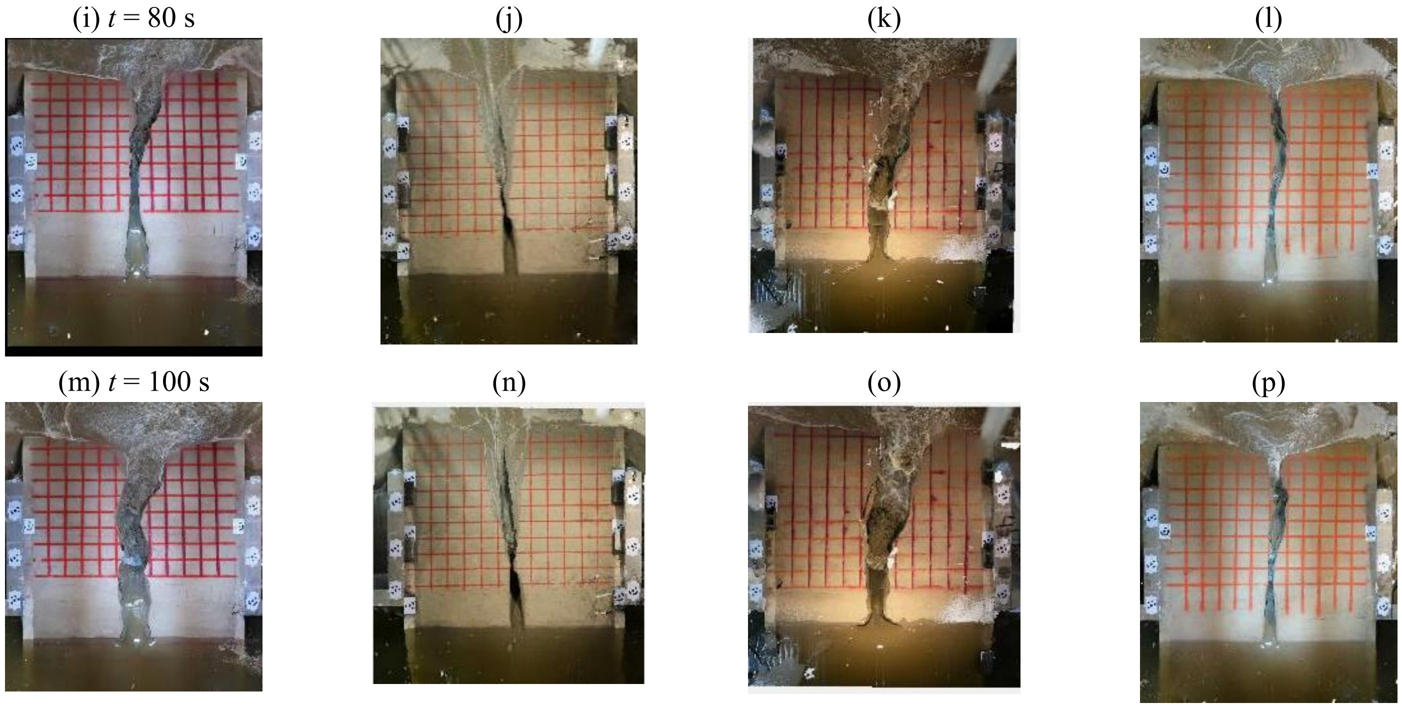

Figure 5.14 Parallel comparison of breach initiation and formation phases for fine sand tests under constant inflow (*fS_Q_5*) (a, e, i, m) and constant reservoir level *fS_H_6* (b, f, j, n), *fS_H_7*(c, g, k, o), *and fS_H_8*(d, h, l, p). The chronological sequence (t = 0, 20, 80, 100 s) illustrates the morphological transition from initial overtopping to upstream headcut migration and the development of the characteristic hourglass planform at the breach entrance. For *fS_H_7*[*], the regulation system was adjusted to trigger overtopping. Panel (c) corresponds to the equivalent reference time (t = 0 s) used in the other experiments.

fS_Q_5	*fS_H_6*	*fS_H_7*	*fS_H_8*
(a) t = 160 s	(b)	(c)	(d)

(e) t = 180 s	(f)	(g)	(h)

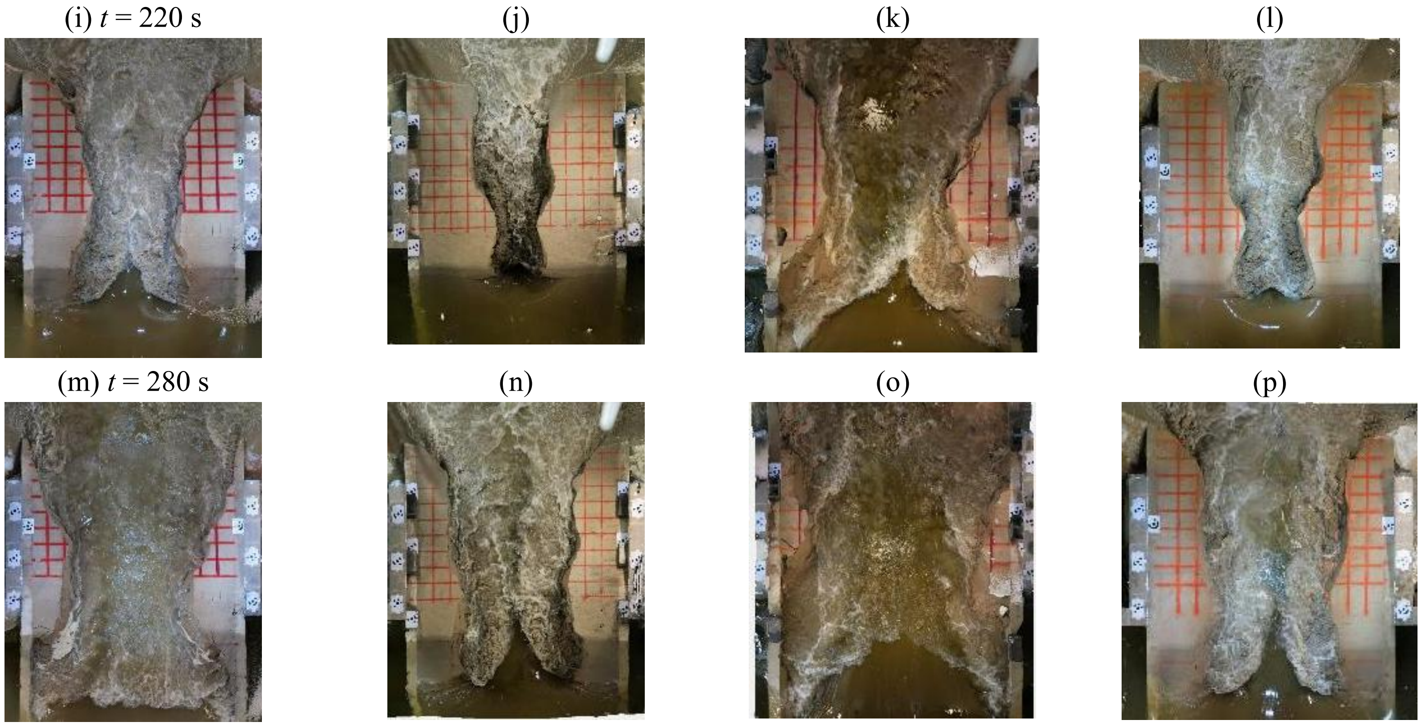

Figure 5.15 Parallel comparison of breach widening and reservoir drawdown phase for fine sand tests under constant inflow (*fS_Q_5*) (a, e, i, m) and constant reservoir level *fS_H_6* (b, f, j, n), *fS_H_7*(c, g, k, o), and *fS_H_8*(d, h, l, p). The chronological sequence (t = 0, 20, 80, 100 s) illustrates the morphological transition from vertical erosion to lateral expansion and full development and stabilization of hourglass planform at the breach entrance

5.7.4 Temporal deepening and widening

The temporal evolution of the breach dimensions was quantified using Digital Elevation Models (DEMs) acquired by photogrammetry and the release timing of the embedded ball tracers. Figure 5.16 illustrates the breach width evolution at three reference cross-sections along the channel axis ($x = -0.25$, +0.25, and +0.75 m).

The widening curves for the constant reservoir level tests *fS_H_6* and *fS_H_8* show remarkable agreement across all three locations (see Figure 5.16a-c), highlighting the high degree of experimental repeatability. These results confirm that under a sustained hydraulic head (H), the process is initially dominated by vertical incision, allowing for a fully developed breach formation phase. At the upstream section ($x = -0.25$ m), lateral widening remains negligible during this initial stage before transitioning into rapid lateral expansion. The consistency in transition timing and widening magnitude between these two runs suggests that the initial state of the dike—specifically density and moisture-induced apparent cohesion—was uniformly replicated.

In contrast, tests *fS_Q_5* and *fS_H_7* exhibited a significantly shortened breach formation phase. In *fS_H_7*, the rapid increase of inflow (reaching the system capacity of 1 $m^3 s^{-1}$) accelerated the transition to lateral widening, resulting in the complete washout of the embankment. The width evolution graphs clearly demonstrate the two distinct phases—formation and widening—separated by a sharp inflection point where the widening rate increases abruptly. This transition initiates at the downstream slope once the headcut retreats to the crest.

Following the rapid expansion, the process becomes governed by reservoir drawdown, leading to a stabilization phase towards the end of all experiments. The maximum breach outflow occurs immediately prior to this stabilization, where the combination of breach width and hydraulic head at the control section is maximized (corresponding to the morphologies in Figure 5.13d and Figure 5.15i).

This spatial and temporal consistency confirms that the breach growth mechanisms are deterministic outcomes of the applied boundary conditions and material properties.

(a)

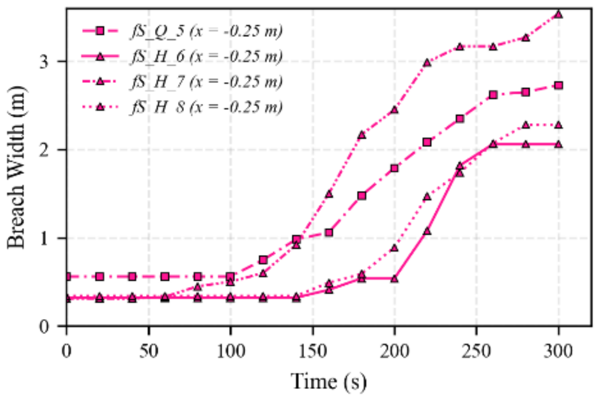

(b)

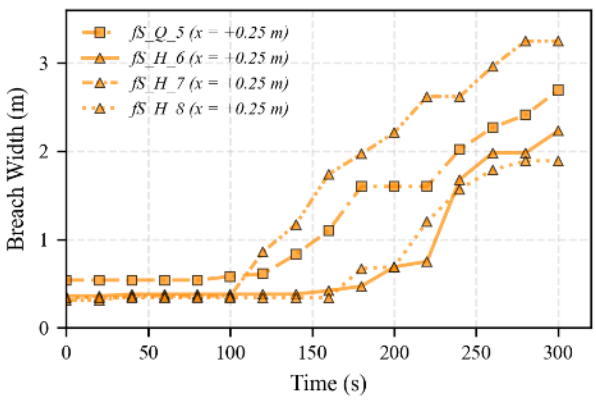

(c)

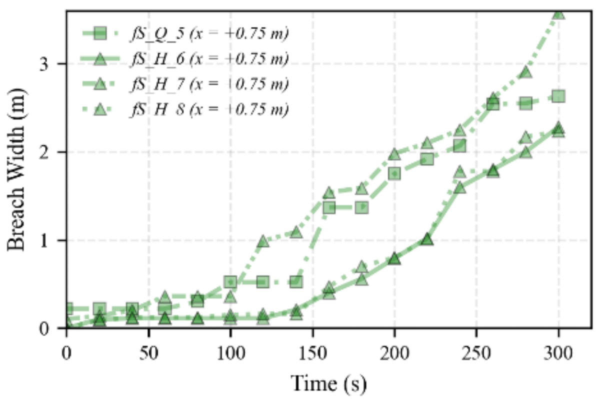

Figure 5.16 Temporal evolution of breach width at (a) $x = -0.25$, (b) $x = +0.25$, and (c) $x = +0.75$ m in tests *fS_Q_5* and *fS_H_6–8*.

The temporal evolution of the breach bed (invert) elevation at the upstream reference section (x=−0.25 m) was monitored via embedded tracers to quantify vertical erosion rates under the two overtopping regimes (*fS_Q_5* and *fS_H_6*). In both experiments, vertical incision accelerated significantly upon the transition to the breach widening phase. Notably, test *fS_Q_5* exhibited a more rapid deepening, characterized by a sharp gradient change followed by a linear erosion trend. This accelerated incision is attributed to discrete mass block failures along the embankment crest, which rapidly destabilized the hydraulic control section and intensified the local stream power acting on the upstream slope.

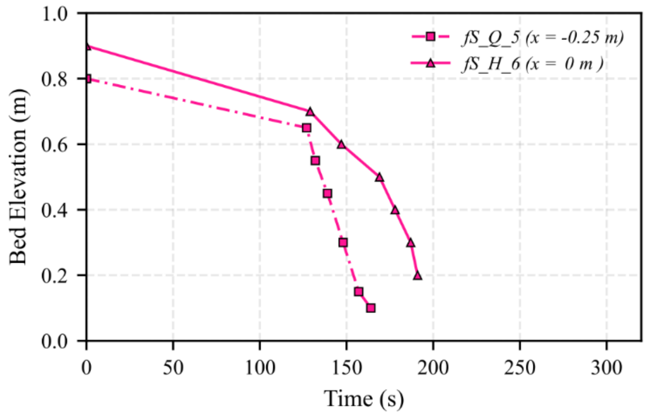

Figure 5.17 Temporal evolution of the breach invert elevation at upstream reference section (x = − 0.25) for fine sand under constant inflow (*fS_Q_5*) and at the middle of crest (x = 0) for constant reservoir level (*fS_H_6)* conditions (balls were only available at this location in this test).

Comparing the breach bed elevation at x = + 0.25 m (orange ball) in *fS_Q_5* and *fS_H_7* (Figure 5.18) implies that apart from an initial time delay the vertical deepening pattern is very close. While the constant reservoir level conditions in *fS_H_7* triggered an earlier onset of erosion at this location compared to the constant inflow test, the vertical incision gradients during the rapid deepening phase are remarkably similar. This observation supports previous discussions across these two experiments.

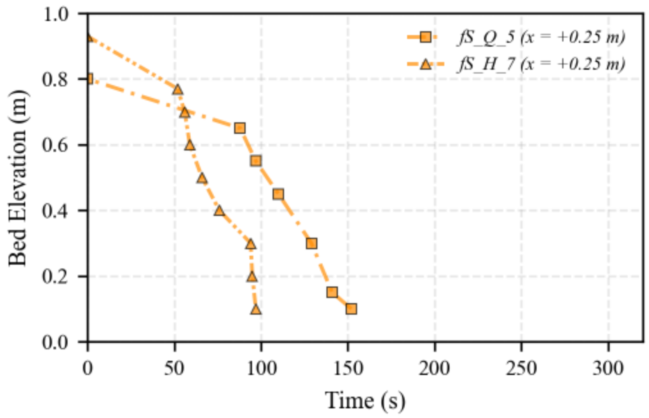

Figure 5.18 Temporal evolution of the breach invert elevation at downstream reference section (x = + 0.25) for fine sand tests under constant inflow (*fS_Q_5*) and constant reservoir level (*fS_H_7*) conditions.

The steep gradient of vertical erosion reflects how well-compacted soil is sheared off in large layers as the accelerating flow enlarges the breach. As introduced in Chapter 4, this phenomenon is driven by the dilatancy effect in dense sands (Bisschop et al. 2016). At high flow velocities, particularly those exceeding 4 m/s, the bulk properties of the sand bed, such as porosity, dictate the erosion process. This dilative behavior fundamentally alters the erosion mechanics, explaining why conventional empirical formulas based solely on grain-by-grain bedload transport cannot accurately predict erosion rates under such extreme conditions.

5.7.5 Conclusion on the influence of overtopping conditions

The comparative analysis of the *fS_H* and *fS_Q* series demonstrates that while the hydraulic boundary condition drives the rate of energy expenditure, the fundamental erosion pattern is intrinsically governed by the material properties. Despite the variations in hydraulic load, the fine sand embankments consistently exhibited a similar morphological sequence i.e. vertical incision followed by lateral widening via mass block failures, dictated by the sediment's apparent cohesion.

The experimental results indicate that the overtopping condition primarily drive the kinematics of the failure rather than the mechanism. Higher inflow rates or sustained hydraulic heads accelerated the breach formation phase, leading to an earlier onset of lateral expansion. However, once the widening phase was triggered, the erosion dynamics proceeded in a nearly identical manner across all tests. Consequently, the specific overtopping condition can be seen as a temporal adjustment factor, inducing a time-lag that influences the breach hydrograph timing and the final breach dimensions, while the failure mode remains a characteristic of the soil nature.

5.8 Influence of Sand Size: Fine vs. Medium Sand

This section analyses the influence of sediment granulometry on the breaching process by comparing the medium sand series (tests *mS_Q_1–3*) with the fine sand series (tests *fS_Q_4, 5*), both conducted under identical constant inflow conditions (Q_{in} =0.224 m³ s⁻¹) as shown in Figure 5.19a. The experimental results demonstrate that the two type of sediments do not erode in the same manner, leading to distinct temporal patterns in breach deepening and widening.

While the medium sand generally exhibited progressive surface erosion, the macro-scale mechanisms in the fine sand were fundamentally governed by apparent cohesion (matric suction) within the unsaturated embankment body. As observed in the *fS* series, negative pore pressures stabilized steeper breach banks, delaying failure until critical undercutting triggered discrete mass block collapses. These variations in soil resistance and failure modes significantly affected the overall morphological evolution and the resulting breach outflow hydrographs.

5.8.1 Reservoir dynamics and discharge hydrographs

The comparative evolution of the reservoir water level for fine and medium sand tests is presented in Figure 5.19b. While both series exhibit an initial rise driven by the constant inflow, distinct temporal behaviors are evident in the approach to hydraulic equilibrium. The fine sand series (*fS_Q_4, 5*) reaches a slightly higher peak elevation (approximately 0.98 m) and initiates the drawdown phase approximately 20 seconds earlier than the medium sand series (*mS_Q_1–3*). Following this peak, the drawdown gradient for the fine sand is notably steeper, indicating a rapid, catastrophic enlargement of the breach cross-section. In contrast, the medium sand exhibits a more gradual, progressive decline, reflecting a slower rate of breach widening and a prolonged reservoir emptying process.

The breach outflow hydrographs for the fine and medium sand series are compared in Figure 5.19c. Consistent with the reservoir level observations, the discharge profiles reveal a fundamental disparity in the hydraulic response of the two materials. The fine sand (*fS*) embankments produced significantly higher peak discharges ($Q_{peak} = 0.920$ m³ s⁻¹) compared to the medium sand (*mS*) ($Q_{peak} = 0.720$ m³ s⁻¹), despite identical hydraulic loading conditions. This demonstrates that decreasing the sediment median size by 50% increased the breach outflow by approximately 28%.

Morphologically, this difference is attributed to the erosion kinetics. The medium sand hydrographs exhibit a broader, flatter peak, indicative of a progressive, surface-erosion-dominated widening process. in contrast, the fine sand hydrographs display a delayed but notably steeper rising limb, culminating in a sharp peak.

(a)

(b)

(c)

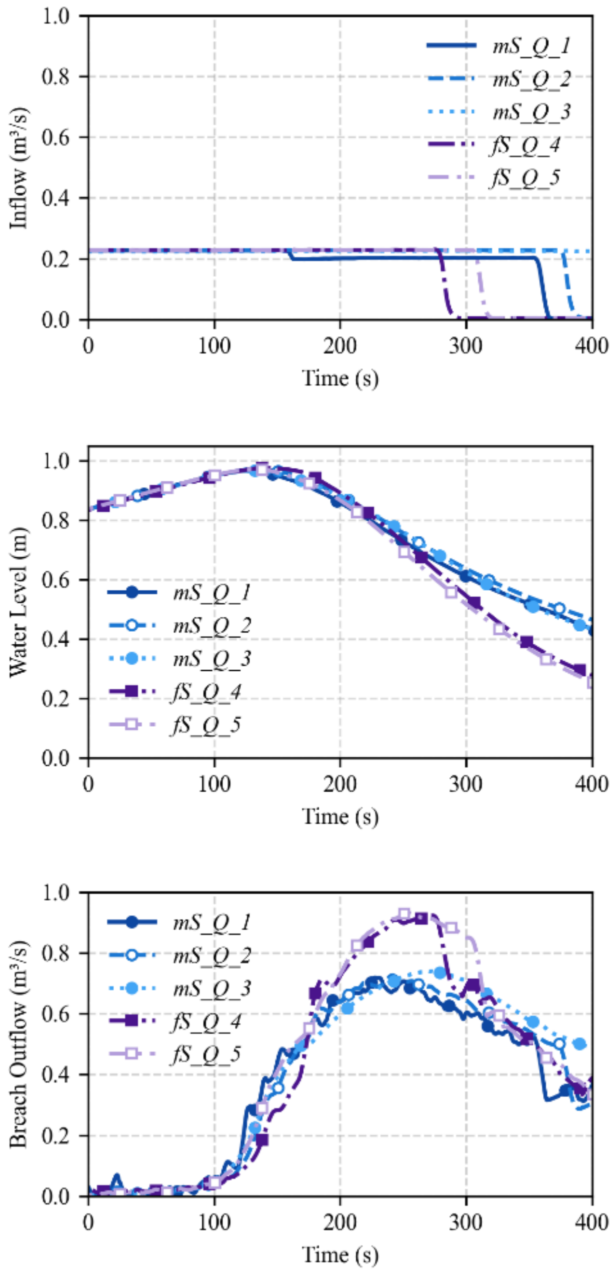

Figure 5.19 Flow characteristics including (a) reservoir inflow hydrographs, (b) water level evolution, and (c) breach outflow hydrographs in experiments *mS_Q_1–3* and *fS_Q_4, 5*.

5.8.2 Morphological evolution and macro-scale erosion

The chronological evolution of the breach morphology, reconstructed from the SfM-photogrammetry models (Figure 5.20a-h and Figure 5.21a-h), confirms that sediment granulometry fundamentally alters the geometry during the breach formation phase (t= 0 to 100 s, in Figure 5.20a-h). In the fine sand (*fS*) embankments, the vertical incision of the pilot channel proceeds through the upstream migration of discrete, localized headcuts. This mechanism generates a characteristic "stair-step" or cascade longitudinal profile, sustained by the material's apparent cohesion which supports transient vertical faces. In contrast, the medium sand (*mS*) exhibits a progressive, uniform erosion of the channel invert, developing a smoother longitudinal slope lacking the distinct discontinuities observed in the fine sand.

Following the incision to the non-erodible foundation (t=160 s, in Figure 5.21a-b), both materials transition into the breach widening phase, yet the mechanisms of bank retreat remain distinct. The fine sand maintains nearly vertical side walls, widening primarily through the undercutting and subsequent toppling of cohesive blocks. The medium sand banks, lacking significant matric suction, retreat through granular sliding, resulting in flatter bank angles. Despite these differences, both morphologies converge towards a hourglass planform (t=220 s, in Figure 5.21e,f), with a more symmetrical form at the upstream and downstream sides in medium sand.

Finally, the flow decelerates into a stable equilibrium state as the reservoir head diminishes (t = 280 s, in Figure 5.21g,h).

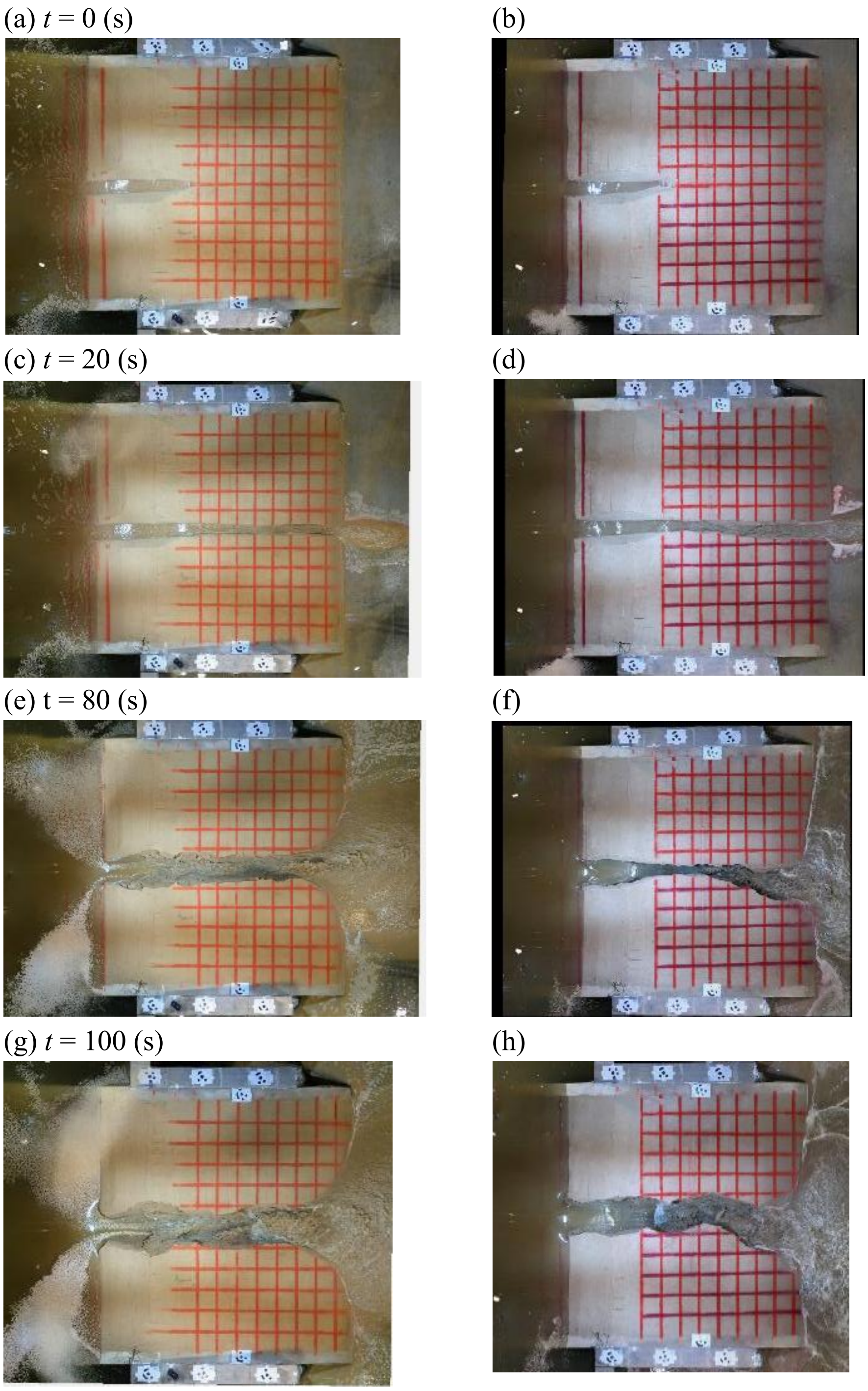

Figure 5.20 Comparison of breach formation in medium (*mS_Q_1:* a,c,e,g) and fine (*fS_Q_4* :b,d,f,h) sand embankments under constant reservoir inflow.

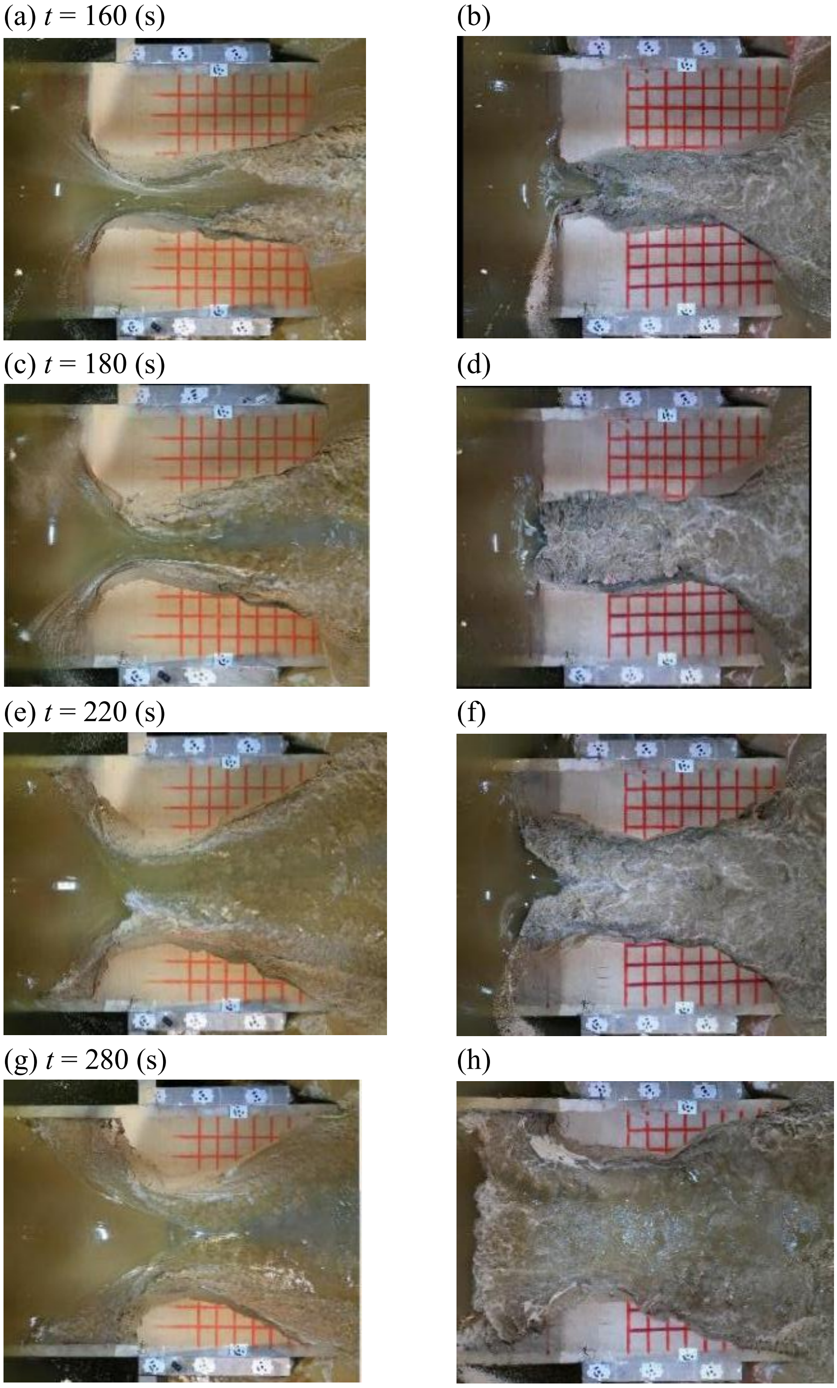

Figure 5.21 Comparison of breach widening and reservoir drawdown phase in medium (*mS_Q_1:* a,c,e,g) and fine (*fS_Q_4* :b,d,f,h) sand under constant reservoir inflow.

synthesizes the distinct macro-scale erosion mechanisms observed for the two sediment types, highlighting the effects of apparent cohesion on the breach morphology and failure kinetics. These are furthermore illustrated in Figure 5.22 and Figure 5.23. The table comprises those observations detailed earlier in section 5.7 Influence of Overtopping Conditions.

Table 5.4 synthesizes the distinct macro-scale erosion mechanisms observed for the two sediment types, highlighting the effects of apparent cohesion on the breach morphology and failure kinetics. These are furthermore illustrated in Figure 5.22 and Figure 5.23. The table comprises those observations detailed earlier in section 5.7 Influence of Overtopping Conditions.

Table 5.4 Dominant morphological changes and macro-scale erosion processes in fine and medium sand embankments at medium scale.

Phase	Feature / Mechanism	Fine Sand (*fS*)	Medium Sand (*mS*)
Breach formation	Gully Incision	Deep Vertical Incision: Flow concentrates on the bed, digging a deep, narrow channel while banks remain stable.	Lateral Surface Erosion: Reduced vertical incision ("digs less") as immediate granular sliding causes the flow to erode laterally, creating a shallower, wider gully.
	Longitudinal Profile	Steep, "stair-step" or cascade longitudinal profile	Gentle, progressive erosion of the channel invert with a uniform slope.
	Erosion Pattern	Formation of a distinct receding front (headcut migration).	A pivot point can in general be identified at the downstream end of the slope, around with the slope «rotates» and decreases almost uniformly; uniform lateral expansion of the gully along the slope.
	Symmetry	Tendency toward non-symmetrical, localized incision.	Generally symmetrical evolution of the pilot channel.
	Side Walls	Vertical breach sides and high failure angles	Near-vertical side slope

	Tailwater / Deposition	High sediment entrainment capacity prevents significant deposition; negligible tailwater effect.	Lower sediment transport capacity leads to alluvial fan formation at the toe, creating a temporary tailwater effect.
Breach Widening	Failure Mechanism	Discrete Block Failure: Cohesive blocks (10–20 cm wide) tilt and topple into the flow while retaining shape.	Granular Sliding: Undermining leads to shear failure and sliding of smaller soil masses (5–10 cm wide).
	Erosion behavior	Vertical erosion is governed by flow shearing thick layers	More progressive vertical erosion
	Bank Geometry	Banks remain vertical or overhanging for prolonged periods due to matric suction.	Banks rapidly adjust to flatter slopes closer to the angle of repose.
	Hydraulic Control	Strong impinging jet formation at the control section (headcut).	Gradually varied flow conditions at the control section.

These behaviors are also reflected in the breach outflow hydrograph, where the occurrence of discrete, rapid, large mass block failures in the fine sand abruptly enlarges the breach cross-section and releases a larger surge of water compared to the medium sand.

5.8.3 Surface erosion and mass block failure

As observed in the present experiments, the process involves episodic mass block failure alongside continuous sediment transport (see Figure 5.22, and Figure 5.23). Mass blocks continuously nourish the flow through local or elongated slumping, generating local turbulence and modifying the bed level. Consequently, the flow dissipates energy through the work required to erode and transport these episodic failures. These mass block collapses may occur both locally and globally along the banks; therefore, the collapsed material can be distributed either locally or uniformly across the breach channel width, depending on the scale of the failure event.

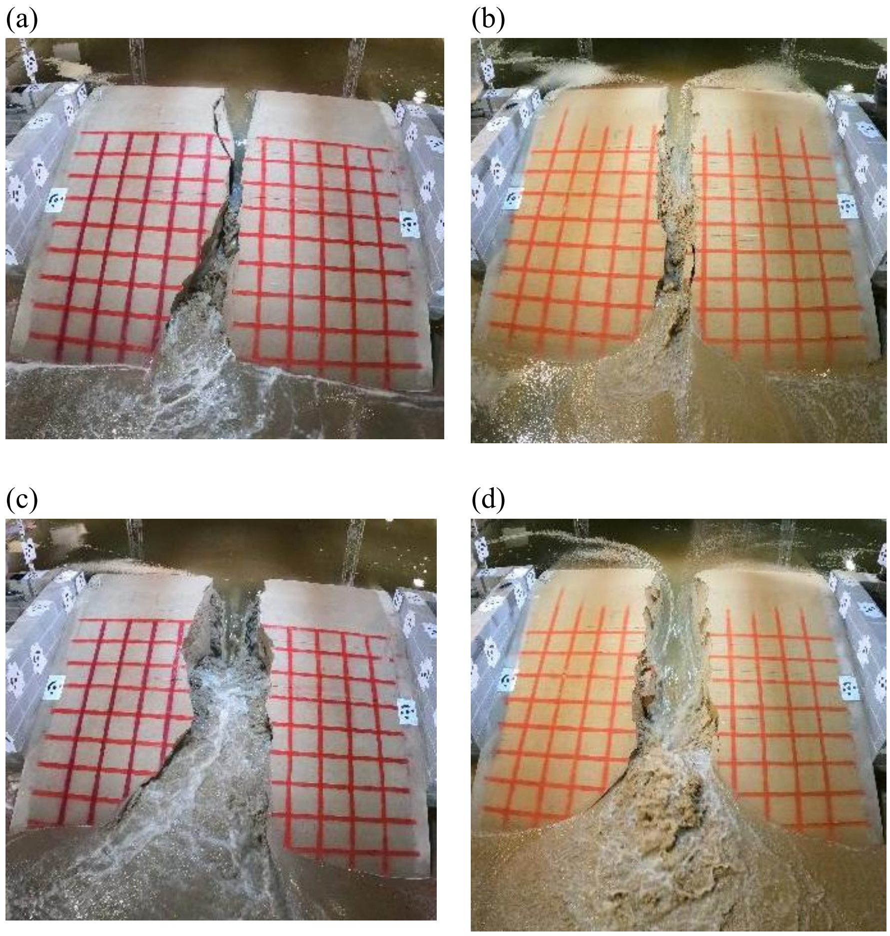

Figure 5.22 Comparison of gully incision, erosion pattern, deposition and tailwater and overall breach channel state for fine (a,c) and medium (b,d) sand embankments.

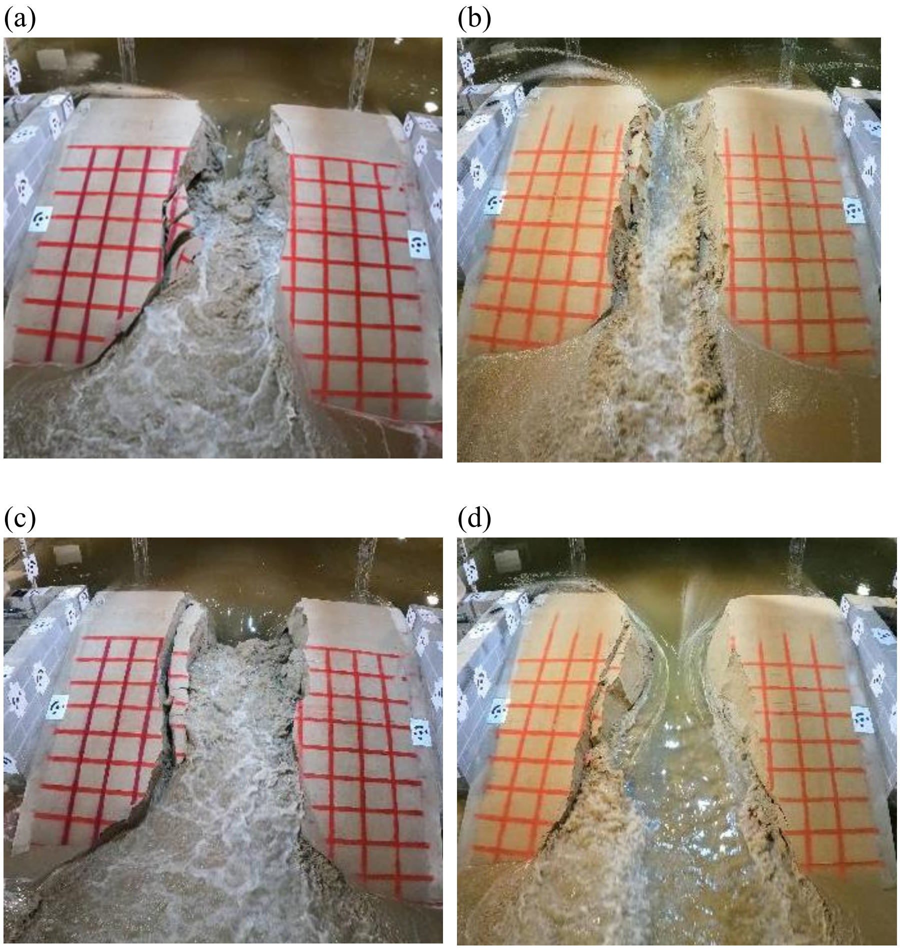

Figure 5.23 Discrete block or cohesive blocks failure in fine sand embankment (a,c) and granular sliding in medium sand embankment (b,d).

5.8.4 Temporal deepening and widening

Temporal evolution of breach cross-sections and longitudinal profiles obtained from the photogrammetry are illustrated in Figure 5.24, Figure 5.25, Figure 5.26, Figure 5.27a-b at three reference locations i.e. $x = -0.25$, +0.25, and +0.75 m and along the breach axis $y = 0$ m and for tests *mS_Q_1* and *fS_Q_5*. It must be recalled that these profiles are extracted from the phogrammetry measurements, hence the longitudinal profiles show the free-surface profile rather than the bed profile. However, considering that the flow is most of the time close to a supercritical uniform flow, the free-surface slope is a good approximation of the bed profile. Exceptions arise when a hydraulic jump forms on the downstream slope, as can be clearly identified in at Figure 5.27 at t = 120 s.

(a) (b)

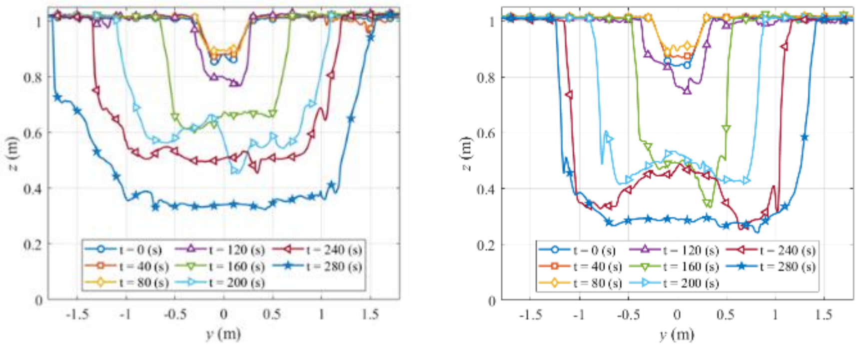

Figure 5.24 Breached dike (above water) cross-section evolution over time at $x = -\,0.25$ m (a) *mS_Q_1* and (b) *fS_Q_5*.

(a) (b)

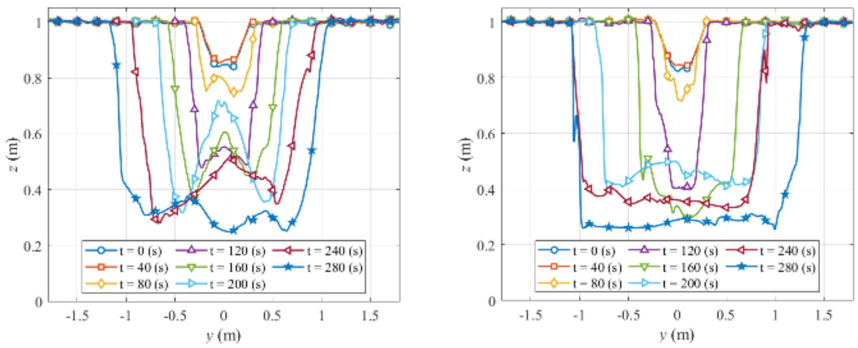

Figure 5.25 Breached dike (above water) cross-section evolution over time at $x = +\,0.25$ m (a) *mS_Q_1* and (b) *fS_Q_5*.

(a) (b)

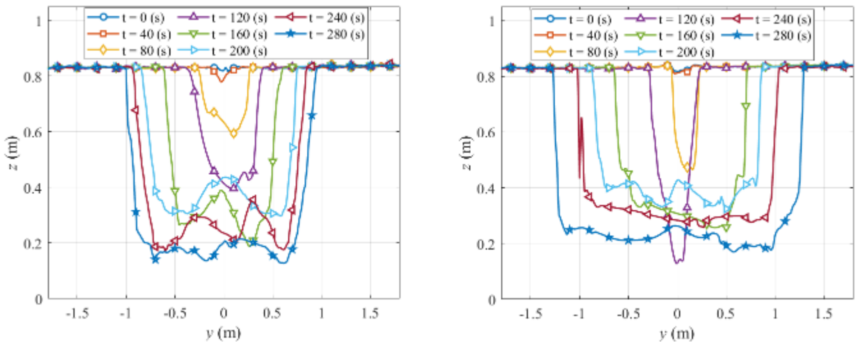

Figure 5.26 Breached dike (above water) cross-section evolution over time at x = + 0.75 m (a) *mS_Q_1* and (b) *fS_Q_5*.

(a)

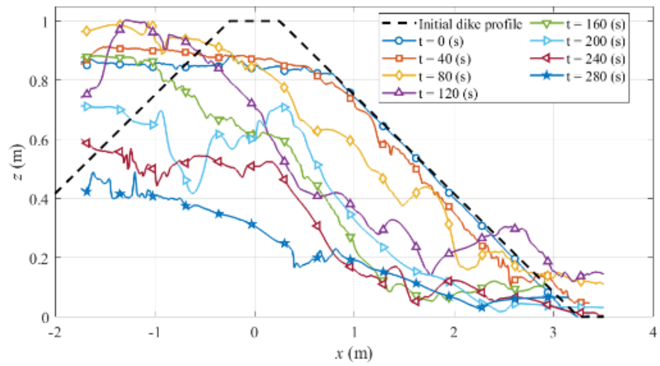

(b)

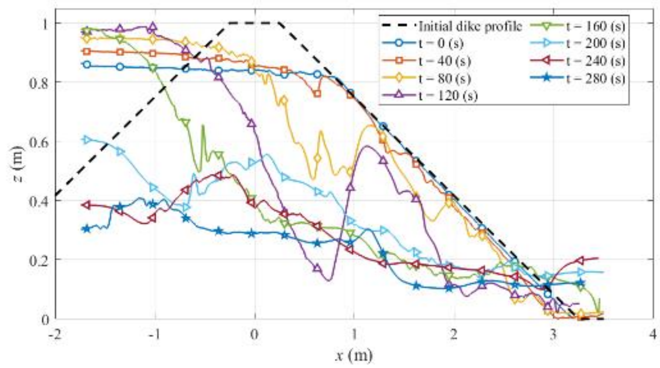

Figure 5.27 Longitudinal evolution of the flow profile through the breached dike at y = 0 m in case of (a) *mS_Q_1* and (b) *fS_Q_5*.

Figure 5.28(a,b) illustrates the temporal evolution of the breach width at these three locations for tests *mS_Q_1* and *fS_Q_5*, highlighting the spatial variability of the channel geometry for each sediment type.

(a)

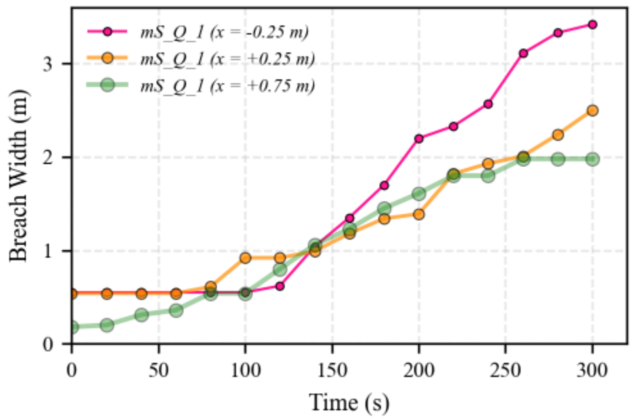

(b)

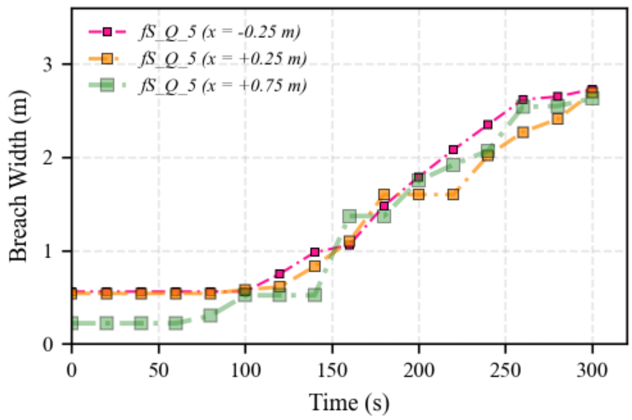

Figure 5.28 Temporal evolution of breach width at the dike crest level (z = 1 m) in tests: (a) *mS_Q_1*, and (b) *fS_Q_5* at $x = -$ 0.25, +0.25, and +0.75 m.

The fine sand (*fS_Q_5*) exhibits overall a remarkable longitudinal uniformity, with the widening curves remaining tightly grouped across all three locations. This suggests a relatively prismatic channel shape maintained by the vertical, cohesive-like banks. In contrast, the medium sand (*mS_Q_1*) displays strong longitudinal variability; the breach width at the upstream section ($x = -0.25$ m) expands significantly faster than at the downstream sections, resulting in a pronounced, progressive hourglass planform.

A direct comparison of the two experiments reveals distinct spatial trends. At the upstream entrance ($x = -0.25$ m), the breach width in the medium sand significantly exceeds that of the fine sand. However, in the downstream reaches ($x = +0.25$ and $+0.75$ m), the widening magnitudes for both materials remain comparable, alternating in dominance throughout the widening phase.

(a)

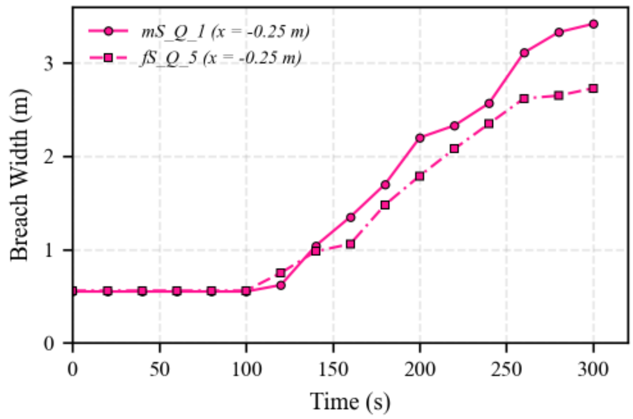

(b)

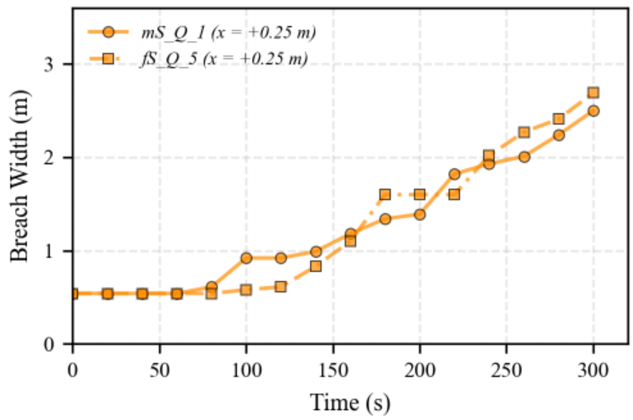

(c)

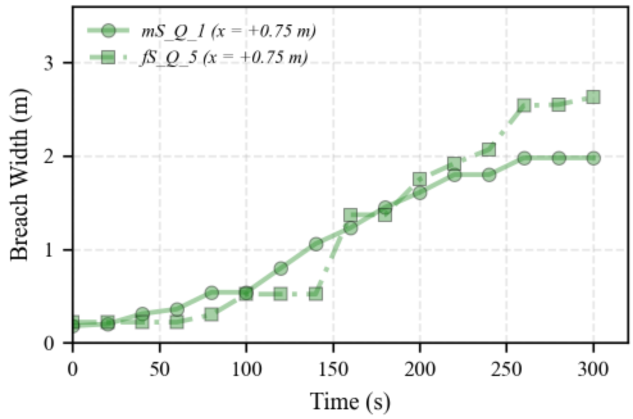

Figure 5.29 Comparative temporal evolution of the breach width at (a) $x = -0.25$, (b) $x = +0.25$, and (c) $x = +0.75$ m in *S_Q_1* and *fS_Q_5* tests.

Correspondingly, the temporal evolution of the breach invert elevation at the three reference sections, derived from the embedded tracers, is presented in Figure 5.30a-c. In the fine sand test (*fS_Q_5*), erosion initiated at the downstream slope, causing the tracers at $x = +0.75$ m (green balls) to release earliest, exhibiting a smooth, curvilinear deepening profile. In contrast, the upstream section ($x = -0.25$ m, pink balls) showed a distinct time lag corresponding to the upstream migration of the headcut; however, once erosion initiated at this location, the bed elevation experienced a significantly faster rate of deepening for fine sand.

Comparing the two materials, the medium sand experienced a progressive and comparatively slower vertical erosion across all locations, maintaining a gentler longitudinal gradient along the channel axis. This contrasts with the fine sand, which displayed steep, abrupt changes in bed elevation driven by the rapid regression of discrete headcuts.

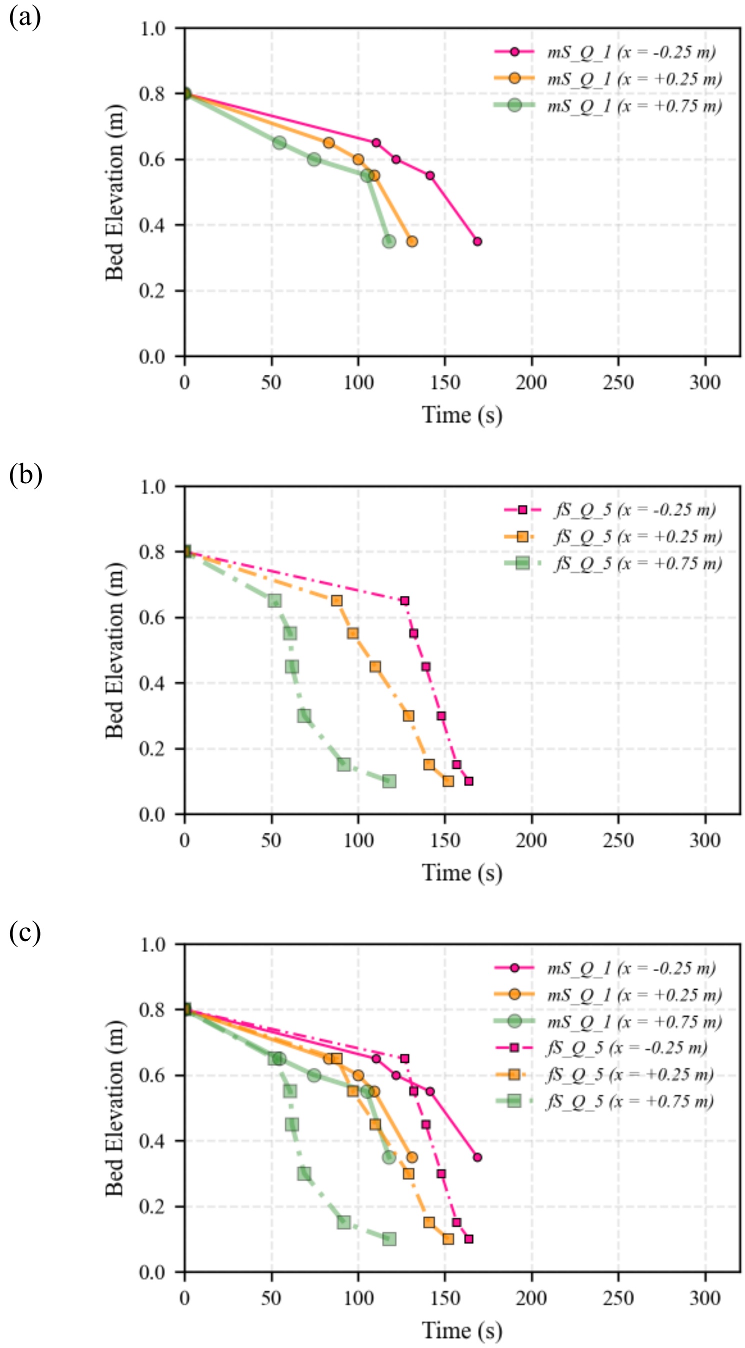

Figure 5.30 Temporal evolution of the breach invert elevation at $x = -0.25$, $+0.25$, and $+0.75$ m in (a) *mS_Q_1* and (b) *fS_Q_5*, and (c) comparative temporal evolution of breach invert elevation.

5.8.5 Flow characterization

Flow velocity and Froude Number values were determined at the instants when the pink balls ($x = -0.25$ m) were released for tests *mS_Q_1* and *fS_Q_5* as flow condition indicates at the upstream side of the dike (approximately right after flow control section discussed by Coleman et al. (2002) and Walder et al. (2015). The order of magnitude of Froude Number shows that the flow is fully supercritical at this location as indicated in Table 5.5.

Table 5.5 Flow characterization at pink ball releasing instants ($x = -0.25$ m) for tests *mS_Q_1* and *fS_Q_5*.

Experiment	Bed elevation (m)	Time (s)	Breach Outflow (m^3/s)	h_m (m)	V (m/s)	Fr
mS_Q_1	0.65	111	0.095	0.1	1.94	1.92
	0.60	120	0.140	0.1	1.71	1.73
	0.55	140	0.352	0.18	2.39	1.79
	0.35	167	0.477	0.18	2.13	1.60
fS_Q_5	0.65	127	0.17	0.09	3.39	3.67
	0.55	132	0.22	0.16	2.34	1.85
	0.45	139	0.30	0.22	1.78	1.21
	0.30	148	0.39	0.22	2.10	1.43
	0.15	157	0.463	0.29	1.85	1.09
	0.10	164	0.509	0.22	1.96	1.32

5.9 Generalization of reservoir storage and inflow conditions

Most parametric breach models derived from historical failure events such as those by Froehlich (1995), Walder and O'Connor (1997), Wahl (1998), Froehlich (2008), and those reported by ASCE/EWRI Task Committee on Dam/Levee Breaching (2011) include or reflect the influence of reservoir storage and overtopping conditions on peak breach outflow. These models rely heavily on the reservoir level and available volume of water stored above the breach invert level (Figure 1.10) at the time of failure. Specifically, Walder and O'Connor (1997) established a dimensionless correlation between reservoir size, water level drop, and breach erosion rate to categorize failure hydrographs. In addition to the present study, other studies such as Halso (2024) highlighted how constant-head (*H*) versus falling-head (*Q*) overtopping conditions alter the speed of breach evolution and peak outflow with a fixed reservoir geometry. His experimental results confirmed that the effect of reservoir head on breach peak outflow and the speed of breach evolution was notable. Consequently, to ensure the replication of a complete breach hydrograph without premature drawdown, many laboratory studies are conducted under constant reservoir levels.

However, reservoir head alone does not govern the peak outflow. The reservoir's dimensions, which determine the total available water volume released during the failure process, critically dictate the peak discharge. In particular, this is deterministic for smaller reservoirs where rapid drawdown occurs. To illustrate this, the results of the present study were combined with well-documented experimental data on sand embankments ranging from 0.3 m to 1.6 m in height (Coleman et al., 2002; Hassan et al[7]., 2004; Pickert et al., 2011; Walder et al., 2015; van den Berg et al[8]., 2025), as summarized in

Table 5.6. This extended comparison highlights the profound influence of reservoir dimensions on breaching dynamics, across varying overtopping conditions (see Figure 5.31). The experimental series were conducted under three distinct conditions: (i) constant reservoir level (*H*) representing an infinite reservoir volume, (ii) constant reservoir inflow (*Q*) resembling a basin of limited storage capacity recharging with a steady discharge and (iii) fixed (or finite) reservoir volume (corresponding to test case of Walder et al., 2015, and *fS_H_6* of present study where the peak outflow was governed by the reservoir volume without recharging). All datasets exhibited high repeatability; therefore, only one representative test per dataset has been selected for comparison. To quantify the influence of reservoir storage capacity (based on maximum achievable water level for a specific embankment) across these datasets, a parameter (β) is defined as the percentage ratio of embankment volume to reservoir storage. This factor provides a scale-independent metric to evaluate how reservoir dimensions influence peak breach outflow.

[7] Reported also in Morris et al. (2007)
[8] Experiments conducted before foreshore integration (R01, R02, R03)

Table 5.6 Experimental parameters and reservoir storage characteristics for sand embankment breaching studies.

Ref./Par.	Coleman et al. (2002)	Hassan et al. (2004)	Pickert et al. (2011)	Walder et al. (2015)	van den Berg et al. (2025)	Present study
Overto. Cond.	*H*	*Q*	*H*	Fixed-Res.	Fixed-Res., *Q*-adj towards end	*H, Q,* and Fixed-Res.
H_{Em} **(m)**	0.3	0.5	0.3	1	1.55	1
d_{50} **(mm)**	0.5; 0.9; 1.6; 2.4	0.25	0.185; 0.365; 0.64	0.21	0.243	0.31
Half or Full model	Half	Full	Half	Full	Full	Full
Up/Down slopes (H:V)	2.7:1	1.73:1	3:1	1.73:1	3:1; 2.5:1	3:1
Crest width (m)	1.685	2.2	1.9	3.5	8.7	6.5
Toe width (m)	0.065	0.2	0.1	0.36	0.175	0.5
Emb. Length (m)	2.4	4	1	2	2	3.6
Emb. volume (m³)	0.63	2.4	0.3	3.86	13.76	12.6

Length (m)	12	50	8.9	6.37	6	17.6
Width (m)	2.4	10	1	2	8.2	10.8
Height (m)	0.3	0.8	0.3	1	1.6	1
Storage volume (m³)	7.718	400	2.535	12.74	100	190.1
Max. Inflow discharge (m³/s)	NA	0.04	NA	0	0.145	0.112; 0.146; 0.437; 0.342
β (%)	8.2	0.6	11.8	30.3	13.8	6.63
Data usage remarks	Results of tests with d_{50} = 0.5, 0.9, 1.6 were used.	Result of Uniform fine sand with constant inflow was used.	Full dataset was used.	Results of "Test 5" was used.	Results of R01 (fixed reservoir volume) and R02 (inflow adjustment after 250 s) was used	Max. inflow respectively for *fS_Q_4*; *fS_H_6*, *fS_H_7*, *fS_H_8*

Crest width: width of embankment crest parallel to flow; Toe width: width of embankment at the toe parallel to flow; Emb. Length: embankment length perpendicular to flow; Reservoir Storage: maximum capacity of the reservoir for the corresponding embankment height; β: Ratio of Embankment volume to Reservoir Storage in percentage.

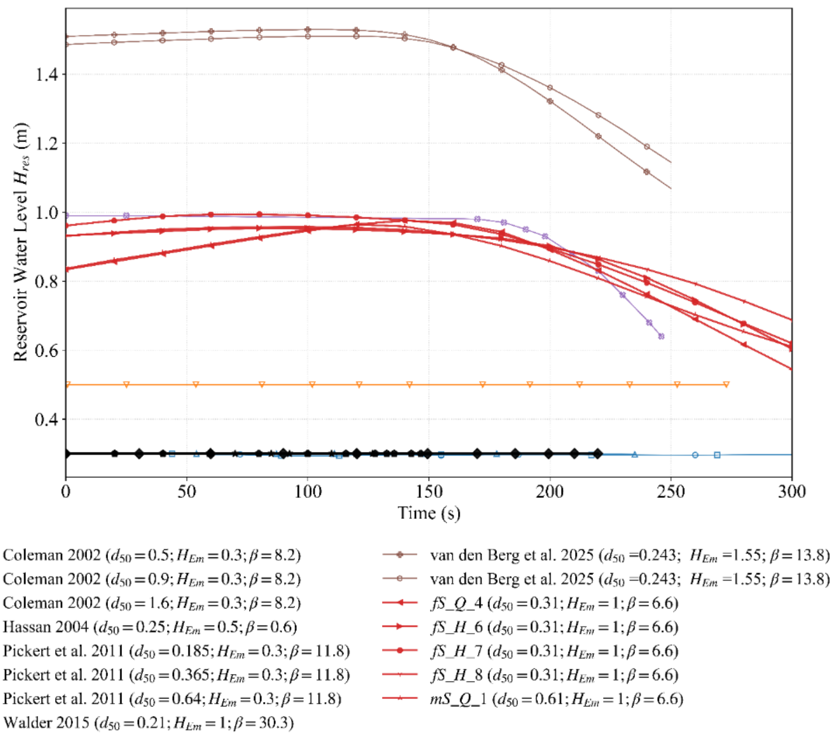

Figure 5.31 Water level evolution in the upstream reservoir for sand embankments across varying model scales. Note: Original data from Hassan et al. (2004) was unavailable and is assumed to be constant.

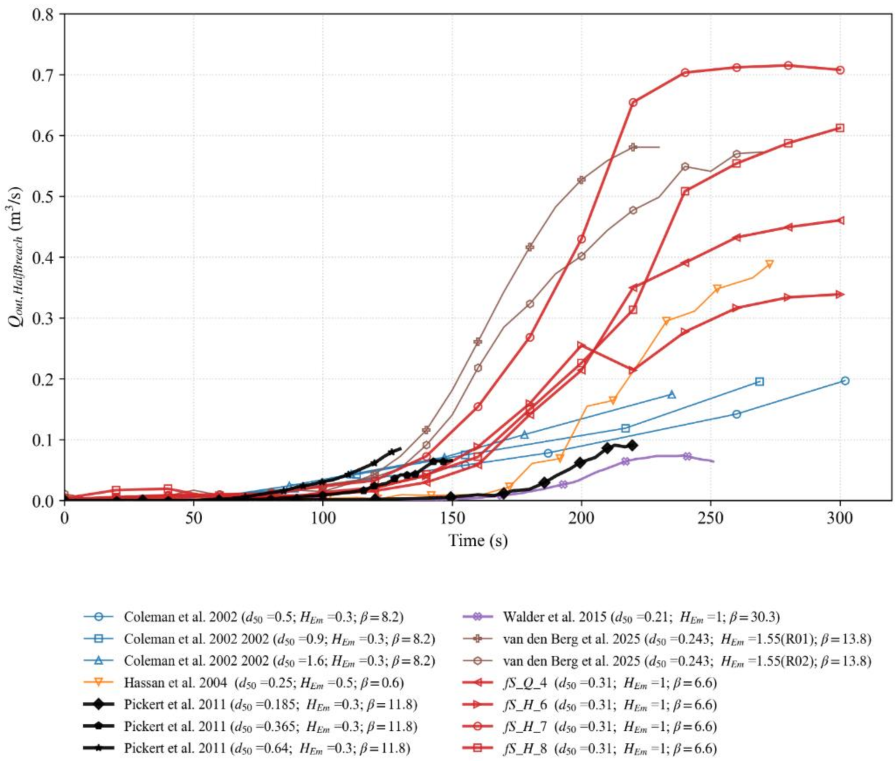

Figure 5.32 Influence of reservoir storage on maximum breach outflow for sand embankments under constant reservoir level conditions across varying model sizes (d_{50} in mm; H_{Em} in m; β in%).

Notably, experiments with higher values of β consistently resulted in lower maximum breach outflows, regardless of the embankment's crest height (or model dimension). First, among smaller models with identical crest heights (e.g., H_{Em} = 0.3 m), a higher β yields a lower peak outflow; for example, Pickert et al. (2011) reported lower outflows at β = 11.8% compared to Coleman et al. (2002) at β = 8.2%.

Second, comparing embankments of identical height (H_{Em} = 1.0 m) under fixed reservoir depletion conditions perfectly isolates this storage effect. For instance, Walder et al. (2015) recorded a maximum breach outflow approximately 5 times smaller for a high β value (30.3%) compared to test *fS_H_6* of the present study, which benefited from a relatively larger reservoir capacity (β = 6.6%).

Third, large reservoir storage can compensate for a smaller embankment model in terms of peak outflow. For example, Hassan et al. (2004) (β = 0.6%)

observed a maximum breach outflow for a 0.5-m-high model that was comparable to the larger embankment models e.g. *fS_Q_4* and *fS_H_6* experiments presented in this research. Fourth, the influence of constant reservoir level can overpower the embankment scale. The maximum breach outflow discharge in tests *fS_H_7*, and *fS_H_8* (H_{Em} = 1 m) was relatively higher than that of van den Berg. et al. (2025) with β = 13.8%, despite their larger 1.55-m-high model operating under a falling reservoir level.

Therefore, it can be concluded that:

- Both reservoir inflow (via water level adjustments maintaining a constant head) and total reservoir size govern the maximum breach outflow. Maintaining a constant reservoir level for a longer duration, given an identical reservoir volume, results in a higher peak outflow.
- In contrast, under constant inflow or falling head conditions, decreasing the reservoir size leads to rapid drawdown, which significantly lowers the breach outflow peak discharge

Recalling the reservoir mass balance Eq (4-1), and assuming a negligible drainage discharge

$$Q_{breach} = Q_{in} - A(z)\frac{dz}{dt}$$

the maximum breach outflow can be directly determined across all cases if the reservoir inflow Q_{in}, the reservoir area $A(z)$, and the nearly constant negative gradient of the water level drawdown follows a nearly constant negative gradient (dz/dt =-Cst) at the time of failure are known.

Another approach in correlating the peak breach outflow directly to the available reservoir volume and to the hydraulic head over the breach invert. This approach aligns with existing empirical and parametric models derived from historical failure events such as Eq (5-1) (Froehlich, 1995), though its precise application to physical scale-series modeling requires further investigation.

$$Q_p = 0.607(V_w)^{0.295}(h_w)^{1.24} \qquad 5\text{-}1$$

In conclusion, this section highlighted the critical influence of reservoir storage and upstream boundary conditions on the breaching process. These parameters require careful selection during model scaling to accurately replicate real-world failures, whether simulating an earth dam with a finite volume recharged by a constant inflow, or a levee subjected to an effectively infinite water volume. While the water level drawdown is inevitable at the time of failure, the recharging inflow, the reservoir area and water level drawdown rate have significant influence on the peak breach outflow.

The significance of these factors will be expanded upon in the next chapter. Specifically, Chapter 6 will explore these dynamics in the context of physical model scaling, through scaling criteria and dimensional analysis, demonstrating how disproportionate scaling of reservoir size can lead to model distortion and the artificial attenuation of peak breach outflow.

5.10 Infiltration, Negative Pore Pressure and Compaction Effects

The degree of soil compaction acts as a critical control on the embankment's initial resistance to hydraulic shear stress. As established by Amaral et al. (2020) and Asghari Tabrizi et al. (2017), embankments with lower relative compaction typically exhibit faster erosion rates and earlier peak discharges due to reduced inter-particle friction and lower bulk density.

Negative pore pressure (matric suction) generates apparent cohesion, binding non-cohesive particles together. This force allows fine sand embankments to sustain vertical or overhanging walls during breaching, as detailed by Pickert et al. (2011). Compaction enhances this mechanism by reducing the void ratio and characteristic pore diameter; according to capillary theory, a smaller pore diameter increases the potential capillary rise and matric suction.

To quantify these effects, efforts were made to monitor infiltration flow and internal pressures. Two measurement tools were employed (Figure 5.33): the TEROS 10 Soil Moisture sensor, measuring volumetric water content, and the TEROS 32 Soil Tensiometer, measuring water potential (–85 to +50 kPa).

However, the temporal resolution of these instruments proved to be a primary limitation during the rapid breaching of sand embankments. While the TEROS 10 sensors (sampling interval of 10 (s)) successfully captured the water content evolution and saturation at three elevations (see Figure 5.34), indicating a relatively fast saturation front, the TEROS 32 sensors were unable to capture data with sufficient frequency to resolve the transient pressure changes during the breach event.

(a) (b)

Figure 5.33 Instrumentation layout for monitoring internal soil states: (a) vertical arrangement of three TEROS 10 soil moisture sensors embedded at elevations Z=0.35,0.50, and 0.60 m above the flume bed (at x = 0 m and y= 1.8 m); and (b) placement of three TEROS 32 soil tensiometers along the embankment crest to measure matric suction.

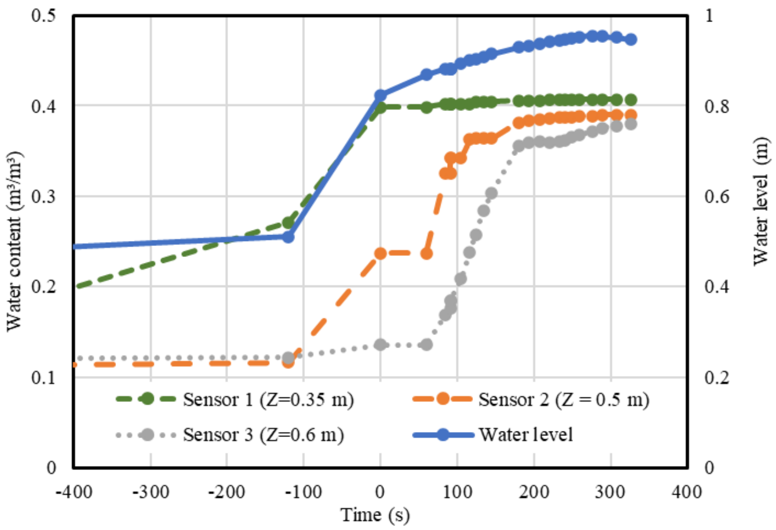

Figure 5.34 Temporal evolution of the volumetric water content within the embankment body at elevations Z=0.35,0.50, and 0.60 m and the associated reservoir water level during the filling and early breach initiation phases of test in test *fS_H_6* (t = 0 s corresponds to the transition to the Experimental Phase and the beginning of overtopping; the data registration was interrupted before the test ends).

5.11 Conclusion and perspectives

A comprehensive experimental campaign, comprising eight medium-scale embankment breaching tests, was conducted to investigate the coupled influence of overtopping hydraulic conditions (*H* vs. *Q*) and sediment granulometry (fine vs. medium sand) on breach formation and outflow hydrographs. Through the generation of high-resolution spatiotemporal data from these experiments, this study contributes a valuable dataset that contribute to bridging the knowledge gap between small-scale laboratory models and prototype scale failures, serving as a benchmark for scaling analysis and numerical model calibration.

The findings emphasize that accurate prediction of embankment failure requires a coupled understanding of hydraulic forcing and geotechnical resistance. As established in the comparative analysis of the *fS_H* and *fS_Q* series, the overtopping conditions, specifically the transition between active inflow and falling reservoir head, dictate the temporal scale of the pre-widening and widening stages. This observation is corroborated by Elalfy et al. (2025), who identified that breaching is highly sensitive to the inlet discharge and reservoir volume.

Furthermore, soil state variables and granulometry play a decisive role in governing the failure mechanism. As observed in this study, fine and medium sand embankments exhibit fundamentally different erosion trajectories: fine sand is dominated by cohesive-like headcut migration and discrete block failure, whereas medium sand fails through continuous surface erosion and granular sliding. Additionally, compaction serves as a fundamental boundary condition that governs the breach initiation timing (Tabrizi et al. 2017, Amaral et al. 2021). The high degrees of dry density achieved in this study through mechanical compaction enhance the material's resistance to surface erosion, a factor that numerical models often simplify through "optimally compacted" assumptions. Asghari Tabrizi et al. 2017 demonstrated that even minor deviations in the initial compaction state can lead to measurable variances in the reservoir water level during the widening phase.

Additionally, apparent cohesion arising from negative pore pressure in non-saturated fine sand was found to govern the failure mode, transitioning the process from continuous surface erosion to discrete mass block failure.

Finally, the apparent cohesion inherent in the fine sand series facilitates the formation of nearly vertical breach profiles prior to mass failure, a phenomenon extensively documented by Pickert et al. (2011). The stabilization of these steep banks is a critical geotechnical feature that defines the effective failure angle. Consequently, integrating these macro-scale erosion processes as discrete source terms in numerical models is essential for capturing the sudden lateral expansion caused by periodic bank slumping, as demonstrated by Elalfy et al. (2025). By bridging high-resolution experimental data with these numerical perspectives, this thesis provides a refined framework for evaluating the resilience of earthen embankments under diverse hydraulic loads.

Future measurements should prioritize high-frequency monitoring of seepage, infiltration, and water potential to capture the rapid transients of the breaching phase. While the TEROS sensors provided valuable saturation data, their frequency was insufficient for dynamic pressure tracking. Implementing a reservoir repose period prior to overtopping could offer a wider window for stable measurements; however, this approach requires careful optimization, as full embankment saturation may inadvertently trigger internal erosion or piping before the hydraulic overflow commences

Additionally, flow characterization remains a challenge in highly turbid breach channels; implementing non-intrusive optical techniques such as Particle Tracking Velocimetry (PTV) or Large-Scale Particle Image Velocimetry (LSPIV) using high-speed cameras would significantly improve the hydrodynamic characterization of the breach outflow.

Finally, extending the validation of these findings by comparing the current dataset with other medium- and large-scale databases available in the literature will offer deeper insights into the influence of reservoir size and scale effects.

Chapter 6

Experimental Investigation of Scale Effects in Sand Embankments Breaching[9]

6.1 Background

While analytical solutions and computer simulations are powerful tools to investigate design and operation issues in hydraulic engineering, physical models remain essential when complex flow patterns are involved, with sediment transport processes that are beyond the resolving capabilities of numerical simulation tools. The practice of using small-scale models to predict large-scale behaviors has a long history, evolving from intuitive trials to a rigorous science. Early pioneers like William Froude and Osborne Reynolds established the foundational dimensionless parameters that relate geometric scale, fluid properties, and flow variables.

The discipline grew significantly with the establishment of formal hydraulic laboratories in the 19th and 20th centuries, allowing for the systematic study of hydraulic structures.

However, accounting for sediment transport introduces an additional layer of complexity because of the change of behavior of the sediments when scaled to small dimensions. Therefore, such experiments are inherently prone to scale effects, requiring the hydraulic experimentalist to navigate the difficult balance between manageable laboratory dimensions and the preservation of prototype physics.

Contemporary hydraulic modeling frequently adopts a 'hybrid' framework, integrating physical models with diverse data sources including field observations, numerical simulations, and supplementary laboratory investigations conducted at different scales. Within this collaborative

[9] This chapter is written as a paper to be submitted to the Journal of Hydraulic Engineering

paradigm, physical models provide the high-resolution data necessary to calibrate and validate numerical simulation tools and resolve intricate local flow features. Then, a well calibrated numerical model then allows for a deeper investigation of the sensitivity of the model to changes in parameters, boundary conditions or temporal scales.

Considering physical models, "scale-series" testing is a strategy designed to isolate and quantify the scale effects that inevitably arise from incomplete similitude. By investigating a series of models at varying scales for a single prototype, researchers can systematically track how hydraulic behaviors deviate as dimensions change.

6.2 Hydraulic Models and Similarity

The theoretical basis of hydraulic modeling is the concept of similarity, which ensures that the physical behavior of a model simulates the prototype in a scaled and predictable manner (Pugh, 1985). According to Yalin (1971): "A small scale reproduction of a physical phenomenon can be a scientifically valid model only if a certain set of its measurable characteristics are related to their counterparts in the actual phenomenon, or prototype, by certain constant proportions which satisfy definite mathematical conditions. These constant proportions are referred to as scales, whereas the mathematical conditions which must be satisfied by the scales are called the criteria of similarity. It follows that the design and realization of a true model of a phenomenon can only be achieved if the similarity criteria of that phenomenon are known."

Complete similarity requires the satisfaction of three conditions (Heller, 2011; Kobus, 1980; Novák & Cabelka, 1981; Pugh, 1985; Yalin, 1971):

1. **Geometric Similarity:** Similarity in form, where the ratios of all homologous length dimensions between model (L_m) and prototype (L_p) are constant (λ_L), where m and p stand for model and prototype.

$$\lambda_L = \frac{L_m}{L_p} \qquad \text{6-1}$$

2. **Kinematic Similarity:** Similarity of motion, requiring that velocities and accelerations at homologous points differ only by a constant scale factor.

$$\lambda_L = \frac{L_m}{L_p}; \lambda_T = \frac{T_m}{T_p} \qquad 6\text{-}2$$

where T_m and T_p are characteristic time units in model and prototype and λ_T is the time scale.

3. **Dynamic Similarity:** Similarity of forces, where the ratios of homologous forces (such as gravity, viscosity, and inertia) are identical in both systems.

$$\lambda_L = \frac{L_m}{L_p}; \lambda_T = \frac{T_m}{T_p}; \lambda_M = \frac{M_m}{M_p} \qquad 6\text{-}3$$

where M_m and M_p are mass units in model and prototype and λ_M is the mass scale.

In order to establish the criteria of dynamic similarity of a mechanical phenomenon, it is necessary and sufficient to know the set of *n* characteristic parameters of that phenomenon. If the set of characteristic parameters is revealed, then the determination of the set of dimensionless variables, and consequently the criteria of dynamic similarity, is a matter of application of exact and simple rules (Yalin, 1971).

In the literature the criteria of similarity (Froude, Reynolds, Webber, Strouhal numbers, etc.) are usually derived either from the expressions of various individual forces or from certain differential equations (such as Navier Stokes eqns.). The fact that the criteria of similarity follow from the parameters themselves rather than from a relation (an equation) among them, forms the most advantageous feature of the dimensional method.

Some of these similarity criteria are defined as follows:

- **Froude Number (Fr):** Represents the ratio of inertial to gravity forces. It is the governing criterion for free-surface flows such as rivers, spillways, and waves:

$$\mathrm{Fr} = \frac{V}{\sqrt{gh}_m} \qquad 6\text{-}4$$

where V is the average flow velocity, $h_m = A/L$ is the mean hydraulic depth defined as wetted area divided by L, the width of the cross section at the free surface.

- **Reynolds Number (Re):** Represents the ratio of inertial to viscous forces. It is crucial for closed-conduit flows and evaluating friction or drag, especially in laminar flows or flows with relatively small Reynolds numbers, below 10^{-6}. In open channel flow, Reynolds number is defined as

$$\mathrm{Re} = \frac{VR}{\nu} \qquad \text{6-5}$$

where R is the hydraulic radius and υ is the kinematic viscosity of water ($\upsilon = 10^{-6}$ m² s⁻¹).

- **Weber Number (We):** Relates inertial forces to surface tension, important for air-entrainment and thin sheet flows.

$$\mathrm{We} = \frac{\rho L V^2}{\sigma} \qquad \text{6-6}$$

where L is a characteristic length, ρ is the fluid density and σ is surface tension.

A fundamental challenge in hydraulic modeling is that it is physically impossible to satisfy all these criteria simultaneously using water as the prototype fluid, which is usually the case in conventional hydraulic models. This means that when determining the scales of a model in which the fluid will also be water, we are compelled to select

$$\lambda_\mu = 1 \text{ and } \lambda_\rho = 1 \qquad \text{6-7}$$

where μ is the dynamic viscosity of the fluid. As a consequence, only one scale can be freely selected, typically the geometric model scale λ_L. If the acceleration due to gravity g is one of the characteristic parameters, then, since both model and prototype are on the same planet, we have no alternative but to choose

$$\lambda_g = 1 \qquad \text{6-8}$$

Given that the quantities μ, ρ, and g have independent dimensions, and their scales are equal to unity, it implies that the realization of a small-scale model with all properties dynamically similar is impossible. For example, scaling a river model according to Froude similarity inevitably results in a Reynolds number that is much lower than in the prototype (Ettema, 2000; Jansen et al., 1979). Therefore, one may ask "how to ensure the dynamical similarity of at least those properties which will be measured and/or observed?". This reduction from all properties to only some gives rise to certain possibilities.

Deviations between the model (m) and prototype (p) caused by some unequal force ratios are termed "scale effects" (Heller, 2011; Hughes, 1993; Yalin, 1971). To manage these effects, modelers often rely on "limiting criteria" such as specific thresholds for Reynolds or Weber numbers above which scale effects are considered negligible. For instance, ensuring the model flow remains fully turbulent often allows for the relaxation of strict Reynolds similarity in Froude-based models. Other strategies include the use of "distorted models" (where the vertical scale is larger than the horizontal scale) to compensate for viscous effects in shallow flows, particularly in river and estuarine modeling (Ettema, 2000; Jansen et al., 1979).

6.3 Sediment Scaling and Scale Effects in Earthen Embankment Breaching

The hydraulic modeling of earthen embankments reveals that the complexity increases significantly compared to rigid-structure hydraulics. For example, pure hydrodynamic dam-break flows accurately follow the Froude similarity as shown by Soares-Frazão (2007). However, the modeling of breaching is not a pure hydrodynamic problem; it is a coupled hydro-morphodynamic and geotechnical phenomenon. The interactions between the fluid (multiphase flow when sediments are transported in suspension) and the erodible structure (soil mechanics) create conflicting similarity requirements that are often impossible to satisfy simultaneously in a reduced-scale model.

6.3.1 Sediment scaling

Geometrical scaling

In models scaled according to Froude similarity, the grain size in the model (d_m) should be also scaled according to the geometrical scale ratio.

$$\lambda_d = \frac{d_m}{d_p} = \lambda_L \qquad 6\text{-}9$$

This frequently leads to significant scale effects. In particular in earth embankment breaching, for a prototype constructed of sand or gravel, applying a large scale factor (e.g., $\lambda_L > 20$) may result in a model sediment size that falls within the silt or clay range ($d_m < 0.06$ mm). Such fine materials exhibit cohesive behavior and viscous dominance inconsistent with the non-cohesive, turbulent erosion processes of the prototype. Consequently, the model embankment may fail to erode or erode via different mechanisms (e.g., block failure vs. particle entrainment), making the scale model unrepresentative.

Sediment transport rate scaling

In models involving movable bed, the model must account for appropriate simulation of sediment detachment, transport, and deposition. In river engineering, this requires the correct scaling of sediment transport rate to ensure the morphological time scale is preserved. However, a critical limitation arises because water is typically used in both model and prototype, leaving fluid viscosity invariant. Consequently, reduced-scale models inherently suffer from Reynolds number distortion; the model flow may exhibit viscous boundary layer effects (transitional regime) that are absent in the fully turbulent prototype, thereby compromising the accuracy of the scaled sediment transport rate. This is further explained below.

Shields developed a diagram that relates dimensionless bed shear stress (τ_b^*) to the grain Reynolds number (Re_*). The Shields diagram is used to define the critical dimensionless shear stress (τ_c^*), which represents the threshold shear stress required for the initiation of sediment motion (the red curve in Figure 6.1). As the shear stresses are proportional to the velocity gradients, the bed shear stress can be defined as function of shear velocity (u_*). In open-channel flows, the shear stress at the bed can be defined as a function of the shear velocity as indicated in Eq. (6-10), and the Shields parameters are defined as given in Eq. (6-11), Eq. (6-10) :

$$\tau_b = \rho_w u_*^2 \qquad 6\text{-}10$$

$$\tau_{b*} = \frac{\tau_b}{g\left(\rho_s - \rho_w\right)d} = \frac{\rho_w u_*^2}{g\left(\rho_s - \rho_w\right)d} = \frac{u_*^2}{g\left(s-1\right)d} \qquad \text{6-11}$$

$$\mathrm{Re}_* = \frac{u_* \, d}{\nu} \qquad \text{6-12}$$

According to the Shields diagram, sediment entrainment is governed by the boundary layer flow conditions, which are divided into three distinct regimes based on the grain Reynolds number Re*.

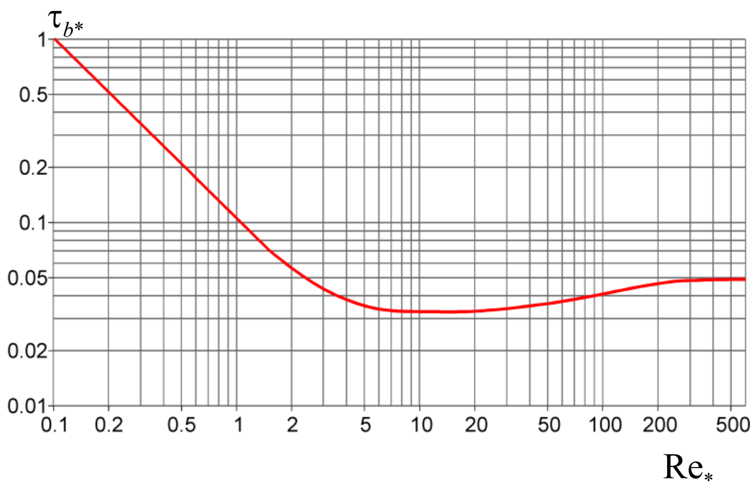

Figure 6.1 Shields diagram representing the threshold for incipient motion using dimensionless shear stress and boundary (grain) Reynolds Number.

Hydraulically Smooth Regime ($\mathrm{Re}^* < 5$**):** In this regime, the roughness elements (sediment grains) are entirely submerged within the viscous sublayer. Viscous forces dominate, and the critical shear stress is relatively high due to the lack of turbulent agitation acting directly on the grains.

Rough Regime ($\mathrm{Re}^* > 70 - 100$**):** The viscous sublayer is disrupted, and the grains are fully exposed to turbulent fluctuations. Sediment entrainment is controlled solely by the ratio of destabilizing turbulent forces to stabilizing gravitational forces (Shields parameter), making it independent of viscosity.

Transitional Regime ($5 < \mathrm{Re}^* < 70$**):** In this intermediate zone, both viscous and turbulent roughness effects are significant. The critical dimensionless shear stress varies non-linearly with the Reynolds number, often reaching a minimum value around before rising again towards the rough limit.

In models governed by Froude similarity, dynamic similarity of sediment transport is theoretically achievable if both the model and prototype operate within the fully rough turbulent regime. In this regime, the critical dimensionless shear stress becomes independent of the grain Reynolds number; therefore, the sediment transport rate (q_s) and morphological time scale are preserved, provided that geometric reduction of the sediment diameter does not result in particles so fine that they exhibit unrepresentative cohesive effects. Preserving the similarity of the non-dimensional shear stress ($\tau_{b,m}{}^{*} = \tau_{b,p}{}^{*}$) leads to the following expression and relations between scale factors, assuming that ρ_s remains identical:

$$\tau_{b*_m} = \tau_{b*_p} = \frac{\tau_b}{g\left(\rho_s - \rho_w\right)d} = \frac{u_*^2}{g\left(s-1\right)d} \qquad 6\text{-}13$$

$$\lambda_g \lambda_d = \lambda_V^2 \qquad 6\text{-}14$$

As $\lambda_V = \lambda_L{}^{1/2}$ in the Froude similary with $\lambda_g = 1$, this results in

$$\lambda_d = \lambda_L \qquad 6\text{-}15$$

The non-dimensional sediment transport rate per unit width is expressed as follows, from which the scale factor can be deduced

$$q_{s*} = \frac{q_s}{u_* d} \; or \; q_{s*} = \frac{q_s}{\sqrt{g\left(s-1\right)d^3}} \qquad 6\text{-}16$$

$$\lambda_{q_s} = \lambda_d^{3/2} = \lambda_L{}^{3/2} \qquad 6\text{-}17$$

The total sediment discharge is $Q_s = q_s L$, and thus scales with $\lambda_L{}^{5/2}$, which is consistent with the Froude scaling for pure hydrodynamic flows.

However, a critical challenge arises when the model and prototype operate in different hydraulic regimes. While prototype flows typically remain in the fully rough turbulent regime, the reduced length scales in the laboratory often force the model sediment into the transitional or hydraulically smooth regime. In this range, viscous effects in the boundary layer disproportionately increases the resistance to motion. Consequently, a strictly Froude-scaled model (using geometrically scaled sediment) effectively underestimates the tractive forces, leading to a significant under-prediction of the sediment transport capacity (or erosion) compared to the prototype.

Settling velocity adjustment

As the Shields parameter similarity does not appear as the most appropriate scaling for flows involving sediment transport, other parameters can be considered. One established solution is the settling velocity adjustment proposed by Pugh (1985). This method involves increasing the model sediment diameter slightly beyond the geometric target (using coarser sand) to ensure the particle's settling velocity (w_s) remains the same in the model and in the prototype, thereby compensating for the Reynolds number distortion.

The settling velocity of particles affects how sediment is transported in suspension and deposited. In small models, geometrically scaled particles settle too slowly compared to the Froude time scale, and the following relation is no longer satisfied.

$$\lambda_{w_s} = \frac{w_{s,m}}{w_{s,p}} = \lambda_V = \lambda_L^{0.5} \qquad \text{6-18}$$

The settling velocity (w_s) of sediment is fundamentally governed by the particle diameter (d), material density (ρ_s), and fluid viscosity (υ).

For coarser sediments (typically $d > 1$ mm), settling is controlled by inertial forces and resisted primarily by turbulent drag. The settling velocity is proportional to the square root of the diameter with $w_s = f\,(d^{\,0.5})$. As cited by Muste et al. (2017), Zanke (1977) proposed a formula for calculating the settling velocity of particles larger than 1 mm, which is presented in Eq. (6-19). This relationship is consistent with Froude similarity, where velocity scales with the square root of the length scale, making Froude scaling naturally applicable to coarse grains.

$$w_s = 1.1\left[\left(\frac{\rho_s}{\rho} - 1\right) g d\right]^{1/2} \qquad \text{6-19}$$

For finer sediments (typically $d < 0.1$ mm), settling is controlled by viscous forces inducing laminar drag. In this range, the velocity follows Stokes' Law and is proportional to the square of the diameter as $w_s = f(d^2)$.

For intermediate gain sizes (0.1 to 1 mm), a transition zone exists where both viscous and inertial forces influence the drag coefficient. Zanke (1977) formula for this range is given in Eq. (6-20)

$$w_s = 10\frac{\nu}{d}\left\{\left[1+0.01\left(\frac{\rho_s}{\rho}-1\right)\frac{gd^3}{\nu^2}\right]^{1/2}-1\right\} \qquad 6\text{-}20$$

Therefore, for models utilizing grain sizes under 1 mm, geometric scaling fails to accurately reproduce the settling velocity due to the dominance of viscous forces. Consequently, it is necessary to adjust the model grain size (d_m) to compensate. Pugh (1985) indicated that for non-cohesive material in the transitional range (0.1 mm < d < 1 mm), the settling velocity of the prototype material should first be scaled according to the Froude velocity scale ratio ($\lambda_L^{0.5}$). Subsequently, the specific model grain size is corrected to achieve the target settling velocity. This often results in a model sediment that is slightly coarser than the value derived from strict geometric scaling.

Scale-series modeling approach

Given the theoretical impossibility of satisfying Froude, Reynolds, and Weber similarity criteria simultaneously in a single reduced-scale model using water and natural soil, the Scale-Series Modeling Approach is adopted to address these inherent distortions. Validated by studies such as Schmocker and Hager (2009) and Al-Riffai (2014), this methodology involves replicating identical embankment configurations at multiple geometric scales (e.g., small, medium, and large/prototype) to isolate the influence of hydraulic forces versus geotechnical resistance.

By analyzing the trends in breach parameters such as peak discharge and failure time across these varying scales, researchers can:

• **Quantify Scale Effects:** Isolate and measure the distortions caused by viscous and surface tension forces that are disproportionately active in small-scale models.

• **Identify Critical Thresholds:** Determine the minimum geometric scale or sediment diameter required for results to become scale-independent, thereby establishing the limits where Reynolds and Weber no longer influence the flow.

• **Extrapolate to Prototype:** Bridge the gap between laboratory observations and real-world behavior, allowing for the correction of erosion rate underestimations common in smaller models.

6.3.2 Soil-water interaction and bank stability

A critical phase of embankment breaching is lateral widening, which dictates the peak discharge and is driven by the complex interaction between soil and water. This process often involves the undercutting of breach side slopes followed by the sudden gravitational collapse (mass failure) of soil blocks as was shown and discussed in Chaper 4 and 5. The stability of these banks in partially saturated soils is governed by apparent cohesion, which can be defined using the extended Mohr-Coulomb criterion as the additional shear strength provided by matric suction (Osman et Thorne 1988, Rinaldi and Casagli, 1999, and Rinaldi et al. 2004).

However, this apparent cohesion is highly transient. As the overtopping flow infiltrates the embankment, progressive saturation weakens the matric suction and drastically reduces the soil's shear strength, a phenomenon which is very similar to streambanks failure (Rinaldi and Casagli, 1999). While the confining pressure of the water within the channel temporarily stabilizes the bank during the rising stage, mass block failures are typically triggered during rapid reservoir level drawdown. This removes the confining hydrostatic pressure while the bank soil becomes more saturated and heavier, leading to collapse.

Replicating these discrete geotechnical failures in reduced-scale models is highly challenging because soil shear strength and pore pressure do not scale linearly alongside hydraulic surface erosion (Schmocker and Hager 2012, Amaral et al 2020). Furthermore, in prototype dams, seepage is relatively slow. If a model uses coarser grains to avoid artificial cohesion, the hydraulic conductivity increases disproportionately. This can lead to excessive seepage, causing the model dike to fail by sliding or slumping before overtopping erosion even begins, which may require adaptations to the experimental setup, like a downstream sand layer (Van Emelen, 2015) or drainage system (Pickert et al. 2011 and Schmocker and Hager 2012), to prevent unrepresentative failure modes.

Osman and Thorne (1988) developed an analytical model to calculate streambank stability by explicitly accounting for the soil's geotechnical parameters. The primary variables and bank failure conditions considered in their framework, such as those during parallel bank retreat, are illustrated in Figure 6.2.

(a)

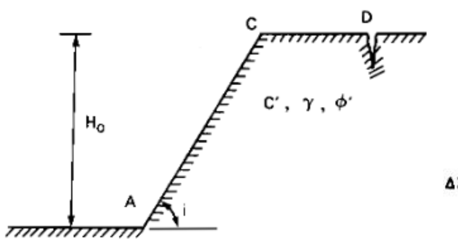

(b)

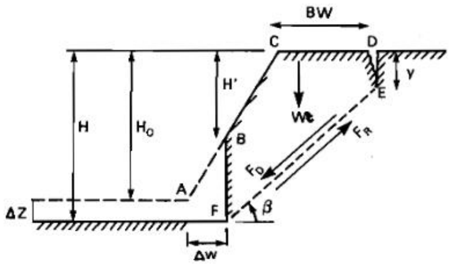

(c)

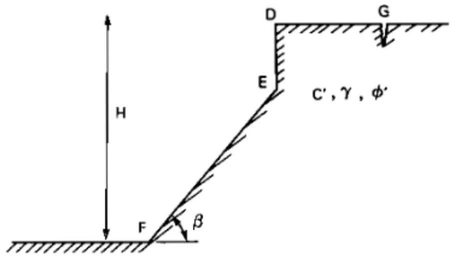

(d)

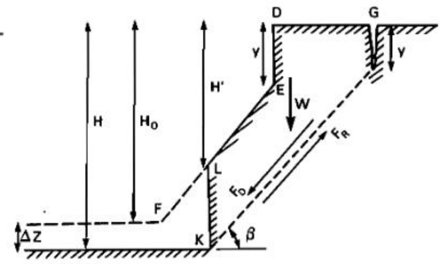

Figure 6.2 Riverbank stability principles in case of parallel bank retreat illustrated through two consecutive mass block failure: (a) initial state of riverbank, (b) right riverbank after erosion to point of failure (first failure) (c) right riverbank after this initial failure, and (d) right riverbank after erosion to point of failure (second failure)

Extensive research, particularly utilizing long-term field monitoring, has investigated the critical influence of transient pore water pressures and varying saturation levels on streambank stability (Rinaldi and Casagli, 1999; Rinaldi et al., 2004; Rinaldi and Nardi, 2013). However such studies are rare in case of embankment breaching.

Pore pressure effects and bank stability

Similar to river and open channel flow, hydraulic processes in embankment overtopping flow are dominated by gravity and inertia which requires Froude similarity. However, the embankment's resistance to erosion depends on geotechnical properties such as mineralogical cohesion, interparticle friction, and pore pressure, which do not linearly follow Froude scaling (Amaral et al., 2020).

A critical challenge in experimental modeling non-cohesive embankments is the scale effect due to the variation of pore pressure across different scales as well as the variation of the pore pressure in partially saturated soils in the model. In reduced-scale models using sand with $d < 1$ mm (and particularly $d < 0.3$ mm), matric suction and capillary forces become significant relative to the destabilizing gravity forces (Pickert et al. (2011)). This "apparent cohesion" stabilizes the breach side slopes, allowing them to stand vertically or even overhang, leading to a failure mechanism driven by undercutting and the episodic collapse of large soil blocks. In contrast, prototype embankments of coarse sand or gravel are typically dominated by surface erosion and shear failure, with slopes closer to the angle of repose. Pickert et al. (2011) and Schmocker and Hager (2012) demonstrated that this cohesion effect distorts the lateral widening rate and the breach cross-sectional shape.

Pickert et al. (2011) and Amaral et al. (2020) explicitly state that while hydraulic driving forces scale according to Froude similitude (λ_L^3), soil resistance properties (specifically apparent cohesion and pore pressure) do not obey Froude scaling. Consequently, in a reduced-scale model, the resistance forces become disproportionately large compared to the hydraulic driving forces.

The physical impossibility of scaling sediment perfectly is further illustrated by the “relative capillary” parameter introduced by Pickert et al. (2011), defined as $\sigma_w/(g\rho_w dH_{Em})$ (detailed in Section 6.10, Dimensional Analysis). Because water is used in both the model and prototype, fluid properties such as surface tension (σ_w) and density (ρ_w), as well as gravity (g), remain constant. Consequently, to maintain similitude for this capillary parameter, any geometric reduction in the embankment height (H_{Em}) would mathematically necessitate a proportional increase in the grain size (d). However, artificially enlarging the sediment into the coarse sand or gravel range to satisfy this relationship would drastically increase permeability and completely eliminate the apparent cohesion effect that governs the failure mechanics of fine sands (also discussed by Amaral et. al. 2020). Ultimately, this conflicting constraint justifies the adoption of a scale-series approach utilizing identical sands, rather than attempting to artificially scale the sediment.

The model distortion due to pore pressure influence can be quantified using a geotechnical Stability Number (N_s), under three major assumptions:

1. **Planar failure mechanism:** The mass slumping is assumed to occur along a discrete, planar failure surface (vertical bank retreat) typically initiated by a deep vertical tension crack.
2. **Homogeneous soil profile:** The soil is treated as homogeneous and isotropic, which allows the bulk unit weight (γ_{bulk}) to be applied as a constant for the entire failing block.
3. **Simplified matric suction:** The apparent cohesion (c'), which is driven by matric suction, is assumed to have a simplified (often linear) distribution across the failure plane and reaches immediate equilibrium with the water level.

and defined as the ratio of destabilizing gravitational forces to stabilizing cohesive forces:

$$N_s = \frac{\gamma_{bulk} H_{Em}}{c'} \tag{6-21}$$

Where γ_{bulk} is the bulk unit weight of soil, and c' apparent cohesion, and H_{Em} is the embankment height. When using the same soil in the model as in the prototype or when cohesion is introduced via fine grains in the model, γ_{bulk} and c' remain effectively constant. However, the destabilizing mass and volume of the potential sliding blocks (represented by H_{Em}) reduces according to the geometric scale ratio. For example, a scale factor of $\lambda_L = 0.2$, results in a Stability Number in the model that is effectively one-fifth of the prototype's ($N_{s,m}$=0.2$N_{s,p}$). This disproportionate stability implies that the model banks are relatively five times more stable than the prototype banks, leading to a systematic underestimation of breach widening rates and outflow magnitudes. On the other hand, implementing such a parameter as a scaling factor for geotechnical similitude without adapting the material properties (e.g. scaling the sediment density) is practically impossible. Artificially reducing apparent cohesion requires using much coarser sediments, which disproportionately increases hydraulic conductivity and causes the model to fail uncharacteristically via seepage or slumping before overtopping even begins. Therefore, instead of using geotechnical parameters to scale the model, one can use them to quantify the scale effects.

6.4 Objective and Scaling Methodology in Present Study

To address the inherent difficulties in physical modeling of embankment breaching failure, this chapter focuses on the investigation of scale effects in sand embankment breaching experiments. Recognizing the fundamental challenge of satisfying simultaneous hydraulic and geotechnical similitude, this study adopts a 'scale-series' approach. The experimental campaign replicates breach tests at two distinct geometric scales: a medium-scale 'prototype' with an embankment height $H_{Em,p}$ = 1.0 m and a small-scale model with an embankment height $H_{Em,m}$ = 0.2 m, representing a scale factor λ_L = 0.2. According to the Froude similarity, the inflow discharge Q_{in} scales with $\lambda_Q = \lambda^{5/2}$ as illustrated in Figure 6.3.

The study builds upon former small-scale experiments conducted in the LEMSC laboratory of UCLouvain by Descantons et Dujardin (2014) and Van Emelen (2015) with two different sands (d_{50} = 0.70 and 1.70 mm) and used to validate numerical models by Delpierre et al. (2024). Two types of new experiments were conducted. As described in Chapter 3 and Chapter 4 , the small-scale experiments were reproduced at a larger scale in the Hydraulic Research Laboratory of Châtelet. Then, a new series of small-scale tests under the same conditions were conducted at the Hydraulic Laboratory of LEMSC at UCLouvain. This new series of tests is presented in this chapter. While the hydraulic conditions between the new medium and small-scale tests were scaled according to Froude similarity, the embankment material remained identical (using the same medium and fine sand) for both scales. This controlled distortion allows for a comprehensive comparative analysis of breach evolution and discharge at two geometrical scales and the study of scale effects arising from the hydro-morphodynamic interactions.

The analysis aims to evaluate "limiting criteria" required to minimize scale effects. Schmocker and Hager (2009) proposed minimum dimensions of $H_{Em} \geq 0.20$ m and grain diameter of $d \geq 1$ mm as well as a minimum unit discharge of 0.020 (m^3 s^{-1}) to avoid significant Reynolds and Weber number scale effects (and therefore to avoid significant viscous and surface tension effects). However, their scale-series tests were limited to planar dike breaching (2D) with $H_{Em} \leq 0.4$ m, i.e. experiments in which the overtopping flow occurs over the full width of the dike. In such cases, morphological evolution is driven purely by longitudinal sediment transport. The present study extends their work to full 3D breaching, where lateral widening is governed by a complex mix of surface erosion and mass block failure, a process significantly more sensitive to apparent cohesion. Furthermore, the scale ratio of 5 used in this research allowed to study the process at an intermediate scale which is relatively large and closer to the prototype conditions.

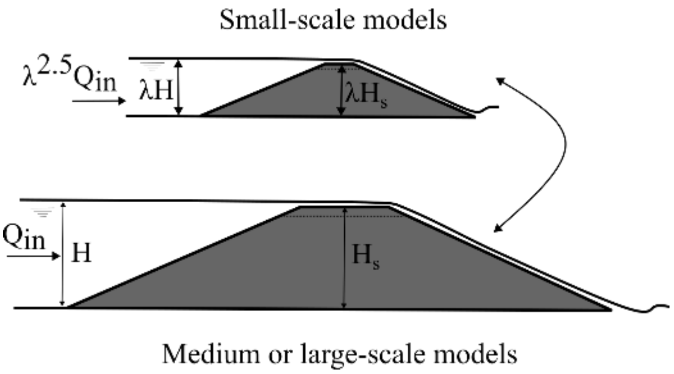

Figure 6.3 Schematic representation of small-scale (model) embankment and medium-scale (prototype) embankment.

Ultimately, these scale-series tests seek to answer a fundamental question: Can we reliably understand full-scale dike failure using smaller-scale experiments? In other words, this chapter seeks to determine if full-scale dike failure mechanisms can be reliably extrapolated from small-scale experiments.

To this end, two distinct analytical methodologies are applied: (i) hydraulic and morphologic comparative analysis, where direct comparison of upscaled variables (water levels, hydrographs, breach width) using Froude scaling were performed; and (ii) dimensionless analysis where a verification of the sediment transport regimes using the grain Reynolds number was used to quantify the divergence between model and prototype physics. The relevancy of settling velocity adjustment application to sand embankment breaching was further investigated.

Finally, the macro-scale erosion mechanisms were characterized at both spatial scales, demonstrating the extent to which dominant physical processes were reproduced. The analysis specifically addressed the impact of reservoir volume distortion on the reservoir water level, and breach hydrograph evolution and further quantified the influence of apparent cohesion.

6.4.1 Froude similarity

Since embankment breaching is a free-surface flow process dominated by gravity, Froude similarity was applied to the hydraulic loads. Assuming the gravitational acceleration *g* is the same for both tests and using the prototype fluid (water) in model, the variables from small embankment (model) can be upscaled to compare with the medium embankment (prototype) using the following ratios:

Table 6.1 Summary of theoretical scale factors for geometric, kinematic, and dynamic parameters derived from Froude similarity criteria.

Parameter	Scale Ratios (Prototype/Model)
Geometric Dimensions (Length, Height, Width)	$\lambda_L = \frac{L_m}{L_p}; \lambda_L = 0.2; L_p = 5L_m$
Area	$\lambda_A = \frac{A_m}{A_p}; \lambda_A = \lambda_L^2 = 0.04; A_p = 25A_m$
Volume ($\mathcal{V}$)	$\lambda_{\mathcal{V}} = \frac{\mathcal{V}_m}{\mathcal{V}_p}; \lambda_{\mathcal{V}} = \lambda_L^3 = 0.008; \mathcal{V}_p = 125\mathcal{V}_m$
Time (t)	$\lambda_t = \frac{T_m}{T_p}; \lambda_t = \sqrt{\lambda_L} = \sqrt{0.2}; T_p = 2.236T_m$
Velocity (V)	$\lambda_V = \frac{V_m}{V_p}; \lambda_V = \sqrt{\lambda_L} = \sqrt{0.2}; V_p = 2.236V_m$
Discharge (Q)	$\lambda_Q = \frac{Q_m}{Q_p}; \lambda_Q = \lambda_L^{2.5} = 0.2^{2.5}; Q_p = 55.901Q_m$

Table 6.2 Comparative summary of geometric and hydraulic parameters for medium-scale (prototype) and small-scale (model) experiments.

Parameter	Medium Scale	Small Scale	Geometry and Froude similitude satisfaction	Expected dimension at small scale
Dike height (m)	1	0.2 to 0.22*	Yes	0.2
Dike crest width (m)	0.5	0.1	Yes	0.1
Dike length (m) (perpendicular to the flow)	3.6	1.2	No (minor impact)	0.72
Dike upstream and downstream slope	1:3	1:3	Yes	NA
Pilot channel dimensions (m)	$l = 0.15$ $b = 0.55$ $h = 0.20$	$l = 0.03$ $b = 0.12$ $h = 0.046$	Not completely	$l = 0.03$ $b = 0.11$ $h = 0.04$
Reservoir area (m²)	190	4.152	No (inducing a. relative error of - 45.4%)	7.6
Inflow (m³/s)	0.224	0.004	Yes	NA
Grain sizes (mm)	0.31 0.61	0.31 0.61	Remained identical in both test series	NA

* was slightly different in practice.

6.4.2 Sediment scale investigation

Applying the geometric scale factor (1:5) to the sediments used in prior small-scale studies (e.g. Descantons et Dujardin, 2014, and Van Emelen, 2015) to design the medium-scale tests for the laboratory of Châtelet would have resulted in a target material within the coarse sand or fine gravel range ($d > 3.5$ mm). Testing such material was outside the scope of this research, which prioritizes the erosion mechanics of sand levees; furthermore, such coarse material would introduce excessive permeability, potentially shifting the failure mode from overtopping erosion to through-flow or seepage instability. Conversely, geometrically downscaling typical prototype sands would result in extremely fine material ($d < 0.06$ mm). As noted by Pickert et al. (2011) and Schmocker and Hager (2012), utilizing such fine sediments in the laboratory inevitably introduces cohesive forces and viscous effects that distort the erosion process, rendering the model unrepresentative of non-cohesive prototype behavior. To address these limitations and the knowledge gaps identified in the state-of-the-art, this research adopts a Scale-Series Modeling Approach. Instead of scaling the grain size, commercially available sands (0.31 mm and 0.61 mm) typical of those found in literature and practice were selected. By replicating experiments at the medium scale using these standard materials, the study isolates the influence of the model size (hydraulic scale) on the breaching process, thereby providing a direct assessment of scale effects without the interference of material-induced distortions.

Table 6.3 outlines the complete matrix of experimental combinations and the resulting possible comparative analyses. While Chapter 5 focused on the influence of sand size and overtopping conditions at the medium scale (*mS_Q*, *fS_Q* and *fS_H*) this chapter introduces the newly conducted small-scale tests. This scale-series approach facilitates a dual analysis: first, examining the influence of grain size at the reduced scale; and second, isolating scale effects by comparing the performance of identical sands across different geometric scales. Collectively, these comparisons reveal whether granulometry dictates the dominant failure mode—specifically, the transition from continuous surface erosion to episodic mass slumping—at both scales. Furthermore, the analysis evaluates the impact of apparent cohesion distortion, tests the validity of Froude scaling for breach outflow and dimensional evolution, and assesses the specific influences of viscosity and turbulence.

Table 6.3 Matrix of experimental combinations and comparative analysis.

Scale/Sediment	Fine (*fS*)	Medium (*mS*)
Medium Scale	✓	✓
Small Scale	✓	✓

6.5 New Small-Scale Experiments: Setup and Measurement Techniques

The small-scale embankment breaching experiments were conducted at the Hydraulic Laboratory of LEMSC at UCLouvain. The experimental setup is depicted in Figure 6.4a-b and dimensions are given in Figure 6.6c. The facility consists of a rectangular flume 12 m long and 1.2 m wide. The incoming flow enters a receptive basin 2 m long with a floor level 0.3 m below the main flume level to reduce the inflow energy and avoid surface perturbations. The embankment is constructed 0.88 m from the beginning of the flume; the exact dimensions of the embankment are reported in

Table 6.2. The inflow was measured using a flowmeter installed on the supply pipe and the water level was measured using ultrasonic sensors at three locations $x = -0.8$, $+0.5$, and $+1$ m along the reservoir area.

In the medium-scale tests, a drainage pipe was installed at the embankment base to minimize seepage risk and prevent premature internal erosion. Because infiltration was observed to be negligible during the medium-scale overtopping, it was initially assumed that seepage would also remain insignificant at the small scale. This assumption was supported by the fact that overtopping was initiated immediately once the reservoir water level surpassed the pilot channel invert, theoretically leaving insufficient time for the soil to become fully saturated.

Consequently, no drain was installed in the small-scale models to preserve identical initial construction conditions. However, this assumption has limitations; as detailed in the scale-effect analysis, reduced-scale models inherently experience faster relative infiltration and saturation due to much shorter internal water trajectories that is not considered in the analysis perfomed in this chapter.

(a)

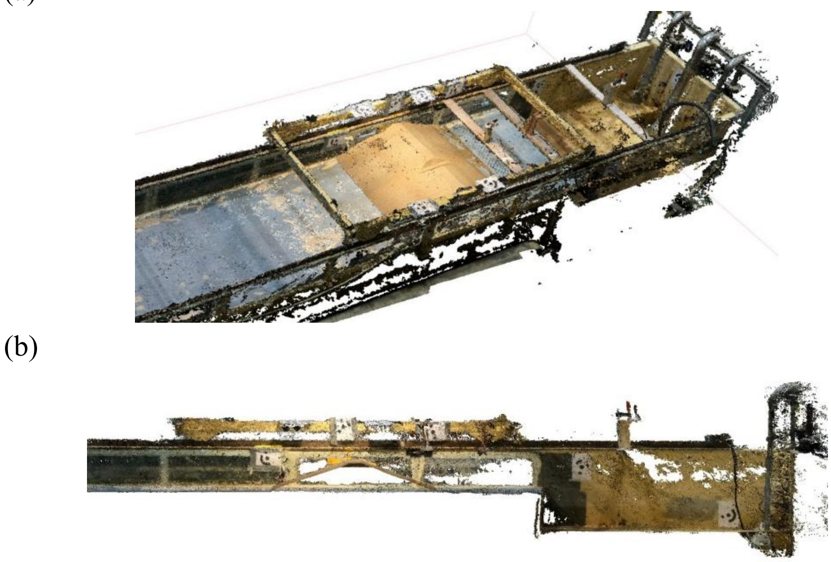

Figure 6.4 Small-scale experimental flume and embankment: (a) global view and (b) lateral view (flow direction right to left).

6.5.1 Close-range SfM-photogrammetry application

The morphological evolution of the embankment was continuously monitored using a close-range Structure-from-Motion (SfM) photogrammetry system. The acquisition setup comprised nine GoPro Hero 9 cameras fixed in stationary positions on the support structure (see Figure 6.4a) around the embankment to ensure complete coverage of the scene. The image processing and 3D reconstruction workflow followed the methodology detailed in Chapter 3 Chapter 4 . To capture the rapid dynamics of the small-scale breaching process, 3D models were reconstructed at a high temporal resolution, with time intervals ranging from 5 to 10 seconds.

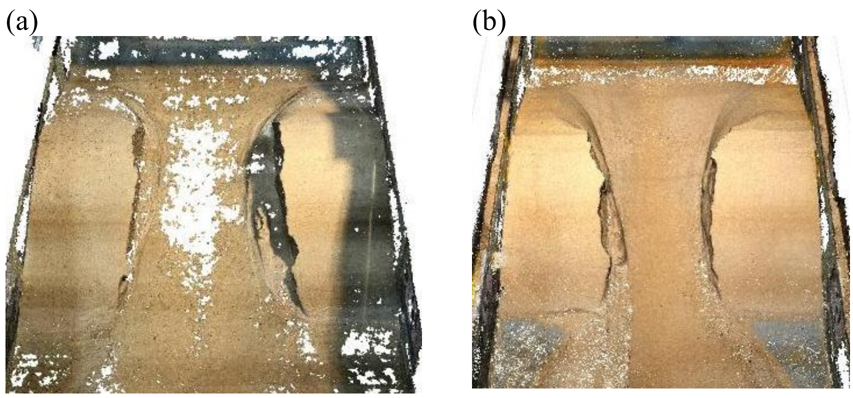

(c) (d)

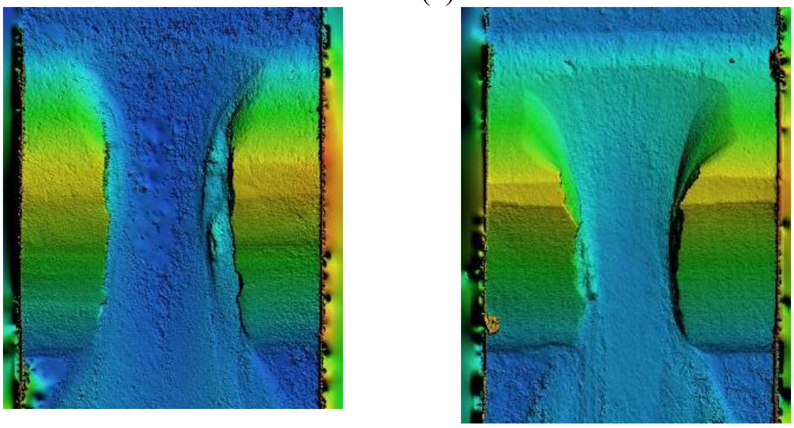

Figure 6.5 Topographic characterization of the final breach state: (a, c) dense point cloud and Digital Elevation Model (DEM) for fine sand embankments; (b, d) corresponding models for medium sand embankments.

High-resolution photogrammetric outputs, including the dense point cloud and Digital Elevation Models (DEMs), are illustrated in Figure 6.5. These models represent the final morphological state of the breached embankments constructed from fine and medium sand, respectively.

6.5.2 Optical fiber application

While the medium-scale experiments relied on embedded colored balls to track bed elevation (as detailed in Chapter 5), the small-scale campaign incorporated Distributed Optical Fiber Sensors (DOFS) as a more advanced, high-resolution monitoring technique. This method, investigated and validated by Delpierre et al. (under review), was deployed in a subset of the small-scale experiments to complement the above-water data derived from photogrammetry.

At least two tests per sand type were conducted to evaluate the sensor's performance and to verify that the presence of the fiber did not mechanically influence the overall breach formation and development. As illustrated in Figure 6.6, the fiber was installed in a snake-like configuration at four distinct vertical elevations at the end of the embankment crest to intercept the bed level at specific altitudes (an average vertical spacing of 4 cm). By analyzing the strain and strain rate recorded along the fiber, the system successfully captured critical physical processes, including breach deepening, lateral widening, and flow infiltration through the embankment body (see. Figure 6.6).

The application of the optical-fiber technique was a collaborative work conducted with Nathan Delpierre, Master students (Arthur Eugène and Cyril Anspach) and researchers from Politecnico di Milano (Alessandro Scaioli, Lorenzo Panzeri, Laura Longoni). The details of the procedure are provided in Delpierre et al. (under review).

(a)

(b)

(c)

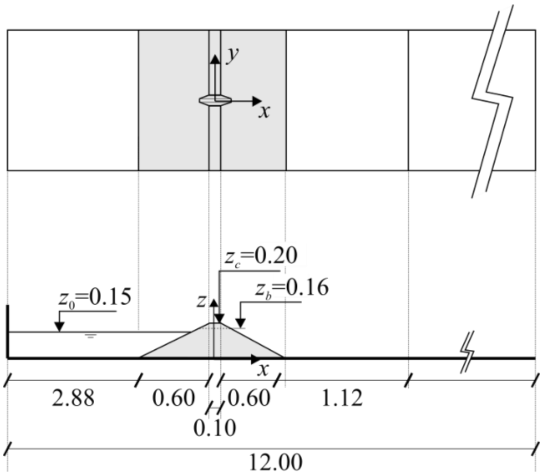

(e)

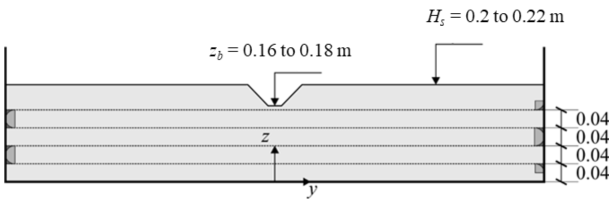

Figure 6.6 Application of Distributed Optical Fiber Sensors (DOFS) for monitoring temporal bed evolution: (a) the fiber support system, (b) post-test view of the breached embankment and exposed fibers, (c) flume dimensions and (d) the idealized design layout (note: as-built configuration varied slightly) (Source: Delpierre et al., 2026).

6.6 Experimental Design and Protocol Validation

The complete experimental program is summarized in Table 6.4. The test naming convention (e.g., *fS_Q_s_3*, *mS_Q_s_OF_10*) is structured to identify the key parameters: *fS* and *mS* denote the sediment type (fine or medium sand), *Q* indicates the constant inflow boundary condition, and *s* designates the small-scale facility. For experiments instrumented with Distributed Optical Fiber Sensors, the identifier *OF* is included. The final integer serves to distinguish between individual test runs. It should be noted that while aspects of the experimental procedure and preliminary analysis were described by Anspach and Eugène (2025) in the framework of their master's thesis, the results and analysis presented in this chapter are original contributions by the author.

The analysis of the experimental results revealed minor variations in the final constructed embankment height across the test series, with vertical deviations of up to 2 cm. However, the dimensions of the initial pilot channel were maintained strictly identical across all experiments to ensure consistent breach initiation conditions. The specific features of each experiment as well as the test cases addressed in this chapter are provided in Table 6.4.

Table 6.4 Small-scale embankment breaching experimental program conducted at LEMSC (UCLouvain).

Test No.	Date (DD-MM)	Test Acronym	Q_{in} (m^3 s^{-1})	d_{50} (mm)	z_{crest} (m)	z_b (m)	Remarks
1	10-02	*fS_Q_s_1*[a]	0.004	0.31	0.190	0.145	Slight initial overtopping of the entire crest.
2	11-02	*NA*	0.003	0.31	NA	NA	Inflow decreased during the test; two sensors were not working correctly. This test left out from analysis.
3	13-02	***fS_Q_s_2***[b]	0.004	0.31	0.200	0.155	Test repeatability
4	17-02	***fS_Q_s_3***[b]	0.004	0.31	0.200	0.152	Test repeatability
5	19-02	***fS_Q_s_OF_4***[b]	0.004	0.31	0.220	0.165	Optical fiber application
6	20-02	***fS_Q_s_OF_5***[b]	0.004	0.31	0.198	0.146	Optical fiber application
7	24-02	*fS_Q_s_OF_6*	0.005	0.31	0.205	0.156	Optical fiber application and inflow influence
8	25-02	*fS_Q_s_OF_7*	0.002	0.31	0.210	0.163	Optical fiber application and inflow influence
9	13-03	*NA*	0.004	0.31	NA	NA	Trial to test bed profiler function and PIV application. This test was left out from analysis.
10	01-04	***mS_Q_s_8***[b]	0.004	0.61	0.216	0.163	Test repeatability with medium sand
11	08-04	***mS_Q_s_9***[b]	0.004	0.61	0.221	0.172	Test repeatability with medium sand
12	15-04	***mS_Q_s_OF_10***[b]	0.004	0.61	0.230	0.182	Optical fiber application
13	15-04	***mS_Q_s_OF_11***[b]	0.004	0.61	0.230	0.184	Optical fiber application

[a] Test results from fine sand embankments and optical fiber application are presented in the paper by Delpierre et al. submitted to the Journal of Hydraulic Research (under review).[b] Results of corresponding experiments are addressed in this chapter

6.6.1 Construction and compaction of small-scale embankments

The small-scale embankments were constructed following a rigorous protocol designed to ensure structural homogeneity and experimental reproducibility. Prior to construction, the initial moisture content of the soil was adjusted to match the Optimum Proctor water content.

A custom support system was installed to laterally confine the soil during the construction phase (see Figure 6.7a and b). The embankment was built in loose layers of approximately 7 cm, which were compacted down to a final layer thickness of 5 cm. Compaction was performed manually using a custom drop-weight tool (Figure 6.8a), which weighs 10.23 kg and has a contact surface area of 15 × 22 cm. To simulate the standard Proctor energy, the tool was dropped from a height of ±40 cm. Each layer received three uniform passes over the entire surface to guarantee consistent densification and stability. Overall, a high compaction level close to the optimum proctor was obtained in all tests.

Once the full height was reached, the final geometry was shaped using a template installed on a rail system to trim excess material and ensure a smooth, precise slope. Finally, the initial pilot channel was carved into the crest using the specific guide illustrated in Figure 6.8b.

(a)

(b)

Figure 6.7 Custom lateral support system and embankment construction: (a) schematic design and (b) embankment configuration in practice prior to final slope shaping.

(a) (b)

Figure 6.8 Embankment preparation tools: (a) custom manual drop-weight compactor and (b) cutting guide for the initial pilot channel.

6.6.2 Fine sand embankments: tests repeatability

The experimental repeatability for the fine sand series was assessed in terms of reservoir water level evolution and breach outflow. The analysis includes four test cases, two of which were instrumented with Distributed Optical Fiber Sensors (*fS_Q_s_2*, *3* and *fS_Q_s_OF_4*, *5*).

As illustrated in Figure 6.9a, the reservoir inflow was maintained constant across all tests. The resulting water level evolution (Figure 6.9b) indicates a high degree of repeatability: the rising limbs follow an identical gradient, while only insignificant variations (as reported in Table 6.5) are observed during the recession phase.

A minor deviation was noted in *fS_Q_s_OF_5*, which underwent a more progressive depletion than the other tests. While *fS_Q_s_2, fS_Q_s_3*, and *fS_Q_s_OF_4* followed an identical construction protocol, procedural adjustments were introduced for *fS_Q_s_OF_5* and subsequent tests. Indeed, due to the fragility of the optical fiber sensors, the compaction effort in the immediate vicinity of the fiber was intentionally reduced to prevent damage and optimize construction time. This localized reduction in density likely facilitated erosion, explaining the attenuated hydraulic response observed in this specific test. Additionally, a systematic vertical shift in the water level curve for *fS_Q_s_OF_4* was observed, corresponding to a slightly higher initial crest elevation.

The reservoir inflow remained constant and identical among all tests as shown in Table 6.3. With regards to the overall trend, the average water level evolution in the reservoir indicates a very close reproduction (see Table 6.5) of the process across the four tests. The rising part of graphs follows the same gradient while insignificant variations in the falling part can be observed across tests. The test *fS_Q_s_OF_5* underwent a more progressive depletion phase than other tests. This could be related to the compaction variation in proximity of the fiber which needs more delicate construction process. The embankment crest elevation was overall higher in *fS_Q_s_OF_4* than other experiments which resulted systematically in a vertical shift in the water level curve.

(a)

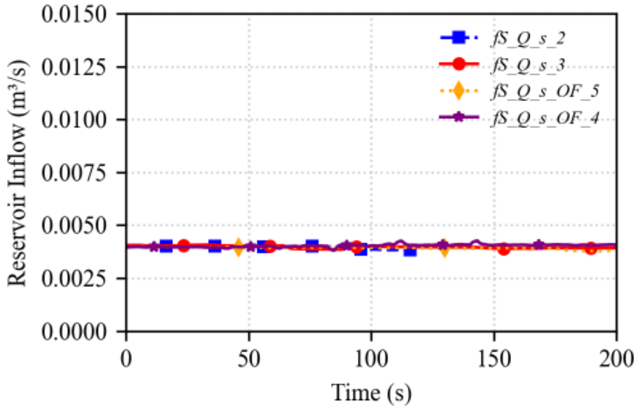

(b)

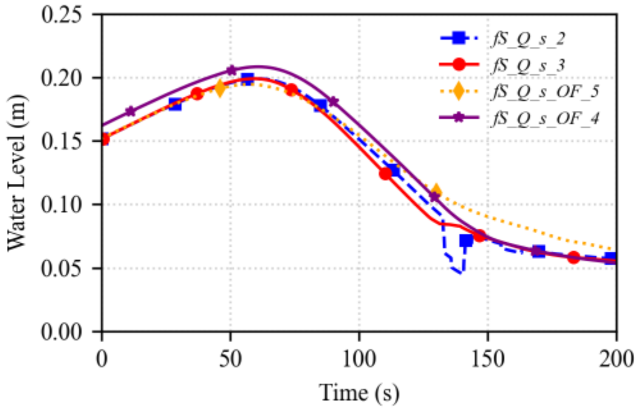

(c)

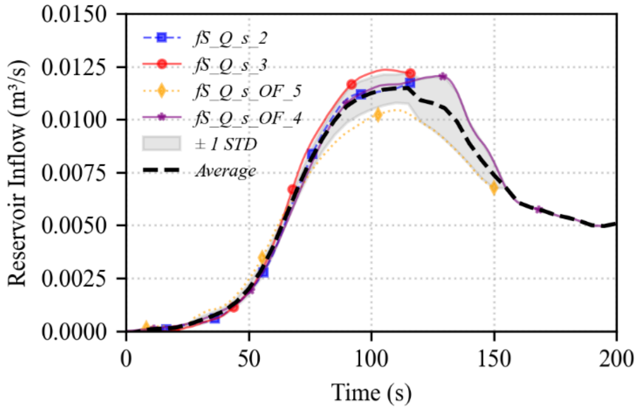

Figure 6.9 Flow characteristics including (a) reservoir inflow, (b) water level evolution (average water level STD of 0.0054 m), and (c) breach outflow in experiments *fS_Q_s_2*, 3 and *fS_Q_s_OF_4,* and *5* with a mean STD of 0.000406 m^3/s.

6.6.3 Medium sand embankments: tests repeatability

Although subjected to identical constant inflow conditions (Figure 6.10a), the medium sand (*mS*) embankments were constructed with a slightly higher initial geometry compared to the fine sand series. Specifically, the crest and pilot channel elevations were approximately 2.5 cm higher. Notably, the embankments instrumented with optical fibers (*mS_Q_s_OF_10* and *11*) exhibited the highest initial elevations within the dataset.

Consequently, higher absolute reservoir water levels were recorded for the medium sand tests (see Figure 6.10b). Despite this vertical shift in magnitude, the temporal evolution of the water level remained highly consistent across all experiments, indicating good repeatability of the hydraulic process. A distinct inflection point in the water level signal is recognizable around $t = 80$ s in all medium sand tests. While present in *mS_Q_s_8* and *mS_Q_s_9*, this feature is particularly pronounced in the optical fiber experiments (*mS_Q_s_OF_10* and *mS_Q_s_OF_11*). It is worth noting that a similar hydrodynamic signature was previously observed in small-scale tests conducted using a similar sediment (Delpierre et al. 2024).

Regarding the breach outflow, the pre-peak behavior is consistent across the series (Figure 6.10c). However, *mS_Q_s_OF_10* and *mS_Q_s_OF_11* exhibited a higher peak discharge, which is directly linked to the steeper time derivative of the water level drawdown (*dz*/*dt*) in these specific tests.

Furthermore, in contrast to the fine sand results, the peak outflow in all medium sand tests was followed by a rapid recession, resulting in a significantly shorter duration of maximum discharge (shorter plateau). The experimental program demonstrated high repeatability across the four test repetitions. An average standard deviation of 0.000296 m³/s was maintained throughout the hydrograph durations. Relative to the average peak discharge of 0.0117 m³/s, this represents a mean variability of only 2.5%, indicating that the breaching process was highly consistent and well-controlled.

(a)

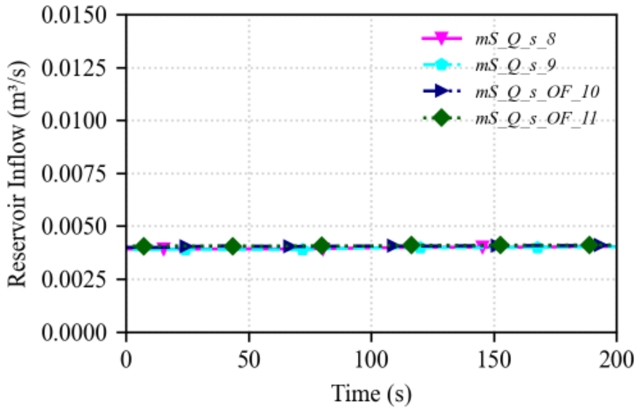

(b)

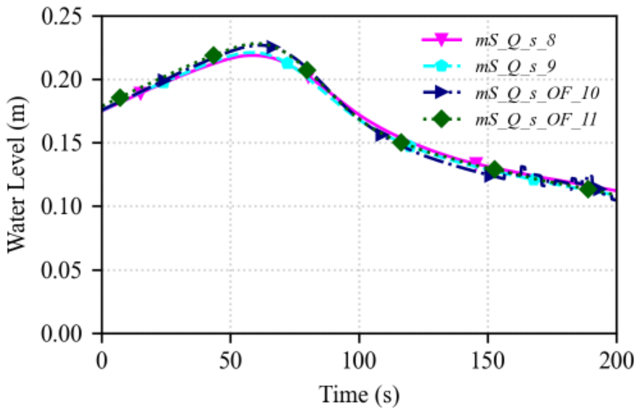

(c)

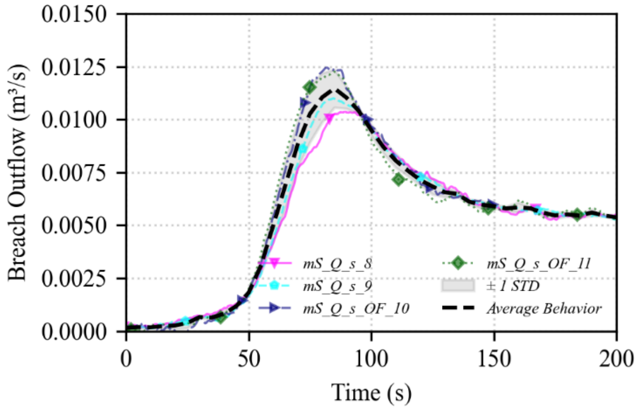

Figure 6.10 Flow characteristics in medium sand (*mS*) including (a) reservoir inflow, (b) water level evolution (average STD of 0.002234 m), and (c) breach outflow in experiments *mS_Q_s_8*, *9* and *mS_Q_s_OF_10*, and *11* with a mean STD of 0.000296 m^3/s.

The experimental program demonstrated remarkable stability and repeatability across both sediment types. The medium sand series exhibited the highest consistency, with a relative error in water level of only 1.04% and a discharge variability of 2.53%. For the fine sand series, although the variability was slightly higher (2.70% for water level and 3.55% for discharge), it remained well below the 5% threshold commonly cited for high-quality experimental data. These low coefficients of variation indicate that the boundary conditions and breach trigger mechanisms were precisely controlled, allowing for a confident analysis of the grain-size effects on the breaching process. In fact, the medium sand is less affected by "apparent cohesion" (capillary suction), which can introduce slight randomness in how soil chunks collapse during a breach.

Table 6.5 Summary of experimental repeatability and statistical consistency across all small test series.

Material	**Parameter**	**Avg. Peak Value**	**Avg. STD (σ)**	**Relative Error (CV)**
Fine Sand	Breach outflow	0.01145 m^3/s	0.000406 (m3/s)	3.55%
	Reservoir water Level	0.20000 m	0.005397 m	2.70%
	Breach outflow	0.01170 m^3/s	0.000296 m3/s	2.53%

Medium Sand	Reservoir water Level	0.21400 m	0.002234 m	1.04%

6.7 Morphological Evolution and Macro-Scale Erosion Mechanisms

The temporal evolution of breach development for fine and medium sand in the small scale experiments is illustrated in Figure 6.11 and Figure 6.12, respectively. In general, the macro-scale erosion mechanisms defined in Table 5.4 (Chapter 5) were well reproduced at small scale, though with distinct morphological signatures attributed to the sediment granulometry. It must be recalled that only the embankment geometry and the inflow discharge were scaled, but the same fine and medium sands were used in all experiments.

In fine sand (*fS*) experiments, headcut migration and apparent cohesion influences were consistent with the medium-scale observations. In particular, the fine sand breach evolution was dominated by headcut erosion. The process transitioned from initial gully incision on the downstream face to a distinct upstream migration of a vertical or overhanging front (Figure 6.11a, b, e, f). During the widening phase, the breach side slopes remained almost vertical and, at specific instants, exhibited negative slopes (overhangs) as can be seen in Figure 6.11 (c, d, g, h). This confirms that even at small scale, the apparent cohesion generated by matric suction governs the stability of the fine sand banks, preventing the formation of a repose-angle slope.

In contrast, the medium sand tests (*mS*) exhibited a more continuous surface erosion process, leading to a progressive lowering of the breach invert and a gentler longitudinal slope (Figure 6.12 a, b, e, f) compared to the fine sand. Furthermore, vertical erosion reaches the non-erodible flume bed at downstream slope earlier in the fine sand embankments compared to the medium sand tests. While the fine sand exhibits more rapid incision during the breach formation stage, the flume base in the medium sand embankments is generally reached only during the subsequent widening phase.

Moreover, contrary to the assumption of purely non-cohesive behavior (where banks would immediately relax to the angle of repose), the breach side slopes in the small-scale *mS* tests remained almost vertical throughout the widening phase (Figure 6.12 c, d, g, h). This observation suggests that scale effects related to apparent cohesion were non-negligible even for the medium sand

(d_{50} = 0.61 mm). As noted by Pickert et al. (2011), capillary effects remain influential for grain sizes smaller than 1 mm, which is confirmed here.

The snapshots in Figure 6.13(a-f) and Figure 6.14(a-h) illustrate the distinct mass failure dynamics. While capillary effects are present in both materials, they are significantly stronger in the fine sand, allowing larger portions of the banks to overhang for longer periods. Consequently, the fine sand failure is characterized by larger, less frequent mass block failures driven predominantly by tension forces (Pickert et al., 2011). Conversely, the medium sand exhibits more frequent, smaller mass block failures, indicating a transitional behavior resulting from a combination of tension and shearing mechanisms.

(a) t = 10 (s) (b) t = 40 (s) (c) t = 60 (s) (d) t=100s

(e) (f) (g) (h)

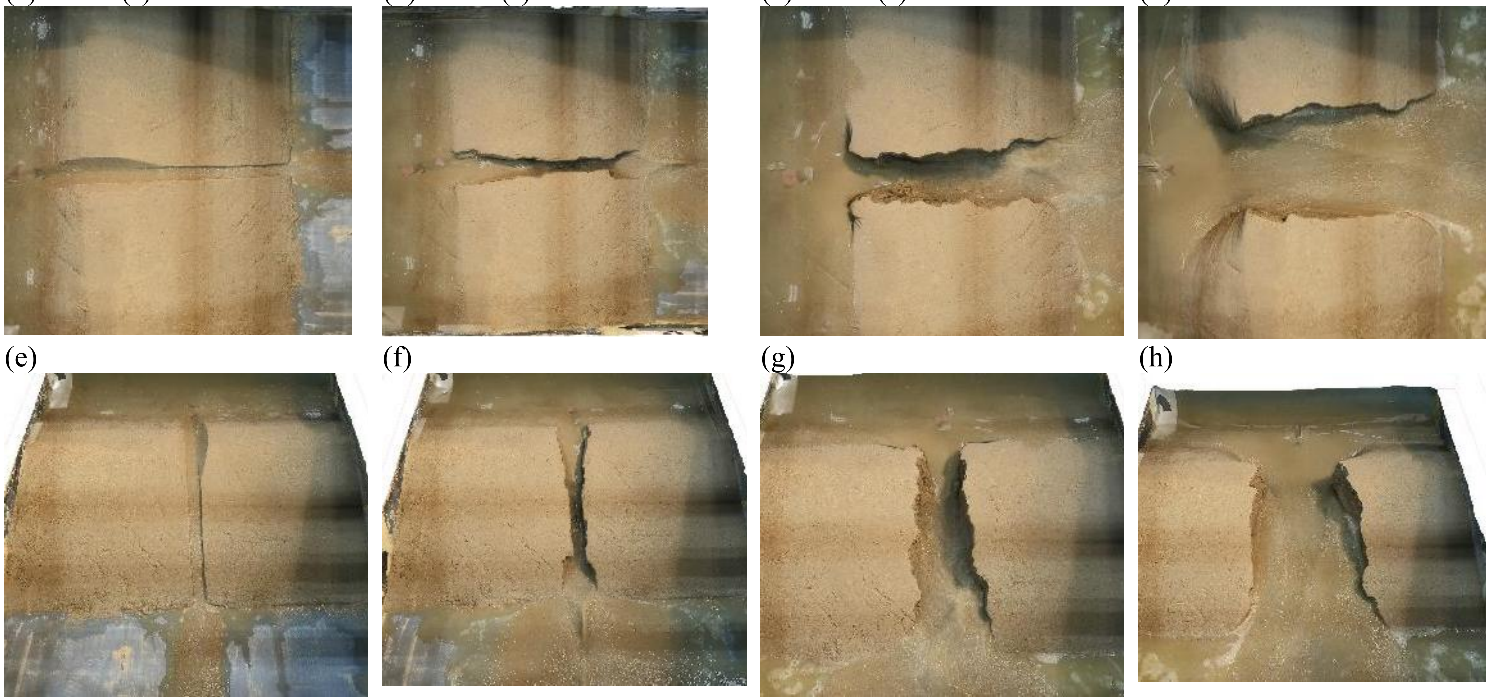

Figure 6.11 Plane and frontal view of small-scale fine embankment breaching (*fS_Q_s_3*) at key instants: (a,b,e,f) breach formation (t = 10, 40s), and (c,d,g,h) widening and reservoir drawdown (t = 60, 100s).

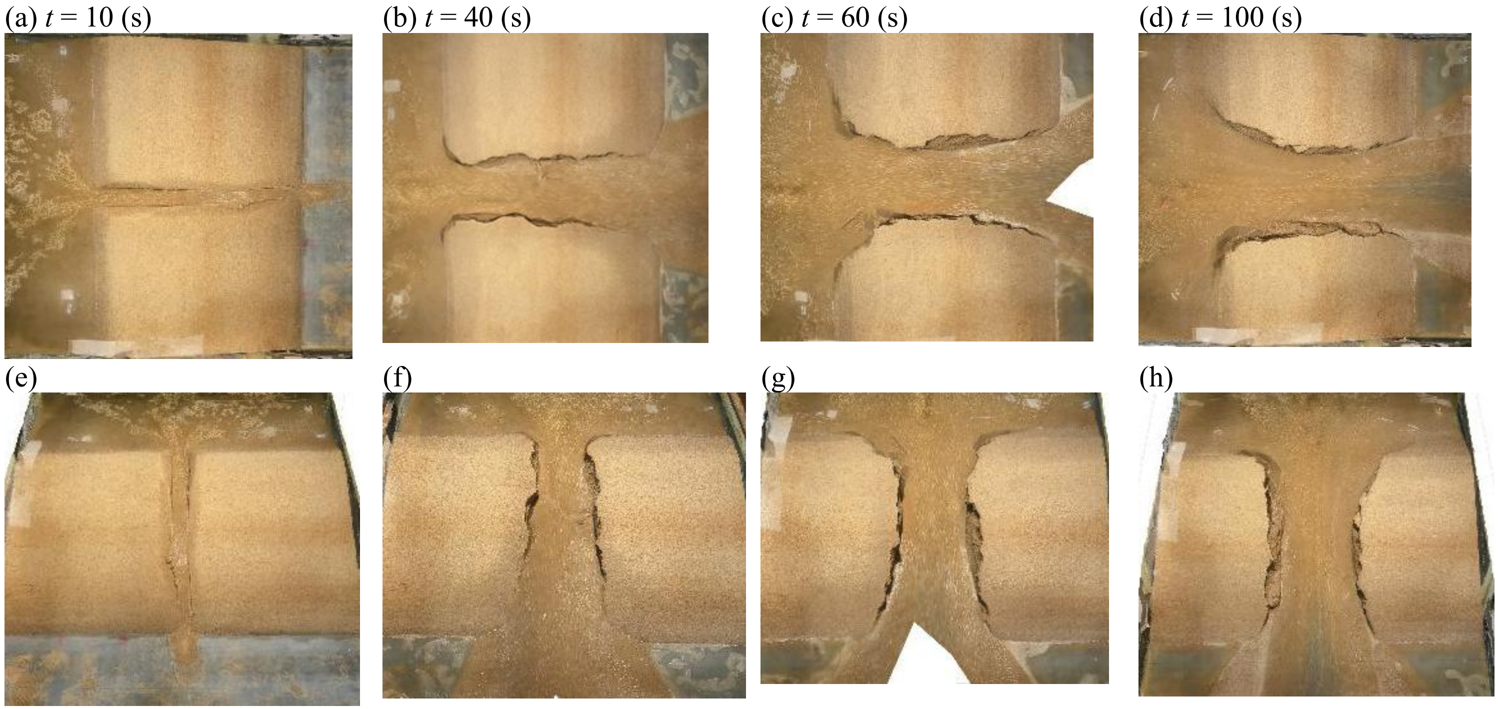

Figure 6.12 Plane and frontal view of small-scale medium embankment breaching(*mS_Q_s_9)* at key instants: (a,b,e,f) breach formation (t = 10, 40s), and (c,d,g,h) widening and reservoir drawdown (t = 60, 100s).

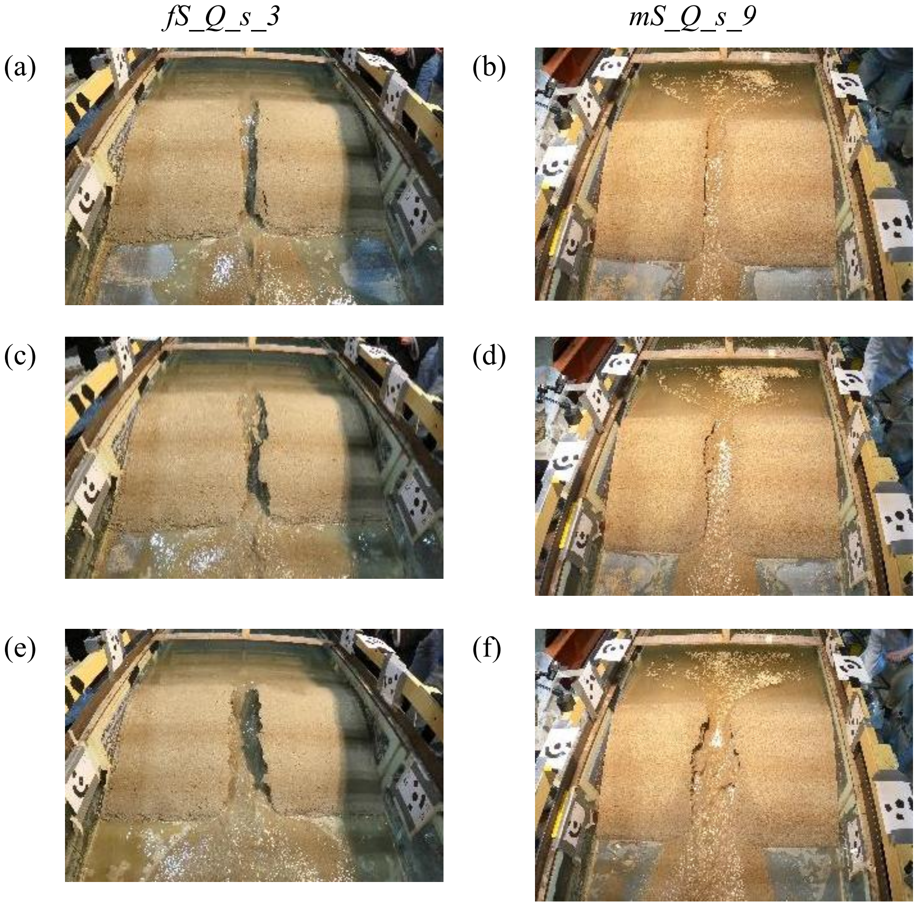

Figure 6.13 Comparison of dominant erosion mechanisms at the small scale: (a, c,e) fine sand (left) exhibiting headcut migration, impinging jet scour, and discrete block failure; versus medium sand (right) characterized by progressive surface erosion and continuous small-scale slumping.

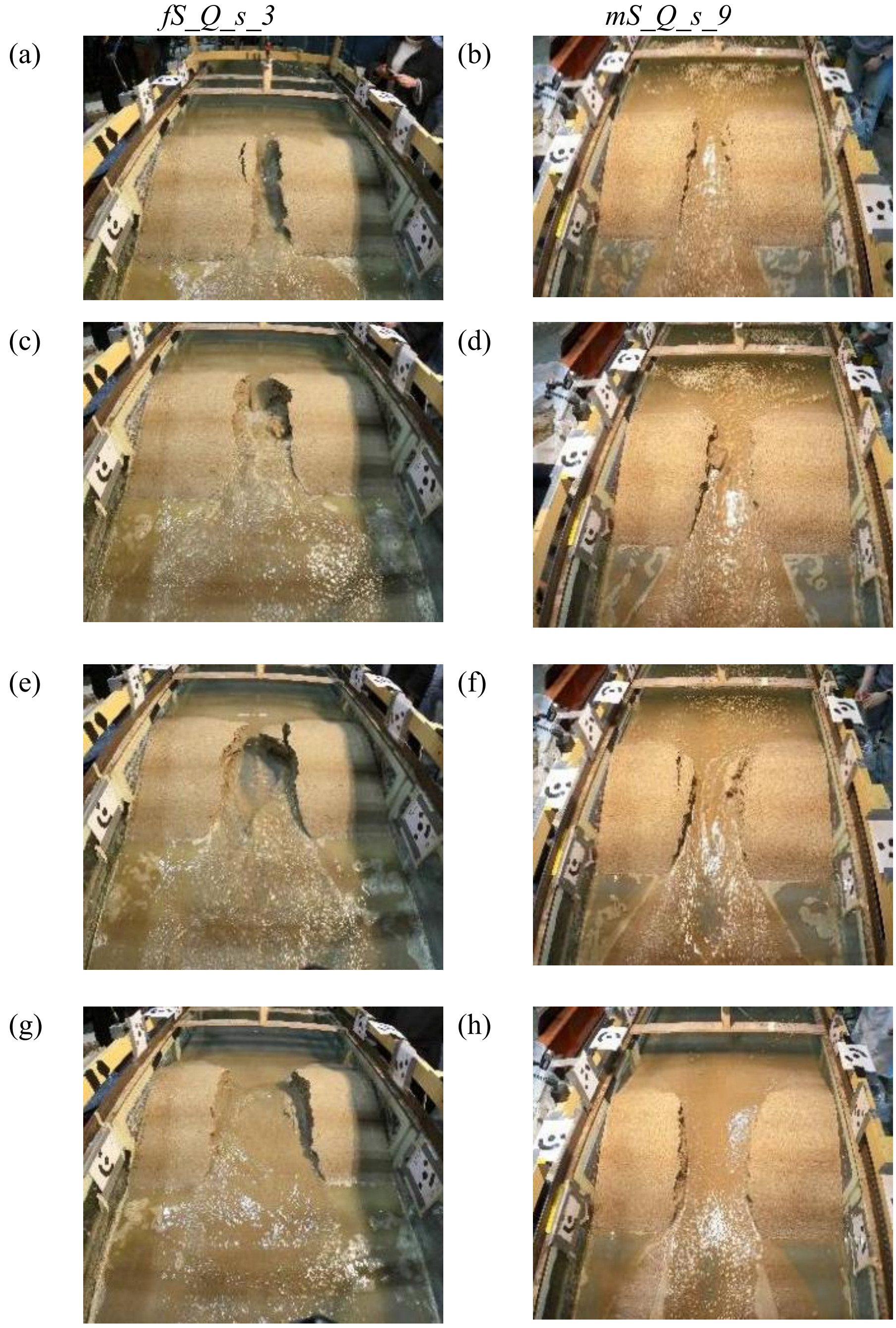

Figure 6.14 Comparison of breach widening dynamics: (a, c, e, g) fine sand (left) dominated by episodic, large tensile block failure, versus (b, d, f, h) medium sand (right) exhibiting frequent, smaller slumping driven by combined shear and tension.

The temporal evolution of the breach cross-section at the dike crest ($x = 0$ m) is illustrated in Figure 6.15a, b. In the case of fine sand (*fS*), the process is dominated by vertical incision for a prolonged duration (approximately until $t = 60$ s), maintaining a narrow channel with steep banks. Conversely, the medium sand (*mS*) exhibits simultaneous widening and deepening from the onset of the breaching phase.

Regarding the data representation, it is important to note that while negative bank slopes (overhangs) were clearly visible in the 3D dense point clouds and meshes, they are not preserved in the Digital Elevation Models (DEMs). This is an inherent limitation of the rasterization process in the photogrammetry analysis, which interpolates vertical coordinates and consequently smooths out undercut features

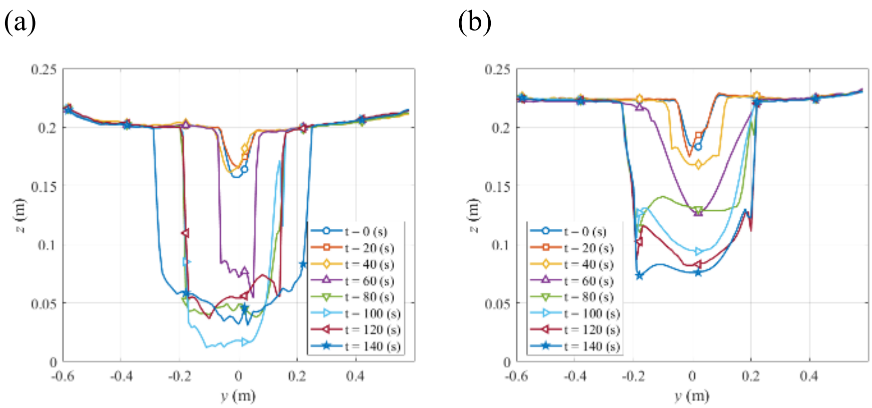

Figure 6.15 Breached dike (above water) cross-section evolution over time at $x = 0$ m (a) *fS_Q_s_3* and (b) *mS_Q_s_9*.

The longitudinal centerline profiles further highlight distinct erosion dynamics. It must however be kept in mind that the profiles illustrated in Figure 6.16 were extracted from the photogrammetry measurements and thus represent mostly the free-surface elevation rather than the true bed elevation. Still, as the water depths are small along the downstream slope, it can be assumed that the profiles are representative of the bed profiles.

The fine sand profiles capture the formation and upstream migration of a sharp headcut, particularly evident at $t = 60$ s and $t = 80$ s. In contrast, the medium sand profiles exhibit a more progressive erosion pattern, characterized by the rotation of the breach invert around a pivot point located near the embankment toe, consistent with observations by Coleman et al. (2002).

(a)

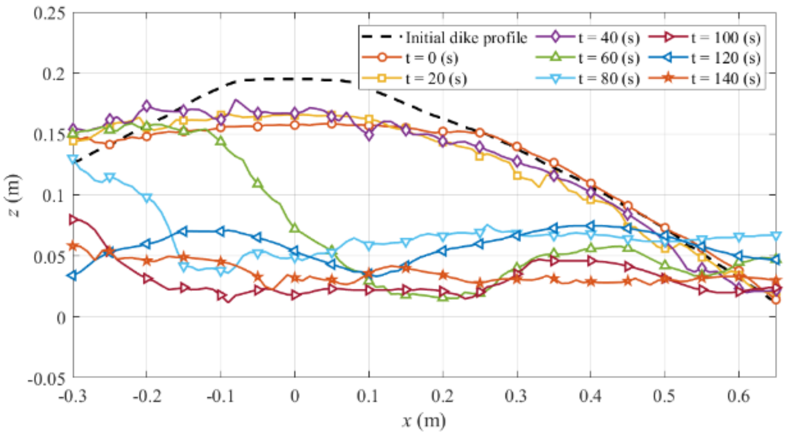

(b)

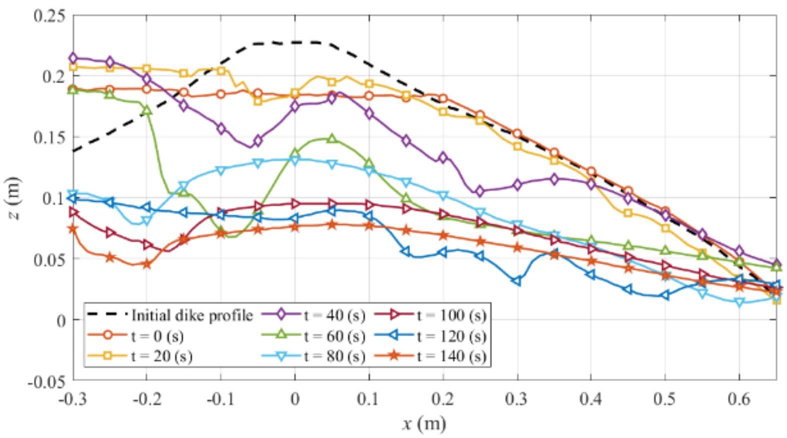

Figure 6.16 Longitudinal evolution of the flow profile along the breach channel axis ($y = 0$ m) in case of (a) *fS_Q_s_3* and (b) *mS_Q_s_9*.

6.8 Flow Characterization

To verify the hypothesis that the breaching process is gravity-controlled, the Froude number (Fr) was evaluated at specific instants when the erosion front intersected the optical fiber levels in experiment *fS_Q_s_OF_4 and mS_Q_s_OF_11*. Indeed, at these times, the exact breach depth is known which allows for a more accurate estimate of the wet area in the breach. The wet cross-sectional area at these instants was determined by integrating the surface topography from photogrammetry with the bed elevation recorded by the optical fibers, applying the trapezoidal extrapolation method detailed in Chapter 5 to determine the wet area. It must be recalled that the optical fibers were located at the mid-section of the dike. Because of the acceleration of the flow from the reservoir to the downstream slope, a control section (Fr = 1) is expected at the transition between the subcritical flow in the reservoir and the supercritical flow on the downstream slope.

As summarized in Table 6.4, in fine sand, the breach flow at mid-crest location remained supercritical (F r> 1) throughout the analyzed sequence. This means that the control section is located towards the upstream end of the initial pilot channel as can de deduced from the headcut migration process illustrated in Figure 6.17. The observed values of the Froude number confirm that the process is governed principally by gravitational and above all inertial forces rather than viscosity (the Reynolds numbers range from 9000 to 40000). The results indicate a phase of rapid flow acceleration, with velocities increasing significantly between $t = 42$ s and $t = 52$ s. However, the subsequent decrease in velocity and Froude number (at $t = 68$ s) suggests temporary flow deceleration. This fluctuation is attributed to local geometric modifications induced by mass block failures, which momentarily obstruct the channel or increase hydraulic resistance before being washed away.

Conversely, in the medium sand embankment, the breach flow remained subcritical (Fr < 1) throughout the entire process, maintaining a relatively uniform Froude number with an average value of 0.51. This indicates that the control section is located towards the downstream end of the initial pilot channel, either because of the erosion process or because of the formation of a hydraulic jump at the location of the crest as can be observed at $t = 60$ s. While the Reynolds numbers for the medium sand (7000 to 25000) were lower than those observed in the fine sand, they remained well above the laminar limits, ensuring that the flow was still turbulent.

Table 6.6 Flow characterization at fiber touching instants ($x = 0.05$ m) for *fS_Q_s_OF_4* and *mS_Q_s_OF_11*.

Test	Bed level (m)	Time (s)	Breach Outflow (m^3/s)	h_m (m)	V (m/s)	Fr	Re
fS_Q_s_OF_4	0.15	42	0.0010	0.0192	0.47	1.1	9.03E+03
	0.12	52	0.0022	0.0135	1.23	3.4	1.66E+04
	0.08	58	0.0032	0.0175	1.29	3.1	2.26E+04

	0.06	68	0.0057	0.0444	0.92	1.4	4.08E+04
mS_Q_s_OF_11	0.155	32	0.0008	0.021	0.35	0.77	7.27E+03
	0.104	45	0.0014	0.030	0.24	0.44	7.19E+03
	0.074	52	0.0026	0.050	0.27	0.38	1.33E+04
	0.030	64	0.0080	0.069	0.36	0.43	2.48E+04

6.9 Scale-Effects in Embankment Breaching Experiments

To investigate potential scale effects, the results from the small-scale (model) experiments (UCLouvain) were upscaled to the dimensions of the medium-scale (prototype) tests conducted at the Hydraulic Research Laboratory of SPW MI (presented in Chapter 4 Chapter 5).

Considering that the breaching process is dominated by gravitational and inertial forces, this comparative analysis applies the Froude similarity criteria as defined in Table 6.1, utilizing a geometric scale factor of λ_L = 5, corresponding to the ratio of the embankment heights ($\lambda_L = H_p/H_m$). These scaling laws were applied to both the hydraulic boundary conditions (inflow, water level) and the morphodynamic parameters (breach width, erosion rate) to assess the degree of similarity between the two scales.

6.9.1 Analysis of the Froude similarity for the flow hydrodynamics

A detailed summary of the specific scale ratios for the governing parameters, alongside an assessment of their adherence to similitude laws, was provided in Table 6.1. Figure 6.18 (a-d) presents a comparative analysis of the Froude-scaled reservoir water levels and breach outflow hydrographs, distinguishing between the medium and fine sand embankments.

To prevent minor variations in the constructed crest elevations from biasing the interpretation of the results, the peak water levels in tests with higher crests were normalized to a standard reference embankment height of 0.20 m. .

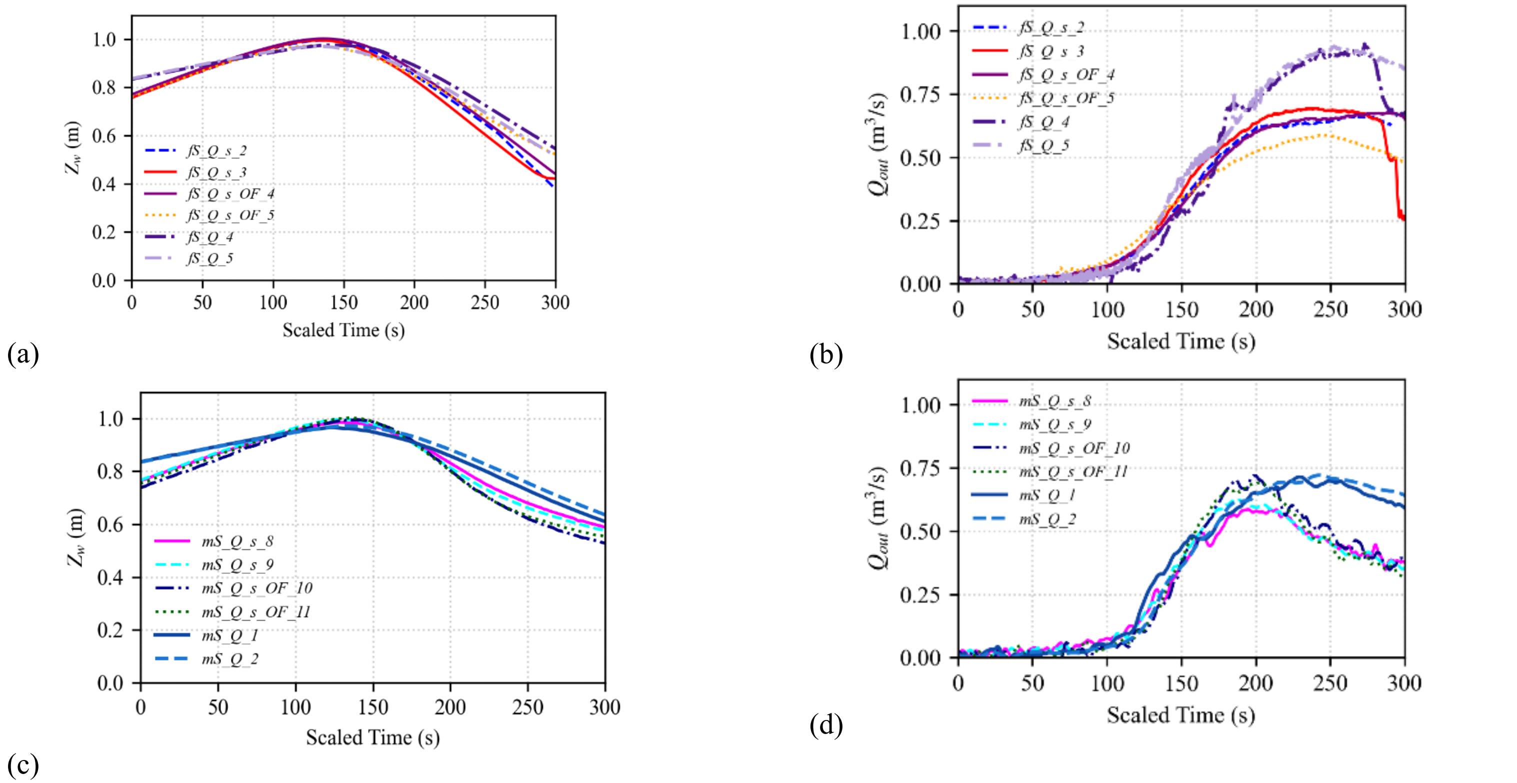

Figure 6.18 Investigation of scale effects: comparison of Froude-scaled hydraulic evolution between small-scale (model) and medium-scale (prototype) experiments: (a) reservoir water level and (b) breach outflow for fine sand; (c) reservoir water level, and (d) breach outflow for medium sand

Regarding the reservoir water level (Z_w), the dimensional scale ratio (λ_L = 5) successfully aligns the peak water levels across scales for the fine sand embankments. However, the temporal evolution reveals significant disparities over the event duration. As can be observed in Figure 6.18a, the rising phase, corresponding to the breach formation stage during which water accumulates in the reservoir because the breach outflow is still lower that the inflow, exhibits different rates between the small and medium scales. This divergence is highly likely attributable to distortions in the reservoir surface area (A_{res}). If the reservoir surface area does not scale exactly by λ_L^2 = 25, the storage capacity relative to the inflow differs, altering the time-derivative of the water level (dz/dt) in the mass balance equation.

In the medium sand series, while the pre-peak behavior is consistent, the post-peak depletion is notably faster at the small scale (see Figure 6.18c). This rapid drawdown suggests that for the more erodible medium sand, the breach widening rate at the small scale was rapid relative to the available reservoir volume, accelerating the drainage phase compared to the prototype.

Overall, it can be concluded that the dimensional scale ratio can be applied to the reservoir water level.

In contrast to the water level results, the maximum breach outflow magnitude was not successfully replicated in the small-scale fine sand experiments. While the rising limbs of the upscaled hydrographs align closely with the medium-scale tests, the peak discharge remained substantially lower (25% lower in small models) across all small-scale tests, regardless of the presence of optical fibers (*fS_Q_s_2, fS_Q_s_3* and *fS_Q_s_OF_4, fS_Q_s_OF_5*) . This also shows that the higher value of water level in test *fS_Q_s_OF_4,* did not significantly influence the breach outflow.

As regards the medium-sand tests, the standard small-scale tests (*mS_Q_s_8, mS_Q_s_9*) exhibited a lower maximum breach outflow compared to the medium-scale experiments. Furthermore, the duration of the peak discharge plateau was notably shorter, indicating a rapid depletion of the available storage relative to the breach expansion rate.

In contrast, the tests equipped with optical fibers (*mS_Q_s_OF_10, mS_Q_s_OF_11*) successfully replicated higher peak discharge values, however with a different shape of the outflow hydrograph. This increase is directly linked to the pronounced inflection point observed in the water level evolution around t = 200 s; this feature, likely representing a temporary stabilization of the breach banks, maintained the hydraulic head for a longer duration, thereby driving a higher peak flow once the expansion resumed.

In all *mS_Q_s* experiments, the peak outflow plateau exhibited a notably shorter duration compared to both the *fS_Q_s* series and the medium-scale benchmarks(*mS_Q_1*), implying a more rapid depletion of reservoir storage relative to the breach evolution process.

As demonstrated by the reservoir mass balance, the breach outflow hydrograph is fundamentally governed by the reservoir surface area and the rate of water level depletion (dz/dt). However, the specific interaction between the breach expansion rate and water level depletion (dz/dt) the term would need further investigation across the tested conditions.

Based on these observations, it can be concluded that with the present setup, conducting embankment breaching at a small scale ($H_{Em,m}$ = 0.2 m) systematically underpredicts the breach outflow. Therefore, extrapolating these laboratory results to prototype dimensions must incorporate a safety factor to account for inherent scale effects related to the reservoir dimensions. Future studies should prioritize perfect scaling of the reservoir surface area to decouple these hydraulic boundary effects from the morphodynamic processes.

Finally, it is observed that small variations in the initial pilot channel dimensions, in particular the invert elevation, have a negligible impact on the maximum breach outflow and event duration, as these peak conditions occur after the breach is fully formed. This low sensitivity is demonstrated by the consistency of the breach outflow hydrographs across all tests during the initial breach formation phase.

6.9.2 Analysis of the Froude similarity for the breach widening and deepening

The breach width and the time were scaled up respectively by $\lambda_L = 5$ and $\lambda_t = \sqrt{5}$ for small-scale tests to verify if the Froude law is applicable to the breach vertical and lateral erosion.

Figure 6.19 compares the temporal breach deepening at the medium scale (tracked via embedded balls at $x = -0.25$, +0.25, and +0.75 in *mS_Q_1* and *fS_Q_5* tests) with the small scale (tracked via optical fibers at the equivalent x = +0.25 m location in *fS_Q_s_OF_4* and *mS_Q_s_OF_10* and *11*).

In the fine sand embankments (Figure 6.19a), the small-scale pilot channel initially exhibited slower vertical erosion and remained largely intact at $x = +0.25$ m, whereas the medium-scale pilot channel deepened significantly earlier and faster. Despite this initial delay, both scales subsequently transitioned into a phase of rapid vertical deepening. This consistent behavioral shift indicates that the fundamental vertical erosion mechanics for fine sand were successfully replicated across both scales.

Conversely, in the medium sand embankments, small scale vertical erosion at $x = 0.25$ m initiated immediately upon overtopping, matching the onset timing of the medium scale. Interestingly, the subsequent rate of vertical deepening in the small-scale tests (*mS_Q_s_OF_10* and *11*) proved to be faster and with almost linear pattern, than the corresponding medium-scale test (*mS_Q_1*).

(a)

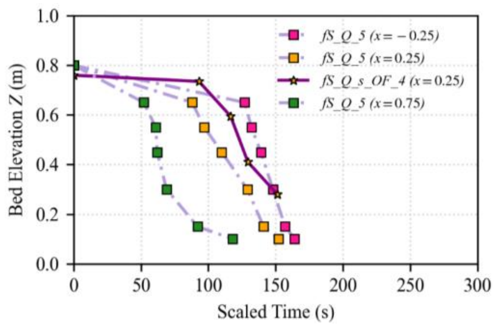

(b)

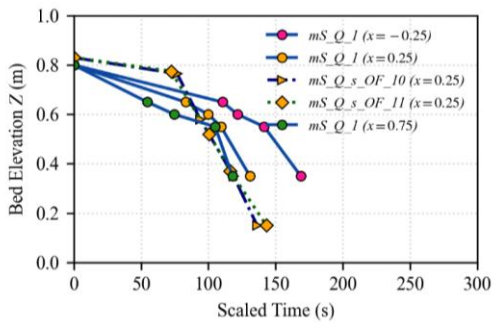

Figure 6.19 Evolution of the breach invert elevation across small and medium scales for (a) fine sand and (b) medium sand.

Moreover, Figure 6.20 compares the breach widening at the three reference locations $x = -0.25$, $+0.25$, and $+0.75$ m selected at the medium-scale (prototype). These graphs illustrate the divergence in widening rates between the two geometrical scales for medium sand and fine sand.

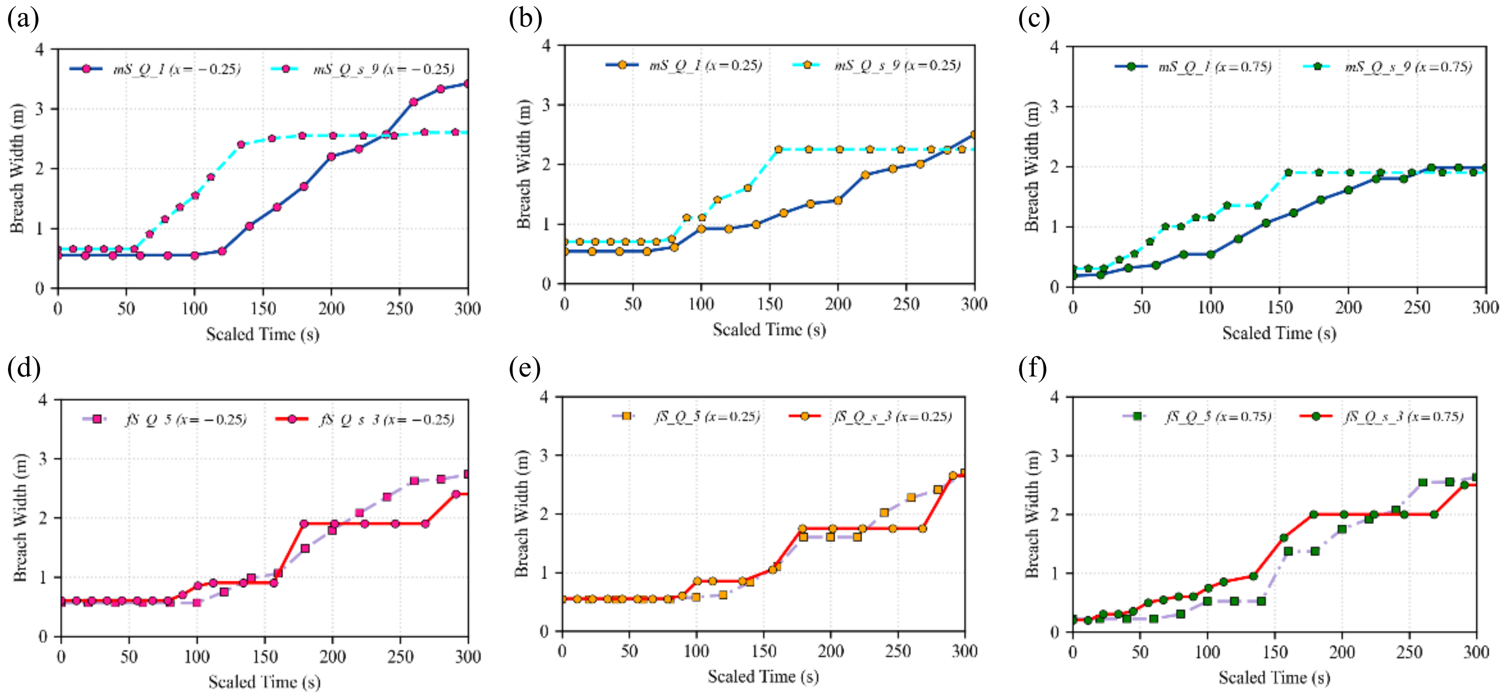

Figure 6.20 Comparative temporal evolution of breach width for medium-scale (prototype) and small-scale (model) experiments according to the Froude similitude at three reference locations: (a) $x = -0.25$, (b) $x = +0.25$, and $x = +0.75$ m

It can be observed that the breach formation phase is shorter in the small-scale tests for the medium sand than in prototype tests (*mS_Q_s_9* vs. *mS_Q_1*) but that for fine sand, the scaling reveals a similar time evolution (*fS_Q_s_3* vs. *fS_Q_5*).

Regarding the medium sand, the upscaled small-scale test (*mS_Q_s_9*) exhibits a steeper widening slope than the prototype (*mS_Q_1*). This confirms that for the medium sand, Froude upscaling tends to over-predicts the erosion rate in the small-scale model despite a disproportional smaller reservoir area. Indeed, the material erodes rapidly through mixed particle-by-particle (shear failure) and mass loss during breach formation and through relatively large mass block failure during breach widening phase.

In case of fine sand, deriving a direct correlation is more complex, despite the fact that the average widening rate are very similar. The small-scale test (*fS_Q_s_3*) is controlled by large, episodic mass block failures that disrupt the linear widening trend (see Figure 6.20a red curve). Specifically, two major mass failure events resulted in sudden, distinct jumps in the breach width evolution. The fine sand possesses apparent cohesion which remains relatively constant across scales. In the small model, this cohesion is disproportionately strong relative to the hydraulic forces (which are scaled down by λ^3), acting as a "stabilizing" force that retards widening and leading to more sudden, very large mass block failure. Therefore, while both *fS_Q_s_3* and *fS_Q_5* exhibit "staircase" widening patterns characteristic of cohesive-like bank collapse (toppling/undermining), the small-scale test displays stronger, distinct jumps followed by prolonged stable plateaus. This implies that the volume of the failure blocks did not reduce according to the geometric scale. Instead, the widening process was governed by the detachment of disproportionately large soil blocks, confirming a major geotechnical distortion: the hydraulic forces were scaled down, but the material's cohesive strength remained constant. However, as already observed, the overall widening rates are comparable.

The final breach width at the three locations, indicates that the breach expanded to its full capacity in nearly all experiments. The notable exception was the small-scale medium sand test (*mS_Q_s_9*); at the upstream location ($x = -0.25$), the final width remained slightly narrower than that observed in the reference medium-scale test (*mS_Q_1*).

6.9.3 Apparent cohesion distortion

Previous analyses indicate that the experimental results are significantly influenced by negative pore pressures, which induce apparent cohesion within the embankment constructed from sand. While this parameter was not directly measured in the current research, its effects can be accurately contextualized using the findings of Pickert et al. (2011). Pickert et al. quantified pore-water pressures at a high spatiotemporal resolution using tensiometer probes (T1, T2, T3, and T4) in 0.3 m high embankments. They tested fine (*fS*, d_{50} = 0.185 mm), medium (*mS*, d_{50} = 0.365 mm), and coarse (*cS*, d_{50} = 0.640 mm) sands. The similarities in both model scale and sediment granulometry make their study a highly relevant comparative baseline for the current setup (see Figure 6.21).

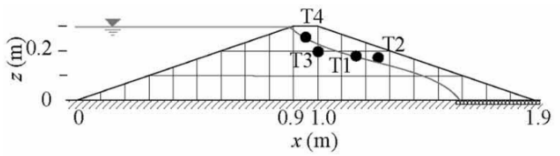

Figure 6.21 Embankment profile and dimensions in Pickert et al 2011 experiments.

As shown in Figure 6.22, Pickert et al. observed distinct morphological differences based on grain size measured using a fringe projection system. For the fine sand, breach development was primarily vertical, maintaining a nearly constant width characterized by vertical or overhanging side slopes. Conversely, the coarse sand demonstrated concurrent vertical and transversal widening with steep, but non-overhanging, slopes. The behavior of their medium sand fell between these two extremes. Overall, an increase in sand size resulted in accelerated lateral breach widening.

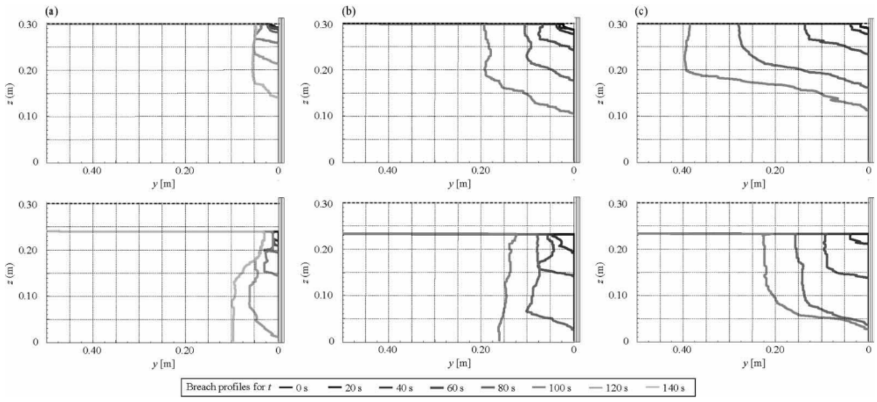

Figure 6.22 Downstream view of breach cross-sectional profiles in steps of 20 s at x = 0.90 m (above) (upstream embankment crest) and x = 1.2 m (below) (the reference x=0m is located at the beginning of the mbankment) for (a) *fS*, (b) *mS* and (c) *cS* as reported in Pickert et al 2011.

The pore-pressure evolution for the medium sand reported by Pickert et al. 2011 (see Figure 6.23) serves as a reliable proxy for the fine sand tests (*fS_Q_s_2* and *3*) conducted in the current study. Pickert et al. 2011 demonstrated that pore-water pressure (u_w) decreases during breaching due to two primary mechanisms. First, the development of the breach channel drains the embankment, lowering the seepage line and expanding the capillary zone. Second, and more importantly, the flow continuously undermines the breach side slopes. This creates overcritical slopes where apparent cohesion temporarily prevents mass collapse until the unsaturated zone can no longer support the overhanging soil.

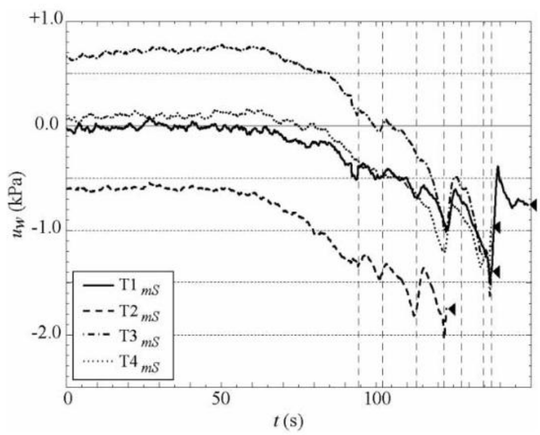

Figure 6.23 Time series of measured pore-water pressure T1 to T4 for *mS* as reported in Pickert et al 2011.

The development of u_w is governed by the capillary height h_{cap}, as $u_w = h_{cap}\,\gamma_w$ which is a function of the grain size distribution and surface tension. Because the capillary height, h_{cap} remains identical in both small- and large-scale models when using the exact same sediment, the stabilizing effect of apparent cohesion becomes disproportionately large in small-scale models relative to the absolute mass and volume of the slope failures. While Pickert et al. did not publish the explicit pore-pressure time series for their coarse sand—which closely matches the medium sand (mS) used in tests *mS_Q_s_8* and *9* of this chapter, the fundamental principles of this scale distortion remain directly applicable to the observed behaviors.

As established in Section 6.3.1 while hydraulic driving forces scale according to Froude similitude (λ_L^3), soil resistance properties (specifically cohesion) do not obey Froude scaling. Consequently, if a reduced-scale model is built with the same soil classification in the fine sand ranges (approximately 0.1 to 0.4 mm) the resisting forces become disproportionately large compared to scaled hydraulic driving forces.

This distortion can be quantified using the geotechnical Stability Number (N_s), defined as the ratio of destabilizing gravitational forces to stabilizing cohesive forces in Eq. (6-21)

While γ_s and c' remained identical in model and prototype, the scale reduction by 5 ($\lambda_L = 1/5$), results in a Stability Number in the model that is effectively one-fifth of the prototype's. This implies the model banks are five times more stable, leading to disproportionately higher slope stability in the small-scale model than the prototype, a behavior consistent with the 'apparent cohesion controlled' regime described by Pickert et al. (2011).

However, the impact of this distortion varies significantly with the grain size. While apparent cohesion over-stabilizes fine sand models, it produces an adverse, destabilizing effect in intermediate medium sands (0.5 to 1 mm). In reduced-scale models, the shorter water trajectories combined with the relatively high permeability of the medium sand lead to much faster infiltration rates. As noted by Schmocker and Hager (2012), this rapid saturation quickly dissipates matric suction, triggering earlier slope instability and more frequent, continuous mass block failures. For sands coarser than 1 mm, apparent cohesion effects become largely negligible (Schmocker and Hager, 2012).

In reduced-scale models, shorter water trajectories within the embankment body may result in faster infiltration and saturation of the soil during breaching process. While the fine sand had benefited from the apparent cohesion effects

Ultimately, these observations demonstrate why strict geometric scaling of sediment size, often used to satisfy dynamic similarity criteria, frequently fails. Instead of accurately replicating prototype erodibility, artificially reducing the grain size introduces or amplifies apparent cohesion. This effectively reinforces the model material relative to the scaled hydraulic forces, hindering the natural erosion process rather than facilitating it (Ettema 2000, Coleman 2002, Morris et al. 2007).

6.9.4 Reservoir size distortion and hydrograph attenuation

As highlighted by the results of this chapter and Section 5.9, the reservoir area distortion can have significant effects on the water level evolution and breach outflow in experimental modeling. Spatial constraints in many laboratory facilities can result in inadequate reservoir area and shape when modeling breaching process. To verify this influence of reservoir scale distortion (about 45% error in the present case) in the small-scale experiments, a dimensionless factor (η) proposed by Walder and O'Connor (1997) was used to investigate the influence of this distortion on the erosion regimes. This factor represents (defined in Eq. (6-22)) the influence of reservoir dimensions on the overall breach evolution through linking erosion rate to the total volume of released water and reservoir level drop.

$$\eta = \frac{k \cdot Vol_{tot}}{g^{1/2} \cdot \Delta h^{7/2}} \qquad 6\text{-}22$$

where k is the erosion rate in m s^{-1}, Vol_{tot} is the total volume of released water in m^3, Δh the water level drop in the reservoir in m, and g the acceleration of gravity (m s^{-2}).

The value of η indicates the dominant control mechanism for the peak discharge (Q_p):

- $\eta \ll 1$: indicates a small reservoir or slow erosion regime. The reservoir drains significantly during the breach formation, and the peak discharge (Q_p) is strongly damped by the falling head. This means that the peak breach outflow is highly sensitive to the erosion rate and the reservoir volume.
- $\eta \gg 1$: indicate a large reservoir or fast erosion regime. The breach fully forms before significant drawdown occurs. Indeed, the reservoir acts as a constant-head source.

In the following analysis, the erosion rate is considered as the lateral erosion rate of breach channel (at the intersection of upstream slope and the crest) and the total volume of released water is calculated as the integral of the breach outflow hydrograph.

The resulting η values for the model (i.e. small scale) and the prototype (i.e. medium scale) are reported in Table 6.7. In all cases, η remains larger than unity, indicating a large reservoir and fast erosion regime.

With fine sand (*fS*), at small-scale test (*fS_Q_s_3) η* is the lowest and closest to unity (η=1.8) while in medium-scale (prototype) test (*fS_Q_5*) η is larger (η = 6.5). This proximity to the transition threshold (η=1) confirms that the small-scale experienced a slower erosion rate and the reservoir drained rapidly enough to dampen the peak discharge, introducing a distortion does not present in the prototype.

For the medium sand (*mS*), the values of η at both scales are closer in magnitude and significantly higher than unity ($\eta \gg 1$). This implies that the reservoir size distortion had a smaller impact on the peak magnitude for the coarser sand material, though the limited volume still accelerated the recession limb of the hydrograph.

In general, this factor (η) is smaller in fine sand compared to the medium sand at both scales, indicating a greater influence of the reservoir volume, specifically during the reservoir drawdown, on the peak breach outflow in fine sand. This is confirmed by the significant difference in peak discharge observed in Figure 6.16b and d.

Table 6.7 Parameters to determine the reservoir influence factor η, and the resulted values in model (small) and prototype (medium) scale in fine and medium sand.

Test	Vol_{tot} (m^3)	d (m)	k (m/s)	η
mS_Q_1	87.367	0.356	0.0163	16.9
mS_Q_s_9	0.783	0.09	0.0099	11.3
fS_Q_5	100.73	0.459	0.0133	6.5
fS_Q_s_3	0.835	0.126	0.0047	1.8

In conclusion, scaling the reservoir surface area correctly is required to sustain the hydraulic head for the correct scale duration. This would maintain the maximum erosion potential for a longer period, leading to a wider final breach and a larger total flood volume.

Nevertheless, correcting the reservoir size distortion is a necessary condition, but not sufficient for dynamic similarity. With fine sand, increasing the reservoir volume would increase the peak outflow, but due to cohesive effects (Stability Number distortion), the widening rate would still be smaller. The resulting hydrograph would likely be broader and flatter than the Froude-scaled prototype hydrograph, with a peak occurring later than predicted.

In the case of medium sand, correcting the reservoir size distortion would prevent the rapid water level drawdown that currently acts as a hydraulic driver. More sediments would be entrained, and deeper vertical erosion would be observed. This vertical erosion extends until the flume level at the downstream slope before the water level drawdown quickly shifts the erosion towards the upstream slope as observed currently.

However, removing the reservoir area constraint would likely cause the small-scale model to significantly over-predict the Froude-scaled peak outflow, as the breach would open too fast and too wide before the water level drops. This highlights the complexity of these scaling issues, that would deserve further investigations.

6.9.5 Viscous effects and Transport Capacity

The reservoir distortion effect is likely balanced by scale effects in sediment transport. Assuming that the breaching of non-cohesive material is governed principally by sediment transport, dynamic similarity requires the accurate simulation of tractive (shear) stresses between model and prototype. As noted by Pugh (1985), dynamic similarity in sediment transport requires that the hydraulic conditions at the walls (or physical boundaries of the eroded cross-section) be comparable across scales. Specifically, if the flow at both scales yields a sedimentologic Reynolds number exceeding the critical threshold ($Re^* \geq 70$ or 100), the boundary layers are hydraulically rough; consequently, the dimensionless shear stress becomes independent of viscous effects, and non-dimensional sediment transport rates remain similar. This regime consistency ensures that the temporal evolution of erosion is appropriately scaled. However, if the model operates in a transitional regime ($5 < Re^* < 70$ or100) while the prototype is in a fully rough regime, the influence of viscosity in the model distorts the tractive forces, leading to an overestimation of the scaled sediment transport rate.

It is important to note that within the transitional hydraulic regime, the critical dimensionless shear stress (τ_c^*) is a non-linear function of the grain Reynolds number (Re^*). As illustrated by the Shields diagram, τ_c^* exhibits higher values at the lower end of Re^*, decreases to a minimum, and then slightly increases before ultimately becoming constant in the fully rough turbulent regime ($Re^* \geq 70$ or 100). Consequently, a reduced-scale model operating at a lower Re^* can inherently possess a higher critical threshold for sediment motion, artificially requiring larger applied shear stresses to initiate and sustain erosion compared to the prototype (see Figure 6.1). The following section evaluates the Shields parameters for the fine and medium sand embankments at both experimental scales. This analysis characterizes the boundary flow regimes and transport capacities, ultimately verifying how accurately the sediment transport rate scales between the models.

As shown in Eq. (6-10) the bed shear stress (τ_b), and therefore the non-dimensional shear stress is directly related to the shear velocity (u_*) at the bed level (boundary). Within the turbulent boundary layer, the velocity distribution normal to the channel bottom follows a logarithmic profile, exhibiting strong velocity gradients close to the bed. However, under transitional and hydraulically smooth conditions, the near-bed velocity distribution deviates from this logarithmic law due to the dominant influence of viscous forces within the viscous sublayer. In order to determine the shear velocity u_* when the average flow velocity is known, Eq. (6-23) linking the depth-averaged flow velocity U and the shear velocity u_* can be used (Jansen et al 1979):

$$\frac{U}{u_*} = \frac{1}{\kappa}\ln\left(Ae^{-1}\chi\frac{h}{k_s}\right) \qquad 6\text{-}23$$

With χ defined as

$$\frac{1}{\kappa}\ln\chi = \left(\frac{1}{\kappa}\ln(\mathrm{Re}_*) - 3.00\right)e^{-0.217(\ln \mathrm{Re}_*)^2} \qquad 6\text{-}24$$

where τ_b is the bed shear stress τ_{b*} is the dimensionless bed shear stress, d is the grain diameter, k_s represent the sand equivalent roughness of the boundary usually equal to thr grain diameter , κ is von Karman constant (usually taken as 0.4), A is a constant that can be considered as equal to 30, h is the water depth. Finally, χ represents the flow regime close to the bed.

Table 6.8 reports the flow Reynolds number and grain Reynolds number calculated for the embankments constructed from fine and medium sand at two scales during breaching experiments.

Table 6.8 Flow Reynolds and Grain Reynolds numbers across scales in fine sand.

Test	h_m (m)	V (m/s)	Fr	Re	u^* (m/s)	Re*
fS_Q_s_OF_4	0.019	0.47	1.1	9.03E+03	0.03	8.47
	0.013	1.23	3.4	1.66E+04	0.08	23.93
	0.017	1.29	3.1	2.26E+04	0.08	24.10
	0.044	0.92	1.4	4.08E+04	0.05	14.86
fS_Q_5	0.09	3.39	3.67	2.96E+05	0.17	51.74
	0.16	2.34	1.85	3.83E+05	0.11	32.93
	0.22	1.78	1.21	3.94E+05	0.08	24.65
	0.22	2.10	1.43	4.62E+05	0.09	28.48
	0.29	1.85	1.09	5.45E+05	0.08	24.24
	0.22	1.96	1.32	4.35E+05	0.09	26.46
mS_Q_s_OF_11	0.021	0.35	0.77	7.27E+03	0.023	13.57
	0.030	0.24	0.44	7.19E+03	0.015	8.73
	0.050	0.27	0.38	1.33E+04	0.016	9.12
	0.069	0.36	0.43	2.48E+04	0.020	11.65
mS_Q_1	0.104	1.94	1.92	2.02E+05	0.103	62.15
	0.100	1.71	1.73	1.71E+05	0.091	55.07
	0.181	2.39	1.79	4.32E+05	0.118	71.5
	0.181	2.13	1.60	3.85E+05	0.105	63.71

The analysis reveals two distinct hydrodynamic regimes:

- Flow: The flow Reynolds number (Re) in the model is approximately one order of magnitude lower than in the prototype. Nevertheless, in all cases, Re exceeds the threshold of 2000 considered as the turbulent threshold in open channel flows, according to e.g. Chow (1959), confirming that the flow remained turbulent at both scales.
- Sediment Boundary Layer: the grain Reynolds number (Re*) for the fine and medium sand in the model lies within the range $5 < \mathrm{Re}^* < 100$

(transitional regime) at both scales, indicating a strong shift towards the lower limits, especially in medium sand at small scale.

These findings demonstrate that at the medium scale (functioning here as the prototype baseline), both fine and medium sands operate near the upper limit of the transitional regime, approaching fully rough turbulent conditions ($5 < Re^* < 70$)**.** In contrary, the small-scale models shift toward lower Re^* values, increasing the relative influence of viscous forces within boundary layer.

For the fine sand, this shift is minimal. The viscous influence on the sediment boundary layer remains comparable across both scales, ensuring hydrodynamic consistency. This explains the high degree of morphological reproducibility, most notably the persistent of headcut migration, observed in the fine sand tests regardless of model size.

For the medium sand, however, the scale reduction causes a severe drop in the grain Reynolds number (from an average of 63 at the medium scale to 11 at the small scale). This pronounced shift alters the boundary layer mechanics and lowers the relative threshold for motion on the Shields curve. Consequently, this leads to disproportionately larger effective shear stresses and a significant increase of both the sediment transport and erosion rates in the small-scale model.

A comparison of the Froude numbers across fine sand tests confirms a fundamental similarity: the breach flow remained supercritical ($Fr > 1$) at both scales.

However, the medium sand exhibited a significant hydrodynamic shift, transitioning from supercritical flow at the medium scale to subcritical flow ($Fr < 1$) at the small scale. As established earlier, the geometric distortion of the reservoir surface area, and thus the resulting limitation on available water volume, disproportionately impacted the overtopping flow conditions for the small-scale medium sand model. Properly scaling the reservoir area in future studies is essential to resolve this boundary condition dissimilarity and ensure an accurate simulation of the breach flow dynamics.

6.9.6 Sediment scaling according to settling velocity adjustment

To address potential scale effects related to sediment transport, settling velocities settling velocity (w_s) were calculated for both tested sands using Eq.(6-19) and (6-20), following the Froude-scaling adjustment procedure proposed by Pugh (1985). Applying this approach to downscale the sediments at a geometric scale ratio of $\lambda_L = 0.2$ yields the equivalent particle sizes presented in Table 6.9. Notably, scaling the medium sand based strictly on Froude-scaled settling velocity results in a required model diameter of 0.26 mm. This calculated diameter closely approximates the 0.31 mm fine sand actually utilized in this research, suggesting the fine sand serves as an appropriate scaled representation of the medium sand's transport behavior.

Table 6.9 Upscaling of settling velocities (w_s) for the tested fine and medium sands under Froude similarity ($\lambda_V = \lambda_L^{0.5}$) and their equivalent model and prototype sediment diameters.

Grain size (mm) used in this research	w_s (m s^{-1})	Reduced w_s ($\lambda_L = 0.2$)	Model diameter (mm)	Upscaled w_s ($\lambda_L = 5$)	Prototype diameter (mm)
0.31	0.0456	0.0204	0.17	0.102	0.80
0.61	0.0843	0.0377	0.26	0.189	1.81

Such scaling approach could be applied to determine the equivalent sediment sizes for a prototype embankment in coarse sediments (for example with a $\lambda_L = 5$ to the medium-scale tests herein). Based on Froude-scaled settling velocities, the fine and medium sands utilized in this study correspond to coarser prototype sediments with equivalent diameters of 0.80 mm and 1.81 mm, respectively.

Finally, the question raised earlier regarding "how to ensure the dynamical similarity of at least those properties which will be measured and/or observed?", must be reframed based on the dominant erosion mechanism in case of earthen embankment breaching: "Is the process governed by particle-by-particle surface erosion and sediment transport (shear stress controlled), or is it driven by mass failure and soil detachment in the form of large blocks (stability controlled) over a large portion of the process?"

6.10 Dimensional Analysis

To generalize the findings, the dimensional analysis derived by Pickert et al. (2011) was used to compare the results of the current research to the existing data from the literature. Pickert et al. (2011) recognized the following key parameters describing breach processes in sand embankments. Limitations such as a constant upstream reservoir water level, no water at the downstream embankment base (negligible tailwater effect) and a non-cohesive embankment material are applied.

The breach discharge Q_{Br} depends on the embankment height H_{Em}, the reservoir water level h_{Res}, the water level downstream of the embankment h_u, the width of the embankment crest b_{Emcr}, the downstream slope inclination DS, water density ρ_w, water surface tension σ_w, water kinematic viscosity ν_w, a characteristic grain diameter d, grain density ρ_s, acceleration due to gravity g and time t, leading to

$$Q_{Br} = f(H_{Em}, h_{Res}, h_u, b_{Emcr}, DS, \rho_w, \sigma_w, \nu_w, d, \rho_s, g, t) \quad \text{6-25}$$

The parameters ρ_w, H_{Em}, and g have independent dimensions and therefore were taken as basic quantities. Besides, Bechteler (1989) concluded that the potential energy of the reservoir water is mostly transferred into kinetic energy $H_{Res} \approx H_{Em} = v^2_{Br}/2g$, thus $v_{Br} \approx (g\ H_{Em})^{0.5}$. Herein, the difference between $H_{Res} \approx H_{Em}$ and $h_u \approx 0$ is constant, which can be true during of the breach formation phase and over a restricted duration within the breaching phase until the available space downstream of the embankment is flooded (tailwater reaches the embankment toe) and/or the reservoir water level decreases significantly. Therefore

$$\frac{Q_{Br}}{(gH^5_{Em})^{0.5}} = f\left(\frac{\sigma_w}{g\rho_w H^2_{Em}}, \frac{\nu^2_w}{gH^3_{Em}}, \frac{d}{H_{Em}}, \frac{t}{(H_{Em}/g)^{0.5}}\right) \quad \text{6-26}$$

The parameter $\sigma_w/(g\rho_w H^2_{Em})$ represents an interaction between the water phase and the embankment geometry. By combining it with the grain size parameter d/H_{Em}, the "relative capillary" parameter $\sigma_w/(g\rho_w dH_{Em})$ results. With $(gh^3_{Em})^{0.5}/\nu_w$ rewritten as $v_{Br}\,H_{Em}/\nu_w$ follows an overall Reynolds number (Re). Combining the other two parameters

$$\frac{Q_{Br}}{(gH^5_{Em})^{0.5}} = f\left(\frac{t}{((\sigma_w / g\rho_w d)/g)^{0.5}}\right) = f\left(\frac{t}{(h_{cap}/g)^{0.5}}\right) \quad \text{6-27}$$

results in the appearance of $h_{cap} = 4\sigma_w/(g\rho_w d_p)$ representing the capillary rise where d_p denotes the characteristic pore diameter, and the dimensionless breach time scale $t^* = t/(h_{cap}/g)^{0.5}$.

The characteristic pore diameter can be calculated by multiplying the characteristic grain size d_w with a factor a, representing the geometric conditions. For a dense material, a = 0.25–0.33 (Smoltczyk 1980).

$$d_w = \frac{1}{\sum_i^k \frac{\Delta p_i}{(\min d_i \cdot \max d_i)^{0.5}}} \tag{6-28}$$

and

$$d_p = a \cdot d_w \tag{6-29}$$

where Δp_i is the interval of percentage finer by weight and the minimum and maximum d_i correspond to the lower and upper grain-size boundaries of that interval.

Pickert et al. (2011) had shown that the choice of the characteristic pore diameter has a significant influence on the capillary height (h_{cap}).

Finally, as previously discussed, defining the dimensionless breach outflow based on the fixed embankment height (H_{Em}) is primarily applicable when the upstream water level remains constant throughout the breaching process. However, as demonstrated by the current experiments and the literature data (Table 5.6), maintaining a constant reservoir level is neither always the intended objective nor physically feasible under all circumstances (see Figure 5.31). Therefore, in scenarios dominated by a falling head (reservoir drawdown), the instantaneous reservoir water level H_{Res} must be applied as the governing length parameter to accurately capture the depleting hydraulic driving force.

The non-dimensional (half) breach outflow was plotted against the non-dimensional time parameter, as derived from the Pickert et al. (2011) study. They determined the conditions where breaching is controlled by apparent cohesion or shear stress using experimental data from their own tests, alongside data from Coleman et al. (2002), Hassan et al. (2004), and Morris et al. (2007). However, a major limitation of the databases they used was the scale of the models (embankment heights were limited to 0.6 m), and the fact that overtopping was governed by a constant reservoir level across almost all tests.

The boundaries between apparent cohesion and shear stress-controlled conditions were primarily based on the characteristic grain size (d) of the material. They determined that breaching in embankments with $d \leq 1$ mm is controlled by apparent cohesion resulting from capillary rise. For this "apparent cohesion-controlled" regime, a best-fit curve for the data was derived, as indicated in equation (6-30)

$$Q_b^* = 3.5 \times 10^{-12} \cdot t^{*3.7} \qquad \text{6-30}$$

Data from Table 5.6 were used to update their results by incorporating the new dataset produced in the current study as shown in Figure 6.24. Surprisingly, a shift to the right for all medium-scale tests ($H_{Em} \geq 1$ m, $d < 1$ mm) indicates a transition in the dominant resisting physics. While Pickert et al. (2011) attributed data points located on the right side of the diagram entirely to coarser grains ($d \geq 1$ mm) lacking apparent cohesion, the medium-scale tests in general introduce much higher flow velocities. At these high velocities (typically 1 m/s), well-compacted sand exhibits dilatancy — the soil volume must expand for shear failure to occur. This expansion draws water into the pores, creating a pressure gradient that significantly increases the dynamic shear resistance (Van Rhee 2010, Bisschop et al. 2011; 2016, and van Damme 2021).

This "dilatancy-reduced pickup" slows the erosion rate down considerably compared to what standard models predict. Consequently, the medium-scale fine sands erode slower in dimensionless time and shifted towards the right of the upper limit defined by Pickert el al. (2011), mimicking the higher resistance that Pickert et al. (2011) originally assumed belonged only to coarse, shear-stress-controlled materials (see Figure 6.24). Indeed, a combination of apparent cohesion and dilatancy-reduced pickup are dominant in fine sand at larger dimensions, including medium-scale.

Interestingly, the *fS_Q_s_3* curve perfectly follows the slope of Equation (6-30), confirming that the fine sand is governed by the exact same apparent cohesion mechanism. The leftward shift means the breach escalated faster in dimensionless time. This shift is primarily caused by the constant inflow condition (Q). An active, constant inflow forces a much faster initial vertical erosion and headcut migration compared to the constant reservoir level condition used by, for instance, Pickert et al. (2011), which typically prolong the breach formation phase.

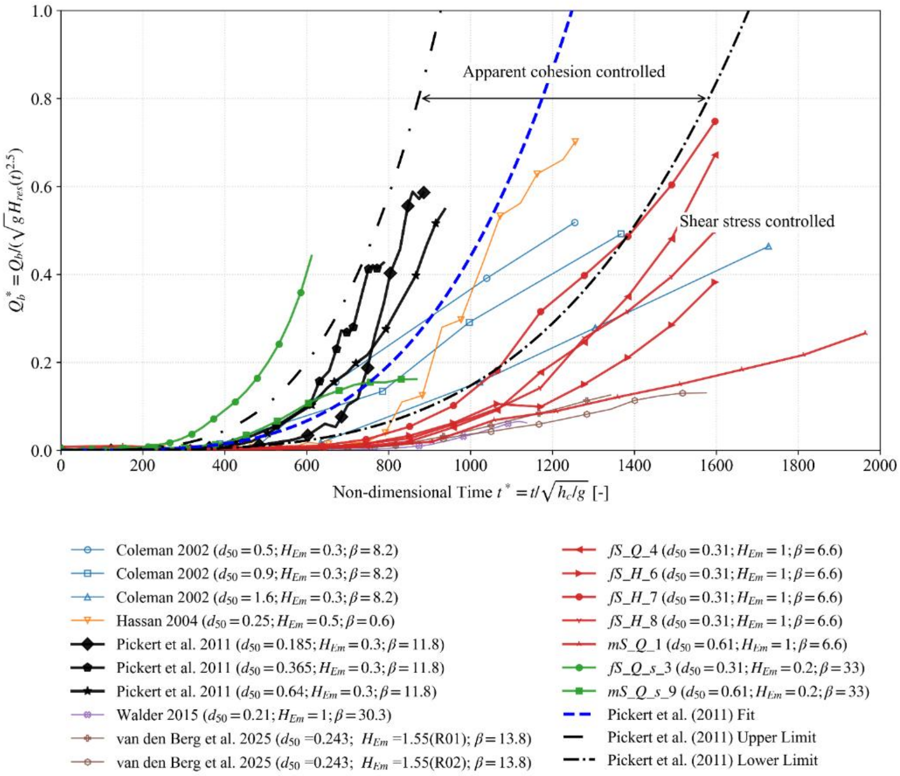

Figure 6.24 Comparison of dimensionless breach discharge hydrographs normalized with the parameter combination from Eq. (6-27), with the blue dashed line representing Eq. (6-30)

Importantly, the results demonstrate that physical scale and overtopping conditions can have a major influence on both the physical processes and the magnitude of the peak outflow, as well as the failure time.

6.11 Conclusions and perspectives

This chapter investigated scale effects in embankment breaching through a 'scale-series' approach. Medium-scale experiments ($H_{Em,p}$ = 1 m, SPW MI) were replicated at a small-scale ($H_{Em,m}$ = 0.2 m, UCLouvain) using a geometric scale factor of $\lambda_L = 5$. Identical sediment granulometries were maintained at both scales while hydraulic loads (overtopping conditions) were scaled according to Froude similitude. A dedicated campaign of new small-scale tests was conducted to ensure strict test repeatability and enable high-resolution monitoring.

The comparative analysis of hydraulic variables revealed that peak water levels in the reservoir were highly sensitive to minor variations in the dike crest height and the initial pilot channel elevation. While construction tolerances could vertically shift the peak water level, they did not influence the magnitude of the resulting breach outflow. However, the influence of reservoir size distortion was evident; the small-scale models exhibited disproportionately faster rising and drawdown limbs compared to the prototype. This effect was notably stronger in the fine sand tests than in the medium sand.

Regarding the breach hydrograph, while the formation and early widening phases showed similar trends, the peak breach outflow was not perfectly reproduced when small-scale results were upscaled using Froude similitude. Overall, breach outflow hydrograph in fine sand as small scale exhibited a higher peak and longer duration than that of medium sand. This trend is consistent with the results obtained at the medium-scale tests. However, in all small-scale medium sand experiments (*mS_Q_s*), the peak outflow plateau exhibited a notably shorter duration compared to both fine sand series and the medium-scale benchmarks, implying a disproportionately rapid depletion of reservoir storage relative to the breach evolution process toward the end.

Consequently, despite promising results, a definitive conclusion regarding the validity of Froude upscaling for breach outflow cannot be drawn without isolating the effects of reservoir geometric distortion. Future studies should prioritize perfect scaling of the reservoir surface area to decouple these hydraulic boundary effects from the morphodynamic processes. While perfect geometric scaling of reservoir length and width is constrained by the current flume dimensions, the effective reservoir area can be enlarged by shifting the embankment placement toward the downstream end of the flume. In these tests, embankments must be constructed with strict adherence to identical scaled dimensions. Monitoring of breach deepening should be enhanced by combining tracer techniques with optical fibers at reference locations, mirroring the protocols used in the medium-scale tests.

In terms of morphological evolution, the macro-scale erosion process was reproduced remarkably well at the small scale for both sediment types, though with distinct intensity differences. In fine sand (*fS*) experiments, the breach evolution was consistently dominated by headcut migration at both scales. The process transitioned from initial gully incision on the downstream face to a distinct upstream migration of a vertical or overhanging front. During the widening phase, the breach side slopes remained vertical. However, negative slopes (overhangs) were more pronounced in the small-scale model, demonstrating that apparent cohesion generated by matric suction was relatively stronger at the reduced scale, allowing larger mass blocks to resist failure for longer durations.

Medium sand material exhibited continuous surface erosion combined with mass block failure at both scales. However, scale effects were evident: the small-scale tests (*mS_Q_s*) displayed faster vertical erosion and disproportionately larger block slumping than the medium-scale prototype. While the 'pivot point' mechanism is generally associated with non-cohesive behavior, it was more distinguishable in the small-scale medium sand tests, albeit modified by the presence of cohesive-like vertical banks.

Apparent cohesion influenced both sands at both scales, preventing the formation of a natural repose-angle slope and sustaining vertical banks. This effect was notably stronger in the small-scale experiments (*mS_Q_s* and *fS_Q_s*). It was demonstrated that apparent cohesion does not scale down when Froude similitude is applied to identical sediments; rather, it becomes relatively dominant at the smaller scale, introducing an additional distortion effect. This is likely compounded by the shorter seepage path in small models, which facilitates faster infiltration and steeper hydraulic gradients, thereby enhancing the stabilizing apparent cohesion forces.

The temporal evolution of breach widening revealed distinct scale effects. In the medium sand experiments, in medium sand, the upscaled small-scale test (*mS_Q_s*) exhibited a steeper widening slope and earlier stabilization than the prototype (*mS_Q*). In contrast, the upscaled fine sand (*fS_Q_s_3*) showed a more complex widening correlation, heavily influenced by large, episodic mass block failures that disrupted the linear erosion trends observed in the prototype.

In both sands, dimensionless analysis confirmed that the grain Reynolds number remained within the transitional regime ($5<Re^*<100$) for both the model and the prototype. However, a general shift towards lower ranges of Re^* in small-scale experiments were observed. This shift in flow boundary regime was much more significant in medium sand resulting in larger effective shear stresses and a significant overestimation of both the sediment transport and erosion rates in the small-scale model.

In fine sand viscous effects at sediment boundary layer remain relatively closer. Together with the apparent cohesion impact on stabilizing forces at both scales, preserving the specific failure mechanism (headcut migration and vertical bank collapse) regardless of the geometric scale. The apparent cohesion effects seems to have adverse impact on the medium sand at small scale and worth further investigation in medium sand at two scales.

The most important observations can be summarized as below:

- **Overtopping conditions dictate timing, not mechanism:** Hydraulic boundaries (Constant Head vs. Constant Inflow) control the *kinetics* of the failure. Constant Head (H) prolongs the initial vertical incision phase, while Constant Inflow (Q) causes faster reservoir drawdown that eventually damps the peak discharge.
- **Granulometry defines the failure mode:** Fine sand (fS) failure is governed by apparent cohesion (matric suction), leading to vertical/overhanging banks and discrete, large block failures. Medium sand (mS) lacks this strong suction and fails via continuous surface erosion and smaller granular sliding.
- **Froude similarity application and interpretations:** The analysis implies that while the Froude scaling criterion can be applied to model dimensions and hydraulic overtopping conditions, its direct validity for upscaling peak breach outflow remains an interpretation rather than a definitive conclusion. It was shown that the reservoir dimension has a more significant influence than the model size on the breach outflow hydrograph. The new small-scale experiments reported in this chapter systematically underpredicted the outflow magnitude and resulted in rapid reservoir drawdown. This discrepancy is driven by two coupled, un-isolated distortions: a disproportionately small reservoir volume (which artificially accelerates drawdown) and apparent cohesion (which alters the temporal morphodynamics of the breach). Therefore, to draw a conclusion with high certainty and decouple the effects of apparent cohesion from reservoir constraints, it is a must to repeat the small-scale tests with properly scaled reservoir dimensions.
- **Apparent cohesion causes important scale distortion:** Because Froude similitude scales down the hydraulic forces but not the soil's cohesive strength, apparent cohesion becomes disproportionately strong at the small scale. This artificially over-stabilizes the small-scale banks, causing delayed but much larger, episodic mass failures compared to the prototype. The exact influence of this factor can be

determined through replication of the small-scale tests with corrected reservoir volume.

- **Viscous effects alter transport capacity in medium sand:** For fine sand, the grain Reynolds number remains comparable across scales, preserving the erosion mechanics. However, reducing the scale for medium sand forces into a lower transitional regime, altering boundary layer mechanics and artificially accelerating the relative erosion rate.
- **The Danger of Direct Extrapolation:** Relying strictly on Froude scaling to upscale peak breach outflow from the new small-scale experiments remains an interpretation rather than a definitive conclusion. Direct extrapolation is highly risky because it introduces severe, coupled distortions, specifically unrepresentative apparent cohesion, unscaled settling velocities, and disproportionately small reservoir limits. To definitively decouple these effects and bridge the scaling gap, it is a must to repeat the small-scale tests with properly scaled reservoir dimensions. Furthermore, integrating complete breach outflow hydrographs from large-scale or prototype sand embankment failures is an absolute necessity to draw a final conclusion on extrapolation.
- These existing scaling results cannot be directly applied to true cohesive soils without further investigations. In non-cohesive fine sands, the apparent cohesion is driven by highly transient matric suction. In contrast, true cohesive soils are governed by electro-chemical bonds and typically fail via distinct mechanisms, most notably headcut migration and cascading profiles. Therefore, while the macro-scale block failure kinematics look similar, the underlying resistance mechanisms and scaling laws are fundamentally different and scaling laws are fundamentally different.

Chapter 7

Conclusion and Perspectives

This research significantly advances the application and validation of close-range Structure-from-Motion (SfM) photogrammetry for monitoring morphological evolutions during earthen embankment erosion and failure across different scales. By processing extensive image datasets, highly accurate 3D models were generated to quantify the temporal evolution of a prototype levee. This successfully addresses a two-decade-long challenge of measuring levee cover erosion under wave overtopping at high spatial and temporal resolutions. Furthermore, a comprehensive experimental campaign comprising eight medium-scale and eleven small-scale embankment breaching tests was conducted. Supported by high-resolution data, these tests provide profound insights into the behavior of non-cohesive sand embankments. Critically, the medium-scale test series bridges the knowledge gap between frequently conducted small-scale tests and rare full-scale prototype experiments.

SfM-Photogrammetry application

SfM photogrammetry offered high flexibility for data acquisition. Specifically, the multi-stationary synchronized camera system proved highly advantageous, successfully merging classical photogrammetry principles with SfM to capture highly dynamic environments. A major limitation, however, is the presence of water—whether as still water pooled in erosion scour holes or as fast-moving, turbulent flow. Light refraction, reflection, and turbidity reduce model accuracy and render the technique impractical for capturing the submerged portions of the breach channel.

The technique was rigorously validated using supplementary measurements. In field tests, pointwise measurements via an RTK GNSS GPS system were used. In the medium-scale tests, accuracy was assessed through root-mean-square reprojection errors of ground control and check points within the software, alongside direct comparisons with dense point clouds from a FARO terrestrial LiDAR scanner and an iPhone LiDAR sensor. These validations confirmed centimeter-scale precision. Overall, the photogrammetry technique slightly overestimated bed elevations, yielding a mean absolute error (MAE) of only a few centimeters across different model scales. Table 7.1 summarizes the photogrammetric configurations, 3D model properties, and spatial accuracy metrics across the three experimental scales evaluated in this research (illustrated in Figure 2.2).

Table 7.1 Summary of photogrammetric configurations, 3D model properties, and spatial accuracy metrics across prototype, medium-scale, and small-scale embankment experiments.

Parameter	Prototype Scale (LLHPP)	Medium Scale (SPW MI)	Small Scale (LEMSC)
Embankment Height	1:1 scale (1-m thick cover)	1.0 m	0.2 m
Camera Configuration	10 (fixed) or 1 (mobile)	11 (fixed)	10 (fixed)
Image Resolution	5184 × 3888 pixels	5184 × 3888 pixels	5184 × 3888 pixels
Ground Resolution	1.25 mm/pix	1.25 mm/pix	0.502 mm/pix
Coverage Area	~43.9 m²	~71.3 m²	~4.28 m²
Dense Point Cloud	~9.4 million points	~2.25 million points	~9.27 million points
Reprojection Error	0.754 pix	1.21 pix	2.33 pix
Accuracy vs. RTK (MAE)	0.04 m (fixed) / 0.05 m (mobile)	N/A	N/A
Accuracy vs. FARO LiDAR	N/A	0.0114 m (mean distance)	N/A

This methodology is highly adaptable to similar challenges, such as levee overflowing, provided intermediate flow interruptions are feasible to allow cameras to capture the soil surface rather than the water. It is also effective for measuring erosion variations linked to different levee materials, protective covers, or spatial scales. Its flexibility, minimal fieldwork requirements, and robustness across various meteorological conditions make it highly favorable. For intermittent monitoring, images can be acquired using standard cameras or even mobile phones. Additionally, recent advancements integrating mobile LiDAR with photogrammetry offer a robust, cost-effective alternative. Finally, while Agisoft Metashape yielded excellent results in this research, partially or fully open-access software alternatives, such as RealityScan and Meshroom, also exist.

To overcome the inherent inability of photogrammetry to capture the submerged portions of the rapidly evolving breach channel, supplementary measurement techniques are required. At the medium scale, this was addressed by embedding colored tracer balls at known spatial coordinates within the embankment. By analyzing video footage to identify the exact release instants of these balls, the temporal evolution of the breach invert elevation was successfully tracked. At the small scale, an innovative technique utilizing Distributed Optical Fiber Sensors (DOFS)—developed through collaborative research—was implemented to continuously detect vertical erosion within the embankment. Upscaling the application of this DOFS technique to medium-scale models represents a highly promising avenue for future research.

Finally, limitations associated with capturing the dynamic water surface—such as poor texture, light reflections, and turbulent motion—were effectively mitigated by deploying floating tracers (e.g., wood chips) and utilizing strictly synchronized imaging. Ultimately, the quality and accuracy of the final 3D models are most heavily governed by photograph sharpness, high resolution, strong color contrast, and the precise, simultaneous triggering of the camera network.

Medium-scale embankment breaching experiments

These new medium-scale tests successfully bridge the critical knowledge gap between frequently conducted small-scale laboratory models and rare full-scale prototype experiments. Supported by highly accurate, high-resolution data, these experiments provide profound insights into the behavior of non-cohesive sand embankments. To guarantee the reliability of these findings, a rigorous construction protocol was developed, ensuring high reproducibility and consistency across all tests.

The experimental campaign highlighted the significant influence of both overtopping boundary conditions (constant reservoir level versus constant reservoir inflow) and sediment granulometry (fine versus medium sand) on breach formation, temporal development, and the resulting outflow hydrograph. Continuous monitoring enabled the precise detection of the macro-scale erosion processes that dictate morphological evolution, from initial overtopping to final breach stabilization. Furthermore, detailed analysis of the generated Digital Elevation Models (DEMs), combined with data from embedded bed-level detectors, allowed for a comprehensive comparison of breach geometry and flow dynamics across different test conditions.

Ultimately, these findings emphasize that the accurate prediction of embankment failure necessitates a coupled understanding of both hydraulic forcing and geotechnical resistance. Specifically, apparent cohesion arising from negative pore pressures in unsaturated fine sands was shown to heavily govern the failure mode, transitioning the breaching process from continuous surface erosion to discrete, gravity-driven mass block failures.

Experimental Investigation of Scale Effects in Sand Embankments Breaching

To systematically investigate scale effects in sand embankment breaching, the medium-scale experiments were downscaled to a small-scale laboratory setting using a geometric scale factor of 5 and strict Froude similarity for the hydraulic boundary conditions. By maintaining identical sand grain sizes across both scales within this scale-series approach, the specific influence of the sediments could be isolated.

While the models exhibited similar macro-scale morphological evolution, distinct deviations in erosion speed were observed. Specifically, disproportionately scaled mass block failures at the small scale resulted in significantly altered lateral breach-widening rates. Furthermore, the relative dimensions of the upstream reservoir were shown to have a dominant impact on both the magnitude and duration of the peak breach outflow.

Crucially, this analysis highlights the fundamental limitations of applying strict Froude similarity to small-scale models. Because geometrically downscaling non-cohesive sediments yields excessively fine particles, it introduces severe scale effects such as apparent cohesion driven by transient matric suction and distorted settling velocities, that misrepresent full-scale erosion mechanics. By systematically examining these sediment scaling laws and fall velocity deviations, this chapter demonstrates the severe risks of directly extrapolating small-scale data to prototype structures. Ultimately, these findings justify the critical implementation of medium-scale physical models to bridge the knowledge gap, accurately reproduce prototype failure mechanisms, and generate the high-resolution data required to properly calibrate advanced numerical models

Research Perspectives

As established previously, contemporary research must integrate field data with reduced-scale laboratory experiments to overcome the severe scale effects inherent in small-scale physical modeling. For example, characterizing cohesive soils reinforced by grass roots remains highly complex; while these materials strongly resist steady overflowing, they are significantly more vulnerable to the dynamic impacts of wave overtopping.

Moving forward, major pilot actions within the Interreg BONSAI project will address this challenge by combining existing field data (such as that from the Polder2C’s project) with targeted reduced-scale tests, including the Erosion Function Apparatus (EFA), Jet Erosion Test (JET), and Fire Hose Erosion testing (Figure 7.1a-f). The primary objective of this ongoing work is to establish robust correlations between laboratory-derived erodibility parameters and full-scale prototype behavior. The data descriptor published within the framework of this thesis provides a critical foundation for these future comparative analyses, while simultaneously serving as a high-resolution baseline for the calibration and validation of numerical models designed to simulate these complex failure processes.

(a)

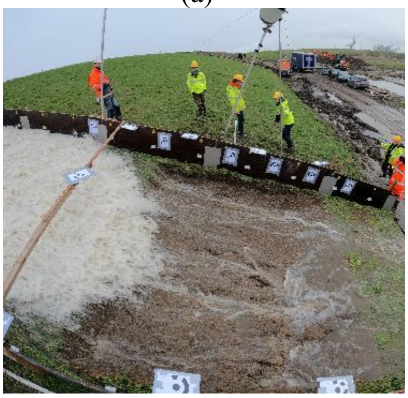

(b)

(c)

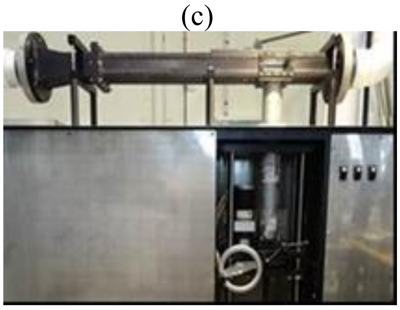

(d)

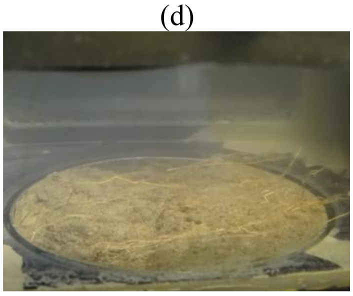

(e) (f)

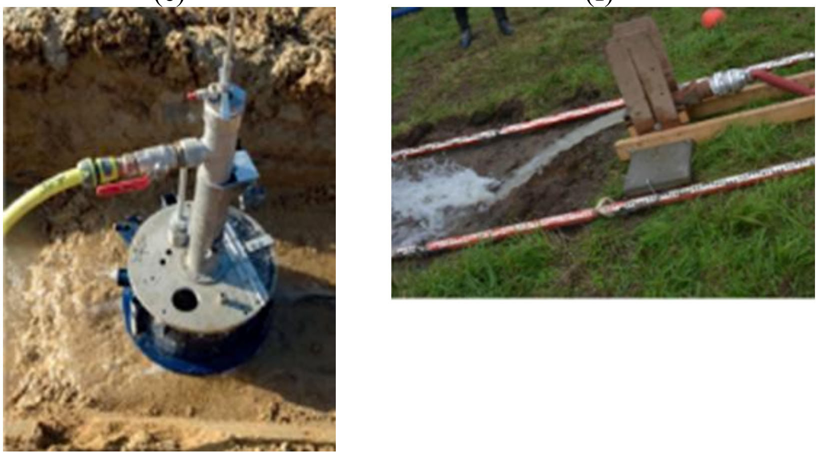

Figure 7.1 Example of full-scale experiments versus small in-situ and laboratory erosion tests: (a) wave overtopping, (b) wave impact, (c) Erosion Function Apparatus as well as (d) exposed soil sample within the apparatus, (e) Mobile Jet Erosion Test and (f) Fire Hose Erosion test.

For medium-scale tests, flow characterization within the highly turbid breach channel remains a significant challenge. Implementing non-intrusive optical measurement techniques, such as Particle Tracking Velocimetry (PTV) or Large-Scale Particle Image Velocimetry (LSPIV) utilizing high-speed cameras, would substantially improve the hydrodynamic characterization of the breach outflow. Furthermore, upscaling the application of Distributed Optical Fiber Sensors (DOFS) to the medium scale would allow for a robust feasibility evaluation, potentially overcoming the major challenge of tracking internal erosion progression in full-scale embankments.

To further isolate and quantify scale effects, the dataset produced in this study can be integrated with existing small-, medium-, and large-scale databases through rigorous dimensional analysis. This comprehensive approach will offer deeper insights into the specific influences of sand granulometry and reservoir dimensions. Additionally, future experimental studies systematically varying the reservoir size are required to fully understand the impact of disproportionately scaled reservoirs in small models.

Numerical modeling of the flow velocity field and shear stresses across different physical scales will provide essential data for quantifying scale effects. This effort could be highly complemented by investigating pure hydrodynamics using 3D-printed models of the breached embankment captured at specific evolutionary instants.

Finally, installing spatially distributed tensiometer probes with relatively high temporal resolution is recommended. This will allow for precise monitoring of seepage and pore-water pressure evolution during the breaching process, enabling a quantitative analysis of the extent to which apparent cohesion influences the stability of breach side slopes.

The apparent cohesion arising from negative pore pressure in non-saturated fine sand was found to govern the failure mode, transitioning the process from continuous surface erosion to discrete mass block failure. The dominance of mass block failure in fine sand highlights the limitations of traditional Equilibrium Sediment Transport (EST) equations, which assume continuous particle entrainment. Integrating geotechnical failure mechanisms is therefore a milestone toward accurate prediction. Sediment transport prediction is a critical component of breach modeling, generally categorized into Equilibrium Sediment Transport (EST) and erosion rate equations. EST formulations (e.g., Meyer-Peter and Müller, 1948; Van Rijn, 1984) rely on the balance between sediment inflow and outflow. While effective for long-term riverbed evolution, these models often face challenges to capture the transient dynamics of breaching, particularly the influence of soil compaction and real or apparent cohesion effects.

The high-resolution datasets generated in this study can serve as a critical basis to the development of advanced breaching formulations. While the excess shear stress formulation ($E=k_d(\tau-\tau_c)$) is highly suitable for cohesive materials, its potential application to fine granular soils requires further investigation. Current observations suggest this formulation cannot accurately model lateral widening, as it inherently fails to capture the discrete, gravity-driven mass block failures and dilatancy effects characteristic of densely compacted sands at high flow velocities. A highly promising perspective for future research is the integration of both widening and deepening mechanisms into a global energy-volume balance model. The high-resolution dataset generated in this study could be utilized to relate the total eroded volume directly to the expended stream power. However, for such an approach to be physically accurate, lateral bank collapse must be treated as a discrete source term rather than a continuous hydraulic erosion process.

References

Agisoft LLC. (2022). Agisoft Metashape User Manual: Professional Edition (Version 1.8). Agisoft LLC. https://www.agisoft.com/pdf

Al-Riffai, M. (2014). Experimental study of breach mechanics in overtopped noncohesive earthen embankments [Doctoral dissertation, University of Ottawa]. https://doi.org/10.20381/RUOR-6578

Al-Riffai, M., Nistor, I., & Bartens, T. (2011). Dam breaching experiments using scale series. 20th Canadian Hydrotechnical Conference, Ottawa, Ontario, Canada.

Amaral, S., Caldeira, L., Viseu, T., & Ferreira, R. M. L. (2020). Designing Experiments to Study Dam Breach Hydraulic Phenomena. Journal of Hydraulic Engineering, 146(4), 04020014. https://doi.org/10.1061/(ASCE)HY.1943-7900.0001678

Arcement, B. J., & Wright, S. G. (2001). Evaluation of laboratory compaction procedures for specification of densities for compacting fine sands (FHWA/TX-02/1874-1). United States Federal Highway Administration.

ASCE Hurricane Katrina External Review Panel. (2007). The New Orleans hurricane protection system: What went wrong and why. American Society of Civil Engineers.

ASCE/EWRI Task Committee on Dam/Levee Breaching. (2011). Earthen Embankment Breaching. Journal of Hydraulic Engineering, 137(12), 1549–1564. https://doi.org/10.1061/(ASCE)HY.1943-7900.0000498

Asghari Tabrizi, A., Elalfy, E., Elkholy, M., Chaudhry, M. H., & Imran, J. (2017). Effects of compaction on embankment breach due to overtopping. *Journal of Hydraulic Research*, *55*(2), 236–247. https://doi.org/10.1080/00221686.2016.1238014

Askar, C., & Sternberg, H. (2023). Use of Smartphone Lidar Technology for Low-Cost 3D Building Documentation with iPhone 13 Pro: A Comparative Analysis of Mobile Scanning Applications. Geomatics, 3(4), 563-579. https://doi.org/10.3390/geomatics3040030

Bakker, M., & Lane, S. N. (2017). Archival photogrammetric analysis of river–floodplain systems using Structure from Motion (SfM) methods. Earth Surface Processes and Landforms, 42(8), 1274–1286. https://doi.org/10.1002/esp.4085

Barker, R., Dixon, L., & Hooke, J. (1997). Use of terrestrial photogrammetry for monitoring and measuring bank erosion. Earth Surface Processes and Landforms, 22(13), 1217–1227.

Bennabi, A., Herrier, G., & Lesueur, D. (2016). Lime treated soil erodibility investigated by EFA erosion testing. In Proc. 8th Int. Conf. on Scour and Erosion (ICSE), 12–15. London: Taylor and Francis.

Bento, A. M., Amaral, S., Viseu, T., Cardoso, R., & Ferreira, R. M. L. (2017). Direct Estimate of the Breach Hydrograph of an Overtopped Earth Dam. Journal of Hydraulic Engineering, 143(6), 06017004. https://doi.org/10.1061/(ASCE)HY.1943-7900.0001294

Bento, A. M., Couto, L., Viseu, T., & Pêgo, J. P. (2022). Image-Based Techniques for the Advanced Characterization of Scour around Bridge Piers in Laboratory. Journal of Hydraulic Engineering, 148(6), 06022004. https://doi.org/10.1061/(ASCE)HY.1943-7900.0001981.

Bisschop, F., Miedema, S. A., Visser, P. J., Keetels, G. H., & van Rhee, C. (2016). Experiments on the Pickup Flux of Sand at High Flow Velocities. Journal of Hydraulic Engineering, 142(7), 04016013. https://doi.org/10.1061/(ASCE)HY.1943-7900.0001142.

Bisschop, F., Visser, P., Van Rhee, C., & Verhagen, H. J. (2011). EROSION DUE TO HIGH FLOW VELOCITIES: A DESCRIPTION OF RELEVANT PROCESSES. Coastal Engineering Proceedings, 1(32), 24. https://doi.org/10.9753/icce.v32.sediment.24.

Carlier d'Odeigne, O., Franzini, F., Da Rosa, G. C. M., Janssens, N., & Soares-Frazão, S. (2018). Measurement of the Free-Surface Elevation for Flows in Complex Topography Using Photogrammetry. In Advances in Hydroinformatics (pp. 145–156). Springer Singapore.

Carrivick, J. L., & Smith, M. W. (2019). Fluvial and aquatic applications of Structure from Motion photogrammetry and unmanned aerial vehicle/drone technology. WIREs: Water, 6(1), e1328. https://doi.org/10.1002/wat2.1328

Chee, S. P. (1978). Mobile Controls for Water Resources Projects. JAWRA Journal of the American Water Resources Association, 14(1), 99–108.

Chinnarasri, C., Tingsanchali, T., Weesakul, S., & Wongwises, S. (2003). Flow Patterns and Damage of Dike Overtopping. International Journal of Sediment Research, 18(4).

Chrbolková, A., Štroner, M., Urban, R., Michal, O., Křemen, T., & Braun, J. (2025). A Comparative Study of Indoor Accuracies Between SLAM and Static Scanners. Applied Sciences, 15(14), 8053. https://doi.org/10.3390/app15148053

Coleman, S. E., Andrews, D. P., & Webby, M. G. (2002). Overtopping Breaching of Noncohesive Homogeneous Embankments. Journal of Hydraulic Engineering, 128(9), 829–838. https://doi.org/10.1061/(ASCE)0733-9429(2002)128:9(829

Corcoran, M. K., Sharp, M. K., Wibowo, J. L., & Ellithy, G. (2016). Evaluating the mechanisms of erosion for coarse-grained materials. E3S Web of Conferences, 7, 03008. https://doi.org/10.1051/e3sconf/20160703008

Costa, J. E. (1985). Floods from dam failures (Vol. 85). US Geological Survey.

D'Eliso, C. (2007). Breaching of sea dikes initiated by wave overtopping: A tiered and modular modelling approach [Doctoral dissertation, TU Braunschweig].

Delpierre, N., Franzini, F., Gousenbourger, P.-Y., Van Emelen, S., Zech, Y., & Soares-Frazao, S. (2024). Breaching of sand dikes: Assessment of 1D and 2D numerical models against laboratory experiments. Journal of Hydraulic Research, 62(5), 461–475.

Delpierre, N., Leyssens, T., Rattez, H., & Soares Frazao, S. (2025). Modelling earthen embankment failure using the Particle Finite Element Method. SimHydro 2025.

Descantons, C., & Dujardin, R. (2014). *Formation, par débordement, d'une brèche dans une digue en matériau non cohésif* [Master's thesis, UCLouvain].

Dezert, T., & Sigtryggsdóttir, F. G. (2024). 3D displacement and axial load of placed riprap supported at the toe: Use of structure from Motion. Journal of Hydraulic Engineering, 150(1).

Ebrahimi, M., Delpierre, N., Swartenbroekx, C., Bousmar, D., & Soares-Frazão, S. (2025b). Investigating the effects of overtopping conditions on dike breach evolution through medium-scale laboratory experiments. Proceedings of the 41st IAHR World Congress.

Ebrahimi, M., Meurice, R., & Soares-Frazão, S. (2022a). Application of Depth-Averaged Bedload Finite-Volume Models to a Progressive Embankment Dam-Failure.

Ebrahimi, M., van Damme, M., van Hemert, H., & Soares-Frazão, S. (2025a). Close-Range Photogrammetry Application to Monitor Levee Erosion in Case of Wave Overtopping. Journal of Hydraulic Engineering, 151(1), 04024057.

Ebrahimi, M., van Damme, M., & Soares-Frazão, S. (2022b). Photogrammetry measurements of wave overtopping erosion on a seashore dike. 11th Int. River Flow Conf.

Elalfy, E., Czapiga, M. J., Viparelli, E., Imran, J., & Hanif Chaudhry, M. (2025). Modeling Breach Evolution in Noncohesive Earthen Dams by Overtopping. Journal of Hydraulic Engineering, 151(1), 04024064.

Ettema, R. (Ed.). (2000). Hydraulic modeling: Concepts and practice. ASCE.

EUCOLD & Comité français des barrages et réservoirs. (2018). European and US levees and flood defences: Characteristics, risks and governance. Éditions CFBR.

Fell, R., Wan, C. F., Cyganiewicz, J., & Foster, M. (2004). Time for Development of Internal Erosion and Piping in Embankment Dams. Journal of Geotechnical and Geoenvironmental Engineering, 129(4).

Flynn, S., Vahedifard, F. & Schaaf, D (2026). A comprehensive dataset of riverine levee overtopping events for advancing risk assessment. Sci Data 13, 36. https://doi.org/10.1038/s41597-025-06349-y.

Foster, M., Fell, R., & Spannagle, M. (2000). The statistics of embankment dam failures and accidents. Canadian Geotechnical Journal, 37(5), 1000–1024.

Frank, P.-J. (2016). Hydraulics of spatial dike breaches. Doctoral thesis, ETH Zurich. VAW Mitteilung 236. http://dx.doi.org/10.3929/ethz-a-010803310.

Frank, P.-J., & Hager, W. H. (2014). Spatial dike breach: Accuracy of photogrammetric measurement system. River Flow 2014. CRC Press.

Froehlich, D. C. (1995). ‘‘Embankment dam breach parameters revisited.’’ Water Resources Engineering, Proc. 1995 ASCE Conf. on Water Resources Engineering, New York, 887– 891.

Froehlich, D. C. (2008). Embankment Dam Breach Parameters and Their Uncertainties. Journal of Hydraulic Engineering, 134(12), 1708–1721. https://doi.org/10.1061/(ASCE)0733-9429(2008)134:12(1708).

Gilles, A., & Zgajewski Delforge, C. (2023). Étude expérimentale de l'écoulement sur une digue et de l'érosion progressive de celle-ci [UCLouvain].

GPL software. (2025). CloudCompare (Version 2.13) [Computer software]. https://www.cloudcompare.org

Hahn, W., Hanson, G. J., & Cook, K. R. (2000). Breach Morphology Observations of Embankment Overtopping Tests. Building Partnerships, 1–10.

Halso, M. C. (2024). Spatial breaching of homogeneous and zoned embankment dams [Doctoral dissertation (VAW Mitteilung 278, R. Boes, ed.), ETH Zurich]. ETH Research Collection. https://doi.org/10.3929/ethz-b-000694277.

Halso, M. C., Evers, F. M., Vetsch, D. F., & Boes, R. M. (2025a). Effect of grain size distribution in non-cohesive spatial dam breach: Hydraulic model investigation and systematic calibration of 2D numerical model. Journal of Hydraulic Research, 63(3), 337–356. https://doi.org/10.1080/00221686.2025.2490172.

Halso, M. C., Evers, F. M., Boes, R. M., & Vetsch, D. F. (2025b). Composite modelling of non-cohesive homogeneous spatial dam breaches with varied grain size distributions. Journal of Hydraulic Research, 63(4), 425-444.

Halter, W., Groenouwe, I., Tonneijck, M., & d'Angremond, K. (2018). Handboek dijkenbouw: uitvoering versterking en nieuwbouw. Hoogwaterbeschermingsprogramma.

Hanson, G. J., Cook, K. R., & Hunt, S. L. (2005). Physical modeling of overtopping erosion and breach formation of cohesive embankments. Transactions of the ASAE, 48(5), 1783–1794.

Hassan, M., Morris, M., Hanson, G., & Lakhal, K. (2004). Breach Formation: Laboratory and Numerical Modelling of Breach Formation. ASDSO.

Heller, V. (2011). Scale effects in physical hydraulic engineering models. Journal of Hydraulic Research, 49(3), 293–306.

Heng, B. C. P., Chandler, J. H., & Armstrong, A. (2010). Applying close range digital photogrammetry in soil erosion studies. Photogrammetric Record, 25(131), 240–265.

Herrero-Huerta, M., Lindenbergh, R., Ponsioen, L., & van Damme, M. (2016). Morphological changes along a dike landside slope sampled by 4D high resolution terrestrial laser scanning. ISPRS Archives, XLI-B3, 227–232.

Hilt, G. H., & Davidson, D. T. (1960). Lime fixation in clayey soils. Highway Research Board Bulletin, 20–32.

Hughes, S. A. (1993). Physical models and laboratory techniques in coastal engineering (Vol. 7). World Scientific.

Intergovernmental Panel on Climate Change (IPCC). (2023). Climate Change 2022 - Impacts, Adaptation, and Vulnerability. Cambridge University Press.

Janga, J., Reddy, K., & Schulenberg, J. (2024). Climate change impacts on safety of levees: A Review. Geotechnical Engineering Challenges.

Jansen, P. P., van Bendegom, L., van den Berg, J., de Vries, M., & Zanen, A. (1979). *Principles of river engineering: The non-tidal alluvial river*. Pitman.

Jergeay, E., & Zhang, W. H. (2024). Étude expérimentale de la rupture progressive d'une digue par surverse [UCLouvain].

Jónatas, R. J. L., Aleixo, R. J. F., Amaral, S. R. C., Mendes, S. V., Viseu, M. T. F. S., & Ferreira, R. M. L. (2025). Laboratory Application of Real-Time LiDAR Technology for Assessing Breach Morphology during the Failure of Earth Dams and Fluvial Dikes. Journal of Hydraulic Engineering, 151(6), 04025033. https://doi.org/10.1061/JHEND8.HYENG-14126

Kakinuma, T., & Shimizu, Y. (2014). Large-Scale Experiment and Numerical Modeling of a Riverine Levee Breach. Journal of Hydraulic Engineering, 140(9), 04014039.

Kingsland, K. (2020). Comparative analysis of digital photogrammetry software for cultural heritage. Digital Applications in Archaeology and Cultural Heritage, 20, e00157.

Ko, D., & Kang, J. (2018). Experimental studies on the stability assessment of a levee using reinforced soil based on a biopolymer. Water, 10(8), 1059.

Kobus, H. (Ed.). (1980). Hydraulic Modeling. German Association for Water Resources, Bulletin 7.

Koelewijn, A. R., Rikkert, S. J. H., Peeters, P., Depreiter, D., van Damme, M., & Zomer, W. (2022). Overflow tests on grass-covered embankments at the Living Lab Hedwige-Prosperpolder: An overview. *Water*, *14*(18), 2859. https://doi.org/10.3390/w14182859

Kurter, E. C., Nemnem, A. M., Chaudhry, M. H., & Imran, J. (2025). A fragility framework for surface erosion with application to earthen dam breaching. Water Resources Research, 61, e2025WR040789. https://doi.org/10.1029/ 2025WR040789

Lane, S. N., Chandler, J. H., & Porfiri, K. (2001). Monitoring river channel and flume surfaces with digital photogrammetry. Journal of Hydraulic Engineering, 127, 871–877.

Løvoll, A., Høeg, K., & Vaskinn, K. A. (2004). Stability and breaching of embankment dams: Field tests on 6 m-high dams. International Journal of Hydropower & Dams, 88–93.

Maron, L. (2026). Analyse par imagerie de la rupture de digue et mesure du débit à travers la brèche [UCLouvain].

Monteiro-Alves, R., Morán, R., Toledo, M., & Morris, M. (2023). The OVERCOME Project: Initial findings from small scale laboratory breach tests. EURCOLD.

Morris, M., Courivaud, J. R., Moran, R., Toledo, M. Á., & Picault, C. (2021). Industry Research into Dam and Levee Breach Erosion Through Coarser Grained Materials. FLOODrisk 2020.

Morris, M., & Hassan, M. (2009). Breach Initiation & Growth: Physical Processes. FLOODsite Project Report, T06-08.

Morris, M., Hassan, M., & Vaskinn, K. (2007). Breach formation: Field test and laboratory experiments. Journal of Hydraulic Research, 45(sup1), 9–17.

Nienhuis, J. H., Cox, J. R., O'Dell, J., Edmonds, D. A., and Scussolini, P. (2022). A global open-source database of flood-protection levees on river deltas (openDELvE), Nat. Hazards Earth Syst. Sci., 22, 4087–4101, https://doi.org/10.5194/nhess-22-4087-2022.

Novák, P., & Cabelka, J. (1981). Models in hydraulic engineering: Physical principles and design applications.

Osman, A. M., & Thorne, C. R. (1988). Riverbank Stability Analysis. I: Theory. Journal of Hydraulic Engineering, 114(2), 134–150.

Özer, I. E., van Damme, M., & Jonkman, S. N. (2020). Towards an International Levee Performance Database (ILPD) and Its Use for Macro-Scale Analysis of Levee Breaches and Failures. *Water*, *12*(1), 119. https://doi.org/10.3390/w12010119.

Pan, S., & Loukola, E. (1993). Chinese-Finnish cooperative research work on dam break hydrodynamics. Vesi- Ja Ympäristöhallinnon Julkaisuja.

Peeters, P., Zhao, G., De Vos, L., & Visser, P. J. (2014). Large-scale dike breaching experiments at Lillo in Belgium. 7th Int. Conf. on Scour and Erosion (ICSE).

Picault, C., Campette, F., Bonelli, S., Nicaise, S., Chaouch, N., Byron, F., Grémeaux, Y., Doghmane, A., Garoui, M., Herbeck, J., & Golay, F. (2022). *Field testing of the overflow erosion of Rhone river levees*. 4th International Seminar on Dam Protections against Overtopping, Madrid, Spain.

Pickert, G., Weitbrecht, V., & Bieberstein, A. (2011). Breaching of overtopped river embankments controlled by apparent cohesion. Journal of Hydraulic Research, 49(2), 143–156.

Ponsioen, L., van Damme, M., Hofland, B., & Peeters, P. (2019). Relating grass failure on the landside slope to wave overtopping induced excess normal stresses. Coastal Engineering, 148, 49–56.

Powledge, G. R., Ralston, D. C., Miller, P., Chen, Y. H., Clopper, P. E., & Temple, D. M. (1989). Mechanics of overflow erosion on embankments. I: Research Activities. *Journal of Hydraulic Engineering*, *115*(8), 1040–1055. https://doi.org/10.1061/(ASCE)0733-9429(1989)115:8(1040

Pugh, C. A. (1985). Hydraulic model studies of fuse plug embankments. Bureau of Reclamation.

Puiatti, D., Herrier, G., Nerincx, N., Bonelli, S., & Fry, J. J. (2018). *The use of lime treated soils in water retaining structures*. IV International Seminar on Earthworks in Europe, Madrid, Spain.

Quante, M., & Colijn, F. (2016). North Sea region climate change assessment. Springer Nature.

Ralston, D. C. (1987). Mechanics of Embankment Erosion During Overflow. Hydraulic Engineering, 733–738.

Richards, K. S., & Reddy, K. R. (2007). Critical appraisal of piping phenomena in earth dams. Bulletin of Engineering Geology and the Environment, 66(4), 381–402.

Rieke-Zapp, D. H., & Nearing, M. A. (2005). Digital close range photogrammetry for measurement of soil erosion. Photogrammetric Record, 20(109), 69–87.

Rifai, I., Erpicum, S., Archambeau, P., Violeau, D., Pirotton, M., El Kadi Abderrezzak, K., & Dewals, B. (2017). Overtopping induced failure of noncohesive, homogeneous fluvial dikes. *Water Resources Research*, *53*(4), 3373–3386. https://doi.org/10.1002/2016WR020053

Rifai, I., Schmitz, V., Erpicum, S., Archambeau, P., Violeau, D., Pirotton, M., Dewals, B., & El Kadi Abderrezzak, K. (2020). Continuous monitoring of fluvial dike breaching by a laser profilometry technique. Water Resources Research, 56(10), e2019WR026941. https://doi.org/10.1029/2019WR026941.

Rikkert, S. J. H., Alleon, C., Khaldi, I., Shaiek, S., Verelst, K., Ebrahimi, M., Soares-Frazão, S., Kaidi, S., Smaoui, H., & Sergent, P. (2021). How strong are our levees? Hydraulic analysis based on Polder2c's project in situ testing. In Proceedings of SimHydro 2021. Springer.

Rinaldi, M., & Casagli, N. (1999). Stability of streambanks formed in partially saturated soils and effects of negative pore water pressures.

Rinaldi, M., Casagli, N., Dapporto, S., & Gargini, A. (2004). Monitoring and modelling of pore water pressure changes and riverbank stability during flow events. *Earth Surface Processes and Landforms*, *29*(2), 237–254. https://doi.org/10.1002/esp.1042.

Rinaldi, M., & Nardi, L. (2013). Modeling Interactions between Riverbank Hydrology and Mass Failures. Journal of Hydrologic Engineering, 18(10), 1231–1240.

Schmitz, V., Erpicum, S., El Kadi Abderrezzak, K., Rifai, I., Archambeau, P., Pirotton, M., & Dewals, B. (2021). Overtopping-induced failure of non–cohesive homogeneous fluvial dikes: Effect of dike geometry on breach discharge and widening. Water Resources Research, 57(7), e2021WR029660. https://doi.org/10.1029/2021WR029660

Schmocker, L., & Hager, W. H. (2012). Plane dike-breach due to overtopping: Effects of sediment, dike height and discharge. Journal of Hydraulic Research, 50(6), 576–586.

Shimada, T., Watanabe, Y., Yokoyama, H., & Tsuji, T. (2009). An experiment on overflow-induced cross-levee breach at the Chiyoda Experimental Channel. River, coastal and estuarine morphodynamics.

Shinozuka, M., Feng, M. Q., Kim, H.-K., & Kim, S.-H. (2000). Nonlinear static procedure for fragility curve development. Journal of Engineering Mechanics, 126(12), 1287–1295. https://doi.org/10.1061/(asce)0733-9399(2000)126:12(1287).

Snavely, K. N. (2008). Scene Reconstruction and Visualization from Internet Photo Collections [Doctoral dissertation, University of Washington].

Spinewine, B., Delobbe, A., Elslander, L., & Zech, Y. (2004). Experimental investigation of the breach growth process in sand dikes. River Flow 2004.

Steendam, G. J., Peeters, P., van der Meer, J., van Doorslaer, K., & Trouw, K. (2013). *Destructive wave overtopping tests on Flemish dikes*. Coastal Structures 2011, Yokohama, Japan. https://doi.org/10.1142/9789814412216_0016

Stoutjesdijk, T. (2022). Overtopping tests on lime treated clay in the Hedwigepolder. Deltares report.

Swartenbroekx, C., Soares-Frazão, S., Staquet, R., & Zech, Y. (2010). Two-dimensional operator for bank failures induced by water-level rise in dam-break flows. Journal of Hydraulic Research, 48(3), 302–314.

Tingsanchali, T., & Chinnarasri, C. (2001). Numerical modelling of dam failure due to flow overtopping. Hydrological Sciences Journal, 46(1), 113–130.

Tinney, E. R., & Hsu, H. Y. (1961). Mechanics of Washout of an Erodible Fuse Plug. Journal of the Hydraulics Division, 87(3), 1–29.

Tobita, D., Kakinuma, T., Yokoyama, H., & Takeda, A. (2014). Quantification of levee breach volume based on levee breach at the chiyoda experimental flume. Journal of JSCE, 2(1), 136–143.

van den Berg, M., Labeur, R. J., Aarninkhof, S. G., & Visser, P. J. (2025). Exploring the effect of foreshores on dike breach development via a mid-scale experiment. Journal of Coastal and Hydraulic Structures, 5. https://doi.org/10.59490/jchs.2025.0043.

Van Damme, M. (2021). Detachment of dilatant soil due to high hydraulic shear stresses explained. Journal of Hydraulic Research, 59(1), 51–60.

van Damme, M., & Visser, P. J. (2015). A SWOT analysis of hydrodynamic models with respect to simulating breaching. 36th IAHR World Congress.

van Damme, M., Ponsioen, L., Herrero, M., & Peeters, P. (2016). Comparing overflow and wave-overtopping induced breach initiation mechanisms in an embankment breach experiment. *E3S Web of Conferences*, *7*, 03004. https://doi.org/10.1051/e3sconf/20160703004

van Damme, M., Alleon, C., Neuts, A., Koelewijn, A., Bennabi, A., Ebrahimi, M., Soares-Frazão, S., Sergent, P., & Samoui, H. (2023). *Modelling erosion progression for steady overflow and wave overtopping conditions* (Technical Report). Polder2C's Project.

van der Meer, J. W., Bernardini, P., Snijders, W., & Regeling, E. (2007). The wave overtopping simulator. *Coastal Engineering 2006*, 4654–4666. https://doi.org/10.1142/9789812709554_0392

van der Meer, J. W., Allsop, N. W. H., Bruce, T., De Rouck, J., Kortenhaus, A., Pullen, T., Schüttrumpf, H., Troch, P., Zanuttigh, B., Arns, A., van den Boogaard, H., Cappietti, L., Coeveld, E., Cuomo, G., Franco, L., Geeraerts, J., Hofland, B., Jensen, T., Lomonaco, P., … Vicinanza, D. (2018). *EurOtop: Manual on wave overtopping of sea defences and related structures* (2nd ed.). www.overtopping-manual.com

Van Emelen, S., Zech, Y., & Soares-Frazão, S. (2015). Impact of sediment transport formulations on breaching modelling. Journal of Hydraulic Research, 53(1), 60–72.

Van Nederkassel, J., Van Zele, S., Van Renterghem, B., Vermeersch, T., & Quaeyhaegens, H. (2015). The use of engineered sediments for dyke construction in the flood control area of Vlassenbroek. *Terra et Aqua*, (139), 20–28.

Van Rhee, C. (2010). Sediment entrainment at high flow velocity. Journal of Hydraulic Engineering, 136(9), 572–582.

Van Veen, J. 1962 Dredge, drain, reclaim, 5th edn. The Hague: Martinus Nijhoff, 200 pp.

Visser, P. J. (1998). Breach growth in sand-dikes [Doctoral dissertation, Delft University of Technology].

Wahl, T. L. (1998). Prediction of embankment dam breach parameters: A literature review and needs assessment. Bureau of Reclamation.

Walder, J. S., & O'Connor, J. E. (1997). Methods for predicting peak discharge of floods caused by failure of natural and constructed earthen dams. Water Resources Research, 33(10), 2337–2348.

Walder, J. S., Iverson, R. M., Godt, J. W., Logan, M., & Solovitz, S. A. (2015). Controls on the breach geometry and flood hydrograph during overtopping of noncohesive earthen dams. *Water Resources Research*, *51*(8), 6701–6724. https://doi.org/10.1002/2015WR017128

Ward, P. J., de Ruiter, M. C., Mård, J., Schröter, K., Van Loon, A., Veldkamp, T., von Uexkull, N., Wanders, N., AghaKouchak, A., Arnbjerg-Nielsen, K., Capewell, L., Carmen Llasat, M., Day, R., Dewals, B., Di Baldassarre, G., Huning, L. S., Kreibich, H., Mazzoleni, M., Savelli, E., ... Wens, M. (2020). The need to integrate flood and drought disaster risk reduction strategies. *Water Security*, *11*, 100070. https://doi.org/10.1016/j.wasec.2020.100070

Westoby, M. J., Brasington, J., Glasser, N. F., Hambrey, M. J., & Reynolds, J. M. (2012). Structure-from-motion photogrammetry: A low-cost, effective tool for geoscience applications. *Geomorphology*, *179-180*, 300–314. https://doi.org/10.1016/j.geomorph.2012.08.021

Yalin, M. S. (1971). Theory of Hydraulic Models. Macmillan Education UK.

Yang, J., Shi, Z., Soares-Frazão, S., Zheng, H., & Shen, D. (2024). Influence of dam and erodible bed material composition on landslide dam failure. Bulletin of Engineering Geology and the Environment, 83(2), 61.

Zhang, C., Sun, A., Hassan, M. A., & Qin, C. (2022). Assessing through-water structure-from-motion photogrammetry in gravel-bed rivers under controlled conditions. Remote Sensing, 14(21), 5351.

Zhu, Y., Visser, P. J., Vrijling, J. K., & Wang, G. (2011). Experimental investigation on breaching of embankments. Science China Technological Sciences, 54(1), 148–155.

Notation

Acronyms and Abbreviations

- **BC:** Bare-clay.
- **CP:** Check Point.
- **DEM:** Digital Elevation Model.
- **DOFS:** Distributed Optical Fibre Sensors.
- **EFA:** Erosion Function Apparatus.
- **fS:** Fine Sand.
- **GCP:** Ground Control Point.
- **LEMSC:** Laboratoire Essais Mécanique, Structures et génie Civil.
- **LiDAR:** Light Detection and Ranging.
- **LLHPP:** Living Lab Hedwige-Prosperpolder.
- **LTC:** Lime-treated clay.
- **MAE:** Mean Absolute Error.
- **mS:** Medium Sand.
- **RMSE:** Root Mean Square Error.
- **SfM:** Structure-from-Motion.
- **WOS:** Wave Overtopping Simulator.

Geometric and Embankment Parameters

- B: Breach width (including B_{avg}, B_{top}, and B_{bottom}) (m)
- H_{Em}: Embankment height (m)
- h_b: Breach depth or height (m)
- Z: Breach side slope(-)
- z_b: Pilot channel invert elevation (m)
- z_c: Dike crest elevation (m)

Hydraulic and Hydrodynamic Parameters

- H or H_{res}: Constant reservoir water level (m).

- H_s: Significant wave height (m).
- h or h_m: Water depth or mean hydraulic depth (m).
- Q_{in}: Constant reservoir inflow (m³/s).
- q: Mean discharge (m²/s).
- V or U : Average flow velocity or depth-averaged flow velocity.
- Vol_{tot}: Total volume of released water (m³).
- χ : Parameter accounting for the flow regime close to the bed.

Geotechnical and Sediment Parameters

- c': Apparent cohesion (matric suction, kPa).
- C_c: Coefficient of curvature (-).
- C_u: Uniformity coefficient (-).
- d: Grain diameter (mm).
- d_{50}: Median grain diameter (mm).
- k: Erosion rate (m/s).
- k_s: Sand equivalent roughness.
- u^*: Shear velocity.
- w_s: Settling velocity (m/s).
- γ_{bulk} : Bulk unit weight of soil (kN/m³).
- τ_0: Tangential shear stress exerted by flow (Pa).
- τ_b : Bed shear stress.
- τ_c: Critical shear stress required for sediment motion.

Scaling and Dimensionless Parameters

- β : Percentage ratio of embankment volume to reservoir storage capacity.
- η : Dimensionless factor linking erosion rate, reservoir volume, and water level drop.
- λ_L, λ_T, λ_M : Scale factors for length (geometry), time, and mass.
- Fr: Froude Number (ratio of inertial to gravity forces).

- N_s: Stability Number (ratio of destabilizing gravitational forces to stabilizing cohesive forces).
- Re : Reynolds Number (ratio of inertial to viscous forces).
- Re^*: Grain Reynolds Number.
- t^*: Dimensionless breach time scale.
- We : Weber Number (ratio of inertial forces to surface tension).
- τ^*_b: Dimensionless bed shear stress (Shields parameter).

Physical Constants and Fluid Properties

- g: Acceleration due to gravity (m²/s).
- κ: von Karman constant (usually 0.4).
- v: Kinematic viscosity of water.
- ρ_s: Density of sediment (kg/m³).
- ρ_w: Density of water(kg/m³).
- σ_w: Surface tension of water (Pa).

Appendix A: Earthen embankment experimental review

Experimental study of earthen embankments breaching at different scales in literature (updated after Wahl (2007), ASCE-EWRI task committee (2011), Al-Riffai (2014))

Performing Organization	Test Description	Literature Citation	Test No.	Scale	Research Focus
Washington State Univ., U.S.	Fuse plug breach—lab and field scales	Tinney and Hsu (1961)	12	Small	Washout mechanics and rate, Similitude relationships
			1	Full	
Univ. of Windsor, Canada	Fuse plug breach—lab scale	Chee (1984)	33	Small	Investigation of erosion mechanics and washout time rates of erodible embankment material. Approx.*
Chinese Ministry of Water Resources	Fuse plug breach—field scale	Pan and Loukola (1993); Loukola and Huokona (1998)	55	Full	Initial water surface level; Scale series; Clay core and other configurations
Chinese-Finnish Cooperative Research Work on Dam Break Hydrodynamics					
Technical University of Graz, Austria	Rockfill dam breach—lab scale 2D overtopping	Simmler and Samet (1982)	22	Small to Medium-2D	Fill material (grain size, uniformity, grain shape, angle of repose); Homogeneous and composite embankments; Embankment zoning (impervious element location) Reservoir storage volume Shoulder slopes Compaction
Chinese-Finnish Cooperative Research Work on Dam Break Hydrodynamics	Rockfill dam breach with fixed opening—lab scale	Mingsen, Shuibo et al. (1993);	7	Small	Flow phenomena in a dam breach opening Time-average pressure distribution and pressure fluctuation in breach opening, The velocity distributions in transversal cross sections The effects of different upstream and downstream water levels. Approx.*

Simons, Li & Assoc. for USDOT FHWA	Highway embankment—overtopping	Chen and Anderson (1986)	35	Large	Highway embankment overtopping - sectional models to develop embankment test methods and tools for predicting erosion damage; Various protection elements; Flume tests of large scale (1.8 m heigh dike)
Simons, Li & Assoc. for USDOT FHWA	Highway embankment—protection	Clopper and Chen (1988)	57	Large	Evaluate embankment damage (bare soil) and protection measures (selected commercially available embankment protection)
Simons, Li & Assoc. for USDOT FHWA	Embankment dam—overtopping	Clopper (1989)	17	Large	Evaluation of articulated concrete block embankment;
USBR (Bureau of Reclamation, U.S.)	Fuse plug breach—lab scale	Pugh (1985)	8	Small	Washout mechanics and rates; Similitude relationships; Embankment size; Pilot channel size and position; Structural configuration
USBR (Bureau of Reclamation, U.S.)	Embankment dams erosion—lab scale overtopping	Dodge (1988)	9	Small	Downstream protection; Downstream slope gradation; Unit discharge; Degree of compaction
University of Colorado, U.S.	Embankment erosion—overtopping	Powledge et al. (1989)	2	Small	Two centrifuge testing - feasibility
			1	Prototype	Prototype test
Colorado State University, U.S.	Overtopping breach—outdoor flume	AlQaser and Ruff (1993)	2	Full	Overfall progression
University of Auckland, New Zealand	Overtopping Breaching of Noncohesive Homogeneous Embankments-Lab scale	Andrews (1998), Jack (1996), Coleman et al. (2002);	26	Small	Sediment size (medium sand to gravel soil); Breach geometry;
USDA-ARS-HERU	Outdoor flume tests	Hanson and Temple (2002)	4	Large	Erosion in cohesive bare-earth and vegetated steep channels
USDA-ARS-HERU	Overtopping breach, breach widening —cohesive	Hahn et al. (2000); Hanson et al. (2003); Hanson et al. (2005), Hunt et al. (2005)	3	Medium	Breach erosion process and headcut migration for various soils and compaction water contents
			7	Large	

	Internal erosion piping—cohesive	Hanson et al. (2010)	4	Medium	
HR Wallingford, UK	Lab-scale sand dike breach—overtopping	Mohamed et al. (1999)	3	Small	Crest width variation, very steep shoulder slopes
IMPACT—HR Wallingford, UK	Lab-scale overtopping and piping—various configurations	Morris and Hassan (2005)	22	Small	Series 1 - Lab-scale overtopping breach of homogeneous noncohesive embankments; Series 2 - Lab-scale overtopping breach of homogeneous cohesive embankments. Series 3 - Piping initiation and development
Norway—IMPACT	Large-scale overtopping and piping breach—various configurations	Morris and Hassan (2005), Vaskinn et al. (2004), EBL Kompetanse (2006)	5	Full	Large-scale tests of overtopping of cohesive, noncohesive, and zoned embankments; and piping through cohesive and zoned embankments
Norway—Other field tests	Rockfill dams—through-flow and breach	Vaskinn et al. (2004), EBL Kompetanse (2006)	2	Full	Through-flow and breaching of rockfill dams
Norway—Lab tests	Rockfill dams—through-flow and overtopping	EBL Kompetanse (2006)	23	Small	Through-flow and overtopping of rockfill dams
Technical Advisory Committee on Water Defences (TAW) (Netherlands)	Overtopping—sand dikes	Visser (1998), Caan (1997)	2 1	Full Small	Field-test of sand dike breaching; small laboratory test; Development and verification of a mathematical model
Delft University of Technology, Netherlands	Laboratory tests of sand dune/dikes	Steetzel and Visser (1992), Visser (1998)	9	Medium-2D	Validations of sediment transport formulations (channel width is 0.4 m)
University of Birmingham, UK	Sand embankments overtopping—Lab scale	Lecointe (1998)	2	Small	Cross-channel dam and river bank failures

University of the Federal Armed Forces (Munich, Germany)	Laboratory tests of overtopped noncohesive embankments	Kulisch (1994); Bechteler and Kulisch (1998); Broich (1998a)	7	Medium-2D	Grain size
Kyoto University and, Japan	Fluvial levee breach—lab scale	Fujita and Tamura (1987)*	32	Small	Impact of flood levee failure on alluvial floodplain
Brno Univ. of Technology, Switzerland	Overtopping—noncohesive	Parilkova 2003a, Jandora and Riha (2009)	4	Medium	Fine sand
Technical University of Lisbon, Portugal	Overtopping—rockfill	Franca and Almeida (2004)	22	Small	Validation and calibration of a numericla model which predict breach formation in rockfill dams
UCLouvain (Université Catholique de Louvain), Belgium	Breach growth process in coarse sand dikes— Lab scale	Spinewine et al. (2004)	11	Small	Development of non-intrusive measurement techniques (laser light sheet); Erodible bed
St. Petersburg State Technical Univ., Russia	Overtopping—noncohesive	Rozov (2003)	4	Small	The process of dam-breach erosion and dam wash-out invistigation and deriving analytical solution describing physical process.
Institute of Hydromechanics, University of Karlsruhe (Karlsruhe, Germany)	Laboratory tests of overtopped noncohesive embankments	Pickert et al. (2004)	3	Small	Unsaturated soil and side slope collapses Grain size
Asian Institute of Technology, Thailand	noncohesive, 2D breach—Overtopping	Tingsanchali and Chinnarasri (2001), Chinnarasri et al. (2003)	20	Medium-2D	Calibration of numerical model Erosion and sliding failure modes in overtopping (2D) Grain size (and gradation) Downstream slope Overtopping height Inflow
Asian Institute of Technology, Thailand	Laboratory tests of overtopped cohesive embankments	Chinnarasri et al. (2004)	9	Small	Downstream slope Grain size Inflow Scaling embankment breaching characteristics
Department of Civil Engineering, University of	Laboratory tests of estuary sand berms	Stretch and Parkinson (2006);Parkinson	24	Small	Scale series;Various geometric scales and berm shapes

KwaZulu-Natal (Durban, South Africa)		and Stretch (2007)			
École Polytechnique de Montréal, Canada	Overtopping—moraine	Zerrouk and Marche (2005)	1	Small	Importance of turbulance and local head loss; Instability of breach sides due to undermining and mass slumping.
University of Ottawa, Canada	Overtopping—effects of compaction and initial breach in smal scale	Al-Riffai and Nistor (2010a), Al-Riffai and Orendorff (2009), Orendorff (2009)	23	Small	Phase1 (Standard tests) of experiments including small (with and without toe drainage) and large flume tests (in both cases dike height is lower than 0.6 m);
			11	Small	Phase2 (3-D Breach Overtopping Tests) including studing these parameters (compaction degree drainage, tilted scale, quasi-exact geometric scale)
			13	Small	Phase 3 (2D overtopping test) Pore-water-pressure distribution inside the dike during overtopping
Leichtweiß-Institute for Hydraulic Engineering and Water Resources (Braunschweig, Germany)	Laboratory tests of overtopped dikes with and without waves	Geisenhainer and Kortenhaus (2006)	16	Small	Overflow and wave overtopping, Clay lining, Landward and seaward breach initiation
Delft University of Technology (TUD) (Delft, Netherlands)	Laboratory tests of overtopped dikes	Zhu et al. (2006), (2011)	5	Medium-2D	Cohesive vs. noncohesive materials, Compaction water content in cohesive embankments
Wairakei Research Centre (Taupo, New Zealand)	Overtopping—replicate landslide dam at lab scale	Davies et al. (2007)	16	Medium	Landslide dams; valley bed slope, upstream and downstream slope factors influence on breach outflow.
University of Canterbury (Christchurch, New Zealand)	Laboratory tests of overtopped noncohesive embankments	Wishart (2007)	44		Rock-avalanche dams, Scaling, Saturation, Armouring
Swiss Federal Institute of Technology (ETH Zurich) (Zurich, Switzerland)	Overtopping—noncohesive, lab scale	Schmocker and Hager (2009)	60	Small	Plane dike tests, Test repeatability, Side-wall effects, Scale effects by means of scale families; 39 (Approx. 60)

Germany-FLOODsite	Overtopping—coastal dike (small and large scales)	Geisenhainer and Kortenkhaus (2006), Geisenhainer and Oumeraci (2008)	11	Small and large	Approx. 11
Nanjing Hydraulic Research Institute, China	Overtopping—cohesive, layered, field scale	Zhang et al. (2009)	5	Large	Soil cohesion
Università di Padova, Italy	Criteria for overtopping failure—landslide dams, small-scale	Gregoretti et al. (2010)	168	Small	
USBR (Denver, CO)*	Laboratory tests of fluvial dike overtopping and piping	Wahl et al. (2011)	3	Small	Physical modeling of fluvial dike breaching; Cohesive soils; Scaling
Wuhan University, China	Overtopping—landslide dams, lab scale	Cao et al. (2011)	28	Small	Differing parameters including inflow discharge, dam composition, damgeometry, and initial breach dimension.
Institute of Hydromechanics, University of Karlsruhe (Karlsruhe, Germany)	Overtopped noncohesive embankments—Lab scale	Pickert et al. (2011)	7	Small	Apparent cohesion influence on breach formation in sand dikes; Unsaturated soil and side slope collapses; Grain size
Hydraulic Engineering Laboratory of Nagoya University, Japan	Laboratory Experiment of Fluvial Levee Breach—Lab scale	Islam, 2012	6	Small	Non-cohesive soils (fine and coarse sand); propagation of levee breach and widening with more sediment deposition on the floodplain area; Data used for validation of a numerical model
USGS Debris-Flow Flume project (2010-2013)	Outdoor flume tests- overtopping of noncohesive fine sand	Walder et al. (2015)	2	Small	Scale-series tests; Crest length
			11	Medium	
UCLouvain (Université Catholique de Louvain), Belgium	2D dike overtopping	van Emelen et al. (2014)	6	Small-2D	2D overtopping experiments for calibration of the transport formulas and 1D numerical model of vertical erosion in dike breaching.
Chiyoda Experimental Channel, Japan	Lateral levee breaching experiments of coarse sediments—lab and field tests	Shimada et al. (2009), Shimada et al. (2010), and	4	Full	Fulivial dike breach experiments; Gravel soil; Improving measurment techniques using accelerator sensors embedded inside the dike.

		Tobita et al. (2014)			Small dike breach (Number?) test for verification and calibration of sensors.
U.S. Army Engineer Research and Development Center (ERDC), Coastal and Hydraulics Laboratory (CHL), Vicksburg.	Combined overflowing and wave overtopping hydraulic modeling—lab-scale tests	Hughes and Nadal, 2011	27	Small	Hydrodynamic characteristics of combined wave and steady overtopping condition; Deriving flow parameters and developing an emprical formula describing average discharge in this case.
O.H. Hinsdale Wave Research Laboratory (Large wave Flume facilit), Oregon State University	Combined overflowing and wave overtopping hydraulic and morphological modeling to evaluate measure protections—flume tests	Li et al. (2012) ,Li et al. (2021) (IAHR monograph)	29	Full	Determing Hydraulics and erosion characteristics under combined steady and wave overtopping conditions. Evaluating levee protection measures including: High-performance turf reinforcement (HPTRM), Articulated concrete blocks (ACB), and Roller compaction concrete (RCC)
Aix-Marseille University, Marseille, France	Lateral levee breaching in cohesive material—lab tests	Charrier (2015)	5	Small	Experimental strudy of fulivial dikes failure; Homogenous levee constructed from cohesive materials (HERODE canal of IRPHE)
Sigmaplan project, Belgium	Overtopping— cohesive dike breach, field scale	Peeters et al. (2015)	2	Full	Headcut migration in cohesive material and breach growth in time;
University of South Carolina	Levee breach —Overtopping	Feliciano Cestero et al. (2015)	8	Small	Experimental investigation of the effects of soil properties on levee breach by overtopping; Wide granulometry
Hydraulics Research Institute, HRI-NWRC, Egypt	Overtopping—sand dike breach, lab scale	Mohamed and El-Ghorab (2016)	1	Large	Scale-series tests to study scale effects on dike breach reduced-scale models
			1	Medium	
			1	Small	
University of South Carolina, Columbia, SC, USA	Influence of compaction on embankment breaching —Overtopping	Tabrizi et al. (2017)	4	Samll-2D	Homogenous sand dike with different compaction levels
French R&D program "DigueELITE"	Lime-treated dike reinforcement—overtopping	Puiatti et al. (2018)	1	Full	The use of lime treated soils in water retaining structures; Surface erosion; Performance of soil-lime mixes

University of Liège, Belgium	Breaching of fluvial sand dikes—laboratory experiments	Rifai et al. (2017), Rifai et al. (2019)	17	Small	Continous monitoring of breach expansion; Main channel inflow variation; Downstream boundry conditions (backwater) influence on breach evolution.
EDF R&D, LNHE Chatou	Breaching of fluvial sand dikes—laboratory experiments	Rifai et al. (2021)	8	Small	
Xi'an University of Technology (State Key Laboratory), China	Rockfill dam breach failure—Overtopping	Li et al. 2021	3	Small	Sand-gravel embankment dams breach laboratory modeling; Inclined rockbed base; with and without drainage zone inside dike body.
Portuguese National Laboratory for Civil Engineering (LNEC) and IST-CERIS Instituto Superior Técnico, Lisbon, Portugal	Cohesive earth dam overtopping—Lab scale	Bento et al. 2017	1	Small	Direct Estimate of the breach hydrograph using surface velocity maps measured with large-scale particle image velocimetry (LSPIV). Silty sand;
	Cohesive earth dam overtopping—Lab scale	Amaral et al. 2021	5	Small	Designing (guideline) dam or dike breach experiments; Investigating hydraulic parameters of flow through a breach.
	Hydrodynamic study of breach outflow	Alvarez et al. 2022		Small	Pure Hydrodynamic breach flow study; 3D print of dike; Half dike breach flow
	Fluvial levee breach—lab scale	Jónatas et al (submitted to JHE)	7	Small	Non-cohesive fine materials; Continous monitoring of breach expansion using Time-of-Flight (ToF) LiDAR and Structure from Motion (SfM)
Sahand Univ. of Technology, 5331817634 Tabriz, Iran	Earth Dam Breaching—Overtopping	Sadeghi et al. (2020)	18	Small	Zoned dam configuration;Outflow Hydrographs of Nonhomogeneous
OVERCOME Project, regional project, France and Spain	Coarse-grained well graded soils dike breaching experiments-small, medium and full scale tests	Morris et al. 2021	1	Medium	Breaching of dikes constructed from coarse-grained well graded soils; scale series
		Monteiro Alves et al. 2023	9	Small	Dikes constructed from sand, Cruched granite, and alluvial soil
		CNR reports, 2023 and 2024	2	Large	Alluvial soil along Rhone River (sand and gravel).

Universidad Politécnica de Madrid	Rockfill Dams downstream slope failure—Overtopping and seepage	Ricardo Monteiro-Alves et al. (2022)	50	Small	Varing parameters such assediment size (uniform gravels), dam configuration, dam height, crest length, downstream slope.
			64	Medium	
Compagnie Nationale du Rhône (CNR), INRAE and Aix-Marseille University	Field test on a Rhone river levee —Overtopping	Picault et al. 2022	2	Prototype	Levee has a composite structure constructed from compacted silt and sandy gravel and gravel fill covered with low quality grass cover
University of Liege, Belgium	Breaching of fluvial sand dikes—laboratory experiments	Vincent Schmitz, 2022?	26	Small	Effect of Dike Geometry on Breach Discharge and Widening
INTERREG Polder2Cs project, Hedwige-Prosperpolder Living Lab	Steady overtopping—prototype levee experiments	Koelewijn et al. 2022	27	Prototype	Impact of quality of grass, overflow discharge, presence of a tree on levee slope, temporary repair measures, etc.
	Levee erosion due to wave overtopping—prototype levee experiments	Ebrahimi et al. 2024	5	Prototype	Photogrammetry application to continous monitoring of erosion progression into clay cover of levee. Impact of wave distrubution (regular, and irregular waves) and test location on erosion of bare clay.
Chalk and Clay project, Hedwige-Prosperpolder Living Lab	Erosion of lime-treated clay dike revetment induced by wave overtopping—prototype levee experiments	Ebrahimi et al. 2024, report of Theo	7	Prototype	Lime-treated clay dike reinforcement; Erosion progression into the new dike revetment specially at the levee-structure transition/interface area. Clay types; Photogrammetry technique application to intermittent monitoring and erosion measurement.
Key Laboratory of Mountain Hazards and Earth Surface Process, Chengdu, China	Landslide dam breaching and induced flood—overtopping	Zhou et al. (2019); (2022)	4	Medium	Study of longitudinal evolution of dam profile, erosion rate relationship; Lab tests
			2	Large	Dam configuration, crest length; Overtopping and combined overtopping- seepage failures; Field tests
Tongji University, Shanghai, China	Lanslide earthfill dams—overtopping	Yang et al. (2024)	8	Small	Wide-graded material heterogenous material, fixed and erodible bed; Final topography and deposition in downstream area.

Swiss Federal Institute of Technology (ETH Zurich) (Zurich, Switzerland)	Composite dike failure—overtopping	Halso et al. 2025a and b	21	Small	homogeneous dams modeling (study of sediment gradation, sediment compaction, reservoir head, scale). Zoned dam constituted of clay core and granular shoulders; Investigation of failure mode and scaling of the cohesive core.
UCLouvain (Université Catholique de Louvain), Belgium	Laboratory tests of overtopped noncohesive dike or embankments	Nathan et al. (2024)	4	Small	Breach formation in sand dikes; Validation and calibration of a numerical model based on the Shallow-water-Exner equations.
TU Delft	Laboratory tests of overtopped sand dike or without and with shoreline protection	van den Berg (2025)	7	Medium	Effect of foreshores on sand dike breach development via a mid-scale experiment (3 tests without foreshore)
UCLouvain-SPW MI Hydraulics Reserch Laboratory collaboration	Modeling sand dike breaching at medium scale—flume experiments	Present study; Ebrahimi et al. (Submitted to JHR)	8	Medium	Breach formation in sand dikes: Influence of sand grain sizes and overtopping conditions; Improvement of measurement techniques. Scale effects in sand embankments.
UCLouvain-LEMSC	Modeling sand dike breaching at small scale	Present study; Delpierre et al. (2026)	11	Small	Scale effects in sand embankments failure due to overtopping; Distributed Optical Fiber Application as a complement to the photogrammetry.

Appendix B: Medium-scale experimental programs

Test No.	Test acronym	d_{50} (mm)	H_s[a]	H_b[c]	H[d]	Date
	Constant inflow					
1	*mS_Q_1*	0.61	1	0.8	N/A	28 Mar 2024
2	*mS_Q_2*	0.61	1	0.8	N/A	24 Apr. 2024
3	*mS_Q_3*	0.61	1	0.8	N/A	20 Mar 2025
4	*fS_Q_4*	0.31	1	0.8	N/A	14 Mar 2024
5	*fS_Q_5*	0.31	1	0.8	N/A	10 Apr 2024
	Constant water level					
6	*fS_H_6*	0.31	1	0.9	0.95	25 May 2023
7	*fS_H_7*	0.31	1	0.93	0.98	14 Sep 2023
8	*fS_H_8**	0.31	1	0.9	0.95	05 Dec 2024
9	*Failed test due to Piping*	*0.31*	*1*	*0.8*	*0.95*	*04 May 2023*
10	*Variable inflow (regulation system did not function due to the initial pilot channel level)*	*0.31*	*1*	*0.80*	*0.95*	*15 May 2023*
11	*Belgian Hydraulic Day: Constant water level, no breach monitoring, low compaction*	*0.31*	*1*	*0.80*	*0.95*	*1 Oct 2023*
12	*Full overtopping (1000 l/s)*	*0.31*	*1*	*0.8*	*N/A*	*01 Mar 2024*
13	*Variable inflow*	*0.31*	*1*	*0.8*	*N/A*	*7 Mar 2024*

Appendix C: On the use of distributed optical fibre sensors to complement photogrammetric measurements of experimental dike breaching

As part of the small-scale experimental campaign conducted in this research, the use of optical-fiber sensors to detect the evolution of the bed elevation in the experiments was investigated. This exploratory work led to the submission of a paper to the Journal of Hydraulic Research, that is now under revision. The abstract of the paper is provided in this Appendix.

Authors: Nathan Delpierre[1], Masoumeh Ebrahimi[1], Alex Bertholet[1], Alessandro Scaioli[2], Lorenzo Panzeri[2], Laura Longoni[2], Hadrien Rattez[1], and Sandra Soares-Frazão[1] (Under review, Journal of Hydraulic Research).

1 Institute of Mechanics Materials and Civil engineering, UCLouvain, Louvain-la-Neuve, Belgium

2 Department of Civil and Environmental Engineering, Politecnico di Milano, Milan, Italy

Abstract

Monitoring dam-breaching experiments is challenging because imaging techniques like photogrammetry cannot penetrate turbid, aerated water to track bed elevation changes. This study presents a measurement campaign of small-scale dike breaching experiments using Distributed Optical Fibre Sensors (DOFS) to complement photogrammetric measurements. The fibre was placed transversally across the dike below the crest to monitor breach dynamics with minimal flow disturbance. Results show that optical fibre effectively tracks the breach bottom location and deepening process. However, careful post-treatment is necessary since optical fibres are sensitive to temperature gradients from infiltration. Strain and strain rate data distinguish between infiltration effects and mechanical processes such as erosion and block failure. Distributed optical fibre proves to be a promising tool that simultaneously generates valuable data on both infiltration and erosion, offering a powerful complement to traditional non-invasive imaging methods for experimental dam breach monitoring.

Appendix D: Spatiotemporal levee erosion and wavefront velocity dataset from in-situ wave overtopping experiments

The Polder2Cs project led to the Bonsai project in which further data analysis about field breaching tests was conducted. As the coordinator of the related working group, I prepared a data paper with the members of this group. This paper has been submitted to Scientific Data of Nature Journal, and the abstract is provided here.

Masoumeh Ebrahimi[1], Myron van Damme[2], Niels van der Vegt[3,4], Andre Koelewijn[5], Vera van Bergeijk[6], Claire Damblans[7], Bilal al Tfaily[7], Abdelkrim Bennabi[7], Ammar Aljer[8], Sandra Soares-Frazão[1] (Under review, Scietific Data of Nature Journal)

1. Institute of Mechanics, Materials, and Civil Engineering (iMMC), UCLouvain, Belgium
2. Rijkswaterstaat WVL, Utrecht, The Netherlands
3. Department of Civil Engineering and Management, University of Twente, Enschede, The Netherlands
4. HKV Consultants, Lelystad, The Netherlands
5. Department of Flood Defence Technology, Deltares, Delft, The Netherlands
6. Department of Coastal Structures and Waves, Deltares, Delft, The Netherlands
7. IRC - ESTP-Paris - COMUE Paris Est, 28, Avenue du Président Wilson, 94230 Cachan
8. Laboratoire de Génie Civil et Géo-Environnement (LGCgE), ULR 4515, Université de Lille, Lille, France

Abstract

During extreme storm events, waves that run-up and overtop levees cause a significant hydraulic load on the landside slopes. In order to determine the effects of these loads on the flood risk, it is necessary to determine the sensitivity of the landside slope to erosion. Models exist for determining the erosion resistance of grass covers to wave overtopping. The challenge has

been to qualitatively describe the erosion process due to wave overtopping and to quantify the erosion rate of clay exposed to wave overtopping loads. To address this challenge, prototype scale wave overtopping experiments have been performed. To facilitate the transfer of the results to other locations and clay types, the Erosion Function Apparatus has been used to predict the erosion characteristics from small samples collected from the test sites.

Here we present a dataset containing measurements from four experimental campaigns designed to evaluate the erosion resistance of existing and newly constructed clay covers under controlled overtopping loads. It includes soil properties, hydraulic loading programs, overtopping characteristics, wavefront velocities, and erosion progression data. The dataset enables comparative analyses across levee types and provides a reproducible foundation for model calibration, erosion assessment, and flood defence design.